

**Dissertation**  
submitted to the  
**Combined Faculty of Natural Sciences and Mathematics**  
**of Heidelberg University, Germany**  
for the degree of  
**Doctor of Natural Sciences**

**Put forward by**  
**Marvin Holten**  
**Born in: Heidelberg**  
**Oral examination: 25.05.2022**



**From Pauli Blocking to Cooper Pairs:  
Emergence in a Mesoscopic 2D Fermi Gas**

**Referees:**

**Prof. Dr. Selim Jochim**

**Prof. Dr. Markus K. Oberthaler**



## Abstract

The emergence of collective and universal behaviour is at the heart of many of the exotic phases of matter that challenge our physical understanding until today. Fermionic superfluidity and superconductivity, for example, are found in a wide range of strongly correlated materials. And while it is understood that pairing is the fundamental prerequisite for their occurrence, the microscopic mechanisms for pair formation remain in many cases unknown.

In this thesis, we study the emergence of collective behaviour and superfluidity at the most fundamental level — from the bottom up. To this end, we deterministically prepare the ground state of a mesoscopic Fermi gas consisting of up to 20 atoms in a two-dimensional harmonic potential. Our ultracold quantum gas allows us to freely tune the interactions from a completely non-interacting state to a regime of strong binding. We apply a novel fluorescence imaging technique to extract the momentum distribution of the strongly interacting Fermi gas and with full spin and single particle resolution. We observe a few-body precursor of a phase transition from a normal to a superfluid phase for a system consisting of as few as six interacting particles. It is revealed by the presence of Cooper pairs we detect directly as correlations between particles of opposite spin and momentum at the Fermi surface. When the attraction strength is increased, we observe how the pair character changes and a transition from Cooper pairs to tightly bound molecules occurs. The collective behaviour we discover in our mesoscopic system is closely related to observations in atomic and nuclear physics, superconducting grains or quantum dots. Our platform, with its completely programmability of interactions, particle numbers, the quantum state and the potential landscape, opens up new pathways to study such strongly correlated mesoscopic systems and their connection to the macroscopic world.



## Zusammenfassung

Die Entstehung von kollektivem und universellem Verhalten liegt vielen der exotischen Materiezustände zugrunde, die bis heute unser physikalisches Verständnis herausfordern. Beispielweise lassen sich fermionische Suprafluidität und Supraleitung in einer Vielzahl stark korrelierter Materialien finden. Und obwohl bekannt ist, dass Paarbildung die grundlegende Voraussetzung für das Auftreten dieser Effekte ist, sind die mikroskopischen Mechanismen die zur Paarung führen oft unbekannt.

In dieser Arbeit untersuchen wir die Entstehung von kollektivem Verhalten und Suprafluidität auf der grundlegendsten Ebene – von kleinen hin zu größeren Systemen. Dazu präparieren wir den Grundzustand von bis zu 20 Atomen eines mesoskopischen Fermigas deterministisch in einem zweidimensionalen harmonischen Potential. Das ultrakalte Quantengas ermöglicht es uns, die Wechselwirkungen von einem völlig wechselwirkungsfreien Zustand bis zu einem Regime starker Bindung beliebig einzustellen. Wir wenden eine neuartige Fluoreszenz-Abbildungsmethode an, um die Impulsverteilung des stark wechselwirkenden Fermi-Gases mit Spin- und Einzelteilchenauflösung zu bestimmen. Wir beobachten die Wenig-Teilchen-Vorstufe eines Phasenübergangs von einem normalen zu einem superfluiden Zustand für ein System aus nur sechs wechselwirkende Teilchen. Der Übergang wird durch das Vorhandensein von Cooper-Paaren offenbart, die wir direkt als Korrelationen zwischen Teilchen mit entgegengesetztem Spin und Impuls an der Fermi-Oberfläche nachweisen. Wenn die Anziehungstärke erhöht wird, beobachten wir, wie sich der Paar-Charakter ändert und die Cooper-Paare zu tief gebundenen Molekülen übergehen. Unser mesoskopisches Fermigas ist eng verwandt mit Systemen in der Atom- und Kernphysik, supraleitenden Nanoteilchen oder Quantenpunkten. Unsere Plattform, mit der vollständigen Kontrolle über Wechselwirkungen, Teilchenzahl, den Quantenzustand und die Potentiallandschaft, eröffnet völlig neue Möglichkeiten um solche stark korrelierten mesoskopischen Systeme und ihre Beziehung zur makroskopischen Welt zu untersuchen.



# Contents

<b>1</b>	<b>Introduction</b>	<b>1</b>
1.1	Superfluidity and Superconductivity . . . . .	2
1.2	Emergence in Ultracold Atoms . . . . .	3
1.3	Outline of the Thesis . . . . .	4
1.4	List of Publications . . . . .	7
<b>2</b>	<b>Quantum Many-Body Systems</b>	<b>9</b>
2.1	Microscopic Model . . . . .	11
2.2	Macroscopic Description . . . . .	15
2.3	The Mesoscopic World . . . . .	27
<b>3</b>	<b>Atomic Physics</b>	<b>37</b>
3.1	Internal Structure . . . . .	37
3.2	Scattering of Cold Atoms . . . . .	40
3.3	External Fields . . . . .	53
<b>4</b>	<b>Experimental Techniques</b>	<b>59</b>
4.1	State Preparation . . . . .	59
4.2	Bottom Up Approach . . . . .	67
4.3	Internal State Manipulation . . . . .	82
4.4	Imaging Schemes . . . . .	85
4.5	Characterizing the 2D gas . . . . .	95
<b>5</b>	<b>Observation of Pauli Crystals</b>	<b>101</b>
5.1	Sampling the Many-Body Wavefunction . . . . .	102
5.2	Pauli Crystals . . . . .	111
5.3	Systematic Effects . . . . .	115
5.4	Conclusion . . . . .	121
<b>6</b>	<b>Emergence of a Quantum Phase Transition</b>	<b>123</b>
6.1	Ground State Preparation . . . . .	124
6.2	Excitation Spectrum . . . . .	129
6.3	Many-Body Picture . . . . .	135

6.4	Different Modulation Schemes . . . . .	145
6.5	Conclusion . . . . .	146
<b>7</b>	<b>Observation of Cooper Pairs</b>	<b>149</b>
7.1	Spin Resolved Imaging . . . . .	151
7.2	Momentum Correlations . . . . .	156
7.3	Emergence of Pairing . . . . .	162
7.4	Systematic Effects . . . . .	171
7.5	Conclusion . . . . .	174
<b>8</b>	<b>The Macroscopic World</b>	<b>177</b>
8.1	Pairing in the Normal Phase . . . . .	177
8.2	Observation of a Quantum Anomaly . . . . .	186
8.3	Conclusion . . . . .	197
<b>9</b>	<b>Summary and Outlook</b>	<b>199</b>
9.1	Real Space Correlations . . . . .	200
9.2	Spin Imbalanced Systems . . . . .	202
9.3	Increasing the Complexity . . . . .	205
9.4	Heidelberg Quantum Architecture . . . . .	206
	<b>Bibliography</b>	<b>209</b>

# List of Acronyms

<b>1D</b>	one dimensional
<b>2D</b>	two dimensional
<b>3D</b>	three dimensional
<b>2D-MT</b>	two dimensional microtrap
<b>AC</b>	alternating current
<b>AOD</b>	acousto-optical deflector
<b>BEC</b>	Bose–Einstein condensate
<b>BCS</b>	Bardeen, Cooper and Schrieffer
<b>BKT</b>	Berezinskii–Kosterlitz–Thouless
<b>CBODT</b>	crossed beam optical dipole trap
<b>CCD</b>	charge-coupled device
<b>CIC</b>	clock-induced charge
<b>DC</b>	direct current
<b>DMD</b>	digital micromirror device
<b>EM-CCD</b>	electron multiplying CCD camera
<b>FFLO</b>	Fulde–Ferrell–Larkin–Ovchinnikov
<b>HQA</b>	Heidelberg Quantum Architecture
<b>LDA</b>	local density approximation
<b>MCMC</b>	Markov chain Monte Carlo
<b>MOT</b>	magneto-optical trap
<b>MT</b>	microtrap
<b>MW</b>	microwave
<b>NA</b>	numerical aperture
<b>ODT</b>	optical dipole trap

<b>PBS</b>	polarizing beam splitter
<b>PCA</b>	principal component analysis
<b>PLL</b>	phase-locked loop
<b>PSF</b>	point spread function
<b>QED</b>	quantum electrodynamics
<b>QCD</b>	quantum chromodynamics
<b>RF</b>	radio frequency
<b>SLM</b>	spatial light modulator
<b>SWT</b>	standing wave optical dipole trap
<b>TOF</b>	time of flight
<b>UHV</b>	ultra-high vacuum

# 1

## Introduction

*“I think a good case can be made that science has now moved from an Age of Reductionism to an Age of Emergence, a time when the search for ultimate causes of things shifts from the behaviour of parts to the behaviour of the collective.”*

– Robert B. Laughlin, *A Different Universe* (2005)

The paradigm of reductionism —the idea that we can explain all phenomena by reducing them to ever smaller entities— has historically always been the driving force of natural sciences and physics in particular. Technical progress and experimental breakthroughs have led to an ever more refined understanding of the most fundamental laws and particles of nature. At the end of the 19th century discoveries like the photoelectric effect [Her87] or the Michelson–Morley experiment [Mic87] have triggered the formulation of modern theories like general relativity or quantum mechanics. The development has culminated in the formulation of the standard model and the detection of the Higgs boson in 2012 as its last previously unobserved fundamental particle [Aad12]. And while a *theory of everything* still remains to be found, the Schrödinger equation alone already covers almost all phenomena we experience in our everyday world in the non-relativist limit [Lau00a]. It is the fundamental law of nature describing everything from atoms to gases, fluids or solids and even more complex structures like molecules or living cells.

The formulation of the Schrödinger equation in 1926 marks not only one of the biggest accomplishments of reductionism but at the same time the beginning of its end as the prevalent scientific worldview. New concepts, summarized under the term *emergence*, came up at the time [Lau05; Wei07]. It was discovered that it is not possible to simply extrapolate from the microscopic laws of nature to larger and larger, increasingly complex structures but “more is different” [And72]. At every scale entirely new collective behaviour emerges, with new effective laws and concepts. Often, the properties of different many-body systems are even universal and do not depend on the microscopic details of the system. The underlying *theory of everything* becomes

irrelevant in the sense that if it were modified within some limits, the phenomena we observe on macroscopic scales would not be altered [Lau00a].

The higher organizing principles that determine the properties of the collective states can generally be described in the framework of phase transitions and broken symmetries [Lan36; Gol62; And72; Sac11]. They lead to self-ordering, new effective degrees of freedom and quasi-particles and in many cases universal low-energy excitation spectra. At a phase transition point, a system might *spontaneously* break an exact symmetry of its underlying Hamiltonian, for example continuous translation invariance when a crystal is formed. This explains in some parts why it is so difficult to predict such effects from first principles even for a moderate number of particles. A further reason is the exponential scaling of the dimensionality or Hilbert space size of the problem with particle number  $N$ . No classical computer will ever be able to solve the Schrödinger equations exactly for large particle numbers required to understand complex systems like cells or proteins [Lau00a]. Instead, progress in the field of quantum many-body systems depends more than ever on experimental discoveries and technical progress.

## 1.1 Superfluidity and Superconductivity

The related effects of superconductivity and superfluidity are prime examples for emergent quantum states that are universally present in a broad range of systems and materials from liquid helium to metals and cold quantum gases. Both phase transitions were first observed in 1911 in the laboratory of Kamerlingh Onnes after he managed to liquify helium for the first time [Van10]. It took almost fifty years before it was realized that the emergent phenomenon of superconductivity is the result of higher organizing principles in the form of symmetries. The *Ginzburg–Landau theory* as a phenomenological theory of superconductivity was formulated in 1950 [Lan66]. A microscopic explanation in terms of bound pairs of electrons or *Cooper pairs* by Bardeen, Cooper and Schrieffer (BCS) followed shortly afterwards [Bar57].

Unconventional or high- $T_C$  superconductors are even more complex. They were first discovered in 1986 in copper oxides also called *cuprates* [Bed86]. Understanding how superconductivity emerges in these materials remains one of the most important problems in modern condensed matter physics, even after more than thirty years of extensive research in the field [Zho21]. It is understood that pairing is an essential ingredient also to high- $T_C$  superconductivity [Yan62]. The pair mechanism, however, is much more complex than the comparatively simple electron-phonon interaction leading to Cooper pairing in conventional superconductors. It is believed that genuine fermionic correlations between the itinerant electrons in the material play the primary role. Accessing pair correlations in cuprates directly is very difficult and numerical or analytical

studies turn out to be even more challenging. This has motivated the search for new experimental approaches to study strongly correlated Fermi systems in the past decade.

## 1.2 Emergence in Ultracold Atoms

Dilute gases of neutral atoms cooled close to absolute zero temperatures represent an attractive platform for the study of many-body physics. They offer a rich palette of tools and tuning knobs that grant control over everything from the external potential of the atoms to their interaction strength or even external artificial magnetic fields [Sta12]. Together with the almost defect free optical potentials and the strong isolation from the environment this allows for the exact implementation of many different theoretical models [Blo08; Blo12]. At the same time, high resolution imaging techniques give access to correlations, sometimes even with single atom and spin resolution, both in-situ and in momentum space [Alt04; Ott16; Gro21].

Ultracold atoms offer the exciting possibility to study emergence starting from the smallest possible building blocks. The system can be assembled from the ground up, one atom at a time [Ser11a; Wen13a]. At the same time genuine collective behaviour and phase transitions are accessible with samples of up to around one million atoms [Gre02]. Quantum gases even promise insights into the still largely unexplored world between the macroscopic and microscopic scales. As Laughlin et al. put it, there is “life in the desert” that exists in the many orders of magnitudes between both limits [Lau00b]. In mesoscopic systems entirely new, still undiscovered, organization principles might appear and these might have profound implications for everything that appears at larger scales. This idea extends to many other fields in science. Even the origin of life might be founded on underlying mechanisms that allow small assemblies of driven systems to self-organize and maximize their energy dissipation [Eng15].

In physics, experiments with helium revealed superfluidity at remarkably small particle numbers of only around 50 atoms [Gre98]. Strong attractive interactions in nuclei generally lead to the emergence of collective modes as well [Gol48]. Spectra consistent with a BCS superfluid have been found [Mig59]. Further examples for collective behaviour at the mesoscopic scale are found in quantum dots, metallic grains or atomic clusters [Alh00; Del01; Cas09]. These different observations show that emergence and self-organization become important already at the smallest scales. The range of tunability in naturally occurring systems is quite limited, however. Ultracold quantum gases with particle numbers and interactions that can be varied by orders of magnitudes provide new opportunities for the field .

To summarize, the formulation of the Schrödinger equation as a fundamental theory of (almost) everything does not provide an immediate solution to all open questions

in many-body physics. Instead, it rather provides a starting point at the microscopic level to go up from and reconstruct larger systems incrementally. Interesting collective effects and new effective laws emerge at every step along the way. Even small mesoscopic structures are more than just building blocks of larger entities. What makes such systems attractive from an experimental viewpoint is that they are often already much too large to be solved exactly. At the same time, with just tens to hundreds of particles, they can not be accurately described by statistical models like thermodynamics that generally work well in the macroscopic limit. Each particle or atom represents a significant fraction of the whole system and the single particle spectra and gaps are large enough to become relevant.

### 1.3 Outline of the Thesis

In our work, we are interested in exploring how collective behaviour and superfluidity emerge in a two dimensional (2D) Fermi gas. The goal is to approach the system “from the bottom up” and to directly study the microscopic (pairing) correlations that lead to phase transitions in the macroscopic limit. To this end, we create an ensemble of ultracold  ${}^6\text{Li}$  atoms that is confined by a highly anisotropic optical potential that restricts all dynamics to a 2D plane. We are able to tune the contact interaction strength between two spin components in the gas from zero all the way to the strongly interacting limit [Zür12a]. A robust fluorescence imaging technique allows us to extract the complete in-situ density or momentum distribution with single particle and spin resolution [Ber18].

The 2D geometry increases the complexity of the quantum state significantly compared to previous studies in one dimensional (1D) samples [Wen13a]. The radial symmetry results in degenerate energy levels and the formation of a shell structure similar to the orbitals of the periodic table of elements. Spontaneous symmetry breaking and long range order are non-existent in 2D systems with short range interactions [Mer66]. The normal to superfluid transition is driven by topological properties instead [Ber72; Kos73]. Fermi gases in 2D are also very interesting from the perspective of high- $T_C$  superconductivity. Many unconventional superconductors are layered structures where electron transport and pair correlations occur predominantly in 2D planes. The relation between reduced dimensionality and high transition temperatures  $T_C$  is an open question in the field [Yu19; Sob21].

In chapter 2, the theoretical framework for all the measurements presented in the thesis is established. The discussion starts at the microscopic level with a brief discussion of the Hamiltonian, single particle spectra and quantum statistics. Phase transitions and spontaneous symmetry breaking are introduced with a focus on the normal to

superfluid transition. BCS theory as the first microscopic model that explains conventional superconductivity is introduced. The chapter is closed by a discussion about the precursors of collective behaviour and modifications to mean field theories that are required for mesoscopic systems.

Chapter 3 contains a review of the most important properties of neutral atoms at ultracold temperatures. Their universal collisional behaviour together with convenient energy spacings in the internal electronic structure have led to the many achievements of quantum gas experiments in the past decade. In chapter 4 all the experimental methods and tools required for the preparation, manipulation and detection of our 2D Fermi gas are presented. This includes a novel spilling technique, initially developed for 1D systems [Ser11a], to prepare pure quantum ground states with deterministic particle numbers for up to 20 atoms. A single atom and spin resolved imaging scheme is introduced that allows us to extract correlations directly in momentum space [Ber18].

In the second part of the thesis, starting with chapter 5, all the experimental results are presented. First studies of completely non-interacting samples in the ground state are shown. We directly observe the Pauli exclusion principle in our continuous system. It manifests itself in the form of higher order correlations that can be visualized with so-called *Pauli crystals* [Hol21b]. The measurement demonstrates that we can extract single particle resolved correlation functions from continuous systems where all the wavefunctions in the initial state overlap. It lays the foundation for the following work.

In chapter 6, attractive interactions are introduced to the system. We perform modulation spectroscopy with ground states of different particle numbers. This allows us to observe a precursor of a quantum phase transition from a normal to a superfluid in our mesoscopic system [Bay20a]. The transition is identified by the non-monotonous energy dependence of a coherent pair excitation resonance together with a detailed comparison to the theory.

The measurement presented in chapter 7 combines all the techniques and abilities that we developed in the preceding studies. We directly observe Cooper pairs in a mesoscopic, weakly attractive 2D Fermi gas [Hol21a]. When we increase the interaction strength, the pairs turn into deeply bound molecules breaking up the Fermi surface. Our observables allow us to precisely characterize the strongly interacting quantum state in terms of the number of pairs and their correlations.

Chapter 8 deals with experiments performed much closer to the thermodynamic limit and with up to  $N = 50\,000$  atoms. The full phase diagram of the 2D BCS-BEC crossover is investigated. We find preformed pairs in the normal phase with an energy that significantly exceeds the expected value from two-body calculations [Mur18b]. They appear in the strongly interacting regime and raise important questions about their relation to the phase transition temperature  $T_C$ . A second study of collective breathing oscillations reveals a *quantum anomaly* of the gas in the same region [Hol18;

[Mur19](#)]. The quantum anomaly describes the violation of a classical scaling symmetry that is present in the 2D gas. The symmetry violation has a profound influence on the collective behaviour of the system. The measurements highlight the richness of the phase diagram of the 2D Fermi gas in the macroscopic limit. This motivates further studies of breathing modes and finite temperature systems also in the mesoscopic regime.

Chapter 9 contains the conclusion of the thesis. Here, the implications of all our measurements for the emergence of collective behaviour in mesoscopic 2D Fermi gases are reviewed. Some of the most promising prospects for future studies with our apparatus are presented in addition. This includes spin imbalanced and finite temperature samples or studies of the emergence of hydrodynamics behaviour at the mesoscopic scale. Our methods hold the potential to improve our understanding of many strongly correlated systems in an unprecedented way.

## 1.4 List of Publications

This thesis is based on the following list of publications:

**High temperature pairing in a strongly interacting two-dimensional Fermi gas**

P. A. Murthy\*, M. Neidig\*, R. Klemt\*, L. Bayha, I. Boettcher, T. Enss, M. Holten, G. Zürn, P. M. Preiss and S. Jochim

[Science](#) **359**, 452-455 (2018)

**Anomalous breaking of scale invariance in a two-dimensional Fermi gas**

M. Holten, L. Bayha, A. C. Klein, P. A. Murthy, P. M. Preiss and S. Jochim

[Phys. Rev. Lett.](#) **121**, 120401 (2018)

**Quantum scale anomaly and spatial coherence in a 2D Fermi superfluid**

P. A. Murthy\*, N. Defenu\*, L. Bayha, M. Holten, P. M. Preiss, T. Enss and S. Jochim

[Science](#) **365**, 268-272 (2019)

**Observing the emergence of a quantum phase transition – shell by shell**

L. Bayha\*, M. Holten\*, R. Klemt, K. Subramanian, J. Bjerlin, S. M. Reimann, G. M. Bruun, P. M. Preiss and S. Jochim

[Nature](#) **587**, 583–587 (2020)

**Observation of Pauli Crystals**

M. Holten\*, L. Bayha\*, K. Subramanian, C. Heintze, P. M. Preiss and S. Jochim

[Phys. Rev. Lett.](#) **126**, 020401 (2021)

**Observation of Cooper Pairs in a Mesoscopic 2D Fermi Gas**

M. Holten, L. Bayha, K. Subramanian, S. Brandstetter, C. Heintze, P. Lunt, P. M. Preiss and S. Jochim

[Preprint, accepted for publication in Nature, arXiv:2109.11511](#) (2021)

Authors marked with \* have contributed equally the publication.



## 2

# Quantum Many-Body Systems

Solving the equations of motion for any quantum mechanical system with interacting particles is remarkably difficult [And72]. Even state of the art supercomputers are limited to tens of particles for the most basic models. Materials in nature typically consist of more than  $10^{23}$  particles. The complexity originates from the exponential scaling of the Hilbert space with particle numbers and interactions that lead to large amounts of quantum correlations and entanglement. The amount of information in the full many-body state becomes too large to even store the wavefunction, let alone use it for calculations.

Instead of solving the problem completely, effective theories and approximations have to be found [Pop99]. In the last century, great progress in the development of such concepts in the field of condensed matter theory has been made. They can be loosely grouped into two subjects [Wen07]. The first one includes models like the band structure and perturbation or Fermi liquid theory. They successfully describe properties like the electric resistivity, heat capacity or optical response of many solids, especially metals and semiconductors. The second group is based on ideas like spontaneous symmetry breaking and renormalization group theory. They are the foundation for phase transitions and descriptions in terms of universal low-energy excitation spectra that emerge due to higher organizing principles. We stress again that the approximate descriptions above are not derived from first principles but rather tailored to experiments [Lau00a].

The discovery of the fractional quantum hall effect in some semiconductors has opened yet another chapter in condensed matter theory [Tsu82]. These materials show a series of plateaus in the Hall conductance that are robust against small perturbations. The plateaus and their values cannot be explained by spontaneous symmetry breaking. Instead, the effect is driven by the topological order of the system [Lau83]. A whole new set of phenomena was discovered including, for example, fractional charges, non-Abelian statistics and edge states. This list highlights the richness of emergent behaviour and represents just the beginning of collective effects that are not completely

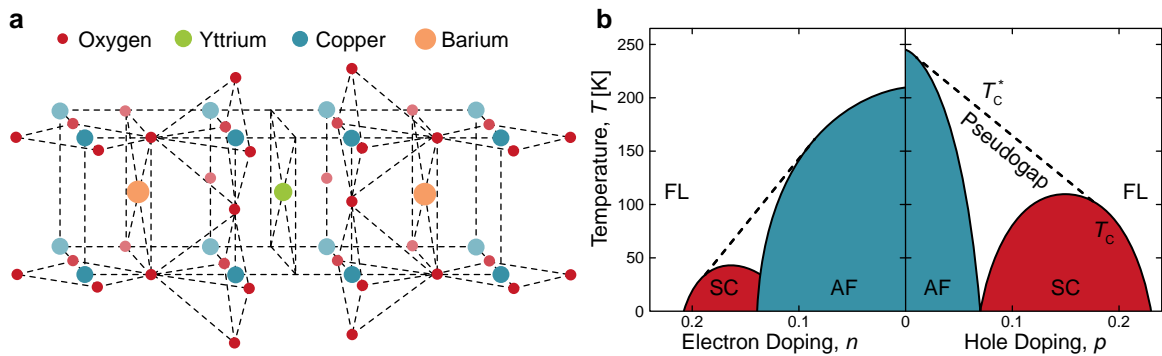


**Figure 2.1: High temperature superconductivity in cuprates.** Segment of the crystalline structure of a yttrium–barium cuprate with a superconducting transition temperature of up to  $T_C = 92$  K (a). The Yttrium atoms act as barrier, confining electron motion to 2D layers. A rich phase diagram emerges in such materials as function of their doping value (b). For small doping an antiferromagnetic (AF) state is found. Superconducting (SC) domes exist left and right of the AF region and at even smaller temperatures. A pairing *pseudogap* region exists in the normal phase above. It is defined by a significant reduction of the density of states close to the Fermi surface. For very large doping the material is well described by Fermi liquid theory (FL).

understood until today [Col03]. High temperature superconductors (see Figure 2.1) and heavy fermion compounds are further prominent examples falling in the same class of strongly interacting fermion systems. Unravelling the mysteries behind these materials belongs to the most important challenges in the 21st century.

In this chapter, the most important concepts developed to describe emergence in many-body systems are presented. The focus is placed on phase transitions and spontaneous symmetry breaking. The BCS-BEC crossover is introduced as general framework describing a large range of interacting Fermi systems. For a more complete introduction to quantum many-body theories the reader is referred to one of the many excellent books on the topic [Alt06; Sac11; Col15]. The chapter is divided into three sections. First, the single microscopic model describing all the systems we study in our experiments is introduced. This is followed by a discussion of the many-body physics that is expected on a macroscopic scale and with large particle numbers. The last section deals with the mesoscopic world in between both limits. Important modifications of the collective behaviour occur in the case of small and deterministic particle numbers. The goal of this thesis is to study how collective behaviour emerges starting from the

smallest possible building blocks of a system.

## 2.1 Microscopic Model

A pure quantum state of  $N$  particles can be represented by its many-body wavefunction in real space  $\Psi_N(\mathbf{r}_1, \dots, \mathbf{r}_N, t)$ . Here,  $\Psi_N$  expresses the probability amplitude of finding the particles at the  $N$  positions  $\mathbf{r}_1, \dots, \mathbf{r}_N$  and at time  $t$ . The wavefunction obeys the Schrödinger equation:

$$i\hbar \frac{\partial}{\partial t} \Psi_N(\mathbf{r}_1, \dots, \mathbf{r}_N, t) = \mathcal{H} \Psi_N(\mathbf{r}_1, \dots, \mathbf{r}_N, t). \quad (2.1)$$

Often, we are most interested in the stationary eigenstate solutions given by the time-independent Schrödinger equation  $\mathcal{H}\Psi_N = E\Psi_N$ . A vast amount of interesting Hamilton operators  $\mathcal{H}$  exists, describing many different aspects of nature. We focus on the specific microscopic model underlying all the experimental studies discussed in this thesis:

$$\mathcal{H} = - \sum_{i=1}^N \frac{\hbar^2}{2m} \nabla_i^2 + \sum_{i<j} \frac{\hbar^2}{2m} g_0 \delta^{(d)}(\mathbf{r}_i - \mathbf{r}_j) + \sum_{i=1}^N \mathcal{V}_{\text{ext}}(\mathbf{r}_i). \quad (2.2)$$

Here, the first term describes the kinetic energy of the particles with mass  $m$ . The second term describes pair-wise, zero-range (or contact) interactions between the particles with coupling constant  $g_0$  and in  $d$  dimensions. The last term describes an external potential  $\mathcal{V}_{\text{ext}}$  that is the same for all particles.

In this thesis, we are most interested in the two dimensional case, where  $d = 2$ . The reduced dimensionality has some profound implications for the behaviour of the system. Even though the Hamiltonian is rather innocuous-looking, it actually leads to the emergence of a very complex phase diagram and collective behaviour that is very challenging to predict.

### 2.1.1 Scale Invariance

A close look at equation (2.2) reveals a very intriguing symmetry of the Hamiltonian in 2D and for  $\delta$  interactions. Ignoring the external potential  $\mathcal{V}_{\text{ext}}$  for now, the total Hamiltonian transforms as  $\mathcal{H} \rightarrow \mathcal{H}/\lambda^2$  under a scale transformation  $\mathbf{r} \rightarrow \lambda\mathbf{r}$ . This does not effect the equations of motion and the 2D system is consequentially *scale invariant* [Pit97]. The sample becomes fully integrable and the dynamics of the full time-dependent many-body wavefunction  $\Psi_N(\mathbf{r}_i, t)$  can be expressed directly in terms

of the initial state  $\Psi_N(\mathbf{r}_i, t = 0)$  [Mur19]. The presence of the scale invariance symmetry on the level of the classical Hamiltonian is therefore expected to greatly simplify the description of collective behaviour of the system.

The truth is, as it turns out so often in many-body systems, much more complicated. A direct quantization of the  $\delta^2$  interaction potential is impossible and gives rise to inconsistent results. A well-defined quantum theory can only be obtained through a renormalization procedure. A new length scale, the 2D scattering length  $a_{2D}$ , has to be introduced that brakes the scale invariance of the bare Hamiltonian. This violation of the exact symmetry of the classical action in the corresponding quantized theory is referred to as *quantum anomaly* [Ols10].

The quantum anomaly in 2D represents a first example for a mechanism by which the collective behaviour of a system can violate the symmetries of its microscopic description. More details on the anomaly and its influence on macroscopic scales can be found in chapter 8.

## 2.1.2 External Potential

As a result of the external potential, the non-interacting or single particle spectrum of the system becomes gapped with discrete energy eigenvalues  $E$ . Often, it is useful to expand the many-body wavefunction in the corresponding basis of single particle wavefunctions  $\Psi_E$  as:

$$\Psi_N(\mathbf{r}_1, \dots, \mathbf{r}_N, t) = \sum_{E_1 \dots E_N} c(E_1 \dots E_N, t) \Psi_{E_1}(\mathbf{r}_1) \dots \Psi_{E_N}(\mathbf{r}_N), \quad (2.3)$$

where the sum runs over all combinations of non-interacting energy eigenvalues  $E$  for each particle. In our experiment, we confine the particles in attractive traps that can be approximated by harmonic potentials. The external potential can generally be written as:

$$\mathcal{V}_{\text{ext}}(\mathbf{r}) = \frac{1}{2}m \sum_{i=1}^d \omega_i r_i^2, \quad (2.4)$$

where  $\omega_i$  is the harmonic oscillator frequency in direction  $i$ . In 1D this leads to the well known spectrum of single particle levels, denoted by  $|n\rangle$  ( $n \in \mathbb{N}_0$ ) and spaced equally in energy  $E_n = \hbar\omega (n + 1/2)$ . The corresponding eigenfunctions  $\Psi_n(x)$  in real space are given by Hermite-Gaussian functions. These are invariant under continuous Fourier transforms and therefore the single particle wavefunctions of the harmonic oscillator in real and momentum space are equivalent  $\Psi_n(x) \equiv \Psi_n(p)$ . This peculiarity of the harmonic potential will become important again for the discussion of *Pauli crystals* in chapter 5.

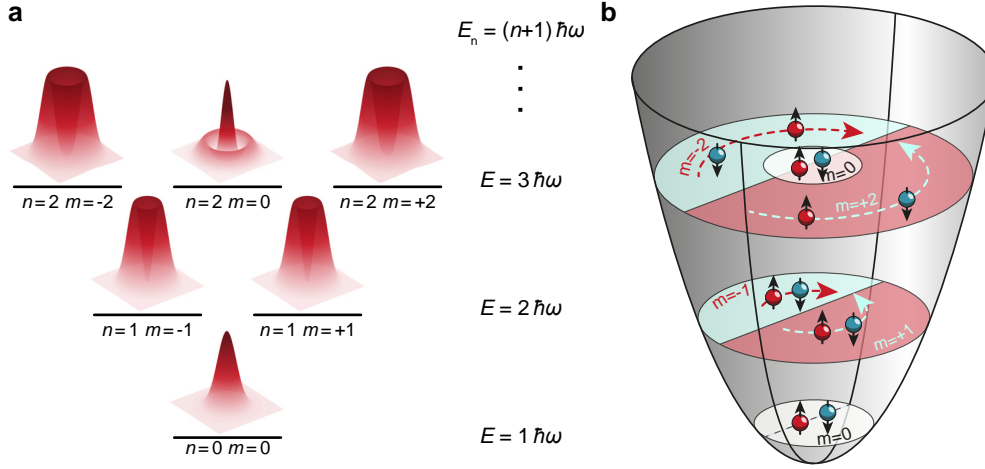


**Figure 2.2: Single particle spectrum of a 2D harmonic oscillator.** The non-interacting levels can be labelled by the quantum numbers  $n$  and  $m$  (a). The 2D probability density distribution corresponding to each wavefunction is depicted in red. The  $n^{\text{th}}$  energy oscillator level is  $(n + 1)$ -fold degenerate. When filled with non-interacting fermionic particles of two different spin components this leads to a shell structure with an energy spacing of  $\Delta E = \hbar\omega$  (b). Particularly stable, closed-shell configurations exist for the magic numbers  $N = 2, 6, 12, 20, \dots$ . These states are akin to the noble gases of the periodic table of elements.

In 2D and with rotational symmetry  $\omega = \omega_x = \omega_y$ , the single particle spectrum shows the same energy spacing  $E_n = \hbar\omega(n + 1)$  as in the 1D case. The important difference is that the  $n^{\text{th}}$  level is now  $(n + 1)$ -fold degenerate (see Figure 2.2 a). The single particle levels can be labelled by  $|n, m\rangle$ , where  $n \in \mathbb{N}_0$  indicates the energy level and  $m = -n, -n + 2, \dots, n - 2, n$  corresponds to the angular momentum  $L_z$  perpendicular to the 2D plane. The typical length and momentum scales of the harmonic potential are defined as the harmonic oscillator length  $l_{\text{HO}} = \sqrt{\hbar/m\omega}$  and momentum  $p_{\text{ho}} = \hbar/l_{\text{ho}} = \sqrt{\hbar m\omega}$  respectively.

### 2.1.3 Symmetrization

So far, we have ignored the symmetry properties of the wavefunction in the case of indistinguishable particles. For fermions (bosons), the complete many-body wavefunction has to be fully antisymmetric (symmetric) when any two identical particles are exchanged. The Pauli exclusion principle, as fundamental law of structure formation,

follows directly from this symmetry: No two fermions can occupy the same quantum state! For the harmonic oscillator discussed above, this leads to a shell structure in the ground states when the potential is filled with non-interacting particles. In the case of a single spin component, competently filled or *closed shell* configurations appear at the magic numbers of  $N = 1, 3, 6, 10, \dots$  particles. We typically work with two different spin components in our experiment so that each level can be occupied by two atoms instead (see Figure 2.2 b).

For a fixed number of fermions, an antisymmetric many-body wavefunction expanded in terms of single particle orbitals  $\Psi_E$  like in equation (2.3) can be constructed through a so called Slater determinant:

$$\Psi_N^{\text{asym.}}(\mathbf{r}_1, \dots, \mathbf{r}_N) = \frac{1}{\sqrt{N!}} \begin{vmatrix} \Psi_{E_1}(\mathbf{r}_1) & \Psi_{E_2}(\mathbf{r}_1) & \dots & \Psi_{E_N}(\mathbf{r}_1) \\ \Psi_{E_1}(\mathbf{r}_2) & \Psi_{E_2}(\mathbf{r}_2) & \dots & \Psi_{E_N}(\mathbf{r}_2) \\ \vdots & \vdots & \ddots & \vdots \\ \Psi_{E_1}(\mathbf{r}_N) & \Psi_{E_2}(\mathbf{r}_N) & \dots & \Psi_{E_N}(\mathbf{r}_N) \end{vmatrix}. \quad (2.5)$$

The number of terms in this determinant scales as the factorial of  $N$ . For 10 particles in the ground state of the 2D harmonic oscillator, for example, this leads to a total of around 720 million Legendre polynomials for the full wavefunction in real space. A much more efficient representation of the many-body state is possible in the language of *second quantization* [Neg18]. Here, the many-body state is created by acting with fermionic creation operators of the form  $c_i^\dagger \equiv c_{\sigma,n,m}^\dagger$  on the vacuum state  $|0\rangle$ . A ground state of three fermions in the 2D harmonic oscillator, for example, can be written as

$$|\text{GS}\rangle = c_{\uparrow,1,1}^\dagger c_{\uparrow,1,-1}^\dagger c_{\uparrow,0,0}^\dagger |0\rangle. \quad (2.6)$$

The correct symmetry is imposed by the anti-commutator relations between the creation operators  $\{c_i^\dagger, c_j^\dagger\} = 0$ .

### 2.1.4 Correlation Functions

Arbitrary many-body states  $|\Psi\rangle$  can generally be characterized by analysing the correlations between their constituents [Alt04; Sch17]. By studying the correlation functions order by order, this perturbative approach can reveal new properties about the collective quantum state at each level. The knowledge of all correlations is equivalent to a full solution of the quantum theory. However, the amount of available information scales exponentially with the system size [Fla12]. It is therefore crucial to identify and detect only those microscopic correlations that most efficiently describe a given state of matter [Zac20].

For an arbitrary operator  $\hat{O}(\alpha)$ , the  $n^{\text{th}}$  correlation function is defined as

$$\mathcal{C}^{(n)}(\alpha_1 \dots \alpha_n) = \langle \Psi | \hat{O}(\alpha_1) \dots \hat{O}(\alpha_n) | \Psi \rangle, \quad (2.7)$$

where  $\alpha$  represents a generalized quantum number like the harmonic oscillator level  $n$ , position  $x$  or momentum  $p$ . The expectation value  $\langle \dots \rangle$  can be evaluated experimentally by averaging over many realizations or large ensembles. A good choice for the characterization of quantum states of attractively interacting fermions are density correlations in momentum space, where  $\hat{O}(\alpha) \rightarrow \hat{n}(\mathbf{p})$ . They allow us to directly access quantities like the paired fraction and pairing mechanism. The latter are key ingredients to emergent superfluid behaviour in fermionic samples. The corresponding measurements are discussed in more details in chapter 7.

### 2.1.5 Energy Scales

Even without an exact solution it is still possible to make some qualitative predictions about the behaviour of the system from the microscopic Hamiltonian in equation (2.2). Each of the three terms can be associated with a different energy or length scale (see Figure 2.3). The kinetic energy term is related to the inter-particle distance  $d \propto 1/k_F$  or Fermi energy  $E_F$ . The contact interactions lead to the presence of a bound state (more on the special role of 2D in section 3.2.8). The binding energy  $E_B$  or size ( $\propto a_{2D}$ ) of this bound state can be used to characterize the interaction strength. In the previous sections we have already discussed how the harmonic confinement leads to a shell structure with energy spacing  $E_{HO} = \hbar\omega$ . Often, we study thermal mixtures instead of pure quantum states in the experiment. In this case the Temperature  $T$  defines a fourth energy scale  $E_T = k_B T$ .

The collective behaviour of the system is determined by the competition between its different intrinsic energy scales. In general, the description becomes simple whenever a single term dominates over all the others. When two or more scales are on the same order, however, this generally leads to the emergence of complex phases that are much more difficult to understand. The qualitative phase diagram of the macroscopic system as a function of the different energy scales will be discussed in detail in the next section.

## 2.2 Macroscopic Description

The limitations of *first quantization*, where observables are represented by operators  $\hat{x}, \hat{p}, \dots$  and the quantum state by the many-body wavefunction  $\Psi_N$ , have already become apparent in section 2.1.3. In nature, we are often concerned with systems that are in equilibrium with their environment and, for example, with fluctuating or unknown

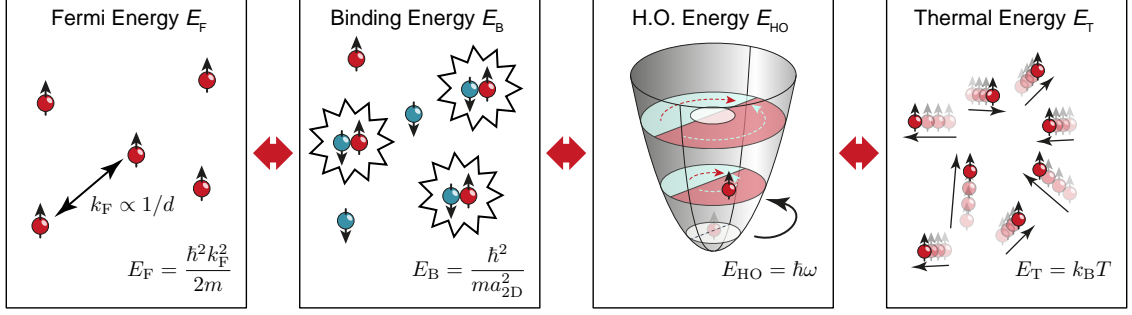


**Figure 2.3: Competition between energy scales of the 2D Fermi gas.** The qualitative behaviour of a system can be predicted by comparing its intrinsic energy scales. Each energy scale can also be associated with a length or momentum scale and a temperature.

particle numbers. For macroscopic materials a much more efficient quantum description of the relevant degrees of freedoms at low energies is required, independent of the location of every single particle. The solution is provided by the language of quantum field theory, directly related to the ideas of second quantization.

The first step is to replace the description in terms of single particle wavefunctions by one in terms of field operators [Col15]:

$$\Psi(\mathbf{r}), \Psi^*(\mathbf{r}) \rightarrow \hat{\Psi}(\mathbf{r}), \hat{\Psi}^\dagger(\mathbf{r}) \quad \text{with} \quad \{\hat{\Psi}(\mathbf{r}_1), \hat{\Psi}^\dagger(\mathbf{r}_2)\} = \delta^{(n)}(\mathbf{r}_1 - \mathbf{r}_2), \quad (2.8)$$

where  $\{\dots\}$  denotes the anti-commutator in the case of fermionic particles. The action of the operators  $\hat{\Psi}(\mathbf{r})$  and  $\hat{\Psi}^\dagger(\mathbf{r})$  on some state  $|\Psi\rangle$  annihilates or creates a single particle at position  $\mathbf{r}$  respectively. The many-body state can be constructed particle by particle from the empty vacuum state  $|0\rangle$  as:

$$|\mathbf{r}_1, \dots, \mathbf{r}_N\rangle = \hat{\Psi}^\dagger(\mathbf{r}_N) \dots \hat{\Psi}^\dagger(\mathbf{r}_1) |0\rangle, \quad (2.9)$$

With annihilation and creation operators efficient descriptions of mixed states with different particle numbers become possible, for example in a grand canonical ensemble. As already discussed in section 2.1.4, the quantum field operators offer an approach that is naturally perturbative and their correlations allow us to characterize the many-body state order by order. In the case of fermionic particles in a 2D harmonic oscillator, it is often useful to express the field operators in real or momentum space in terms of the creation or annihilation operators of the respective eigenstates  $|\sigma, n, m\rangle$  like

$$\hat{\Psi}_\uparrow^\dagger(\mathbf{r}) = \sum_{n,m} \Psi_{n,m}(\mathbf{r}) c_{\uparrow,n,m}^\dagger, \quad (2.10)$$

where  $\Psi_{n,m}$  are the corresponding single particle (Hermite-Gaussian) wavefunctions. The basis transformation for field operators in momentum space follows analogously.

The most important feature of quantum field theory is that it establishes a formalism for the description of the coarse grained behaviour of a many-body system. The excitation spectrum of some solid might for example be described by collective fields. The corresponding quasiparticle excitations are created by the action of those fields on the ground state  $|\text{GS}\rangle$ . A simple example are acoustic and optical phonons that appear as quantized excitations in crystalline lattices like metals. In general, the action of some collective field  $\Phi(\mathbf{r})$  involves many different creation and annihilation operators, or in other words, many different particles [Col15]

$$\Phi(\mathbf{r}) = \sum_{\mathbf{k}} \left[ \phi(\mathbf{k})\Psi^\dagger(\mathbf{k}) + \tilde{\phi}(\mathbf{k})\Psi(\mathbf{k}) \right]. \quad (2.11)$$

Here,  $\phi(\mathbf{k})$  and  $\tilde{\phi}(\mathbf{k})$  are some general expansion coefficients. By formulating an effective action  $S$  for the collective fields in the low energy limit, predictions about the dynamical response and phase transitions in large systems become possible.

### 2.2.1 Phase Transitions and Symmetry Breaking

Phase transitions lie at the very heart of emergent phenomena in many-body systems. They describe a significant and often discontinuous change in the physical properties like the conductivity or volume of some medium as a result of a change in the external parameters like temperature  $T$  or pressure  $p$ . Many phase transitions go hand in hand with a reduction of the symmetry of the system. For example, the continuous translational invariance is broken when water freezes or rotational symmetry is violated by iron when it becomes magnetic [Col15]. There are, however, also some very notable exceptions where the phase transition is driven by topological effects rather than the symmetry of the material, as already pointed out in the beginning in this chapter [Col03].

Landau was the first one to develop a general phenomenological model for symmetry breaking phase transitions in 1937 [Lan37]. He introduced the abstract concept of an order parameter  $\Psi$  that quantifies the behaviour of the medium at the phase transition point, for example as a function of the temperature:

$$|\Psi| = \begin{cases} 0 & \text{for } T > T_C, \\ |\Psi_0| > 0 & \text{for } T < T_C. \end{cases} \quad (2.12)$$

In general, the order parameter is zero in the unordered phase, typically at larger temperatures and becomes finite in the symmetry broken state. A classification into two

groups of phase transitions is possible. A *first order* phase transition is characterized by a jump in the order parameter at the critical point and involves latent heat, for example when ice is melting. The second group of *continuous phase transitions* does not involve a jump of the order parameter, as the name suggests. Typical examples are the transition from a para- to a ferromagnet or from the normal to the superconducting phase.

While Landau's description is applicable to a broad range of materials, the form of the order parameter  $\Psi$  varies from case to case. It can be expressed as a single complex number for example or a spinor or a vector field. On the microscopic scale, any order parameter is connected to the expectation value of a quantum field [Col15]. For example, the order parameter for a Heisenberg ferromagnet is given by the expectation value of the spin vector  $\mathbf{m} = \langle \mathbf{S} \rangle$ . A very simple and instructive case, we discuss in the following section, is given by superfluid or superconducting states. Here, the order parameter can be expressed as the expectation value of the bosonic quantum field itself  $\Psi = \langle \hat{\Psi}_B \rangle$ , where  $\hat{\Psi}_B \propto \hat{\Psi}_\uparrow \hat{\Psi}_\downarrow$  for fermionic particles.

### 2.2.2 Ginzburg-Landau Theory

Based on the ideas of spontaneous symmetry breaking, Ginzburg and Landau developed the first accurate description of superconductivity in 1950, the so-called Ginzburg-Landau theory [Gin50]. While it describes many of the properties of conventional superconductors correctly, it is a purely phenomenological model, inspired by a close comparison to experiments rather than microscopic insights. Motivated by the close similarities to Bose-Einstein condensates (BECs), especially the long range order and phase rigidity of the medium, the order parameter is defined as a macroscopic complex scalar field  $\Psi(\mathbf{r}) = |\Psi(\mathbf{r})| e^{i\phi(\mathbf{r})}$ .

In absence of external electromagnetic fields, the effective action describing the equilibrium state of the order parameter  $\Psi(\mathbf{r})$  near the superconducting phase transition is defined as [Sac11; Pek15]

$$S[\Psi]_{\text{static}} = \int d^3r \left[ \frac{\hbar^2}{2m^*} |\nabla\Psi|^2 + \alpha |\Psi|^2 + \frac{\beta}{2} |\Psi|^4 \right]. \quad (2.13)$$

Here,  $m^*$ ,  $\alpha$  and  $\beta$  are phenomenological parameters that depend on the temperature  $T$  and have to be fitted to experiments. Since the action should be bound from below, we require  $\beta > 0$ . One of the most important properties of the action (2.13) is that it is invariant under the U(1) symmetry group. These transformations can be represented as  $\Psi \rightarrow \Psi e^{i\phi}$  with  $\phi \in [0, \pi]$ .

The expectation value of the order parameter in equilibrium  $\langle \Psi \rangle$  is obtained by minimizing the action  $\delta S / \delta \Psi = 0$ . In a spatially uniform situation, we can neglect the

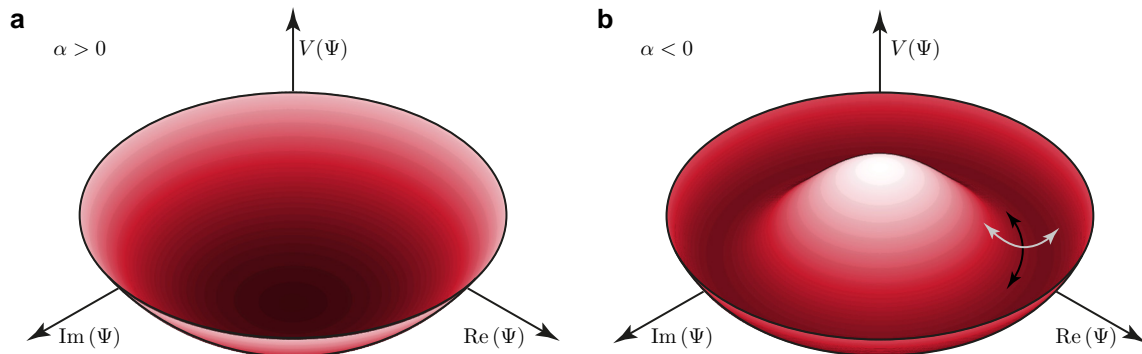


**Figure 2.4: Spontaneous breaking of U(1) symmetry.** The effective potential  $V(\Psi)$  in the action for the complex field  $\Psi$  is shown in red for different signs of the parameter  $\alpha$ . In the normal phase, when  $\alpha > 0$ , the potential minimum is located at  $\Psi_0 = 0$  (a). Below the phase transition point, when  $\alpha < 0$ , the effective potential has the shape of a *Mexican hat* (b). An infinite number of degenerate minima exists at a finite value for the order parameter  $\Psi_0 = \sqrt{-\alpha/\beta}e^{i\phi}$  ( $\phi \in [0, 2\pi]$ ). By choosing a single minimum with some phase  $\phi_0$ , the medium *spontaneously* breaks the U(1) symmetry of the underlying action. The low energy excitations around the minimum in amplitude or phase direction are referred to as Higgs (grey arrow) and Goldstone (black arrow) modes respectively.

first term and are left with the effective potential  $V(\Psi) = \alpha |\Psi|^2 + \frac{\beta}{2} |\Psi|^4$  (see Figure 2.4). We can distinguish between two important cases: If  $\alpha > 0$ , the potential minimum is located at  $\Psi = 0$ . Consequentially, the ground state is U(1) symmetric and the system is in the normal phase without long range phase coherence. If  $\alpha < 0$ , the potential takes the shape of a *Mexican hat* and there are an infinite amount of degenerate ground states at  $\Psi_0 = \sqrt{-\alpha/\beta}e^{i\phi}$  ( $\phi \in [0, 2\pi]$ ). By *spontaneously* picking one phase  $\phi_0$ , the ground state of the system breaks the U(1) symmetry. The expectation value for the order parameter becomes finite and long range phase coherence builds up. The material is in the superconducting state.

There are several important properties that can be derived from the model [Col15]. Since the transition occurs by definition when  $T = T_C$ , it is useful to expand  $\alpha$  to leading order in  $T$  as:

$$\alpha = \alpha_0(T - T_C) \quad (2.14)$$

We identify  $m^*$  with the effective mass of the bosonic particles (or pairs). The correla-

tion length  $\xi$  is then given by [Col15]

$$\xi = \sqrt{\frac{\hbar^2}{2m^*|\alpha|}} = \xi_0 \left|1 - \frac{T}{T_C}\right|^{-\frac{1}{2}}, \quad (2.15)$$

where we define the coherence length  $\xi_0$  as

$$\xi_0 = \sqrt{\frac{\hbar^2}{2m^*\alpha_0 T_C}}. \quad (2.16)$$

$\xi_0$  corresponds to the length scale over which a local perturbations in the density  $|\Psi(\mathbf{r})|^2$  affects the medium around it. Finally, the penetration depth  $\lambda$ , indicating the distance over which an external magnetic field decays inside the superconductor, is given by

$$\lambda = \sqrt{\frac{m^*}{4\mu_0 e^2 |\Psi_0|^2}} = \sqrt{\frac{m^* \beta}{4\mu_0 e^2 |\alpha|}}. \quad (2.17)$$

In order to understand the low energy behaviour of the superconductor, we need to consider the possible excitation around the ground state. To this end the full action  $S = S_{\text{dynamic}} + S_{\text{static}}$  including the dynamical part

$$S[\Psi]_{\text{dynamic}} = \int d^3r \left[ iK_1 \Psi^*(\mathbf{r}, t) \frac{\partial}{\partial t} \Psi(\mathbf{r}, t) - K_2 \left( \frac{\partial}{\partial t} \Psi^*(\mathbf{r}, t) \right) \left( \frac{\partial}{\partial t} \Psi(\mathbf{r}, t) \right) \right] \quad (2.18)$$

has to be considered [Pek15]. By solving the equations of motion and expanding the low energy modes into amplitude and phase fluctuations as  $\Psi(\mathbf{r}, t) - \Psi_0 \approx \delta_a(\mathbf{r}, t) + i\delta_\phi(\mathbf{r}, t) + \dots$  respectively, we obtain two coupled differential equations [Pek15]

$$\left(-2\alpha + \frac{\hbar^2}{2m^*} \mathbf{q}^2 - K_2 \omega^2\right) \delta_a + iK_1 \omega \delta_\phi = 0, \quad (2.19)$$

$$\left(+\frac{\hbar^2}{2m^*} \mathbf{q}^2 - K_2 \omega^2\right) \delta_\phi - iK_1 \omega \delta_a = 0. \quad (2.20)$$

Here, we have already Fourier transformed to the wave-vector  $\mathbf{q}$  and frequency  $\omega$  variables. Equation (2.19) shows that the amplitude  $\delta_a$  and phase  $\delta_\phi$  fluctuations are generally coupled in the Mexican hat potential. As a result, no independent stable amplitude mode can be observed [Pek15].

A special situation occurs when  $K_1 = 0$ , as for example guaranteed in particle physics since  $K_1 \neq 0$  would violate Lorentz invariance. Here, phase and amplitude modes decouple into separate excitations (see Figure 2.4 b) with dispersion relations

$$\omega_\phi^2 = \frac{\hbar^2 \mathbf{q}^2}{2m^* K_2} \quad \text{and} \quad \omega_a^2 = \frac{\hbar^2 \mathbf{q}^2}{2m^* K_2} + \frac{2|\alpha|}{K_2}. \quad (2.21)$$

The massless phase excitations are generally referred to as Goldstone modes, while the gapped or massive amplitude excitation is known as the Higgs mode in particle physics [Hig64]. In condensed matter systems, a different mechanism is required in order to make the observation of a distinct Higgs mode possible [Pek15]. This is provided by (approximate) particle-hole symmetry, that analogously leads to  $K_1 \approx 0$ . Amplitude modes have successfully been observed in a range of different mediums from superconductors to cold atoms [End12; Mat13; Méa14; Léo17]. Even without a perfect particle-hole symmetry a distinct Higgs mode can still be observed if the coupling  $K_1$  is small enough [Beh18]. The amplitude mode simply becomes broadened and unstable due to possible decay channels into the Goldstone modes that are much lower in energy.

### 2.2.3 BCS Theory

While the Ginzburg-Landau theory predicts many effects of the superconducting phase transition correctly, it does not explain the microscopic mechanism behind the formation of a condensate and electron pairing. A complete microscopic picture was provided only a few years later by Bardeen, Cooper and Schrieffer (BCS) [Bar57]. The development was triggered by the experimental discovery of the isotope effect that brought the attention to interactions between electrons and the ionic crystal lattice of the superconductors. The final connection between the microscopic and phenomenological model was achieved by Gor'kov in 1959 [Gor59].

The origin of conventional superconductivity is an attractive interaction between electrons in a metal that is mediated by phonons of the ionic crystal lattice [Tin04]. Intuitively, it can be imagined as originating from a tube of ions that are displaced towards the path of an electron moving with momentum  $\mathbf{k}$  through the lattice. Their positive charge acts as a negative, attractive potential for other electrons. They feel the force to a full extent only when moving head on with respect to the original electron with opposite momentum  $-\mathbf{k}$  [Wei81]. In general, a weak attractive force alone does not guarantee the presence of paired bound states if the interaction is not strong enough. This is different in the presence of the Fermi sea that is created by Pauli blocking between the fermions. For two electrons, opposite to each other on the quasi-2D Fermi surface, an arbitrary weak attraction with coupling strength  $g$  is enough to form a bound state with energy  $E_B = 2\omega_D e^{-2/g\nu_0}$  [Coo56]. Here,  $\omega_D$  is the Debye frequency and  $\nu_0$  is the density of states at the Fermi surface. The presence of the bound state leads to a macroscopic ground state that consists of a coherent superposition of many of these *Cooper pairs*.

A simplified Hamiltonian, implementing the phonon mediated attractions and with-

out external fields can be written down as [Col15]:

$$\mathcal{H}_{\text{BCS}} = \sum_{\mathbf{k}, \sigma} \xi_{\mathbf{k}} c_{\mathbf{k}\sigma}^\dagger c_{\mathbf{k}\sigma} - \frac{g}{V} \sum_{\mathbf{k}, \mathbf{k}'} c_{\mathbf{k}\uparrow}^\dagger c_{-\mathbf{k}\downarrow}^\dagger c_{-\mathbf{k}'\downarrow} c_{\mathbf{k}'\uparrow}, \quad (2.22)$$

where  $\xi_{\mathbf{k}} = \frac{\hbar^2 k^2}{2m} - \mu$  is the electron dispersion relative to the chemical potential,  $V$  is the volume and in the second sum  $\mathbf{k}$  and  $\mathbf{k}'$  run over a small shell around the Fermi sphere  $|\epsilon_{\mathbf{k}}| < \omega_{\text{D}}$ . An approximate solution to the problem can be obtained by expanding the pair operator  $\frac{1}{V} \sum_{\mathbf{k}} c_{-\mathbf{k}\downarrow} c_{\mathbf{k}\uparrow}$  around its expectation or *mean-field* value  $\Delta = \frac{g}{V} \sum_{\mathbf{k}} \langle c_{-\mathbf{k}\downarrow} c_{\mathbf{k}\uparrow} \rangle$  as

$$\frac{1}{V} \sum_{\mathbf{k}} c_{-\mathbf{k}\downarrow} c_{\mathbf{k}\uparrow} = \frac{\Delta}{g} + \left[ \frac{1}{V} \sum_{\mathbf{k}} c_{-\mathbf{k}\downarrow} c_{\mathbf{k}\uparrow} - \frac{\Delta}{g} \right]. \quad (2.23)$$

For weak interactions, we assume that the correction term in [...] is small and we only keep it to first order. This leads to the following mean-field BCS Hamiltonian

$$\mathcal{H}_{\text{MF}} = \sum_{\mathbf{k}} \begin{pmatrix} c_{\mathbf{k}\uparrow}^\dagger & c_{-\mathbf{k}\downarrow} \end{pmatrix} \begin{pmatrix} \xi_{\mathbf{k}} & -\Delta \\ -\Delta^* & -\xi_{\mathbf{k}} \end{pmatrix} \begin{pmatrix} c_{\mathbf{k}\uparrow} \\ c_{-\mathbf{k}\downarrow}^\dagger \end{pmatrix} + \sum_{\mathbf{k}} \xi_{\mathbf{k}} + \frac{V|\Delta|^2}{g}. \quad (2.24)$$

It is important to note that the Hamiltonian contains terms like  $\Delta c_{\mathbf{k}\uparrow}^\dagger c_{-\mathbf{k}\downarrow}^\dagger$  and it is therefore not particle number conserving. It can be diagonalized by applying the Bogoliubov transformation that expresses the electron creation operators ( $c_{\mathbf{k}\sigma}$ ,  $c_{\mathbf{k}\sigma}^\dagger$ ) in terms of new fermionic quasiparticles ( $\gamma_{\mathbf{k}\sigma}$ ,  $\gamma_{\mathbf{k}\sigma}^\dagger$ ) [Bog58]

$$\gamma_{\mathbf{k}\uparrow} = \cos \theta_{\mathbf{k}} c_{\mathbf{k}\uparrow} + \sin \theta_{\mathbf{k}} c_{-\mathbf{k}\downarrow}^\dagger, \quad (2.25)$$

$$\gamma_{-\mathbf{k}\downarrow}^\dagger = \sin \theta_{\mathbf{k}} c_{\mathbf{k}\uparrow} + \cos \theta_{\mathbf{k}} c_{-\mathbf{k}\downarrow}^\dagger. \quad (2.26)$$

In the new basis, the Hamiltonian becomes diagonal

$$\mathcal{H}_{\text{MF}} = \sum_{\mathbf{k}, \sigma} E_{\mathbf{k}} \gamma_{\mathbf{k}\sigma}^\dagger \gamma_{\mathbf{k}\sigma} + \sum_{\mathbf{k}} (\xi_{\mathbf{k}} - E_{\mathbf{k}}) + \frac{V|\Delta|^2}{g}, \quad (2.27)$$

with the excitation energy  $E_{\mathbf{k}} = \sqrt{\xi_{\mathbf{k}}^2 + |\Delta|^2}$  and  $\sin^2 \theta_{\mathbf{k}} = \frac{1}{2} \left( 1 - \frac{\xi_{\mathbf{k}}}{E_{\mathbf{k}}} \right)$ .

The quasi particle excitations  $\gamma$  consist of both particle creation and annihilation operators. Therefore, the bare electron dispersion  $\xi_{\mathbf{k}}$  splits into two branches  $\pm E_{\mathbf{k}}$  that are gapped with distance  $2\Delta$  at  $|\mathbf{k}| = k_{\text{F}}$  (see Figure 2.5 a). In the ground state, the lower branch is completely filled, while the upper branch is empty. No low-energy quasi particle excitations are possible below a certain threshold in the superconductor.

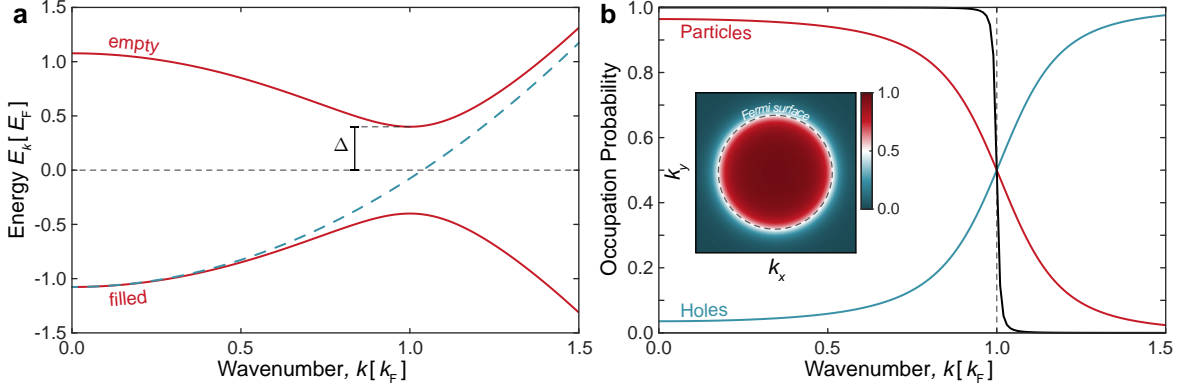


**Figure 2.5: BCS dispersion relation and occupation probability as a function of the momentum.** The attractive interactions between the electrons at the Fermi surface lead to a splitting of the bare dispersion relation (a, dashed blue line) into two branches gapped by  $\Delta$  (red lines). In the ground state, the lower branch is completely filled while the upper branch is empty. This leads to a minimum energy that is required to excite the superconductor. In (b), the electron occupation probability in the BCS ground states is shown as a function of the wavenumber  $k$  (red). Cooper pairs are excited across the Fermi surface (dashed line) by the interactions. The inset shows the occupation probability in 2D. In the limit of vanishing attraction strength  $\Delta \rightarrow 0$ , the non-interacting Fermi sea is restored (black).

From equation (2.27) it is clear that the BCS ground state  $|\text{BCS}\rangle$  is the state without any quasiparticle excitations, defined by  $\gamma_{k\sigma} |\text{BCS}\rangle = 0$ . It can be constructed as

$$|\text{BCS}\rangle = \mathcal{N} \prod_{\mathbf{k}} \gamma_{-\mathbf{k}\downarrow} \gamma_{\mathbf{k}\uparrow} |0\rangle = \prod_{\mathbf{k}} \left( \cos \theta_{\mathbf{k}} - \sin \theta_{\mathbf{k}} c_{\mathbf{k}\uparrow}^{\dagger} c_{-\mathbf{k}\downarrow}^{\dagger} \right) |0\rangle. \quad (2.28)$$

Compared to a non-interacting Fermi sea this shows that a conventional superconductor is described by the coherent excitations of electron (Cooper) pairs with opposite spin and momentum ( $c_{\mathbf{k}\uparrow}^{\dagger} c_{-\mathbf{k}\downarrow}^{\dagger}$ ) above the Fermi surface (see Figure 2.5 b). Close to the Fermi surface and in the limit of small interactions  $\Delta \rightarrow 0$ , a BCS superconductor is particle hole symmetric (red and blue curves), as required for the observation of a stable Higgs mode. The BCS model is directly implemented by the Hamiltonian we access in our experiments (see equation 2.2) in the limit of weak, attractive contact interactions  $g_0 \rightarrow 0^-$  and in a homogenous gas  $\mathcal{V}_{\text{ext}} \rightarrow 0$ . In terms of the characteristic energy scales of the medium this corresponds to the case where  $E_{\text{F}} \gg E_{\text{B}}$ . Note that  $E_{\text{B}}$  refers to the two-body bound state in 2D here and not to the Cooper pair binding

energy. The superfluid gap is given by  $\Delta = \sqrt{2E_F E_B} \gg E_B$  in this case [Ran89]. In our experiment, we are not limited to this regime but, in contrast to a real superconductor, we are able to tune the interactions freely until  $E_F \sim E_B$  or even  $E_F \ll E_B$ . Here, the BCS description breaks down and quantum fluctuations around the mean-field value become significant.

### 2.2.4 BCS-BEC Crossover

When the binding energy  $E_B$  is increased, starting from the BCS limit of Cooper pairs, the ground state remains the superfluid and there is a smooth transition all the way to the point where  $E_B \gg E_F$ . In this opposite limit the description of the macroscopic system becomes simple again, as expected whenever a single energy scale dominates over all others. The fermions form tightly bound molecules that interact repulsively and that can be approximated by point-like bosonic particles. The ground state of the gas is described by a molecular BEC [Joc03; Gre03; Zwi03]. The smooth transition of the superfluid between both limits is referred to as the BCS-BEC crossover [Zwe12; Par14; Str18].

In our experiments we can access a large region of the phase diagram of the BCS-BEC crossover in 2D by tuning the interaction parameter  $g_0$  and temperature  $T$  (see Figure 2.6) [Rie15a]. We observe a phase transition at temperature  $T_C$  from a normal to a superfluid at any value for the interaction strength (dashed black line). The highest transition temperature  $T_C$  is found in the strongly correlated region  $E_B \sim E_F$ , where any mean-field model like the BCS theory breaks down. No accurate theoretical descriptions for macroscopic particle numbers are known in this regime and new insights require further experimental research [Par14; Str18].

The macroscopic condensate wavefunction breaks the U(1) symmetry of the Hamiltonian. The low temperature spectrum of the superfluid is therefore given by the different excitation modes in the Mexican hat potential (see section 2.2.2). A particle-hole symmetry is, however, only present in the BCS limit and the stable Higgs mode vanishes when going towards the BEC regime [Beh18]. The BEC superfluid is described by the Gross-Pitaevskii equation and its low energy modes are referred to as Bogoliubov quasi-particles [Pet08]. Single particle, pair-breaking, excitations are gapped by the two-body binding energy  $E_B$  in the BEC limit. This is in contrast to the BCS limit, where the many-body gap  $\Delta$  is generally much larger than  $E_B$ .

Emergent behaviour is found not only at the lowest temperatures but also in the normal phase of the gas. In the BCS theory both the formation of Cooper pairs and their condensation occur at the same critical temperature  $T_C$ . This is obviously different far in the BEC limit when  $E_B \gg E_T, E_F$ . Here, the normal phase consists of bosonic molecules. The strongly correlated region where  $E_B \sim E_T \sim E_F$  is most

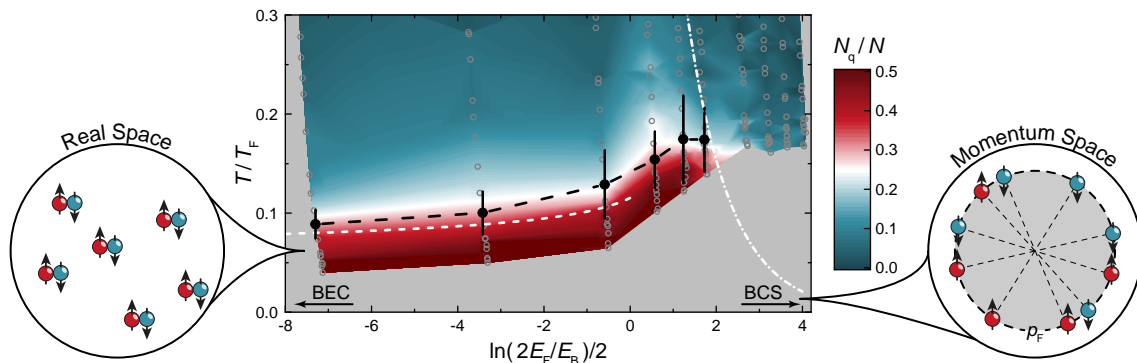


**Figure 2.6: Phase diagram of the 2D BCS-BEC crossover.** A measurement of the pair condensed fraction  $N_q/N$  of a 2D Fermi gas as a function of temperature  $T$  and interaction parameter  $\ln(2E_F/E_B)/2$  is shown. In the BEC limit (left), the pair size is much smaller than the inter-particle spacing  $E_B \gg E_F$  and a molecular BEC forms. The opposite limit, where a Fermi sea is formed  $E_B \ll E_F$ , is well described by the BCS theory (right). There is a smooth crossover between both limits with a maximum critical temperature  $T_C$  (black dashed line) in the region where pair size and inter-particle spacing are of the same order. The white dashed line shows the BCS prediction for  $T_C$ . Adapted from [Rie15a].

complex. Here, in a measurement that is discussed in more detail in chapter 8, we have found preformed pairs in the normal phase with a larger binding energy than what is expected from a two-particle solution [Mur18b]. This indicates that the pair formation is a genuine many-body effect in this region and raises important questions about the relationship of this phase to the superfluid below.

### 2.2.5 Role of Dimensionality

In this thesis, we are primarily concerned with systems in 2D. The reduced dimensionality has a profound influence on the collective behaviour of the gas. In 2D no spontaneous breaking of continuous symmetries, like  $U(1)$ , is possible in systems with finite range interactions and at non-zero temperatures [Mer66]. The reason are low-energy excitations of the Goldstone modes that destroy phase coherence on large length scales in 1D and 2D and restore the symmetry of the Hamiltonian [Hoh67]. There are different mechanisms that explain emergent behaviour in lower dimensions instead. One of the most important examples is the Berezinskii–Kosterlitz–Thouless (BKT) phase transition to a superfluid with quasi-long range order [Ber72; Kos73].

The BKT phase transition is linked to the topology of the macroscopic wavefunction. In the normal phase free vortices, local windings of  $2\pi$  in the phase of the wavefunction, proliferate and destroy any coherence [Had11]. These vortices cannot be *unwound* by a continuous deformation — they affect the topology of the wavefunction. At the transition temperature  $T_C$ , vortices of opposite winding bind together and form pairs, effectively annihilating each other. Only the effect of the phononic excitations remains. They lead to smooth variations in the field  $\Psi$  that can, in contrast to the vortices, be smoothed out by continuous transformations. Below the phase transition, the gas is topologically equivalent to a medium with true long range order, for example a three dimensional (3D) superfluid [Had11].

It is useful to quantify the degree of coherence or long range order to apply it as a criterion for the presence of a superfluid [Pen56]. At the microscopic level, this is possible through the definition of the first order correlation function  $g_1(\mathbf{r}) = \langle \hat{\Psi}^\dagger(\mathbf{r}_0)\hat{\Psi}(\mathbf{r}_0 + \mathbf{r}) \rangle$  [Yan62]. For a homogeneous superfluid in 3D, phase correlations are finite even at large distances and  $\lim_{r \rightarrow \infty} g_1(r) = \alpha$ , with a constant  $\alpha > 0$ . The hallmark of quasi-long range ordered systems in 2D are correlations that decay algebraically instead [Had11]

$$\begin{aligned} g_1(r) &\propto e^{-r/\gamma} && \text{for } T > T_C, \\ g_1(r) &\propto r^{-\eta} && \text{for } T < T_C. \end{aligned} \tag{2.29}$$

We have confirmed experimentally that this type of quasi-long range order is present in our system at low temperatures [Mur15b].

Another important consequence of the choice of a 2D geometry is the scale invariance symmetry of the classical Hamiltonian with contact interaction we already discussed in section 2.1.1. In 3D, scale invariance is not a symmetry of the Hamiltonian but it appears at a particular point in the centre of the BCS-BEC crossover. In this so-called *unitary regime*, all observables can be expressed in terms of the only remaining scale of the systems: its density or Fermi energy  $E_F$ . The description of the *unitary Fermi gas* becomes remarkably simple [Zwe16]. For a 2D system, scale invariance is present everywhere in the crossover, at least on the classical level. However, as opposed to 3D, there is a quantum bound state with energy  $E_B$  present at any interaction strength. Scale invariance is restored when  $E_B \rightarrow 0$  or  $E_B \rightarrow \infty$  and the description of the collective behaviour becomes simple in the BCS and BEC limits. In the centre of the crossover, scale invariance is broken and a *quantum anomaly* appears [Ols10] (see chapter 8).

### 2.2.6 Open Questions

Emergent collective behaviour in Fermi gases with contact interactions has been studied in great detail both on the experimental and theoretical level [Str18]. Above, we have

reviewed some of the most important mechanisms leading to the phase diagram of the BCS-BEC crossover. Both limiting cases are well explained by mean-field models and a direct link between the collective behaviour and the underlying microscopic theory has been established. This is different for the central region of the 2D superfluid. Here, the nature of the correlations between Fermions is not fully understood. Are they similar to molecules as in the BEC regime, or rather explained by Cooper pairs in momentum space? Due to the strong interactions in this region, even higher order correlations, between three or more particles are most likely present. All of these questions extend to the normal phase of the gas and the region of preformed many-body pairs. A more detailed understanding of the strongly correlated, central region of the crossover might help to address many general questions in the field, like the role of the 2D geometry for unconventional superconductivity beyond the BCS model [Sob21].

The work presented in this thesis is the starting point of a new approach to understanding strongly correlated Fermi systems in general. We want to establish new methods to link the macroscopic collective behaviour to the underlying microscopic description of the systems. To this end, we prepare many-body states starting from the smallest instances and with precise control over the macroscopic details. Single atoms detection allows us to observe emergent behaviour starting at a much smaller scale and particle number. The mesoscopic world promises to provide new paths between the atomic and macroscopic scales in the regimes where they are still missing [Lau00b].

## 2.3 The Mesoscopic World

There is no rigorous definition that distinguishes the discipline of mesoscopic physics from the microscopic or macroscopic limits. The field covers everything starting from ensembles of a few atoms on the nanoscale up to materials of several micrometers size. One common property of mesoscopic composites is that the coherence- or wavelength of the particles is generally of the order of the system size. As a result, quantum confinement effects become important, leading to discrete spectra with finite single particle energy gaps [Kha03]. Descriptions in terms of local quantities like conductivity break down and the whole sample has to be treated as a whole [Alh00]. The small particle number leads to large relative amplitudes of quantum and thermal fluctuations and mean-field or statistical theories cannot be applied directly. The persistent advances in the development of semiconductor devices and photolithography, leading to smaller and smaller process sizes, are demanding for better insights into the world of mesoscopic systems. Nanotechnology and nanofabrication promise to remain at the forefront of technological breakthroughs in the coming decades [Poo03].

In this thesis, we are interested in the mesoscopic limit of the BCS-BEC crossover.

We want to find answers to questions like how many-particles are required to observe emergent behaviour like phase transitions and superfluidity and in what ways the small and fixed particle numbers affect their description. Our 2D Fermi gas closely resembles many other systems in nature, for example nuclei [Boh98; Lau17], quantum dots [Alh00], small helium droplets [Gre98], atomic clusters [Cas09] or small superconducting grains [Del01]. Indications of superfluid behaviour have been found for as few as tens of particles in these systems [Mig59; Gre98]. Apart from performing experiments, there are two main approaches to solving mesoscopic quantum systems, where mean field models like the standard BCS theory break down. The size of the Hilbert space can be reduced far enough, for example by introducing some energy cut-off and working at very small particle numbers  $N \lesssim 20$ , such that numerical techniques like exact diagonalization or Monte-Carlo methods become applicable. Or, as presented in this section, the microscopic model can be modified such that it can be applied to mesoscopic systems and simplified enough to be solvable. Here, the art lies in identifying which approximations are justified while retaining a correct physical description of the sample. This process relies heavily on experimental feedback and verification, as we will see in chapter 7.

### 2.3.1 Quantum Confinement Effects

The confinement required to obtain a mesoscopic sample of interacting fermions does inevitably lead to a discrete single particle spectrum. In section 2.1.2, we have already discussed how a 2D harmonic trap introduces a shell structure with an additional energy scale  $E_{\text{HO}}$ . For small particle number ground states, when  $E_{\text{HO}} \sim E_{\text{B}}, E_{\text{F}}$  this clearly affects the phase diagram of the BCS-BEC crossover. A breakdown of superconductivity is expected as soon as the distances between single particle levels in the spectrum are larger than the many-body pairing gap  $E_{\text{HO}} \gtrsim \Delta$  [And59; Del01]. This effect can be observed for example in band insulators, where a critical interaction strength is required before particles can surpass the band gap and a phase transition from a normal to a superconducting state occurs [Koh90; Noz99].

Interacting Fermi gases confined to harmonic 3D potentials have been extensively discussed in Refs. [Bru01; Bru02b; Hei02; Bru02a]. Here, we focus on a 2D geometry [Bru14; Bje16]. Depending on the total particle number  $N$ , two possible situations can occur that determine the nature of the ground state. Either all of the degenerate states of the highest energy level  $n_{\text{F}}$  of the harmonic oscillator that contains atoms are filled (a *closed shell*) or some of the degenerate levels remain empty (an *open shell*). For two interacting spin components, closed shell configurations occur at the *magic* numbers of  $N = 1 + 1, 3 + 3, 6 + 6, \dots$  particles (see Figures 2.2 and 2.7). Here, we have introduced the notation  $N = N_{\uparrow} + N_{\downarrow}$  that will be used throughout this thesis. For open shells,

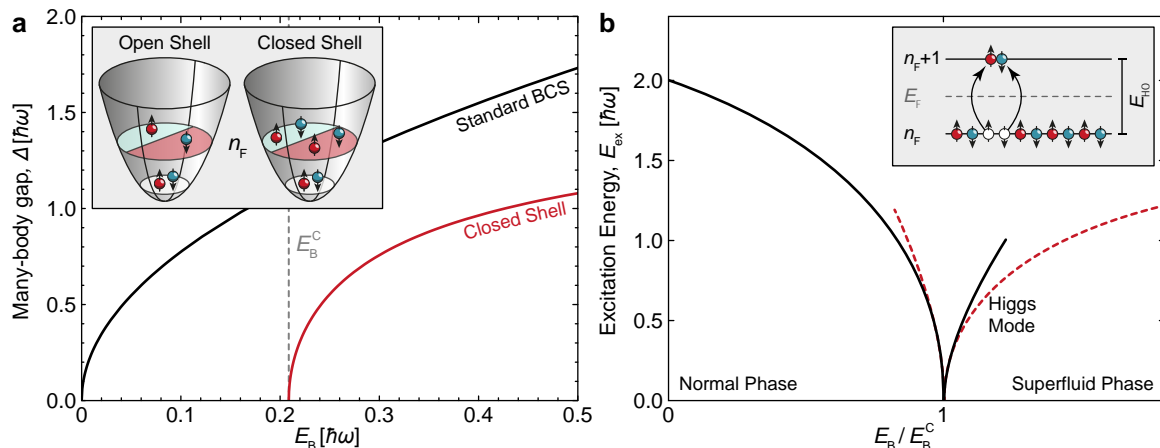


**Figure 2.7: Pairing in closed shell configurations.** At zero temperature and for closed shell configurations pairing is suppressed for small interaction strength (a). A critical two-body binding energy  $E_B^C$  is required before the ground state becomes superfluid and a many-body gap emerges (red) [Bru14]. The low energy excitation spectrum of the system is shown in (b). In the non-interaction limit the lowest monopole mode consists of pair excitations across the Fermi surface with an energy cost of  $E_{\text{ex}} = 2E_{\text{HO}}$  (inset). With increasing interaction strength, the energy cost of pair excitations reduces until the excitation gap closes and the phase transition occurs. In the superfluid phase, the lowest excitation mode is given by the Higgs mode with energy  $2\Delta$ . The solid and dashed lines correspond to numerical and analytical calculations respectively. Pabel (b) adapted from [Bje16].

the ground state is degenerate and in the spectrum there is no gap between filled and empty levels. At zero temperature a normal to superfluid phase transition occurs at any arbitrary small attraction strength larger than zero [Bru14].

A more interesting situation occurs for closed shells. Here, the ground state is unique and the next empty states are separated by the harmonic oscillator energy  $E_{\text{HO}} = \hbar\omega$ . This energy gap stabilizes the state against small perturbations, similar to noble gases in the periodic table of elements. Pairing for small binding energies  $E_B \ll E_{\text{HO}}$  is suppressed and even at zero temperature the system remains in the normal state. A critical interaction strength  $E_B^C$  is required before it becomes energetically favourable for fermions to occupy the empty states at higher energies and to form pairs. The value of  $E_B^C$  depends on the highest filled harmonic oscillator level  $n_F = \sqrt{N + 1/4} - 3/2$ ,

where  $E_F = (n_F + 1)E_{\text{HO}}$ . It can be calculated in a mean-field approximation as [Bru14]

$$E_B^{\text{C}} = E_B \frac{\gamma + 4 \ln 2 + \ln n_F}{2\zeta(2)} \left( \sqrt{1 + \frac{4\zeta(2)}{(\gamma + 4 \ln 2 + \ln n_F)^2}} - 1 \right). \quad (2.30)$$

Here,  $\gamma = 0.577$  is the Euler-Mascheroni constant and  $\zeta(z)$  the Riemann zeta function. When  $E_B > E_B^{\text{C}}$  the ground state becomes paired and a quantum phase transition into a superfluid occurs (in the limit  $n_F \rightarrow \infty$ ). The many-body gap  $\Delta$  in the weakly paired but superfluid regime ( $E_{\text{HO}} > E_B > E_B^{\text{C}}$ ) is then given by [Bru14]

$$\frac{\Delta}{E_{\text{HO}}} = \sqrt{\frac{n_F + 1}{7\zeta(3)} \left[ \frac{E_{\text{HO}}}{E_B^{\text{C}}} - \frac{E_{\text{HO}}}{E_B} + \zeta(2) \left( \frac{E_B}{E_{\text{HO}}} - \frac{E_B^{\text{C}}}{E_{\text{HO}}} \right) \right]}. \quad (2.31)$$

The result for  $N = 12$  and  $n_F = 2$  is plotted in Figure 2.7 (a) together with the mean-field approximation for the homogeneous 2D Fermi gas  $\Delta = \sqrt{2E_F E_B}$  [Ran89].

The quantum phase transition from a normal to a superfluid (in the limit  $n_F \rightarrow \infty$ ) at the critical interaction strength can be identified and understood by studying the low energy excitation spectrum of the gas. In the non-interacting limit, the lowest energy monopole mode (without angular momentum transfer  $\Delta L_z = 0$ ) of a closed shell ground state is given by coherent pair excitations across the Fermi surface (see Figure 2.7 b). It is separated from the ground state by a gap of  $2E_{\text{HO}} = 2\hbar\omega$ . When the attractive interaction strength is increased, the particles that are now located in the almost empty higher energy level  $n_F + 1$  can make use of the degenerate unfilled states and increase their wavefunction overlap. This allows them to gain binding energy and reduces the cost of the monopole excitations monotonously as the interaction strength increases (solid black line). At the critical binding energy  $E_B^{\text{C}}$  the gap closes and coherent pairs can be excited without any energy cost. The system becomes unstable and a second order phase transition to a superfluid state takes place. The lowest energy monopole excitation of the trapped superfluid is given by the Higgs mode with energy  $2\Delta$  (dashed red line).

For  $n_F \rightarrow \infty$ , the number of degenerate states in the highest filled ( $n_F$ ) and first empty ( $n_F + 1$ ) energy levels is almost equal. Therefore, the system is particle-hole symmetric and the Higgs and Goldstone modes decouple into independent excitations. A peculiarity of the closed-shell configuration is that they lead to a stable Higgs mode even in the low-particle number limit  $n_F \rightarrow 0$ . All other collective monopole excitations in the harmonic oscillator require excitation energies of  $E_{\text{ex}} \geq 2\hbar\omega$  [Pit97]. The Higgs mode at  $E_{\text{ex}} = 2\Delta$  is isolated in the spectrum and separated in energy from the discrete Goldstone modes. No direct decay channels are available and the Higgs modes becomes long-lived [Bru14].

In our experiment, we study what remnants of the many-body phase transition at  $E_B^C$  can be observed in mesoscopic closed shell configurations with as little as  $N = 3+3$  particles. An advantage of the small system size is that we can compare our results directly to precise numerical solutions before advancing to larger particle numbers [Bje16]. The numerical and experimental results for the excitation spectra of mesoscopic systems are discussed in great detail in chapter 6. We are able to detect and identify the few-body precursor of the stable Higgs mode that is discussed above.

### 2.3.2 Reduced BCS Model

The systems we study in our experiment are described to a very good approximation by the Hamiltonian in equation (2.2), we already discussed in the beginning of the chapter. In the mesoscopic limit, it is natural to express the contact interaction term  $\delta^2(\mathbf{r}_i - \mathbf{r}_j)$  in second quantization in terms of creation and annihilation operators  $c_{\sigma,i}^\dagger$  and  $c_{\sigma,i}$  in the harmonic oscillator basis. Here,  $\sigma$  is the spin projection and  $i = [n, m]$  is used as a generalized quantum number, encoding both the energy level  $n$  and angular momentum  $m$  of the harmonic oscillator state. This leads to the following expression:

$$\mathcal{V}_{\text{int}} = \frac{\hbar^2}{2m} g_0 \sum_{i,j,k,l} V_{ijkl} c_{\uparrow,i}^\dagger c_{\downarrow,j}^\dagger c_{\uparrow,k} c_{\downarrow,l}, \quad (2.32)$$

where the matrix element  $V_{ijkl} = \langle \uparrow, i; \downarrow, j | \delta^2(\hat{\mathbf{r}}_\uparrow - \hat{\mathbf{r}}_\downarrow) | \uparrow, k; \downarrow, l \rangle$  is most conveniently evaluated in the real space basis.

A sequence of approximations allows us to simplify the interaction term significantly (see Figure 2.8). In the *intrashell* regime, defined by  $E_{\text{HO}} \gtrsim E_B$ , we can assume that significant pairing correlations occur exclusively between *time-reversed* levels [Bru02b; Bru14; Bje16]. The time-reversed state corresponding to a harmonic oscillator level with quantum numbers  $|\uparrow, i\rangle \equiv |\uparrow, n, m\rangle$  is given by  $|\downarrow, i'\rangle \equiv |\downarrow, n, -m\rangle$ . Keeping only the coupling between these pairs reduces the interaction to

$$\mathcal{V}_{\text{int}} = \frac{\hbar^2}{2m} g_0 \sum_{i,j,k,l} V_{ii'jj'} c_{\uparrow,i}^\dagger c_{\downarrow,i'}^\dagger c_{\uparrow,j} c_{\downarrow,j'}, \quad (2.33)$$

In closed shell configurations and in the limit  $n_F \rightarrow \infty$  only harmonic oscillator states close to the Fermi surface with  $E_i \sim E_F > E_{\text{HO}}$  contribute to pair correlations in the ground state. When the interacting system is large enough, such that a local density approximation is applicable, this leads to approximately constant couplings  $V_{ii'jj'} \approx \tilde{g}$  for all time-reversed pair wavefunctions close to the Fermi surface  $|\uparrow, i; \downarrow, i'\rangle$  with  $E_i \approx E_F$ . Including the harmonic oscillator spectrum  $E_i$ , we arrive at the full

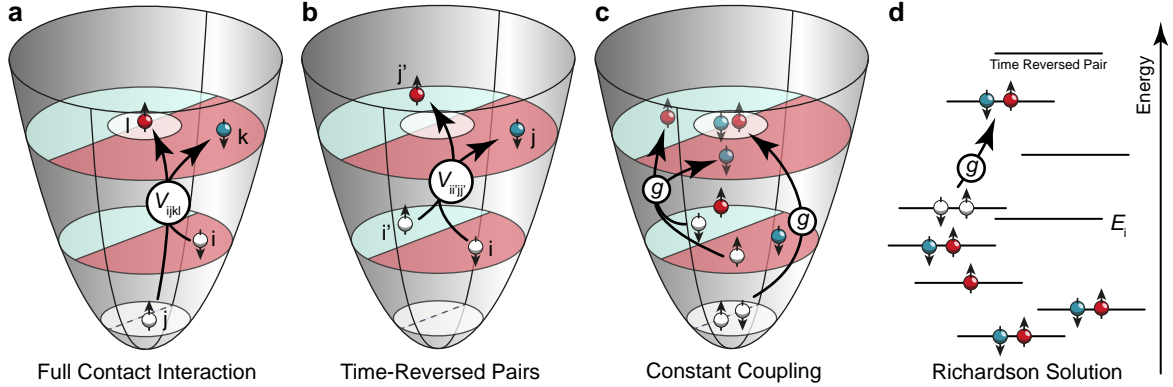


**Figure 2.8: Contact interactions and the reduced BCS model.** The full contact interactions leads to a coupling between opposite spins and any combination of harmonic oscillator levels (a). When the energy spacing  $E_{\text{HO}}$  is large enough, it is justified to assume that pairing correlations occur predominately between time-reversed pairs  $i, i'$  at the same energy level. The coupling between other states can be neglected (b). The assumption of a constant coupling term  $V_{ii'jj'} \equiv g$  for scattering between any of the time-reversed pairs leads to the reduced BCS Hamiltonian (c). The so-called Richardson model generalizes this problem to arbitrary energy level spectra  $E_i$  (d). It provides an exact analytical solution to our system given that the approximations (b,c) are well fulfilled. Note that each energy level (black lines) in (d) directly represents an empty or filled time-reversed pair state in the many-body system. In panels (a-c) the single particle states of the Hamiltonian are shown instead.

Hamiltonian of the form:

$$\mathcal{H}_{\text{BCS}} = \sum_{i,\sigma} E_i c_{\sigma i}^\dagger c_{\sigma i} - g \sum_{i,j} c_{\uparrow,i}^\dagger c_{\downarrow,i'}^\dagger c_{\uparrow,j} c_{\downarrow,j'}. \quad (2.34)$$

We immediately recognize the reduced BCS hamiltonian we already introduced in equation (2.22), the only difference being the discrete energy spectrum  $E_i$  of the 2D harmonic oscillator compared to particles in free space with  $E \propto p^2$ .

It is not a priori obvious that the approximations we used in order to arrive at the reduced BCS Hamiltonian are accurate for mesoscopic samples as  $N \rightarrow 0$ . Nevertheless, they have been applied with great success to systems like nuclei [Bri05] or small metallic grains [Bla96; Del01]. In chapter 7, we present experiments allowing us to examine to what degree the simplified description captures the physical behaviour of ultracold

atoms. The important feature of the model is that it can be solved analytically as presented briefly in the following.

### 2.3.3 Richardson's Solution

An exact solution to the reduced BCS Hamiltonian in equation (2.34) and for arbitrary sets of single particle states  $E_i$  was found by Richardson in the context of nuclear physics [Ric63; Ric64]. Here, we follow the review in Ref. [Del00] to recall the most important ideas of the solution. We start from a set  $S$  of time-reversed states with arbitrary energies  $E_i$  and  $i = 1, \dots, N_S$  (see Figure 2.8 d). The interaction term in the Hamiltonian does not couple to any singly occupied level that we denote by the subset  $B \subset S$ . Consequentially, a general eigenstate of  $N_B$  singly occupied levels and  $n$  time-reversed pairs can be written as [Del00]

$$|n, B\rangle = \prod_i^B c_{\sigma i}^\dagger \left( \sum_{j_1, \dots, j_n}^{S \setminus B} a_{j_1, \dots, j_n} b_{j_1}^\dagger \dots b_{j_n}^\dagger \right) |0\rangle, \quad (2.35)$$

where we have introduced the pair operator  $b_i^\dagger = c_{\uparrow, i}^\dagger c_{\downarrow, i'}^\dagger$ . The  $n$  pairs are distributed among the remaining set of  $U = S \setminus B$  available levels with expansion coefficients  $a_{j_1, \dots, j_n}$ . The sum runs over all possible combinations  $j_i \in U$  with  $j_i \neq j_{i'}$  for all  $i \neq i'$ . The singly occupied levels  $c_{\sigma i}^\dagger$  remain blocked by the Pauli principle independent of the interactions and the solution of the problem factorizes into the unblocked  $U$  and blocked  $B$  level subsets.

We can separate the Hamiltonian into two parts of the form  $\mathcal{H} = \mathcal{H}_B + \mathcal{H}_U$  with [Del00]

$$\mathcal{H}_B |n, B\rangle = \sum_i^B E_i |n, B\rangle = \xi_B |n, B\rangle \quad (2.36)$$

and

$$\mathcal{H}_U |n, B\rangle = \sum_{ij}^U (2E_i \delta_{ij} - g) b_i^\dagger b_j |n, B\rangle = \xi_n |n, B\rangle. \quad (2.37)$$

We note that the singly occupied states merely add an overall energy offset  $\xi_B$  to the total eigenstate while the solution to the unblocked sector is given by the eigenvalue equation (2.37). If we assume for now that the creation operators  $b_i^\dagger$  correspond to true bosonic particles with commutation relations  $[b_i, b_j^\dagger] = \delta_{ij}$ , the eigenenergies  $\xi_n$  are simply obtained by the roots of the equation [Del00]:

$$1 - \sum_i^U \frac{g}{2E_i - \xi_n} = 0. \quad (2.38)$$

This equation is of order  $N_U = N_S - N_B$  in  $\xi_J$  and therefore has multiple solutions  $J = 1, \dots, N_U$ . The many-body ground state  $|\Psi_0\rangle$  is given by the state where all  $n$  pairs occupy the lowest energy time-reversed state, denoted by  $\xi_0$ :

$$|\Psi_0\rangle = \prod_i^B c_{\sigma_i}^\dagger \prod_{j=1}^n b_0^\dagger |0\rangle \quad \text{with} \quad \mathcal{H}_U |\Psi_0\rangle = n\xi_0 |\Psi_0\rangle. \quad (2.39)$$

The full solution of the reduced BCS Hamiltonian is more complicated. The bosonic pairs  $b_i^\dagger$  consist of fermionic particles and therefore no more than one pair can occupy each quantum level at any given time. Hard-core bosonic commutation relations have to be imposed [Del00]:

$$(b_i^\dagger)^2 = 0, \quad [b_i, b_j^\dagger] = \delta_{ij} (1 - 2b_i^\dagger b_i). \quad (2.40)$$

This leads to a further coupling of the eigenvalue equations. This is expected since the levels that are available for scattering of a single pair depend on the location of the other pairs that block an additional  $n - 1$  levels of the subset  $U$ . The full solution of equation (2.37) for hard-core bosons is given by [Del00]:

$$1 - \sum_i^U \frac{g}{2E_i - (\xi^\nu)_J} + \sum_{\mu=1(\neq\nu)}^n \frac{2g}{(\xi^\nu)_J - (\xi^\mu)_J} = 0, \quad \text{with} \quad \nu = 1, \dots, n. \quad (2.41)$$

This equation describes a set of  $n$  coupled equations for the list of  $n$  time-reversed pair energies  $\xi^\nu$ ,  $\nu = 1, \dots, n$ . The total number  $N_T$  of different solutions  $(\xi^\nu)_J$  is given by all possible combinations of distributing the  $n$  pairs across the  $N_U$  available levels and can be calculated as  $N_T = N_U! / (N_U - n)! n!$ . The total eigenenergy  $\xi_J$  of each many-body state  $J = 1, \dots, N_T$  is given by the sum  $\xi_J = \sum_\nu (\xi^\nu)_J$ .

In Figure 2.9 we show the numerical solution of equation (2.41) for the level structure of the 2D harmonic oscillator with  $E_i \equiv E_{n,m} = (2+2n)\hbar\omega$ . Note that here  $E_{n,m}$  already represent the energies of the time-reversed pairs instead of single particle harmonic oscillator levels  $\tilde{E}_{n,m} = (1+n)\hbar\omega$ . The calculation is carried out with 3 pairs or  $N = 6$  particles and without any singly occupied levels such that the ground state corresponds to one of the closed shell configurations. The harmonic oscillator levels  $E_i$  are constrained to a total number of 4 shells ( $n \leq 3$ ) to reduce the computation time. The number of available single particle levels is therefore given by  $N_U = 10$  and there are  $N_T = 120$  many-body states in the spectrum. For moderate values of the interaction strength  $E_B \lesssim E_{\text{HO}}$  the energy cut-off leads only to small quantitative changes in the energies of low lying states in the spectrum. Higher lying harmonic oscillator orbitals with ( $n \geq 4$ ) are only occupied significantly for large binding energies or for states higher up in the spectrum.

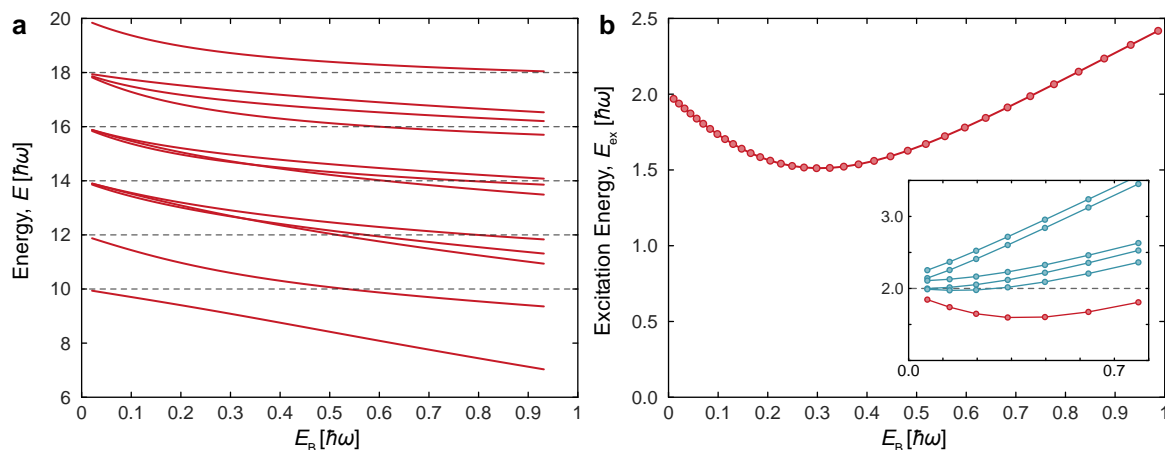


**Figure 2.9: Richardson's solution for  $n = 3$  pairs in a 2D harmonic oscillator.**

In (a) different solutions to the eigenvalue equation of the reduced BCS Hamiltonian are shown as a function of the interaction strength (red lines). The calculation is restricted to the four lowest shells to reduce computation time. The many-body spectrum of the non-interacting Hamiltonian is shown as a comparison (dashed lines). Note that only time-reversed states are coupled by the interactions and all other states are neglected. From the spectrum we can directly obtain the low energy modes of the medium (b). The lowest energy mode shows a non-monotonous dependence on the attractive interaction strength. The inset shows a less accurate calculation with smaller energy cut-off ( $E_i \leq 6\hbar\omega$ ). Here, all  $N_T$  solutions of the eigenvalue equation are found (blue).

We find that all the many-body states are lowered in energy compared to their non-interacting values as the interaction parameter  $g$  is increased (see Figure 2.9 a). This is expected for the purely attractive interaction term in the Hamiltonian. To map each coupling strength  $g$  to its corresponding two-body binding energy  $E_B$ , we perform the same calculation for just two particles in the trap. The binding energy is calculated as the energy difference between the non-interacting and interacting ground states  $E_B = 2\hbar\omega - \xi_0$ . The numerical method we apply to extract the roots of the eigenvalue equation misses some of the  $N_T = 120$  solutions. To obtain the complete spectrum, the degeneracy between the harmonic oscillator levels has to be lifted by adding a small offset  $\Delta E_{n,m} = m\epsilon$ . This drastically increases the required computation time and becomes unfeasible for larger systems with the hardware and numerical methods currently available to us. Nevertheless, we have checked that the full  $N_T$  states in the spectrum are found as solutions to equation (2.41) for an even smaller energy cut-off (see

Figure 2.9 inset). At this level, our calculation is sufficient for qualitative statements.

One observation that is particularly interesting can be made in the low energy excitation spectrum of the interacting many-body system (see Figure 2.9 b). The lowest mode energy is calculated by simply subtracting the energy of the ground from the one of the first-excited state. We find that the excitation is non-monotonous as a function of  $E_B$  with a minimum at some finite value for the binding energy  $E_B^C$ . As we will discuss in great detail in chapter 6, the non-monotonous behaviour signals the presence of a precursor of the normal to superfluid phase transition that exists in the many-body limit (see Figure 2.7). This demonstrates that even the highly simplified Richardson model can capture some of the emergent collective behaviour in our mesoscopic systems, at least on a qualitative level.

# 3

## Atomic Physics

Since the first realizations of BECs in 1995 [Dav95; And95], cold atoms experiments have quickly become one of the major platforms for simulating quantum many-body systems [Blo08; Blo12]. In this chapter, we review some of the most important features of neutral atoms having enabled this success. The discussion can be divided into three general topics: internal structure of the atoms, interactions between them, and their response to external electromagnetic fields.

Compared to other platforms, like experiments based on ions for example, the interactions of a neutral gas of atoms with stray electromagnetic fields are rather small. This is advantageous since it facilitates the design of quantum systems that are well isolated from the environment and have very long coherence times. At the same time, by choosing the right frequency or sufficiently large field intensities, we have an unprecedented amount of control over the many-body state of assemblies of cold atoms. From the inter-particle interaction strength over the single particle potential landscape to the topology the gas evolves in, almost every aspect of ultracold gases is tunable in a very large range. Until today, few tens of different elements and isotopes have been Bose-condensed [Sta12]. Each element comes with its own properties and benefits like, for example, strong dipolar interactions or finely tunable scattering rates. Most importantly, the choice of the isotope determines the most fundamental quantity of the many-body system: the inter-particle exchanges statistics. In this thesis, we will focus the discussion on Lithium and omit details that are important only to other species. This element is used for all the experiments presented in the following chapters.

### 3.1 Internal Structure

The main requirement for the creation of an ultracold gas of neutral atoms is a cycling transition in its electronic excitation spectrum at or close to optical wavelengths. This is generally fulfilled by Alkali metals and is, together with their simple hydrogen-like electron configuration, one of the reasons for their popularity in experiments. We have

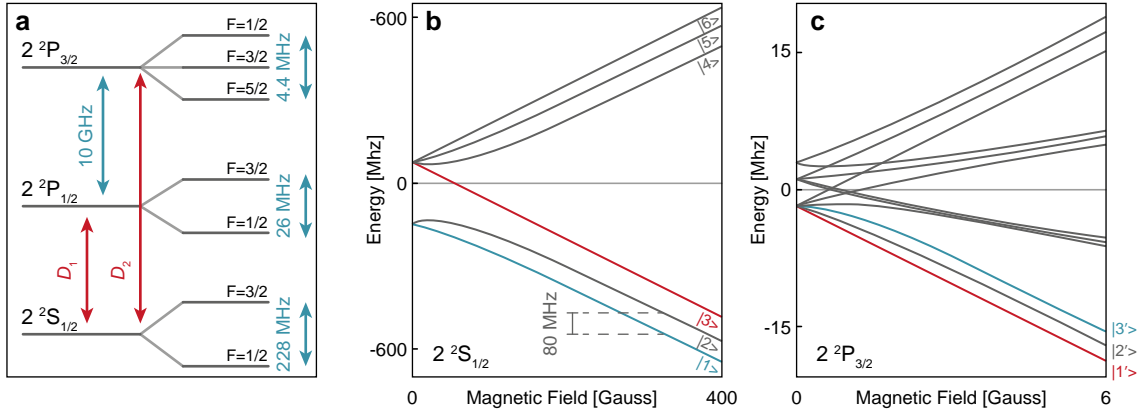


**Figure 3.1: Hyperfine splitting of  $^6\text{Li}$ .** The electronic ground state is given by  $2^2S_{1/2}$  and splits into two hyperfine manifolds at zero field (a). The next higher excited states are the  $2^2P_{1/2}$  and  $2^2P_{3/2}$  states. They couple to the ground state via the characteristic  $D_1$  and  $D_2$  lines of Lithium. At small magnetic offset fields, the ground and excited states split further with an energy shift proportional to the magnetic quantum number  $m_F$  (b, c). When the magnetic field is increased, the Paschen-Back regime is entered and the energy splitting becomes proportional to  $m_J$  instead. In our experiment, we generally use mixtures of the hyperfine states  $|1\rangle$  and  $|3\rangle$ . For cooling and imaging we use light resonant to the  $D_2$  line and, more specifically, the  $\sigma^-$  transition to the corresponding hyperfine states  $|1'\rangle$  and  $|3'\rangle$ .

chosen Lithium, the lightest of the Alkali metals, in our setup. It has a naturally occurring fermionic isotope,  $^6\text{Li}$ , with stable hyperfine mixtures especially well suited for precise measurements in the strongly correlated regime, as discussed below. A very detailed presentation of the atomic properties of  $^6\text{Li}$  can be found in Ref. [Geh03], we will limit ourselves to the most important details here.

### 3.1.1 Properties of Lithium

Like all other Alkali metals,  $^6\text{Li}$  has a single electron in the s-orbital of its outermost shell and a total electron spin of  $S = \frac{1}{2}$ . Its nucleus consists of three protons and neutrons each and has a total nuclear spin of  $I = 1$ . As a result, the total spin is half-integer valued and the isotope is fermionic. The electronic ground state configuration is given by  $1s^22s^1$  or equivalently  $2^2S_{1/2}$ . It is split into two manifolds by the hyperfine

coupling with total spins  $F = \frac{3}{2}$  and  $F = \frac{1}{2}$  respectively and a distance of  $\nu = \frac{\Delta E}{h} = 228$  MHz at zero field. The next higher excited states are given by the  $2^2P_{1/2}$  and  $2^2P_{3/2}$  states (see Figure 3.1 a). They are separated from each other by  $\nu = 10$  GHz and from the ground state by  $\nu = 447$  THz or  $\lambda = \frac{c}{\nu} = 671$  nm. The optical transitions into these states give rise to the characteristic red  $D_1$  and  $D_2$  lines in the spectrum of  $^6\text{Li}$ .

All our experiments are performed at finite magnetic offset fields. This leads to a further splitting of ground and excited state manifolds due to the Zeeman effect. In Lithium the Paschen-Back regime is entered already for fields on the order of  $B = 100$  G, much lower than the fields of 300 G to 1000 G we typically work with. Here, the Zeeman shift is proportional to the quantum number  $m_J$  and each line splits into a triplet corresponding to the different nuclear spin orientations  $m_I = \pm 1, 0$ . We label the states of the ground state manifold  $2^2S_{1/2}$  from  $|1\rangle$  to  $|6\rangle$  according to their energy at a finite magnetic field (see Figure 3.1 b). In our experiments, we work with different combinations of the *high-field seeking* states  $|1\rangle$ ,  $|2\rangle$  and  $|3\rangle$ . In the high-field regime, they are split by 80 MHz and any of their possible two component mixtures is collisionally stable.

### 3.1.2 Optical Transitions

For cooling and detecting neutral atoms we have to drive a cycling transition in the optical range of the electronic excitation spectrum. To this end, we use the  $D2$  line from  $2^2S_{1/2}$  to  $2^2P_{3/2}$  exclusively. The excited state has a lifetime of  $\tau = 27$  ns before it decays back into the ground state, corresponding to a linewidth of  $\Gamma = 5.87$  MHz. This is larger than the hyperfine splitting of 4.4 MHz of the excited state at zero field, which is therefore not resolved in this case. In the high-field regime, we choose to drive the  $\sigma^-$  transition to the states  $|1'\rangle$ ,  $|2'\rangle$  and  $|3'\rangle$  of the  $m_J = -3/2$  manifold (see Figure 3.1 c).

It is important to note that only the optical transition of the so-called stretched state  $|3\rangle \rightarrow |1'\rangle$  has a closed cycle. For  $|1\rangle \rightarrow |3'\rangle$  or  $|2\rangle \rightarrow |2'\rangle$  there remains a small probability to decay back into  $|5\rangle$  or  $|4\rangle$  rather than into the original state. There are several options to deal with this issue in the experiment. The simplest solution is to avoid imaging states  $|1\rangle$  and  $|2\rangle$  completely. Each state is converted to  $|3\rangle$  with the help of radiofrequency or microwave pulses prior to its measurement. Alternatively, the loss in states  $|1\rangle$  and  $|2\rangle$  can simply be accounted for when the images are analysed. This is especially useful when the atom number is large enough ( $N \gg 100$ ) and for spatially averaged observables without single atom resolution. The third possibility is to drive the atoms back into  $|1\rangle$  or  $|2\rangle$  with a second laser while the image is exposed and to close the imaging cycle in this way.

The saturation intensity of the  $D2$  line is given by  $I_{\text{sat}} = 2.54$  mW cm $^{-2}$ . Together

with the linewidth  $\Gamma$  this allows us to calculate the spontaneous scattering rate  $\Gamma_{\text{sc}}$  when we excite the atoms with some laser field as follows:

$$\Gamma_{\text{sc}} = \frac{\Gamma}{2} \frac{I/I_{\text{sat}}}{1 + I/I_{\text{sat}} + (2\Delta/\Gamma)^2}. \quad (3.1)$$

Here,  $I$  and  $\Delta$  are the laser intensity and frequency detuning from resonance respectively. In the limit of strong driving  $I/I_{\text{sat}} \gtrsim 8$  where we typically perform our experiment, this leads to scattering rates on the order of 16 photons/ $\mu\text{s}$ . This is close to the maximal possible value of  $\frac{\Gamma}{2} = 18.4$  photons/ $\mu\text{s}$ .

## 3.2 Scattering of Cold Atoms

Interactions between particles are a fundamental ingredient to the emergence of non-trivial quantum many-body states and rich phase diagrams (see chapter 2). From the experimental viewpoint, collisions are essential as well, since they lead to thermalization of the atom cloud and make efficient evaporative cooling possible (see chapter 4). At the same time, inelastic scattering processes set a maximum limit to the achievable densities and lifetimes in ultracold gases and have to be suppressed.

Scattering of neutral atoms at low temperatures is discussed in great detail in the literature, see for example [Dal99; Fri13; Sak17]. The crucial result is that their collisional behaviour becomes astonishingly simple to describe with just a few parameters: the interaction range  $r_0$ , the  $s$ -wave scattering length  $a$  and the effective range  $r_e$  [Blo08]. Universal behaviour emerges making knowledge of the microscopic details, like the exact shape of the interaction potential, irrelevant.

In the following, we review the most important steps in the derivation leading to a universal description. Furthermore, we discuss some of the modifications that arise when the atoms are trapped in anisotropic confinements so that the collisions become effectively two-dimensional. In the next section, we see how an external magnetic field can be used to tune the scattering rate of an ultracold gas at will.

### 3.2.1 Van der Waals Interactions

The interactions occurring between most species of neutral atoms available for ultracold experiments are dominated by Van der Waals interactions. Only recently, breakthroughs in cooling exotic elements like Erbium or Dysprosium have made it possible to study systems that show significant dipole-dipole interactions in addition [Bar12]. Since they are not relevant for experiments with Lithium we neglect them here. Van

der Waals interactions, on the other hand, have a very short range ( $\sim r^{-6}$ ) of the order of the so-called Van der Waals length defined as

$$r_0 = (2\mu C_6/\hbar^2)^{1/4}, \quad (3.2)$$

where  $\mu$  is the reduced mass and  $C_6$  the Van der Waals coefficient.

For a dilute gas with density  $n$ , the inter-particle spacing is typically much larger than the range of the interactions  $r_0 \ll n^{-1/3}$ . As a result, we can assume that the collisional behaviour of the gas is described by binary interactions between two atoms at a time. This approximation may break down in degenerate quantum gases with strong interactions where inelastic three body collisions appear. They lead to particle loss and limit the interaction range that can be accessed in experiments, especially for bosonic particles [Dal99]. In two component Fermi gases, like the two  ${}^6\text{Li}$  hyperfine states we use, the Pauli principle leads to a substantial suppression of three body collisions even for strong interactions [Ket08; Zwe16]. Here, the approximation of purely binary collisions holds and the description of interactions is strongly simplified.

### 3.2.2 Elastic Two-Body Scattering

For the description of two-body scattering, it is convenient to work in the relative coordinate system with  $\mathbf{r} = \mathbf{r}_1 - \mathbf{r}_2$ ,  $\mathbf{R} = (\mathbf{r}_1 + \mathbf{r}_2)/2$  and reduced mass  $\mu = m_1 m_2 / (m_1 + m_2)$ . Here,  $\mathbf{r}_1$  and  $\mathbf{r}_2$  are the three dimensional coordinates of the two colliding particles. The scattering potential  $V_{\text{int}}(\mathbf{r})$  depends only on the relative coordinate  $\mathbf{r}$  and therefore the calculation reduces to a single particle problem:

$$\left( \frac{\hbar^2}{2\mu} \nabla_{\mathbf{r}}^2 + V_{\text{int}}(\mathbf{r}) \right) \Psi_k(\mathbf{r}) = E_k \Psi_k(\mathbf{r}), \quad (3.3)$$

where we introduced the wave number  $k$  of the relative wavefunction. Since the potential  $V_{\text{int}}(\mathbf{r})$  has a finite range  $r_0$ , the solution for large particle separations  $r \rightarrow \infty$  before and after the collision reduces to that of a free particle with energy  $E = \frac{\hbar^2 k^2}{2\mu}$ . The Van der Waals potential leads to elastic scattering and therefore both energy and wavenumber  $k$  of the wavefunction before and after the collision are conserved. Only the phase of the wavefunction can be affected by the scattering process. Making use of the spherical symmetry of the interaction potential  $V(\mathbf{r}) \equiv V(r)$ , we can express the general solution as follows:

$$\Psi_k(\mathbf{r}) = \Psi_{\text{in}}(\mathbf{r}) + \Psi_{\text{out}}(\mathbf{r}) \underset{r \rightarrow \infty}{\simeq} e^{ikz} + f(k, \theta) \frac{e^{ikr}}{r}, \quad (3.4)$$

where  $0 \leq \theta \leq \pi$  is the polar angle with respect to the ingoing wave  $\Psi_{\text{in}}$  and the scattering amplitude  $f(k, \theta)$  contains phase shift and magnitude of the scattered outgoing wave  $\Psi_{\text{out}}$  (see Figure 3.2 a).

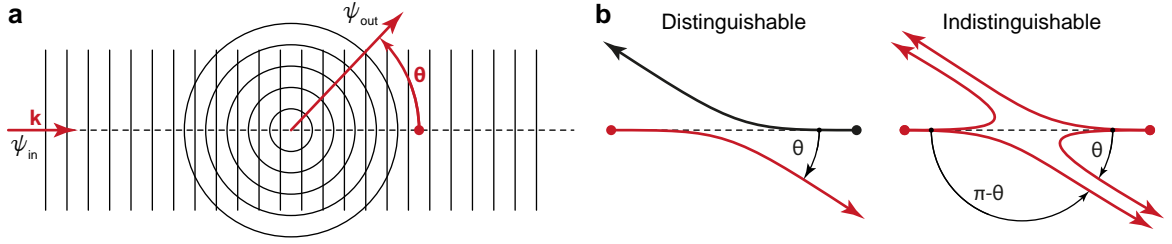


**Figure 3.2: Elastic two-body scattering.** A general ansatz for the relative wavefunction of two particles scattering elastically in a short-range potential is given by an ingoing plane wave  $\Psi_{\text{in}}$  and a scattered spherical wave  $\Psi_{\text{out}}$  (a). The wavefunction has to be symmetrized according to the particle exchange symmetry (b). For indistinguishable particles the two possible paths interfere.

### 3.2.3 Partial Wave Expansion

The derivation of an expression for the scattering amplitude  $f(k, \theta)$  from the Schrödinger equation (3.3) comes down to the solution of the motion of a single particle in a central potential. We omit the details here, but the key idea is to perform a partial wave expansion and to write the wavefunction  $\Psi_k(r, \theta)$  in terms of Legendre polynomials  $P_l(\cos \theta)$  as:

$$\Psi_k(r, \theta) = \sum_{l=0}^{\infty} A_l P_l(\cos \theta) R_{kl}(r), \quad (3.5)$$

where  $A_l$  are the expansion coefficients and  $R_{kl}(r)$  satisfies the radial wave equations. Here, we have already made use of the azimuthal symmetry of the problem that prohibits any  $\phi$ -dependent terms in the expansion. The radial wave equations are given by:

$$\left[ \frac{\partial^2}{\partial r^2} + \frac{2}{r} \frac{\partial}{\partial r} + k^2 - \frac{l(l+1)}{r^2} - \frac{2m_r}{\hbar^2} V_{\text{int}}(r) \right] R_{kl}(r) = 0. \quad (3.6)$$

The crucial insight is that the total scattering potential is now given by an effective potential  $V_{\text{eff}} = V_1(r) + V_{\text{int}}(r)2m_r/\hbar^2$ . Its difference to the bare interaction potential  $V_{\text{int}}(r)$  is the rotational barrier  $V_1(r) = l(l+1)/r^2$  that appears for  $l > 0$  (see Figure 3.3 a). In the small energy limit  $k \rightarrow 0$  this potential barrier prevents the particles from entering the regime  $r < r_b = l(l+1)/k^2$  and the wavefunction decays exponentially for  $r < r_b$ . As a consequence, a short range interaction potential  $V_{\text{int}}$  with  $r_0 < r_b$  is relevant only for the  $l = 0$  (*s*-wave) term in this limit. The higher angular momentum parts  $l > 0$  of the radial wave equation do not lead to a phase shift of the scattered wave  $\Psi_{\text{out}}$  and can therefore be neglected for collisions between ultracold atoms.

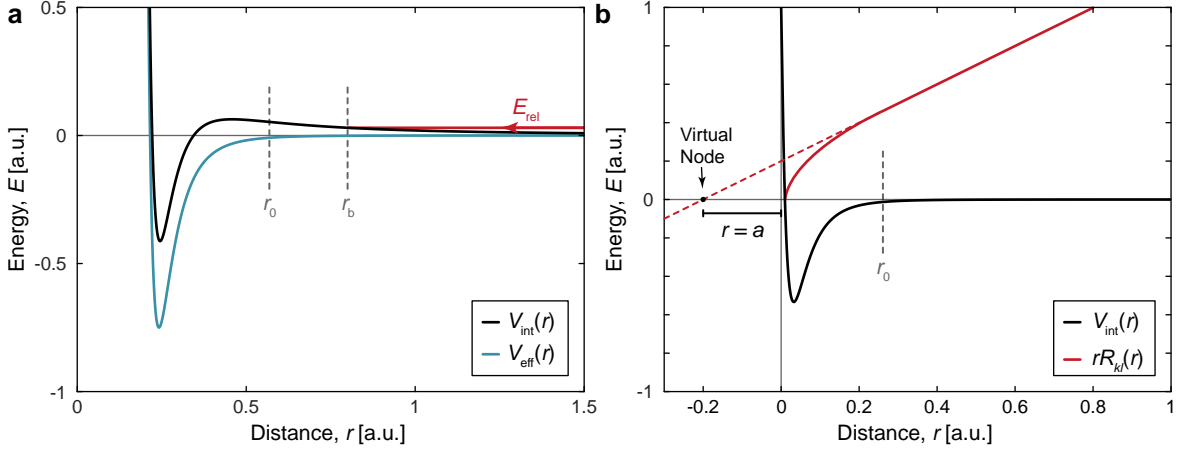


**Figure 3.3: Rotational barrier.** A rotational barrier is present in the effective potential for the radial wave equation with angular momenta  $l > 0$  (a). For particles scattering with small relative kinetic energies  $E_{\text{rel}}$  (red) this leads to a classically forbidden region  $r < r_b$  where the wavefunction decays exponentially. As a result, in the low energy limit  $k \rightarrow 0$  and for short range potentials with  $r_0 < r_b$ , the interaction potential  $V_{\text{int}}$  is relevant only for the  $l = 0$  term of the partial wave expansion. (b) The interaction potential  $V_{\text{int}}$  leads to a phase shift  $\delta$  of the reduced radial wavefunction  $rR_{kl}$  far away from the scattering centre  $r \rightarrow \infty$ . For  $k \rightarrow 0$  the phase shift is independent of  $k$  and can be described by the single parameter named the scattering length  $a$ . The scattering length can be read from the position of the first (virtual) node of the asymptotic wavefunction.

The solutions for equation (3.6) in the far distance limit  $r \rightarrow \infty$  can be written in terms of phase shifts  $\delta_l$  as:

$$R_{kl}(r) \simeq \frac{1}{kr} \sin(kr - l\pi/2 + \delta_l). \quad (3.7)$$

Following [Pet08], we expand the plane wave in equation (3.4) in Legendre Polynomials as well and compare to equations (3.5) and (3.7). We find that  $A_l = i^l(2l+1)e^{i\delta_l}$  and:

$$f(k, \theta) = \frac{1}{2ik} \sum_{l=0}^{\infty} (2l+1)(e^{i2\delta_l} - 1)P_l(\cos \theta). \quad (3.8)$$

As discussed above, the phase shifts  $\delta_l \propto k^{2l+1}$  for  $l > 0$  vanish for  $k \rightarrow 0$  and the final result for the scattering amplitude is:

$$f(k, \theta) = \frac{1}{2ik} (e^{i2\delta_0} - 1) = \frac{1}{k/\tan \delta_0 - ik} \quad (3.9)$$

In the low energy limit, it is convenient to expand the  $s$ -wave phase shift  $\delta_0$  in terms of the wavenumber  $k$ :

$$\frac{k}{\tan \delta_0} = -\frac{1}{a} + \frac{1}{2}k^2 r_e + \dots, \quad (3.10)$$

where  $a$  is the *scattering length* and  $r_e$  is the *effective range*.

Using the approximations above, the description of the scattering process between cold atoms becomes completely independent of the details of the interaction potential  $V_{\text{int}}$ . To first order, the  $s$ -wave phase shift  $\delta_0$  of the wavefunction is  $k$ -independent and determined solely by the scattering length  $a$ . It can be interpreted geometrically as the position of the first node of the asymptotic  $r \rightarrow \infty$  wavefunction (see Figure 3.3 b). The effective range  $r_e$  of the potential, on the other hand, describes the next term in the expansion and determines at what point the approximation of a  $k$ -independent phase shift  $\delta_0$  breaks down. In the case of  ${}^6\text{Li}$  the effective range is  $r_e = 87 a_0$ , where  $a_0 = 5.3 \times 10^{-11}$  m is the Bohr radius [Zür12a]. As a result, the effective range and therefore the momentum dependence of  $\delta_0$  can be neglected for all measurements presented in this thesis.

The scattering length for a repulsive hard sphere potential ( $V_{\text{int}}(r) = \infty$  for  $r < r_0$  and 0 otherwise) is positive and given by  $a = r_0$ . For attractive potential wells  $a$  can generally also become negative. A general approximation that can be made for short range potentials is that  $a \approx r_0$ . For Van der Waals interactions this leads to  $a \approx 50 - 100 a_0$ . However, there are important exceptions to this simple guess, especially when the interaction potential supports a bound state close to the continuum. In such cases both the sign and absolute value of the scattering length are modified and values of  $a \gg 10\,000 a_0$  become possible [Wal19]. As discussed in the next section, scattering resonances can be exploited to change the scattering length dynamically, for example through magnetic fields. In this way, collisions between cold atoms are not only very simple to describe but also highly tunable.

### 3.2.4 Scattering Cross Section

In the discussion above, we have focused on obtaining the scattering amplitude  $f(k, \theta)$  by solving the two-body scattering problem. To describe the scattering behaviour of the gas it is often useful to translate the scattering amplitude to quantities like the *mean-free-path*  $l$  or the *collision rate*  $\nu$  that are more accessible in experiments. They are given by:

$$l = \frac{1}{n\sigma}, \quad (3.11)$$

and

$$\nu = nv\sigma, \quad (3.12)$$

where the atomic velocity  $v$  and density  $n$  of the gas are set by the external trapping confinement in the experiment. The remaining parameter is the collisional cross section  $\sigma$  and can be calculated directly from the scattering amplitude  $f(k, \theta)$ . To this end, we start from the partial cross section  $d\sigma(\theta, \phi)$  for scattering in the direction  $(\theta, \phi)$  defined as:

$$d\sigma(\theta, \phi) = \frac{dI_{\text{out}}(\theta, \phi)}{j_{\text{in}}}, \quad (3.13)$$

where  $dI_{\text{out}}$  is the probability current for scattering into an infinitesimal surface element  $d\Omega$  at  $(\theta, \phi)$  and  $j_{\text{in}}$  is the probability current density of the incoming plane wave. Using the ansatz for the asymptotic wavefunction (3.4) we obtain:

$$d\sigma(\theta, \phi) = |f(k, \theta)|^2 d\Omega \quad (3.14)$$

The total cross section  $\sigma$  follows after integration over all angles. With the solution of  $f(k, \theta)$  in terms of the  $s$ -wave scattering length as derived in equations (3.9) and (3.10) we obtain:

$$\sigma = \frac{4\pi a^2}{1 + k^2 a^2} \quad (3.15)$$

This leads to two different limiting cases for the collisional behaviour of the gas. If  $ka \gg 1$  we obtain:

$$\sigma = \frac{4\pi}{k^2}, \quad (3.16)$$

where the cross section is independent of the scattering length and the system can be described completely in terms of a single scale: its density  $n$ . This is called the *unitary regime*. If  $ka \ll 1$ , on the other hand, we obtain:

$$\sigma = 4\pi a^2. \quad (3.17)$$

Here, the scattering length  $a$  is the single parameter that determines all collisional properties of the gas.

### 3.2.5 Effective Potential

In the discussion above, we have established a description of scattering between ultra-cold atoms that is completely independent of the details of the interactions potential  $V_{\text{int}}$ . This motivates the introduction of an effective zero range interaction potential:

$$V_{\text{eff}}(r) = g\delta(r), \quad (3.18)$$

where the coupling constant  $g = 4\pi\hbar^2 a/\mu$  can be expressed directly in terms of the scattering length  $a$  and  $\delta(r)$  is the appropriately normalized Dirac delta function [Ket08].

The effective potential is defined such that the same asymptotic scattering behaviour is reproduced while calculations are much simpler than in more realistic descriptions like the Lennard-Jones potential. The sign of interaction energy  $E_{\text{int}} \propto g \propto a$  justifies the commonly used labelling of  $a > 0$  as the repulsive and  $a < 0$  as the attractive interaction regimes.

### 3.2.6 Identical Particles

The ansatz for the wavefunction shown in equation (3.4) is valid only for distinguishable particles. In the case of indistinguishable particles, like identical atoms in the same internal state, the wavefunction of the relative motion has to be symmetric under particle exchange. It is not possible to distinguish between the situation where the particle coming from the left scatters with an angle  $\theta$  and the situation where the particle from the right scatters with an angle  $\pi - \theta$  (see Figure 3.2 b). Both possible paths interfere and lead to the combined scattering amplitude. The asymptotic wavefunction with the correct symmetrization for bosonic (+) and fermionic (-) particles is therefore given by:

$$\Psi_k(\mathbf{r}) \underset{r \rightarrow \infty}{\simeq} \left( e^{ikz} \pm e^{-ikz} \right) + \left( f(k, \theta) \pm f(k, \pi - \theta) \right) \frac{e^{ikr}}{r}, \quad (3.19)$$

where  $\theta$  is limited to  $[0, \pi/2]$ . For the total  $s$ -wave cross section  $\sigma$  this results in:

$$\begin{aligned} \text{Bosons:} & \quad \sigma = 8\pi a^2 \\ \text{Distinguishable Particles:} & \quad \sigma = 4\pi a^2 \\ \text{Fermions:} & \quad \sigma = 0 \end{aligned} \quad (3.20)$$

From equation (3.20) it follows that at low temperatures a single component Fermi gas is completely non-interacting (under the assumption that dipolar interactions are negligible). Significant scattering rates only appear close to higher order partial wave resonances, that exist for example in  ${}^6\text{Li}$  with  $l = 1$  ( $p$ -wave) [Zha04]. In our experiment, we make use of two different hyperfine components instead (see Section 3.1). Here, all the equations for distinguishable particles, as discussed above, apply. This allows us to enter the strongly interacting regime that is required both for efficient thermalization and preparation as well as for the study of highly correlated quantum many-body states.

### 3.2.7 Scattering in 2D

All the measurements that are presented in this thesis are carried out in a quasi-2D setting, where dynamics of the atoms along the third dimension are strongly suppressed

(see chapter 4). While most of the assumptions made for 3D scattering between ultra-cold atoms still hold, we discuss some of the important modifications for 2D scattering here. In 2D, the partial wave expansion of the scattering amplitude  $f(k, \theta)$  (compare equation (3.8)) leads to [Lev15]:

$$f(k, \theta) = \sum_{l=0}^{\infty} (2 - \delta_{l0}) \cos(l\theta) \frac{-4}{\cot \delta_l(k) - i}, \quad (3.21)$$

where  $\delta_{l0}$  is the Kronecker delta and  $\delta_l$  the phase shift of the asymptotic wavefunction. The  $l = 0$  phase shift  $\delta_0$  can be expanded as:

$$\cot \delta_0(k) = \frac{2}{\pi} \ln(ka_{2D}) + \mathcal{O}(k^2), \quad (3.22)$$

where we have introduced the 2D scattering length  $a_{2D} > 0$ . Finally, the total elastic  $s$ -wave cross section is given by:

$$\sigma = \frac{\pi^2}{4k^2 \ln^2(ka_{2D}) + k^2 \pi^2}. \quad (3.23)$$

Similar to 3D, we can introduce an effective potential  $V_{\text{eff}}(r) = g_{2D} \delta(r)$  with [Frö12]:

$$g_{2D} = \frac{-2\pi \hbar^2}{\mu \ln(ka_{2D})}. \quad (3.24)$$

There are a few notable qualitative differences between 2D and 3D. First, the scattering amplitude and cross section are always  $k$ -dependent, even in the low energy limit. There is no unitary regime where the scattering length dependence drops out completely. The equations above indicate that a good choice for a dimensionless parameter to characterize the collisional properties of a 2D Fermi gas is given by  $\ln(k_F a_{2D})$ . Here, we have used the approximation  $k \approx k_F$ , where  $k_F$  is the Fermi momentum of the gas (see chapter 2). As in 3D, the  $s$ -wave cross section is the only relevant contribution in the low energy limit while all higher partial wave terms  $l > 0$  become zero [Lev15].

From equation (3.22) we find that the scattering phase shift  $\delta_0$  diverges logarithmically in the low  $k$  limit and the scattering amplitude approaches zero (much more slowly than the  $p$ -wave part however). Therefore, it is not possible to unambiguously define the scattering length  $a_{2D}$  in 2D as the low energy limit of the phase shift. More generally, a zero-range potential  $V_{\text{int}} \approx \delta^2(r)$  in 2D always leads to divergent quantities, like for example mean-field interaction energies. We have to regularize and renormalize the divergencies of the 2D contact interaction potential by introducing some momentum or energy cut-off scale. This additional energy scale breaks the scale invariance

symmetry of the bare hamiltonian and leads to a *quantum anomaly*. The implications of the quantum anomaly —a concept originally known from high energy physics— for the behaviour of the quasi-2D gas will be discussed in detail in chapter 8.

A well known peculiarity in quantum mechanics for attractive potentials  $V_{\text{int}}$  in 2D is that they always support at least one bound state. This is different to 3D for example, where the potential depth has to come below some threshold before the first bound state is supported. It is convenient to make use of the 2D two-body bound state for the renormalization procedure [Lev15]. By fixing its binding energy  $E_B$  to a finite value, we can remove all divergent terms and it is possible to obtain a well defined quantum theory and scattering length  $a_{2D}$ . Bound states in the interaction potential  $V_{\text{int}}$  are not only important on a theoretical level as a means of renormalization, they also strongly affect the scattering phase shift  $\delta_l$  as we discuss in the following.

### 3.2.8 Two-Body Bound States

So far we have ignored the possibility of bound state solutions that might exist for the two-particle Schrödinger equation (3.3). This is justified as long as the (virtual) bound state energies  $E_B$  are far away from the energy of the scattering particles. However, if a bound state is coming very close to the continuum ( $E_B \lesssim 0$ ) or if there is a virtual bound state that is almost bound ( $E_B \gtrsim 0$ ), a so called *shape resonance* occurs. These resonances strongly modify the scattering length and allow for values  $|a| \gg r_0$  and even  $a \rightarrow \pm\infty$ . While the shape and position of the resonances depend very much on the details of the scattering potential  $V_{\text{int}}$ , the general behaviour when a bound state exists close to the continuum is universal. Therefore, following [Wal19], we limit ourselves to the discussion of scattering in a spherical potential well with flat bottom here.

The attractive potential is defined to have a constant depth of  $V_0 < 0$  for  $r \leq r_0$  while it is zero everywhere else (see Figure 3.4 a,b). By plugging  $V_{\text{int}}$  into the Schrödinger equation (3.3) and solving for the scattering length, we obtain [Wal19]:

$$a = r_0 \left( 1 - \frac{\tan \gamma}{\gamma} \right), \quad (3.25)$$

where  $\gamma = r_0 \sqrt{-2mV_0/\hbar^2}$  is called the *well parameter*. In 3D a bound state appears when  $\gamma = (n + 1/2)\pi$ , where  $n$  is an integer. We find that as  $V_0$  is increased starting from zero, the attractive potential pulls the wavefunction in and leads to a negative scattering length (see Figure 3.4 c). The scattering length continues to increase towards minus infinity until the first bound state appears at  $\gamma = 1/2\pi$ . Here, the phase shift  $\delta_0$  jumps from  $\pi/2$  to  $-\pi/2$  and the scattering length shifts from  $-\infty$  to  $+\infty$ . The same behaviour occurs at each new level  $n$  that becomes bound. For away from the positions of the shape resonances we find that the naive guess  $a \approx r_0$  holds.

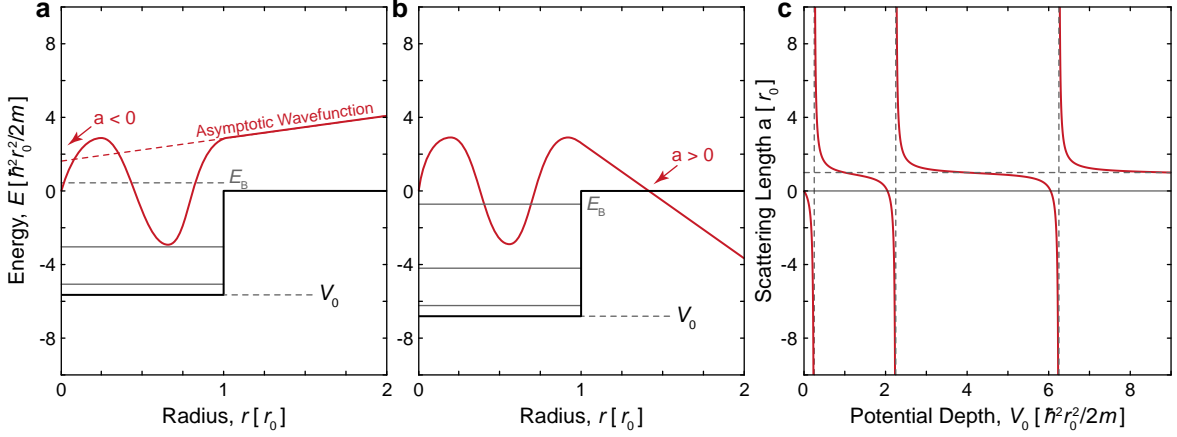


**Figure 3.4: Scattering in a spherical potential well with flat bottom.** The presence of a bound state in the interaction potential  $V_{\text{int}}$  significantly affects the phase of the asymptotic wavefunction (red) and therefore the scattering length  $a$ . For a virtual bound state with  $E_B \gtrsim 0$  the scattering length becomes negative and diverges towards minus infinity (corresponding to  $\delta_0 \rightarrow +\pi/2$ ) as  $E_B \rightarrow 0^+$  (a). For a bound state just below the continuum  $E_B \lesssim 0$  the scattering is positive and becomes plus infinity (corresponding to  $\delta_0 \rightarrow -\pi/2$ ) when  $E_B \rightarrow 0^-$  (b). As the depths on the potential well  $V_0$  increases, a *shape resonance* occurs whenever a new level becomes bound (c). At these positions the scattering length diverges  $a \rightarrow \pm\infty$ , while the approximation  $a \approx r_0$  holds far away from the resonances.

From the solution of the spherical potential well we find that a positive scattering length  $a$  is always related to the presence of a bound state with energy  $E_B$  close to the continuum. It turns out that this connection can be generalized for attractive interaction potentials and the energy of the bound state can be approximated by [Sak17]:

$$E_B \simeq \frac{\hbar^2}{2\mu a^2}. \quad (3.26)$$

In 3D this two-body bound state exists only for repulsive interactions ( $a > 0$ ). For very small repulsive interactions  $a \rightarrow 0^+$ , the binding energy increases  $E_B \rightarrow \infty$  until the particles form point-like dimers. In this limit the atom-dimer  $a_{\text{ad}}$  and dimer-dimer  $a_{\text{dd}}$  scattering lengths are given by [Gio08]:

$$a_{\text{ad}} = 1.18 a \quad a_{\text{dd}} = 0.6 a \quad (3.27)$$

In 2D an attractive potential of any depth supports a bound state and with  $a_{2D} > 0$  the same relation  $E_B \simeq \hbar^2/2\mu a_{2D}^2$  holds for both attractive and repulsive mean-field interactions. Since the bound state is always present in 2D, we generally use its energy  $E_B$  to characterize the interaction strength of the system [Ran90].

### 3.2.9 Scattering in Quasi-2D

Up to this point we have discussed scattering and the occurrence of bound dimers in both 3D and 2D. Our experiments are naturally always carried out in a 3D world. The Van der Waals interaction range of  $r_0 \approx 3$  nm is always much smaller than the length scales of the atom confinement  $l \gtrsim 500$  nm and the two-body scattering processes are always 3D. However, it is possible to use tailor made potentials that confine the atoms so strongly along one dimension that their low energy dynamics becomes effectively 2D. We use an approximately harmonic confinement with trap frequency  $\omega_z$  along the  $z$ -direction in our experiment (see chapter 4). The quasi-2D regime is reached when all other energy scales of the many-body system, like the chemical potential  $\mu$ , temperature  $k_B T$  or the Fermi energy  $E_F$  are much smaller than the trap level spacing in  $z$ -direction  $\hbar\omega_z$ . In this case the particles always remain in the ground state in  $z$ -direction and we describe the system with an effective 2D model by integrating out the wavefunction along the third axis. The scattering length  $a_{2D}$  of the effective 2D model is then given by [Pet01; Lev15]:

$$a_{2D} = l_z \sqrt{\frac{\pi}{B}} \exp\left(-\sqrt{\frac{\pi}{2}} \frac{l_z}{a}\right), \quad (3.28)$$

where  $a$  is the 3D scattering length,  $B = 0.905$  and  $l_z = \sqrt{\hbar/m\omega_z}$  is the harmonic oscillator length in the confined direction.

The additional length scale of  $l_z$  entering the 2D scattering length  $a_{2D}$  as opposed to a true 2D setting makes the calculation of the bound state energy more involved. When  $E_B \ll \hbar\omega_z$  the dimer wavefunction is large and quasi-2D. We can calculate its energy  $E_B = \hbar^2/2\mu a_{2D}^2$  with the effective  $a_{2D}$  from equation (3.28) as before. In the opposite limit, when  $E_B \gg \hbar\omega_z$ , the dimer becomes point like and its wavefunction is not modified by the  $z$  confinement anymore. Its energy then is simply given by  $E_B = \hbar^2/2\mu a$  in terms of the 3D scattering length  $a$ . While the dimers are clearly 3D in this case, the interactions between molecules are still 2D. For the relevant degrees of freedom of the gas, a description in terms of a quasi-2D theory remains valid. In between the two extreme cases  $E_B \approx \hbar\omega_z$ , the following implicit expression is obtained

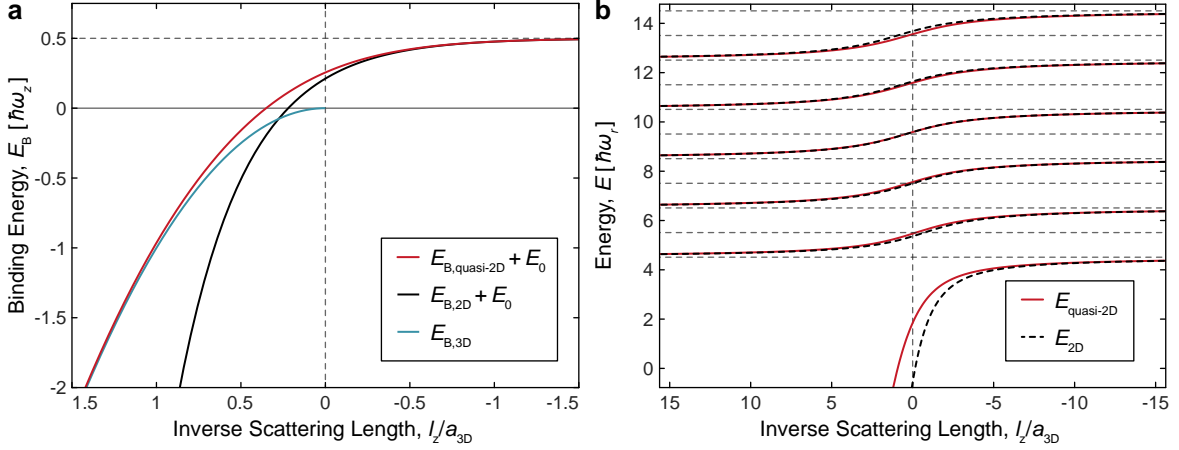


**Figure 3.5: Bound states in quasi-2D.** (a) The red solid line shows the full solution for the two-body binding energy  $E_B$  of the bound state in a quasi-2D setting with a harmonic confinement along the  $z$ -direction. The lines in blue and black show the limiting cases of a 3D and 2D dimer respectively. The quasi-2D and 2D solutions are offset by the ground state energy  $E_0 = 0.5 \hbar\omega_z$  of the harmonic oscillator. In quasi-2D the confinement induces a bound state also for negative scattering lengths where it is absent in 3D. (b) The full energy spectrum of two particles that are confined radially in addition to the quasi-2D confinement and with  $\eta = \omega_r/\omega_z = 1/7$ . The spectrum is shown as a function of the 3D scattering length (red solid line). The calculations for a true 2D system are shown in comparison (black dashed line). The grey dashed lines indicate the unperturbed harmonic oscillator levels without interactions.

for the quasi-2D dimer binding energy [Lev15]:

$$\frac{l_z}{a} = \int_0^\infty \frac{dx}{\sqrt{4\pi x^3}} \left( 1 - \frac{\exp\left(-\frac{E_B}{\hbar\omega_z} x\right)}{\sqrt{\frac{1 - \exp(-2x)}{2x}}} \right). \quad (3.29)$$

In Figure 3.5 a, the solution of this equation for  $E_B$  is shown as a function of  $l_z/a$ . We find that it interpolates between both limiting cases as expected.

### 3.2.10 Radial Confinement

An additional potential in radial direction, orthogonal to the  $z$ -axis, is required in order to confine the atoms in the 2D plane. In our experiment, we use a harmonic

trap with frequency  $\omega_r$  and aspect ratios between  $\eta = \omega_r/\omega_z \approx 1/300$  and  $\eta \approx 1/7$  (see chapter 4). The additional confinement influences the relative wavefunction of molecules and modifies the binding energy  $E_B$  further. For two particles interacting via the effective delta potential  $g\delta(r)$ , a solution was first presented in Ref. [Bus98] for isotropic harmonic potentials in 1D, 2D and 3D ( $\omega_i \equiv \omega$  for  $i = 1 \dots d$ ). The analytical solutions were later extended to 3D harmonic confinements with axial symmetry [Idz06] and by now even to arbitrary aspect ratios ( $\omega_x \neq \omega_y \neq \omega_z$ ) [Che20]. The energy spectrum relevant for our experiment, of two particles in harmonic 3D traps with integer inverse aspect ratios  $1/\eta = n$  can be obtained from the equation [Idz06]:

$$\frac{l_z}{a} = \frac{\sqrt{2\pi}}{n} \sum_{m=0}^{n-1} \frac{\Gamma\left(-\frac{\mathcal{E}}{2\hbar\omega_z} + \frac{m}{n}\right)}{\Gamma\left(-\frac{\mathcal{E}}{2\hbar\omega_z} - \frac{1}{2} + \frac{m}{n}\right)}, \quad (3.30)$$

where  $\Gamma$  is the Euler gamma function, and the solutions for  $\mathcal{E} = E - E_0$  are the energy levels in the trap relative to the ground state energy of  $E_0 = \hbar\omega_z(1/2 + \eta)$ .

In Figure 3.5 b, we show the solution of equation (3.30) for the lowest  $i$  levels  $E_i$  of the energy spectrum (red solid line). Here, a realistic aspect ratio for our experiments with mesoscopic systems of  $n = 1/\eta = 7$  was used. In the non-interacting limits  $a \rightarrow 0^\pm$  the radial confinement leads to a discrete level spectrum, spaced by the harmonic oscillator energy  $\hbar\omega_r$ , as expected (grey dashed lines). When the scattering length increases, the levels shift to higher (lower) energies for  $a > 0$  ( $a < 0$ ), consistent with an interaction that is effectively repulsive (attractive). Odd-numbered energy levels of the harmonic oscillator are not shifted by the interaction since they have a node in the relative wavefunction at  $r = 0$  and are therefore unaffected by the zero range  $\delta(r)$  potential. The lowest energy level lies always below the non-interacting ground state energy for two particles. This is consistent with the observation that in quasi-2D, the confinement induces a bound state also for negative scattering lengths.

In the same Figure 3.5 b, we also plot the energy spectrum of a true 2D system confined radially with trap frequency  $\omega_r$  (black dashed line). The curves are obtained from the solution in Ref. [Bus98] with the effective 2D scattering length from equation (3.28) and are offset by the ground state energy  $\hbar\omega_z/2$  in axial direction for better comparison. The 3D and 2D solutions show a remarkable agreement, confirming again the validity of a quasi-2D description even for rather small aspect ratios of  $n = 1/\eta = 7$ . The only clear deviation of the full 3D solution occurs for the lowest bound state level. Here, the binding energy of the dimer becomes of the order of the axial energy spacing  $E_B \approx \hbar\omega_z$  and higher energy levels in the third dimension have to be taken into account. This is the same behaviour that we have already discussed for the quasi-2D system without radial confinement (see Figure 3.5 a).

## 3.3 External Fields

Up to this point, we have discussed the complex internal structure of neutral atoms offering different spin (hyperfine) states, bosonic or fermionic exchange statistics and easily accessible transitions in the visible spectrum. We have seen that at low energies the description of collisions becomes universal and independent of the details of the interaction potential  $V_{\text{int}}$ . This final section of chapter 3 deals with the response of ultracold atoms to external fields. The numerous possibilities we have to tune the potential environment, internal properties and collisional behaviour with external fields make ultracold atoms so attractive as platform for quantum simulations [Blo08; Blo12].

In the first part, we discuss the response to direct current (DC) magnetic fields. They allow us to almost freely tune the interactions between particles with so-called *Feshbach resonances*, one of the hallmarks of ultracold quantum gas experiments. In the second section, we discuss how far off resonant AC electromagnetic fields can be used to tailor trapping potentials of arbitrary geometries for the atom clouds. The experimental methods to switch between different internal hyperfine states of the atoms by using radio frequency (RF) and microwave (MW) pulses or Raman transitions are discussed in chapter 4.

### 3.3.1 Magnetic Fields

Neutral atoms couple to a magnetic field  $\mathbf{B}$  via the term  $\mathcal{H}_B = -\boldsymbol{\mu} \cdot \mathbf{B}$ , where  $\boldsymbol{\mu}$  is the magnetic dipole moment. In figure 3.1, we have already seen how this term leads to the Zeeman effect at finite magnetic fields and an energy splitting of different hyperfine levels. In the high field regime  $B > 300$  G, where we typically work at, the energy shift  $E_B$  is proportional to the projection of the total angular momentum  $m_J = \pm 1/2$  along the magnetic field [Sta12]:

$$E_B \approx m_J g_J \mu_B B + A_{\text{HF}} m_J m_I, \quad (3.31)$$

where  $g_J$  is the magnetic moment,  $\mu_B$  is the Bohr magneton,  $m_I = 0, \pm 1$  is the projection of the nuclear spin and  $A_{\text{HF}} = 152$  MHz is the hyperfine constant. The Zeeman shift is not just important to split the hyperfine states labelled  $|1\rangle \dots |6\rangle$  in energy and to make them distinguishable. When the magnetic field strength has a spatial dependence, it also leads to an effective potential given by  $V(\mathbf{r}) = E_B(r) \propto \mathbf{B}(r)$  (see equation (3.31)). We distinguish between *high-field seeking* states  $|1\rangle$  to  $|3\rangle$  with a potential minimum at the point of the largest magnetic field strengths and *low-field seeking* states  $|4\rangle$  to  $|6\rangle$  with a potential minimum at the point of the smallest magnetic field strengths. Since by Maxwell's equations local maxima in the magnetic field can

not exist in free space, only the low-field seeking states can be trapped purely magnetically [Sta12]. In our experiments, the magnetic confinements are often negligible compared to the other potentials we apply. However, they are generally very useful for the application of matter wave optics [Mur14]. Here, the potential acts as a (matter wave) lens that allows us to severely magnify the atom cloud and to swap between real- and momentum-space. The process is very sensitive to inhomogeneities and defects in the potential. These are generally suppressed in a magnetic field as compared to the optical potentials we discuss later.

For experiments with lithium, a field strength of particular importance is located at  $B = 27$  G. Here, the magnetic moment of state  $|2\rangle$  is exactly zero (see Figure 3.1 b). This allows us to create state depend potentials, where a gradient in magnetic field strength only acts on other hyperfine states that are present. We are able to create imbalanced or even completely spin polarized samples in this way (see chapter 4).

### 3.3.2 Feshbach Resonances

The differential energy shift of different hyperfine levels with an applied magnetic field does not only affect the potential landscape of the atoms. It becomes even more important when we consider the two-body scattering problem again. In the discussion of collisions above, we have treated the atoms as two point-like particles and without taking their internal structure into account. In a single interaction potential  $V_{\text{int}}$  a shape resonance with  $a \rightarrow \pm\infty$  occurs, whenever a (virtual) bound state is close to the collisional energy  $E$  of the particles (see Figure 3.4). Unfortunately, the potential  $V_{\text{int}}$  is set by the internal properties of the atoms and cannot directly be manipulated in order to tune the bound state levels and scattering length  $a$ . This changes when we consider the presence of other hyperfine states when modelling the scattering process.

A collision between two neutral atoms can in principle lead to a change of their internal state. As a result, not only the interaction potential of the incoming states has to be taken into account but also the ones from other internal states that the atoms might scatter into. Each scattering potential (or *channel*) asymptotically ( $r \rightarrow \infty$ ) connects to two free atoms of the ultracold gas. They can be distinguished into *open channels*, that are energetically allowed by the collision energy of the incoming particles  $E$ , and *closed channels*, that are energetically forbidden (see Figure 3.6 a). A very special situation occurs when there is a bound state with energy  $E_B \approx E$  in a closed channel of the scattering particles. Even a small coupling (for example through spin spin interactions) between the closed and open channels will strongly affect the phase of the scattered wave and lead to a singularity in the scattering length  $a$ . This behaviour is generally called a *Feshbach resonance*. The crucial difference to the shape resonance discussed before is that for the Feshbach resonance we have access to the exact value of

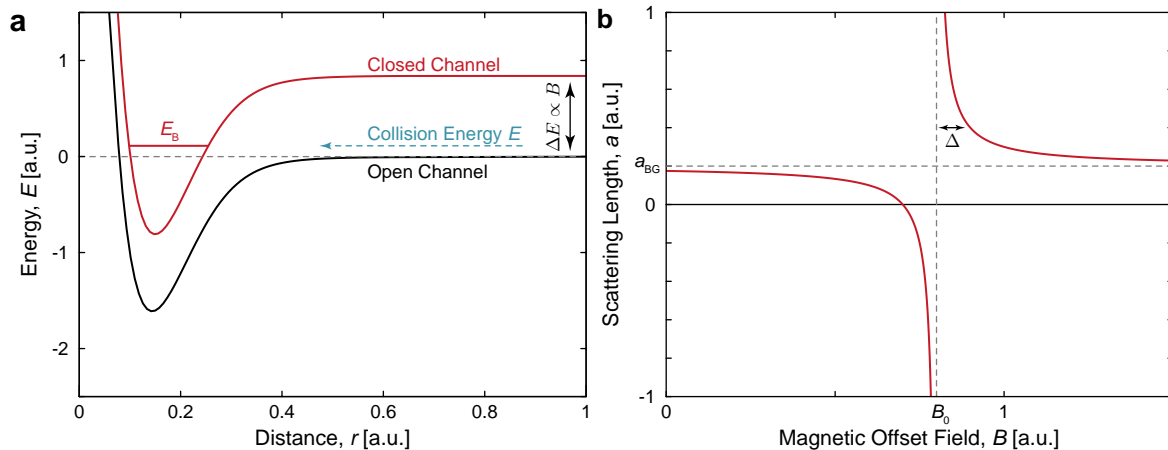


**Figure 3.6: Feshbach resonances.** A Feshbach resonance occurs when a bound state exists in a closed, energetically forbidden, channel (a). The energy  $E_B$  of this bound state relative to the open channel that the particles scatter in can often be tuned via a differential Zeeman shift. When the bound state comes into resonance with the scattering particles the phase shift  $\delta_0$  jumps by  $\pi$  and the scattering length diverges ( $a \rightarrow \pm\infty$ ). This allows us to freely tune the scattering length  $a$  of an ultracold gas by simply applying an external offset field  $B$  (b). Everything from the strongly repulsive  $a \rightarrow \infty$  to the strongly attractive  $a \rightarrow -\infty$  as well as the non-interacting  $a = 0$  regime is accessible.

$E_B$  relative to the open channel. Since open and closed channel correspond to different asymptotic hyperfine states, they might have a differential Zeeman shift (see equation (3.31)). In such cases we can directly control their energy difference simply by applying a magnetic offset field  $B$ . The behaviour of the 3D scattering length  $a$  as a function of magnetic field  $B$  can be described by the phenomenological expression [Chi10]:

$$a(B) = a_{bg} \left( 1 - \frac{\Delta}{B - B_0} \right), \quad (3.32)$$

where  $a_{bg}$  is the background scattering length (generally  $a_{bg} \approx r_0$ ) of the open channel and  $B_0$  and  $\Delta$  describe the position and width of the resonance respectively (see Figure 3.6 b).

In the case of  ${}^6\text{Li}$  the scattering potentials are given by the molecular *triplet* ( $\mathbf{S} = 1$ ) and *singlet* ( $\mathbf{S} = 0$ ) potentials  $V_T$  and  $V_S$ . Here the spin  $S$  refers to the total electron spin  $\mathbf{S} = \mathbf{S}_1 + \mathbf{S}_2$  of the two colliding atoms. The entire two electron wavefunction is antisymmetric under particle exchange. For the spin triplet this leads to a spatial

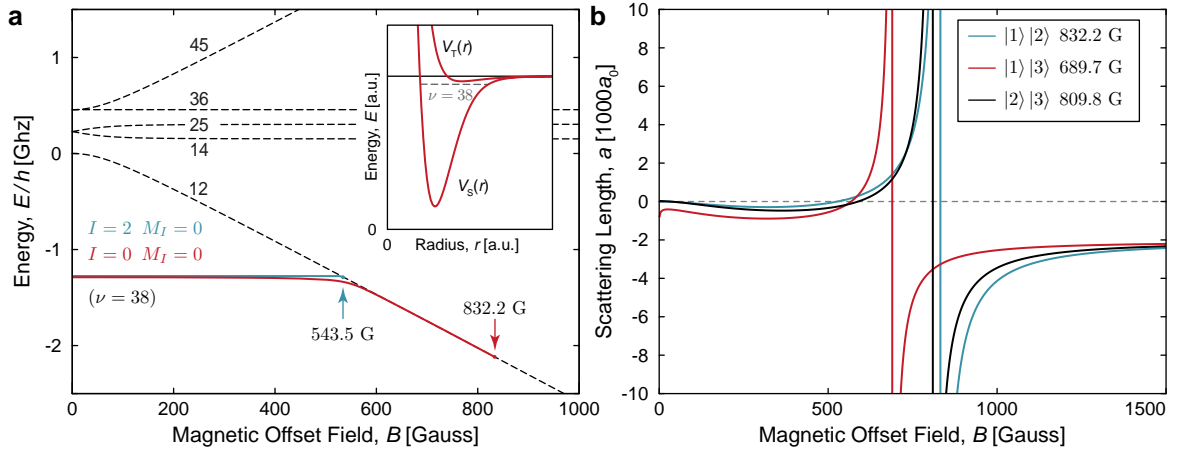


**Figure 3.7: Feshbach resonances of  ${}^6\text{Li}$ .** (a) The last vibrational levels  $\nu = 38$  of the triplet potential  $V_T$  (inset) can be tuned into resonance for scattering in the  $|1\rangle|2\rangle$  mixture (dashed line indicated by 12). The bound states have a total nuclear spin of  $I = 0$  and 2 and disappear into the continuum at 832.2 and 543.5 G respectively. This leads to a broad Feshbach resonance at 832.2 G that can be used to freely tune the scattering length of the  $|1\rangle|2\rangle$  mixture. The second resonance at 543.5 G is very sharp and its presence is negligible for our purpose. The same effect leads to broad resonances also for the  $|1\rangle|3\rangle$  and  $|2\rangle|3\rangle$  mixture (b). For other hyperfine mixtures no resonances are expected due to their respective Zeeman shifts (dashed lines in a). Figure (a) is recreated from Ref. [Chi10]. Figure (b) uses the data from the appendix in [Zür12a].

electron wavefunction that is antisymmetric under particle exchange, leading to a reduced probability of finding the electrons in the region between the nuclei. As a result, the triplet potential  $V_T$  is much more shallow than the singlet potential  $V_S$  with a symmetric spatial electron wavefunction (see Figure 3.7 a, inset).

The triplet potential does not support any bound states, but a virtual bound state lies in the continuum just above  $E = 0$ . This leads to a shape resonance and explains the anomalously large and negative scattering length of  $a_T = -2113(2) a_0$  [Zür12a]. The deep singlet potential, on the other hand, supports a molecular bound state with the last vibrational level  $\nu = 38$  close to the continuum  $E_B \approx 1.38$  GHz [Chi10] and scattering length of  $a_s = -45.154(10) a_0$  [Zür12a]. For the hyperfine mixtures  $|1\rangle|2\rangle$ ,  $|2\rangle|3\rangle$  and  $|1\rangle|3\rangle$ , the differential magnetic moment between the triplet and singlet potentials allow us to tune the  $\nu = 38$  vibrational levels into resonance (see Figure 3.7 a). This leads to broad Feshbach resonances in each of these channels that are directly

accessible in experiments. In this way we can set the scattering length  $a$  of a given mixture to (almost) any desired value by applying the correct magnetic offset field (see Figure 3.7 b). For other mixtures no further Feshbach resonances are expected since their differential Zeeman shift is either zero or goes in the wrong direction.

### 3.3.3 Optical Dipole Potentials

Spatially inhomogeneous magnetic fields are one approach to create conservative potentials for ultracold atoms. However, as already presented above, they lead to highly state dependent potentials, limiting the possible hyperfine for trapping immensely. In addition, Feshbach resonances as an essential tool to control the interactions also rely on magnetic fields. The solution is to make use of the polarizability  $\alpha$  of the neutral atoms. It leads to an induced dipole moment of the atom proportional to an applied electric field  $\mathbf{d} \propto \alpha \mathbf{E}$ .

The resulting *Stark shift* for the atoms is then proportional to the quadratic field strength  $V(\mathbf{r}) \propto \mathbf{d}\mathbf{E}(\mathbf{r}) \propto \mathbf{E}^2(\mathbf{r})$ . The polarizability of alkali atoms is generally too small in order to create potentials of relevant depths with electric DC fields. However, the energy shift can be dramatically enhanced (by factors on the order of  $10^8$ ) by applying an AC field near an optical resonance of the internal states instead [Sta12]. A detailed derivation of the potential  $V_{\text{dip}}$  that is created by these so-called optical dipole traps (ODTs) can be found in Ref. [Gri00]. The main result can be summarized with the following equations:

$$V_{\text{dip}}(\mathbf{r}) = -\frac{3\pi c^2}{2\omega_0^3} \left( \frac{\Gamma}{\omega_0 - \omega} + \frac{\Gamma}{\omega_0 + \omega} \right) I(\mathbf{r}), \quad (3.33)$$

$$\Gamma_{\text{sc}}(\mathbf{r}) = \frac{3\pi c^2}{2\hbar\omega_0^3} \left( \frac{\omega}{\omega_0} \right)^3 \left( \frac{\Gamma}{\omega_0 - \omega} + \frac{\Gamma}{\omega_0 + \omega} \right)^2 I(\mathbf{r}). \quad (3.34)$$

Here, we identify  $I(\mathbf{r}) \propto E^2(r)$  and  $\omega$  as intensity and frequency of the external optical field respectively. The resonance frequency and linewidth (see section 3.1.2) of the optical transition of the atom are given by  $\omega_0$  and  $\Gamma$  respectively and  $c$  is the speed of light. The unwanted single photon scattering rate of the atoms is given by  $\Gamma_{\text{sc}}$ .

From equation (3.33), we find that the potential depth  $V_{\text{dip}}$  scales at  $1/\Delta$ , where  $\Delta = \omega - \omega_0$  is the detuning from resonance. At the same time, the single photon scattering rate, that acts as a dispersive term and leads to atom loss from the trap, scales as  $\Gamma_{\text{sc}} \propto 1/\Delta^2$ . For the creation of conservative potentials it is therefore best to use optical fields with very high intensity  $I$  and far detuned from resonance  $\Delta \gg \Gamma$ . For *red detuned* fields ( $\Delta < 0$ ) the confinement is attractive  $V_{\text{dip}} < 0$  while *blue detuned* ( $\Delta > 0$ ) light beams create repulsive potentials  $V_{\text{dip}} > 0$ . This can be understood by the

oscillation of the induced dipole moment in dependence of the driving field frequency. In analogy to a classical driven harmonic oscillator, this oscillation is in phase when  $\omega < \omega_0$  and out of phase when  $\omega > \omega_0$ .

For  ${}^6\text{Li}$  we make use of lasers at  $\lambda = 1064\text{ nm}$  with light powers up to 200 W. At this wavelength the rate of single particle scattering  $\Gamma_{sc}$  is negligible. Due to the *red detuning* compared to the *D1* and *D2* lines at  $\lambda_0 \approx 671\text{ nm}$  all the optical potentials we currently create in our experiment are attractive.

# 4

## Experimental Techniques

In this chapter, the experimental techniques required for studying many-body physics with ultracold atoms are summarized. Experimentally, the crucial challenges that have to be addressed are an effective isolation of the atoms from the environment, an efficient cooling scheme far into the quantum degenerate regime and the control of internal states and potential landscapes. We focus on the points that are important for our experiments with  ${}^6\text{Li}$  here, more general reviews can be found for example in Refs. [Foo05; Blo08; Sta12]. More detailed descriptions of our experimental apparatus can be found in the following theses [Wen13b; Rie15b; Nei17].

The chapter can be split into three sections. First, all the techniques that are required for the preparation of between  $10^4$  and  $10^5$  degenerate Fermions at ultracold temperatures as well as mesoscopic samples of up to 20 atoms close to the energetic ground state are presented. The preparation process includes different cooling stages as well as multiple transfers of the atoms between different tailor-made optical potentials. The second section deals with the manipulation of the internal states of the atoms. By accessing the internal degrees of freedom we are able to switch between mixtures with different interaction strengths or binding energies. Finally, in the last part, different approaches to image the atoms and to extract information about the many-body state are shown.

### 4.1 State Preparation

The experimental sequence that is used to prepare a desired many-body state can be broken down into two general parts. In the first steps, different cooling stages are used to create a large reservoir of around  $10^5$  atoms at the smallest achievable temperatures. This cloud is then transferred to different optical dipole potentials and, together with external magnetic fields, the desired many-body Hamiltonian is engineered. In our experiment, this final state is always confined very strongly in the axial direction such that a quasi-2D description becomes applicable.

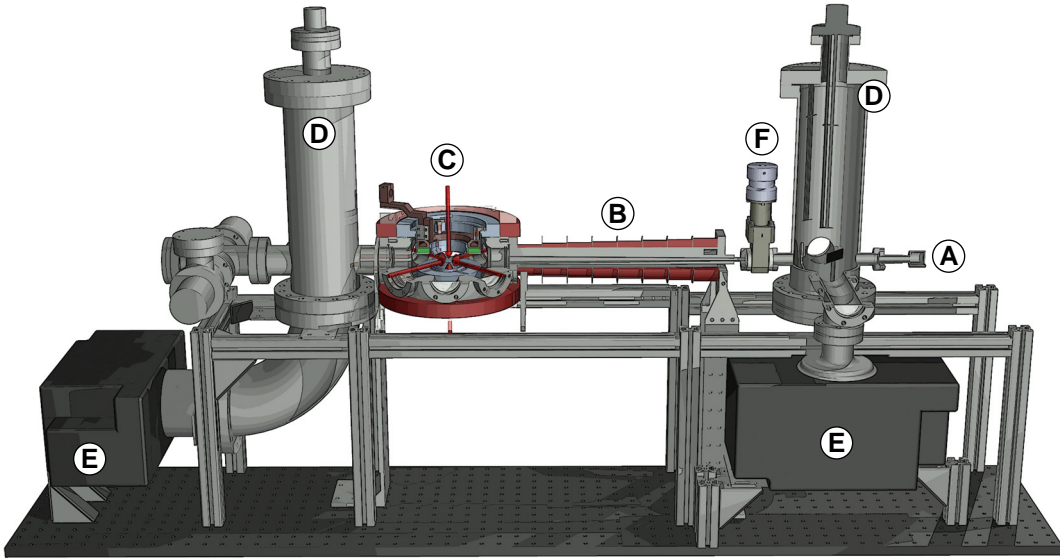


**Figure 4.1: Sketch of the vacuum chamber.** An atomic beam of hot  ${}^6\text{Li}$  atoms is leaving the oven (A) through a small pinhole. The beam is cooled in the Zeeman slower (B) and finally the atoms are trapped in the centre of the main experiment chamber (C). The UHV is created and maintained by titanium sublimation (D) and ion pumps (E). A gate valve (F) allows us to separate the main and oven chamber in case maintenance is required. Taken from [Wen13b].

An experimental control system is required to play-back the sequence with precise analog and digital control signals. We use the ADwin-Pro II as a real-time processor with 32 analog (16 in, 16 out) and 64 digital-IO channels. They run with time steps of  $\Delta t_{\text{AIO}} = 2 \mu\text{s}$  and  $\Delta t_{\text{DIO}} = 0.5 \mu\text{s}$  respectively. A major advantage of the completely digital approach is that we can setup PID feedback loops that are linearized and where the gain parameters can be varied within one experimental run. A LabVIEW interface, running on a standard desktop computer, is used to program the sequences into the local memory of the ADwin and to communicate with all other devices in the laboratory like function generators and cameras.

### 4.1.1 Vacuum System and Coils

In order to create and trap ultracold quantum gases and to achieve the long coherence times these systems promise, they have to be isolated very well from the environment. To this end, all our experiments are carried out in an ultra-high vacuum (UHV) chamber

(see Figure 4.1). Here, we achieve pressures below  $2.3 \times 10^{-11}$  mbar so that collisions with the background gas become negligible for the timescales of all our experiments. A beam of approximately  $\dot{N}_{\text{hot}} = 10^{16}$  atoms/s is created by heating a block of lithium in an oven to around  $T \approx 360$  °C (A). The beam is collimated with a pinhole aperture and can be switched on and off by using a mechanical shutter inside the vacuum. The atoms, having been cooled down with a *Zeeman slower* (B), are trapped in the main experiment chamber (C). It offers sufficient optical access to the atoms through six windows in the horizontal plane with a numerical aperture (NA) of 0.15 and two re-entrant viewports at the top and bottom with a high NA of 0.88 [Rie10].

Two sets of coils (named *MOT*- and *Feshbach-coils*) close to a Helmholtz configuration are placed around the main chamber with their symmetry axis in vertical ( $\equiv z$ ) direction. They allow us to create magnetic offset fields of up to  $B_z = \pm 1500$  G and with hold times of several seconds or field gradients of several hundred G/cm. The Feshbach coils are optimized for fast ramps so that the field strength can be increased with a maximal speed of  $dB/dt \lesssim 1$  G/ $\mu$ s. Using an H-bridge circuit we can switch the current direction in both Feshbach coils or to quench the field off with a maximal speed of  $dB/dt \gtrsim -2.4$  G/ $\mu$ s.

### 4.1.2 Laser Cooling

As mentioned above, the Li atoms leave the oven with a temperature of  $T \approx 630$  K, around 9 orders of magnitude hotter than the temperatures of  $T_F \approx 500$  nK that are required in order to reach quantum degeneracy. In the first step, we slow down around  $\dot{N}_{\text{cold}} = 10^{10}$  atoms/s out of the hot beam from the oven with a mean thermal velocity of  $v_{\text{th}} = \sqrt{8k_B T/m\pi} \approx 1500$  m/s down to  $v_{\text{th}} \approx 50$  m/s using a Zeeman slower. A detailed description of the slower and all its parameters can be found in Ref. [Sim10]. It is operated by setting up a beam resonant to the *D2* line and counter-propagating to the atoms (see Figure 4.2 B). Whenever an atom absorbs a photon from the beam, a momentum of  $\Delta p = h/\lambda$  is transferred opposite to its direction of propagation. Since the spontaneous re-emission events of the photons are isotropic, their average momentum transfer is zero and the overall result is a net force that slows the beam of atoms down. To compensate for the spatially dependent Doppler shift of the *D2* transition frequency a magnetic field gradient is applied that keeps the slowed atoms in resonance along the Zeeman cooler.

After the Zeeman cooler has decelerated the atoms, they are slow enough to be captured in a magneto-optical trap (MOT) in the main experiment chamber. The MOT is based on the same working principle as the Zeeman slower. Three pairs of two counter propagating beams are arranged orthogonal to each other so that they intersect

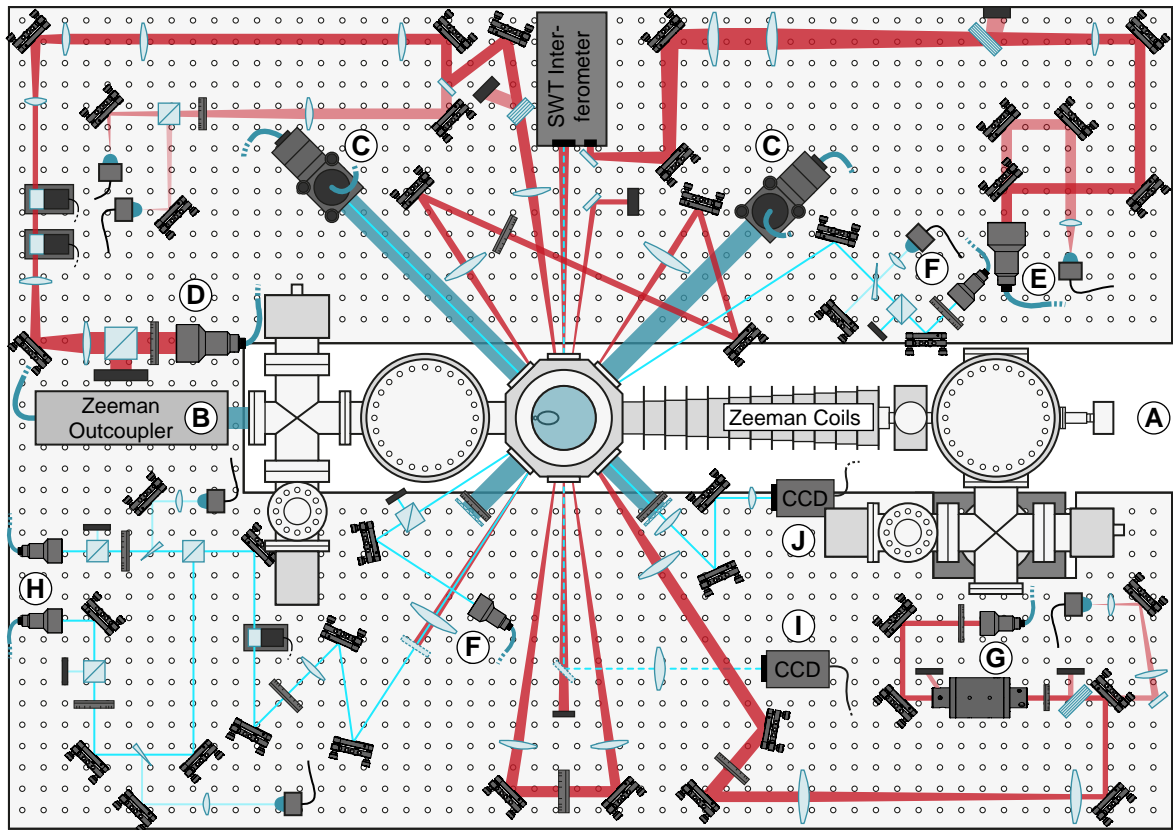


**Figure 4.2: Main breadboard of the experiment.** The atom beam is created in the oven (A). It is first cooled by a counter-propagating laser beam (B) in the Zeeman slower. The horizontal MOT beams (C) are retro reflected by polarization dependent *Moxtek* mirrors. The high power lasers that create the crossed beam optical dipole trap (CBODT) and the SWT are coupled out at (D) and (E). Two counter propagating *flashing* beams are used to illuminate the sample for imaging (F). An optical lattice in a bow-tie configuration can be used to pin the atoms while we image them or for lattice physics experiments (G). The Raman laser setup (H) is used for quasi-instantaneous manipulations of the internal state of the atoms. Two cameras allow us to take fluorescence and absorption images under different angles (I,J).

in the centre of the vacuum chamber (see Figures 4.2 and 4.6 C). By red-detuning the beams from resonance and by applying a current through the MOT coils, the Zeeman shift and beam polarizations can carefully be adjusted such that whenever an atom is

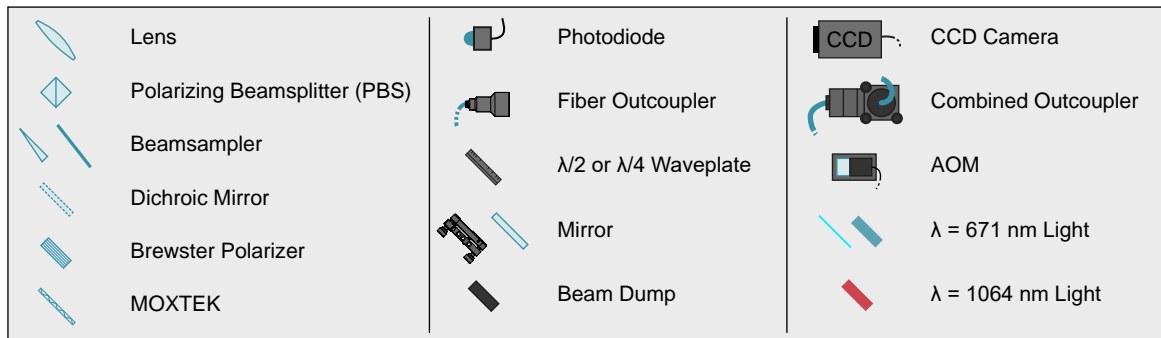


Figure 4.3: List of optical components in Figure 4.2.

displaced from the centre, only the opposing beam becomes resonant (see for example [Dem06]). The result is an effective restoring force that slows down the atoms from the Zeeman beam further and traps them in the centre of the chamber. In practise we have to use two laser frequencies (*cooler* and *repumper*) in each beam for laser cooling since the optical transitions of  ${}^6\text{Li}$  are not closed at low fields and the hyperfine splitting between the  $F = 3/2$  and  $F = 1/2$  ground states is much larger than the linewidth (see section 3.1).

With optimal parameters we can achieve loading rates of around  $\dot{N} \gtrsim 10^8$  atoms/s into our MOT and maximal atom numbers of  $N_{\text{max}} \approx 10^9$  atoms [Sim10]. This demonstrates that laser cooling is both efficient and fast. However, the phase space density we can achieve in the MOT is limited to  $D \lesssim 10^{-5}$  for the reasons given in the following. Due to the presence of near resonant laser beams, light assisted collisions between pairs of atoms become possible as soon as the inter-particle distance is on the order of the wavelength  $d \approx \lambda = 671$  nm. These collisions lead to losses and limit the maximal achievable densities in the trap to around  $n \lesssim 10^{11}$  atoms/cm $^3$ . The lowest temperatures that can be achieved are limited by the random walk the atoms perform due to the spontaneous emission of photons. The random walk result in the so-called *Doppler limit* for the temperature of  $T_D = \hbar\Gamma/2k_B = 141$   $\mu\text{K}$ . In principle sub-Doppler cooling methods make it possible to realize much colder samples, close to the recoil temperature of  $T_{\text{recoil}} = \hbar^2k^2/mk_B = 6$   $\mu\text{K}$ . However, for lithium these techniques are quite hard to implement and still not effective enough to obtain a degenerate cloud.

### 4.1.3 Evaporative Cooling

In section 3.3.3 we have already discussed how far-off-resonant laser beams can be used to create conservative optical potentials. Resonant light scattering is then absent and neither the photon recoil nor light assisted collisions limit the phase space densities we

can achieve. Therefore, as the next step after the MOT, we transfer the cloud into a crossed beam optical dipole trap (CBODT). This trap is created by intersecting two laser beams with wavelengths of  $\lambda = 1064$  nm, orthogonal polarizations and light powers of  $P = 200$  W each under a small angle (see Figure 4.2 D). For these parameters both the potential depth  $V_{\text{CBODT}} \gtrsim 1.5$  mK and volume are large enough to efficiently transfer and trap around  $10^6$  atoms. During the transfer, we switch off the laser resonant to the  $F = 1/2$  ground state manifold first so that the atoms start to accumulate in this hyperfine level. Once we increase the magnetic offset field starting from  $B = 0$ , this leads to a mixture of states  $|1\rangle$  and  $|2\rangle$  (see Figure 3.1).

The collisions between the two component mixtures in the CBODT can be controlled precisely using the broad  $s$ -wave Feshbach resonance (see section 3.3.2). This allows us to implement a very efficient evaporative cooling scheme. To this end, we apply a magnetic field of  $B = 795$  G, slightly below the Feshbach resonance, so that we obtain quick re-thermalization rates. Then, the optical potential depth is slowly lowered — over a time between 1 to 4 seconds depending on the final state — so that the hottest atoms of the cloud are continuously evaporated from the trap. After the evaporation is finished,  $N = 10^5$  atoms per spin state remain in the trap. While we lose a large fraction of atoms in this process, these atoms remove most of the thermal energy of the system such that the final temperature is on the order of  $T \lesssim 100$  nK. After the single evaporation ramp in the CBODT, the cloud is therefore already deep in the degenerate regime with  $T/T_F \approx 0.1$ . It is the starting point for all the experiments presented in this thesis and provides a reservoir from which we can load all the target potentials that we perform our measurements in.

#### 4.1.4 2D Standing Wave Trap

We are mainly interested in strongly interacting Fermi gases that are confined to 2D (for a motivation see chapter 2). In chapter 3 we have already discussed how the dynamical behaviour of the gas can become 2D when the trap level spacing in the third direction  $\Delta E_z$  (e.g. for a harmonic potential  $\Delta E_z = \hbar\omega_z$ ) is increased. As soon as  $\Delta E_z$  dominates over all other energy scales of the many-body system, like its Fermi energy  $E_F$ , chemical potential  $\mu$  or Temperature  $k_B T$ , all the particles remain in the ground state in  $z$ -direction and a quasi-2D description becomes accurate. This allows us to study the peculiarities of 2D quantum mechanics in an experiment in a 3D world.

In practise, we reach the 2D limit by transferring the atoms into a highly anisotropic single layer of a standing wave optical dipole trap (SWT). The SWT is created by splitting a single Gaussian beam with aspect ratio of 8 : 1 into two and interfering both arms under an angle of  $14^\circ$  again (see Figure 4.4 a). This setup leads to an interference pattern with a stack of quasi-2D potentials (*pancakes*) at the centre of

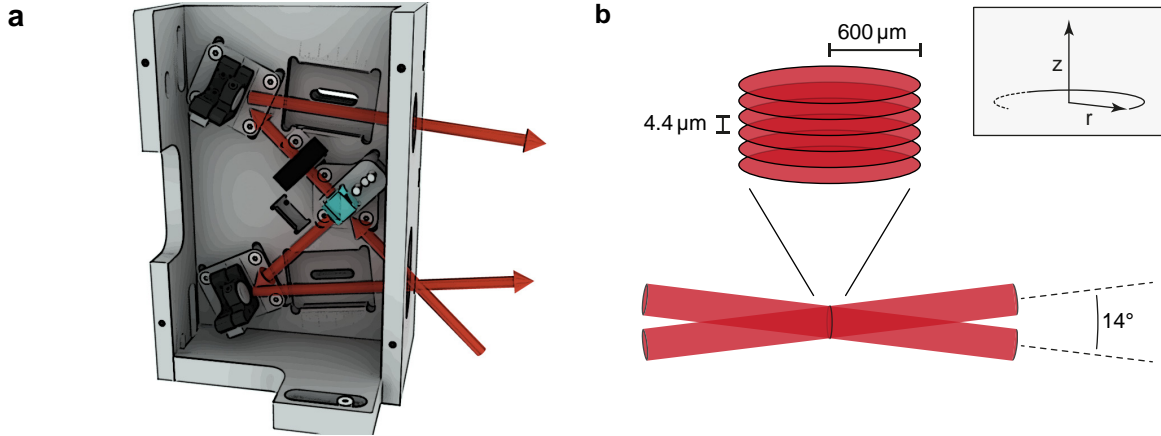


**Figure 4.4: Standing wave trap interferometer.** The SWT is created by splitting a single beam with  $\lambda = 1064 \text{ nm}$  into two and interfering both arms under  $14^\circ$  again (a). The setup is optimized for stability such that the relative phase between both arms in the atom plane drifts less than  $\Delta\phi < \lambda/8$  over one week [Rie15b]. The interference pattern consists of many layers that are separated along the  $z$ -direction by  $d = 4.4 \mu\text{m}$  (b). We load our gas into one of these layers before we perform any of the experiments discussed in this thesis. Adapted from [Wen13b].

the vacuum chamber (see Figure 4.4 b). The radial size of the *pancakes* corresponds to the horizontal beam waist of  $w_0 = 600 \mu\text{m}$  and they are spaced by approximately  $d = 4.4 \mu\text{m}$ . At a typical light power of  $4 \text{ W}$ , each layer has a trap depth of around  $V_{\text{SWT}} \approx 650 \text{ nK}$  and the trap frequencies are given by  $\omega_z = 2\pi \times 7 \text{ kHz}$  and  $\omega_r^{\text{opt}} = 2\pi \times 18 \text{ Hz}$  respectively. Together with a small harmonic confinement in radial direction produced by the Feshbach coils of  $\omega_r^{\text{mag}} = 2\pi \times 10 \dots 15 \text{ Hz}$  (depending of the exact value of the offset field  $B$ ), this leads to a total trap frequency in radial direction of  $\omega_r \approx 2\pi \times 22 \text{ Hz}$ . The total aspect ratio for atoms trapped in the SWT is therefore given by  $\omega_z : \omega_r \gtrsim 300 : 1$ .

#### 4.1.5 Preparing a 2D Fermi Gas

In our experiment, we have developed two alternative preparation sequences for quasi-2D Fermi gases (see Figure 4.5). The first one, described in this subsection, allows us to create balanced two component mixtures (typically states  $|1\rangle$  &  $|2\rangle$  or  $|1\rangle$  &  $|3\rangle$ ) of up to  $10^5$  atoms. To this end, we transfer the atom cloud from our reservoir in the CBODT into a single layer of the SWT (see Figure 4.5 a). This procedure relies

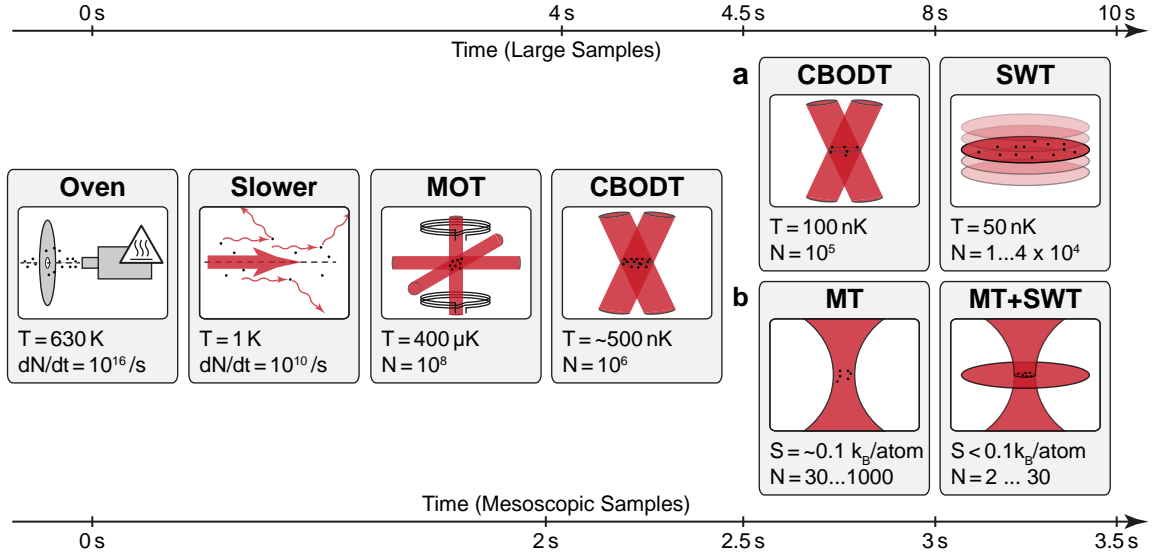


**Figure 4.5: Experimental preparation sequence.** The figure shows a sketch of the complete preparation cycle in the experiment both for large samples (a) and mesoscopic systems (b). Depending on the desired final state we start from a lower or higher atom number in the MOT (loading times of 2 s and 4 s respectively). To prepare mesoscopic samples, the evaporation sequence in the CBODT is kept short ( $\approx 500 \text{ ms}$ ) and we quickly transfer the atoms to the MT for much faster thermalization times. The preparation of large samples of atoms in the SWT requires much longer evaporation times in the CBODT (indicated by the two separate blocks) and is in general slower due to the smaller trap frequencies. The total sequence time for the preparation of large samples is around 10 s. For mesoscopic samples we only need less than 3.5 s.

on modifying the CBODT potential and tuning the interactions such that the cloud becomes as compressed as possible in  $z$ -direction before we can load the SWT. The transfer is described in more detail in Ref. [Rie15b] and results in more than 90% of the atoms being trapped in a single layer, while the remaining atoms sit in the adjacent lattice sites. A final evaporative spilling step in the SWT sets the final particle number  $N$  and ensures that we reach the quasi-2D limit. We achieve temperatures of  $T \approx 50 \text{ nK}$  corresponding to  $T/T_F = 0.05$  with around  $N = 40\,000$  atoms per spin state. The size of the ground state wavefunction in axial direction is given by the harmonic oscillator length of  $l_z = \sqrt{\hbar/m\omega_z} = 460 \text{ nm}$ . This is much smaller than the layer spacing and therefore tunnelling between different 2D sheets can be neglected completely.

## 4.2 Bottom Up Approach

The large cloud of a two component 2D Fermi mixture already offers a very rich phase diagram to explore experimentally (see chapter 2). Our recent measurements in this system, some of which will be discussed in chapter 8, have already significantly improved our understanding of strongly correlated Fermi gases [Rie15a; Boe16; Mur18b; Hol18]. Nevertheless, many open questions remain and a complete theoretical description is still missing. This is also owed to the fact that with the current state of the art techniques the experimental control over quantum systems with  $N \gg 1000$  particles is limited, especially when the atoms are not confined to a lattice. And while the atoms are deeply degenerate at  $T/T_F = 0.05$  and, depending on the interaction strength, even forming a condensate, the initial state that we prepare is certainly mixed and difficult to characterize precisely. In addition, we are limited to observables like densities averaged over an area much larger than the typical inter-particle spacing only. In this way, we can only study the gas through indirect measurements like energy spectra or collective mode excitations. It is not possible to directly access the fundamental ingredient of collective behaviour of Fermions: their pair correlations.

In order to address all of the challenges listed above, we have decided to take a novel bottom up approach. Our idea is to start from the smallest possible instance of the 2D gas and slowly work our way up to larger and larger particle numbers, keeping the system precisely under control at every step along the way. To realize this vision, we have significantly improved on the capabilities of our experimental apparatus during the work for this thesis. The upgrade has been designed around three main components that have already been implemented: a high-resolution objective to both manipulate and probe the atoms with a resolution below  $1 \mu\text{m}$  (see Figure 4.6), a spatial light modulator (SLM) with red-detuned light to tailor any desired attractive and even time dependent potential for the atoms (see Figure 4.8) and a highly sensitive electron multiplying CCD camera (EM-CCD) with single photon counting capability (see Figure 4.19).

In the following, we discuss how the SLM setup allows us to project arbitrary potentials through the microscope objective onto the 2D plane that is defined by the SWT. In section 4.4.3, our imaging scheme using the EM-CCD and that enables us to detect the cloud in free space and with single atom resolution is presented.

### 4.2.1 High-Resolution Objective

The optical setup around the microscope objective is shown in Figure 4.6. The objective was custom-designed to meet the requirements of our apparatus [Ser11b]. Chromatic shifts are compensated such that both our wavelengths of  $\lambda = 1064 \text{ nm}$  and  $\lambda = 671 \text{ nm}$

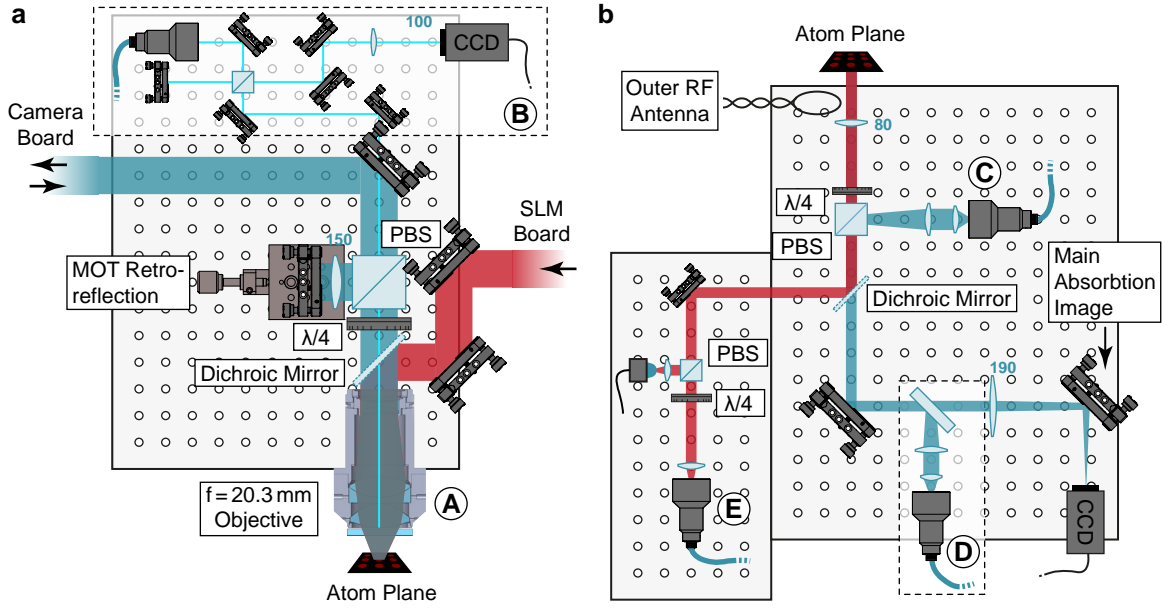


**Figure 4.6: Optical setups above (a) and below (b) the experimental chamber.** The optical components are mounted on a vertical breadboard and cage systems respectively. Dichroic mirrors and PBS cubes are used to split the different beam baths for imaging, trapping and cooling light. The objective (A) is placed close to the upper re-entrant viewport of the vacuum chamber. A green  $\lambda = 532$  nm guide beam setup (B) is used to optimize the alignment and angle of the objective with respect to the vacuum chamber. The MOT (C) and an optional absorption imaging beam (D) are shined in from below the chamber. A second optical potential (E) allows us to magnify the atom cloud by up to a factor of 50 before imaging.

have the same focal length of  $f = 20.3$  mm. The large focal length  $f$  is required in our setup due to the large distance of atoms from the vacuum window. The objective was designed with a high target NA of 0.6. For  $\lambda = 671$  nm light, we measured an actual resolution of  $r = 0.86(1)$   $\mu\text{m}$ , slightly below the expected value of  $r_{\text{theo}} = 0.68$   $\mu\text{m}$  [Kle18]. The resolution for  $\lambda = 1064$  nm is given by  $r_{\text{theo}} = 1.08$   $\mu\text{m}$ . There are no recent measurements, however we expect that we are close to the optimal value in the experiment since we are able to correct for all the optical aberrations at this wavelength with the SLM (see next section). The nominal design values for the field of view diameter of the objective are as large as  $d_{671} \approx 480$   $\mu\text{m}$  and  $d_{1064} \approx 700$   $\mu\text{m}$  [Ser11b].

Thanks to the chromatic compensation, we are able to utilize the objective both to project optical potentials onto the atoms as well as to collect resonant fluorescence light onto a camera for imaging. A dichroic mirror on top of the objective is used to split the two wavelengths used for those purposes (see Figure 4.6 a). Since the objective fills the complete re-entrant viewport on top of the vacuum chamber, we had to setup an additional beam path through the objective that can be used for laser cooling with the MOT. Imaging and cooling light are separated by a polarizing beam splitter (PBS) cube. Figure 4.6 b shows the corresponding optical setup below the experimental chamber. Here, a secondary charge-coupled device (CCD) camera is placed to take absorption images through a  $f = 80$  mm lens with lower resolution but a much larger field of view. This is useful for alignment purposes as well as measurements of averaged quantities in the large 2D cloud prepared in the SWT. Recently, we have added a second optical trapping potential from the bottom that allows us to magnify the cloud by a factor of up to 50 before imaging. The matter wave magnification technique will be discussed in more detail in section 4.4.7.

## 4.2.2 SLM Setup

In order to achieve our goal to precisely control mesoscopic quantum systems, we need the ability to tailor arbitrary potentials, beyond what is possible by simply interfering two or more laser beams. Computer programmed light modulators have found widespread application in the field of ultracold quantum gases for this purpose. They allow us to project arbitrary intensity distributions onto the atom cloud through some optical imaging setup. The resulting effective potential for the atoms is then directly proportional to the light intensity ( $V(\mathbf{r}) \propto I(\mathbf{r})$ ), as discussed in the previous chapter [Gri00]. Most commonly used devices are spatial light modulators (SLMs) or digital micromirror devices (DMDs), capable of modulating the amplitude or phase of some incident beam of light on some array of pixels [Ber04; Zup16].

There are two main configurations that can be used for the purpose of optical beam shaping (see Figure 4.7). The modulating device can be placed either in the Fourier- or imaging-plane with respect to the atoms [Gau16; Zup16; Bar18]. When placed in the imaging plane, the modulated amplitude  $\tilde{A}$  corresponds directly to the amplitude  $A_{\text{atom}}$  of the electric field in the atom plane. This setup is therefore well suited for the creation of continuous potentials with larger length scales. For smaller sized potentials however, the light utilization efficiency becomes very small and corrections to the potential that are on the order of the resolution limit are impossible (see Figure 4.7 b). Since we are interested in creating precise potentials with high efficiency for the preparation of mesoscopic Fermi systems, we place our SLM in the Fourier plane instead. Here, the field distribution in the atom plane is given by the Fourier transformation  $\mathcal{F}[E_{\text{mod}}]$

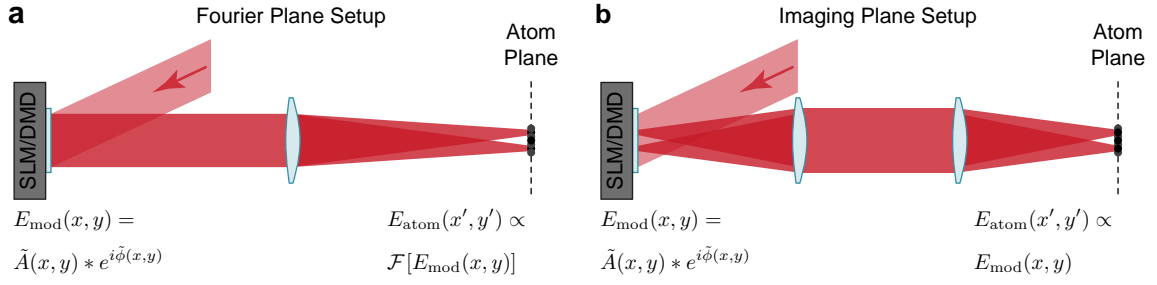


**Figure 4.7: Tailored Optical Potentials.** Programmable light modulation devices like SLMs or DMDs can be placed in either the Fourier- (a) or imaging-plane (b) with respect to the atoms. With the imaging plane-setup it is very simple to create large scale potentials without small scale structures close to the resolution limit. For small tailored potential or optical tweezer arrays, the placement in the Fourier plane is the better option.

of the modulated field (also called hologram), so that we are able to correct optical aberrations and deformations of the potential on the scale of the resolution limit. In addition we achieve very high light utilization efficiencies for a single optical tweezer or tweezer arrays of above 50%. As one of the next experimental upgrades, we will add a DMD in the imaging plane in addition to the SLM. It is projecting blue detuned repulsive potentials, for example steep walls, onto the atoms (see chapter 9) [Hei20].

In our experiment, we use a parallelly aligned liquid crystal SLM that can control the phase of the incident light field on  $600 \times 792$  pixels in steps of approximately  $0.01\pi$  from 0 to  $2\pi$  (X10468-03 from Hamamatsu). Compared to a DMD, the advantages of the SLM are its higher dynamic range and the much higher theoretical light utilization efficiencies of up to 80%. In addition, due to the nature of the liquid crystals used for the phase modulation, the SLM naturally interpolates between two consecutive images when a time varying movie of holograms is displayed. The theoretical refresh rate of the X10468-03 is 120 Hz. The true settling time for the pixels is on the order of  $t \gtrsim 80$  ms, however. Therefore, only potentials with slow time variation with respect to the typical trap frequencies  $\omega \gg 1$  kHz can be displayed. The biggest drawback of the SLM, especially compared to a DMD, is that the pixels constantly have to be driven with alternating current (AC) (here with 240 Hz). The oscillation leads to some intensity noise of the created potentials at all integer multiples of the drive frequency. We minimize this effect as far as possible by synchronizing the whole experiment to the refresh cycle of the SLM and by implementing a feed-forward loop using the exact waveform of the noise signal.

The complete setup for the SLM is shown in Figure 4.8. For the tailored potentials

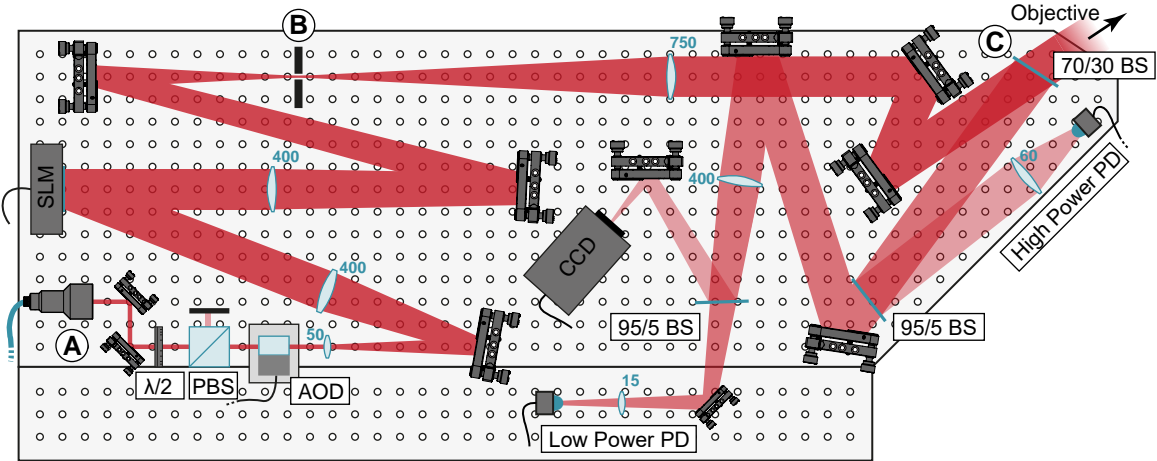


**Figure 4.8: Sketch of the SLM setup.** Up to  $P = 500$  mW of light are coupled out of the fibre at (A). The light is modulated by the AOD and SLM and imaged onto the atoms through a  $6f$ -setup. A razor blade (B) removes the  $0^{\text{th}}$ -orders that appear due to the limited efficiency of both light modulating devices. Some of the light is reflected by a beam sampler (C) before it enters the objective and is imaged on the atoms.

we currently use up to  $P = 500$  mW of laser power with a damage threshold of the SLM of around  $P_{\text{max}} = 5$  W. When this light is focused to a single optical tweezer by our microscope objective, this leads to trap frequencies exceeding 1 MHz and trap depths around 1 mK. An acousto-optic deflector (AOD) is imaged onto the SLM to be able to manipulate the potential even further. The AOD is not as versatile, but allows for much faster dynamics, with a bandwidth on the order of a few MHz. After the incident light beam has been modulated by the SLM, it is imaged onto the atoms through a  $6f$ -setup including the objective as last lens (compare Figure 4.6). We use a razor blade to remove the unwanted  $0^{\text{th}}$ -order of the SLM. Around 30% of the light is reflected by a beam sampler before entering the objective. The reflected light is focused on two photodiodes and a camera used for power stabilization and diagnostics respectively.

With the setup completely implemented in our experiment, the remaining challenge is to find the correct phase modulation pattern to produce the desired intensity distribution in the plane of our 2D atom trap. There is no exact analytical solution for this problem, also known as *phase retrieval*. However, there are many numerical approximation methods that generate holograms for any target potential [Pas08; Har14]. Here, one of the most important prerequisites for obtaining high-quality traps is that the optical setup is free of aberrations. One of the crucial features of the SLM is that

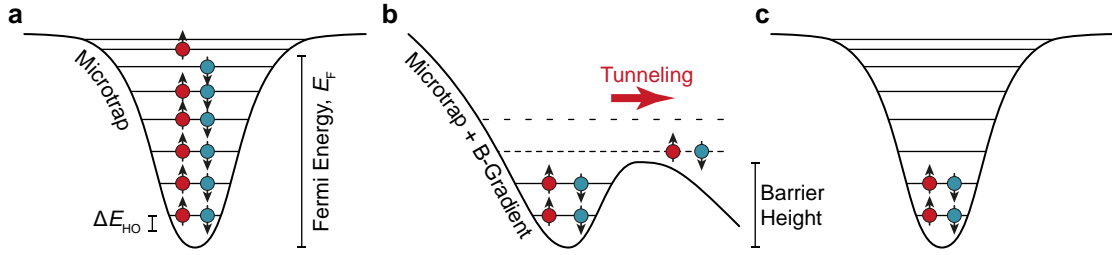


**Figure 4.9: Deterministic preparation in 1D.** We start from Fermi sea of atoms trapped in an approximately 1D harmonic oscillator potential (a). Due to the Fermi-Dirac distribution all low lying energy levels are completely filled with almost unity probability. By tilting the potential and lowering the trap depth, we can deterministically remove all the atoms above some *spill level* (b). We end up with the desired number of atoms prepared in the ground state of the potential with high fidelity (c).

it is able to both detect and correct all the aberrations in its optical path with a very high precision [Bij13]. We make use of the aberration correction to be able to create optical tweezers with sizes close to the diffraction resolution limit of our objective [Bay20b]. This leads to larger ratios of harmonic trap frequencies  $\omega$  over the trap depth  $V_0$ . Large trap frequencies are essential for the deterministic preparation of quantum ground states in the tweezer potential described in the next section.

### 4.2.3 Deterministic Preparation

The SLM setup opens up a whole realm of new possible Hamiltonians to explore in our experiment. Here, with our bottom up approach in mind, we will focus on the creation of a single highly tunable optical tweezer, also called microtrap (MT). Further possible applications of the SLM like tweezer arrays for future studies of Hubbard model physics and itinerant magnetism or ring and box structures will be discussed in chapter 9. The single MT allows us to refine a method that was initially developed in our group for the preparation of ground states in a quasi one dimensional (1D) harmonic oscillator trap with almost unity probability [Ser11a]. We have extended the technique to a 2D harmonic oscillator, where we are now able to prepare pure quantum states of up to  $N = 20$  particles.

The preparation scheme is based on the idea that the small MT, when superimposed with a large reservoir of atoms, can locally enhance the chemical potential  $\mu$  by a large amount, while the temperature  $T$  of the gas remains the same [Sta98]. This leads to a small region of enhanced densities deep in the degenerate regime with  $T/T_F \approx 0.05$

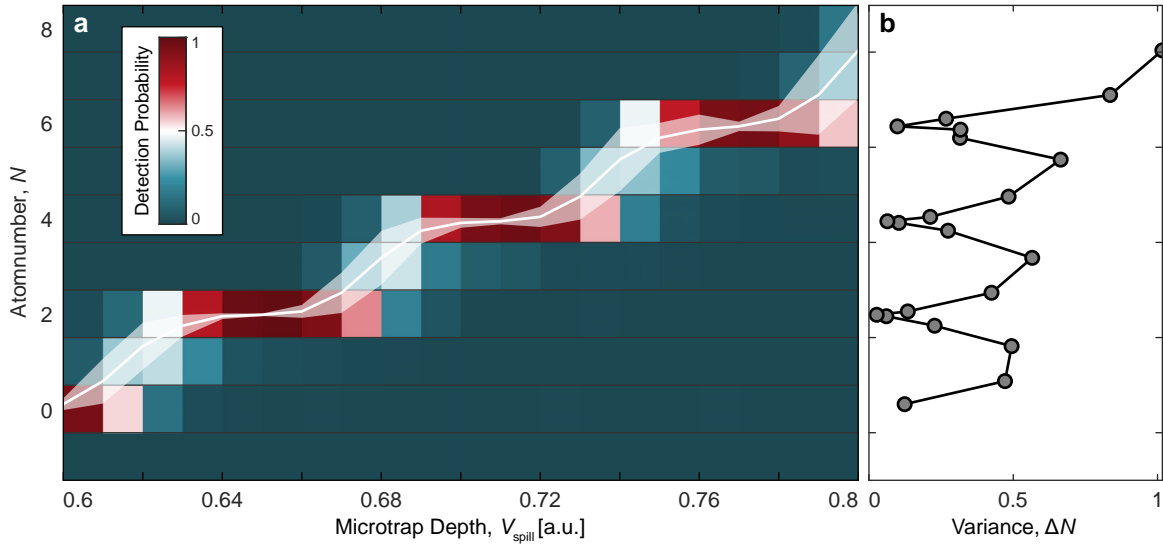


**Figure 4.10: Experimental preparation of ground states in a quasi-1D harmonic oscillator potential.** The mean atom number (white solid line) is shown as a function of the MT depth during the deterministic spilling process (a). The full counting statistics for each depth setting is shown as density plot in addition. We find stable plateaus at all even atom numbers. These correspond to the levels of the 1D harmonic oscillator, where the stability of the preparation increases significantly and the variance in prepared atom numbers becomes small (b).

and a filling of many of the energy levels of the MT potential. Thanks to the Fermi-Dirac statistics the lowest levels of the potential are completely filled with very high probabilities of  $P > 99\%$  in this situation (see Figure 4.9 a) [Ser11b]. By tilting the potential and lowering its depth in a precisely controlled way, we can reduce the number of quasi-bound states in the well (b). The lifetime of these states is orders of magnitudes larger than that of any of the higher levels that become unbound and quickly leave the trapping region. We end up with a pure ground state where all the levels up to the desired *spilling threshold* are completely filled (c). This method works best for tightly confined mesoscopic samples where the energy level spacing becomes large. Then, the requirements on the stability of the spilling barrier height in order to remain exactly between two adjacent energy levels in the spilling process become less strict.

To implement the spilling sequence in our experiment, we begin by loading around 1500 atoms from the CBODT into the MT with the smallest possible focus created by

the SLM (see Figure 4.5 b). The transfer takes around 150 ms and is started already after 500 ms of evaporation time in the CBODT, long before the final temperature is reached. In the MT we reach trap frequencies of  $\omega_z \gg 2\pi \times 100$  kHz and the corresponding collision and thermalization rates are large enough to complete the full evaporative cooling stage deep into the quantum degenerate regime with  $T/T_F \approx 0.05$  in only 10 ms. This significantly speeds up the preparation time to around 3 s. With further improvements of the laser cooling stages, experimental cycle rates of more than 1 Hz are well within reach with our scheme.

We end up with around 300 atoms in the MT as a starting point for the deterministic preparation scheme described above. The spilling step is initiated by applying a magnetic field gradient of  $dB/dz = 24$  G/cm and lowering the optical power of the tweezer from  $P_{\text{hold}} = 500$   $\mu$ W to  $P_{\text{spill}} = 5 \dots 50$   $\mu$ W depending on the target atom number ground state. The spilling takes  $t_{\text{spill}} = 40$  ms before the potential depth is increased to its hold value again. This results in the best compromise between higher, unbound levels leaving the trap and unwanted tunnelling out of the quasi-bound states below the spilling barrier. In Figure 4.10, we plot the mean atom number as a function of final spill depth  $V_{\text{spill}}$ , averaged over 350 cycles of the experiment for each data point. The procedure to count the exact number of atoms remaining in the trap after spilling is described in detail in section 4.4.2.

We find stable plateaus at even atom numbers of 2, 4 and 6 atoms. They correspond to the lowest levels of our quasi-1D harmonic oscillator potential that are filled with two spin components each. For larger atom numbers, a deterministic preparation of atom numbers becomes difficult since the aspect ratio of our quasi-1D MT is only  $\omega_r/\omega_z = 3.40(3)$ . The additional excitations in radial direction for  $E > 3\hbar\omega_z$  increase the density of states and a precise adjustment of the spilling barrier between the energy becomes more difficult. We achieve ground state preparation fidelities of 97(1) %, 93(2) % and 85(2) % for 2, 4 and 6 atoms respectively. To ensure that the atoms are really in the ground state and no excitations are created, for example when ramping the trap power back after the spilling process, we spill the MT to the same level twice in the same experimental sequence. We find that the second spill does not lead to an additional, unexpected atom loss for this control measurement (see Figure 4.11 a). For 2 atoms, we estimate the probability to prepare excited states to be on the order of  $P_{\text{exec}} \sim 10^{-4}$  [Bay20b].

#### 4.2.4 Von Neumann Entropy

We prepare the final state with a fixed energy and well isolated from the environment. Therefore, the system is better described in terms of its entropy than by a thermal state of some temperature  $T$ . The von Neumann entropy for a mixed quantum state

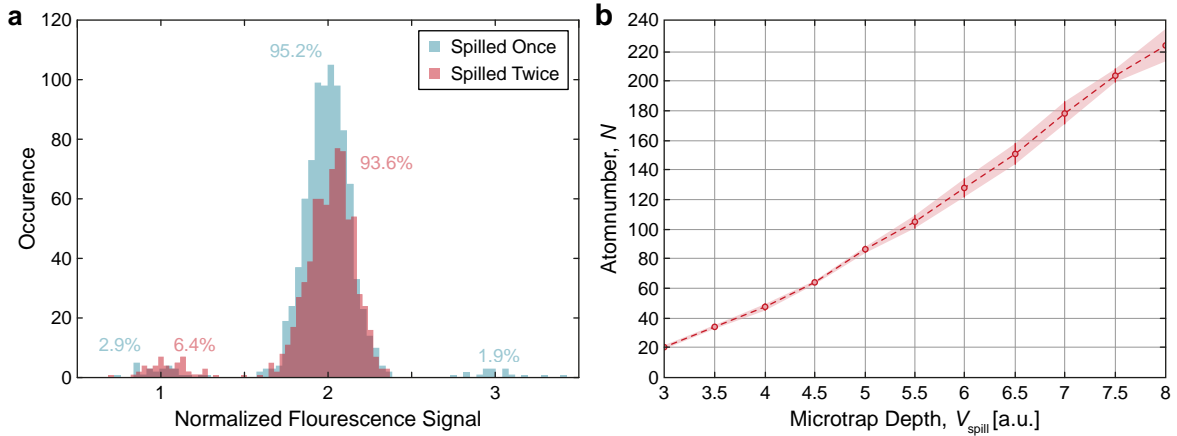


**Figure 4.11: Characterizing the performance of the deterministic preparation technique.** By spilling twice in a row, we can check if we have really prepared the ground state after the first spilling process (a). We find that the probability to obtain two atoms after the second spilling process of  $P_{N=2}^{\text{twice}} = 93.6(9)\%$  agrees well with the assumption of the two spilling processes being independent. In this case we expect  $P_{N=2}^{\text{twice}} = 1 - (P_{N=1}^{\text{once}})^2 = 94.3(10)\%$ . For larger atom numbers the fidelity of preparing a ground state with target particle number  $N$  reduces significantly. This can be explained by the larger density of states of the system at larger barrier heights. Nevertheless, the standard deviation of the prepared atom number, indicated by the error band, becomes very small below an atom number of around  $N = 100$  (b). This indicates that we are able to prepare very low entropy states in this regime. Panel (a) adapted from [Kle18].

with density matrix  $\rho$  is defined as [Sch06]:

$$S = -k_B \text{tr}(\rho \ln \rho) = -k_B \sum_i p_i \ln p_i, \quad (4.1)$$

where  $p_i$  is the probability to detect the system in its eigenstate  $i = 1 \dots n$ . When we assume that the atoms are prepared almost entirely in their ground state, this allows us to directly calculate the entropy  $S$  from the histogram of final atom numbers at each setting for the spill depth (see Figure 4.10 a). We obtain an entropy per particle of  $S/N = 0.10(2) k_B$  for up to  $N = 6$  particles. For larger prepared atom numbers it becomes difficult to calculate the von Neumann entropy directly since excitations in radial direction lead to additional degeneracies of the ground state. However, we observe that the standard deviation of the prepared atom number remains as low as

$\Delta N \sim 5\%$  for up to  $N = 100$  atoms (see Figure 4.11 b). This indicates that the entropy per particle does not significantly increase up to those particle numbers. An entropy per atom of  $S/N = 0.1 k_B$  is on par with or even better than what has been achieved in the most recent lattice experiments in the superfluid regime [Bol16; Chi18].

### 4.2.5 Quasi-2D Microtrap

So far we have discussed the deterministic preparation of ground states in a quasi-1D harmonic potential with  $\eta = \omega_r/\omega_z > 1$ . To perform experiments in quasi-2D we need to invert this aspect ratio to  $\eta \ll 1$ . For a single focused beam trap in the harmonic approximation, valid when the atomic sample is small compared to the beam waist, the trap frequencies are given by [Gri00]:

$$\omega_r = \sqrt{\frac{4V_0}{mw_0^2}} \quad \text{and} \quad \omega_z = \sqrt{\frac{2V_0\lambda^2}{m\pi^2w_0^4}}, \quad (4.2)$$

where  $V_0$  is the potential depth and  $w_0$  the beam waist at the focus. The aspect ratio of the optical tweezer can accordingly be calculated as:

$$\eta = \omega_r/\omega_z = \frac{\sqrt{2\pi}w_0}{\lambda}. \quad (4.3)$$

It follows that the aspect ratio of the MT alone is always larger than one and  $\eta \ll 1$  is only possible by superimposing additional potentials. From equation (4.3), we can calculate the beam waist of the focused MT from the measured aspect ratio as  $w_0 = 0.82(1) \mu\text{m}$ . This value is very close to the expected minimum of  $w_0 = 0.72 \mu\text{m}$  given by the resolution of the objective. The small achieved waist highlights the capabilities of the SLM in removing optical aberrations once more.

To obtain mesoscopic samples in quasi-2D, independent of the limitations of the MT, we make use of the standing wave optical dipole trap (SWT) again. As discussed in section 4.1.4, it produces a harmonic confinement in axial direction of  $\omega_z = 2\pi \times 7 \text{ kHz}$ . Following equation (4.2), one might think that it is enough to simply reduce the optical power  $P_{\text{MT}}$  and trap  $V_0 \propto P_{\text{MT}}$  of the MT far enough until  $\omega_r \ll 2\pi \times 7 \text{ kHz}$ . However, a problem occurs when the potential becomes so shallow that no more bound trap levels remain in the MT. This issue can be circumvented by increasing the waist of the focus  $w_0$  instead. At a constant depth of the potential  $V_0$  this allows us to reduce the radial trap frequency as  $\omega_r \propto 1/w_0$ . Consequentially, this leads to an increase in the number of trapped levels in the potential approximately given by  $V_0/\omega_r$ . In practise, it is often more convenient to keep the total power in the trapping beam  $P_{\text{MT}}$  constant instead of the potential depth  $V_0$ . Then, the central depth of the potential scales as

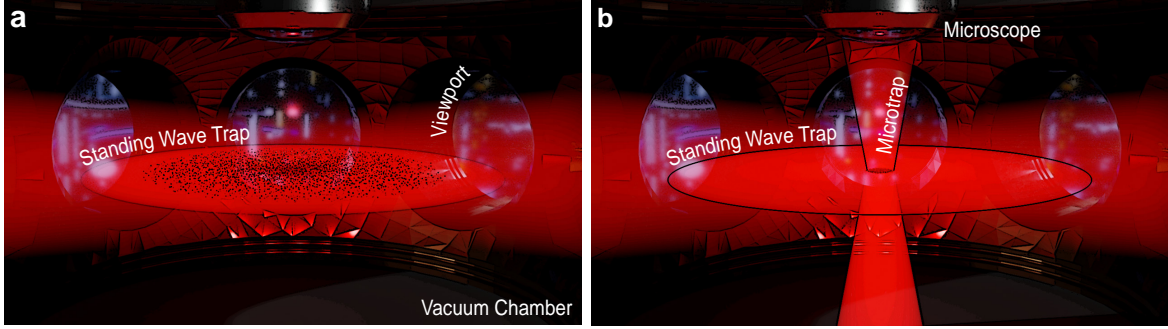


**Figure 4.12: Different potential configurations for experiments in quasi-2D.**

To prepare many-body systems with several tens of thousands of atoms, we load the atoms in a single layer of the SWT (a). Here, the trap frequencies are given by  $\omega_r \approx 2\pi \times 20$  Hz and  $\omega_z = 2\pi \times 7$  kHz with  $\eta > 1/300$ . To create mesoscopic samples of up to hundred atoms, we superimpose the SWT with the MT from the top. This leads to a much stronger radial confinement with  $\omega_r \approx 2\pi \times 1$  kHz and  $\eta = 1/7$  (b).

$V_0 \propto P_{\text{MT}}/w_0^2$ , the radial trap frequency as  $\omega_r \propto \sqrt{P}/w_0^2$  and the number of trapped levels remains approximately constant.

The SLM allows us to dynamically tune the waist  $w_0$  of the MT during the experimental cycle. To this end, we simply superimpose the hologram that we display with a circular aperture mask of diameter  $d$  that cuts off the waist of the trapping beam  $w_{\text{in}}$  before entering the objective. This reduces the effective numerical aperture  $\text{NA}_{\text{eff}} = \text{NA} * d/d_{\text{objective}}$  and leads to a final MT waist of:

$$w_0 = 0.85 \frac{\lambda}{2\text{NA}_{\text{eff}}} \propto \frac{1}{d}. \quad (4.4)$$

A more detailed derivation of equation (4.4) can be found in Ref. [Bay20b].

In practise we typically increase the waist of the MT from  $1 \mu\text{m}$  to around  $5 \mu\text{m}$ . This allows us to reach radial trap frequencies of the MT in the range of  $\omega_r = 2\pi \times 100 \dots 1000$  Hz. The axial confinement of the MT scales as  $\omega_z^{\text{mt}} \propto \sqrt{P}/w_0^3$  and is negligible compared to the confinement of the SWT. Likewise the radial confinement of the SWT of  $\omega_r^{\text{swt}} = 2\pi \times 18$  Hz is negligible compared to the radial confinement of the MT. As a result, in the combined potential the atoms are confined radially by the MT and axially by the SWT and with a total aspect ratio of  $\eta < 1/7$  (see Figure 4.12). Reducing the radial frequency  $\omega_r$  much further is impractical because it keeps increasing the density of states. A large level spacing  $\hbar\omega_r$  is an essential prerequisite for the deterministic spilling technique into ground states as discussed above. The

combined potential, also referred to as two dimensional microtrap (2D-MT), contains several bound states and can be used for the preparation of quasi-2D quantum states for tens of atoms when  $E_F < 2\pi \times 7 \text{ kHz}$ .

### 4.2.6 Transfer to 2D

To load the atoms in the superimposed 2D-MT potential, we start with 20 . . . 50 atoms in the MT that are prepared using our deterministic spilling scheme. The first step is to load this sample into a single layer of the SWT (see Figure 4.13 a). To this end, we first lower the magnetic offset field from  $B = 800 \text{ G}$  to  $700 \text{ G}$  to increase the interaction strength and decrease the width of the atom cloud in  $z$ -direction  $\sigma_z$ . With the spacing of the SWT layers of  $4.4 \mu\text{m}$ , we are currently able to load up to  $N_{\text{max}} = 50$  atoms before atoms are filled into the adjacent layers. This limit could be extended by increasing the MT power  $P_{\text{MT}}$  to compress the cloud further or by replacing the SWT by an accordion lattice.

The SWT is ramped up from  $P_{\text{SWT}} = 0 \text{ W}$  to its full power of  $4 \text{ W}$  in  $20 \text{ ms}$  while the MT power is kept constant. To ensure that the centre of the mesoscopic atom cloud overlaps exactly with the centre of one SWT layer, we utilize the capabilities of our SLM again. It allows us to shift the focal position of the MT in  $x, y$  and  $z$  direction with a step size on the order of a few nanometres. To find the optimal position, we reduce the depth of the 2D-MT far enough that only three bound levels, corresponding to 6 atoms, remain in a single layer. By tuning the focal shift  $\Delta z_{\text{MT}}$  and recording the final atom number, we optimize the overlap to reliably load a single layer (see Figure 4.13 b). By placing the MT exactly in between two layers, we can deterministically prepare two exact copies of the system in two adjacent layers. This capability might become very interesting for future interference or tunnelling experiments between independently prepared mesoscopic systems.

Once the atoms are loaded into a single layer of the SWT and a strong axial confinement is present, the final step is to increase the waist  $w_0$  of the MT from  $1 \mu\text{m}$  to  $5 \mu\text{m}$ . This leads to a combined quasi-2D potential with an aspect ratio of  $\eta = 1/7$  as discussed in the previous section. The waist is increased by adding an aperture phase pattern to the SLM in a single frame update. The slow response time of  $80 \text{ ms}$  of the liquid crystals naturally smoothens the ramp of the MT waist. During the dimensional crossover several energy levels of the initial quasi-1D potential cross. This creates holes in the final atom distribution whenever an unoccupied level crosses an occupied one. Experimentally, we have found that strong interactions ( $a = -20\,000 a_0$ ) lead to strong coupling between different levels and avoided crossings with large gaps emerge. This allows us to stay adiabatic and remain in the ground state during the transfer from a 1D to a 2D geometry. When the transfer is carried out for a non-interacting gas

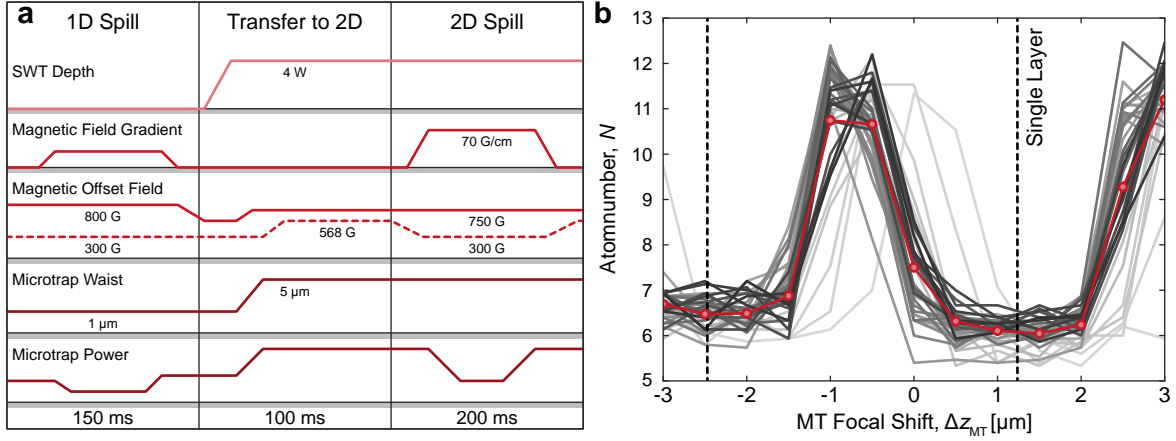


**Figure 4.13: Transfer into the SWT.** A sketch of the transfer sequence adapted from [Bay20b] is shown in (a). We start by preparing 20 to 50 atoms close to the ground state in the MT. The cloud is transferred into the superimposed quasi-2D potential by ramping up the SWT and increasing the MT waist. A second spilling step in 2D is used to prepare pure ground states with high fidelity. We make sure to reliably load a single layer of the SWT by precisely adjusting the focal shift in  $z$  direction of the MT  $\Delta z_{\text{MT}}$  using the SLM (b). When we spill to 3 levels corresponding to 6 trapped atoms in the 2D-MT, the recorded atom number increases whenever a second layer is loaded. The atom numbers are averaged over 500 experimental cycles for each data point (red line). As expected, the SWT layers are periodic and separated by approximately  $4 \mu\text{m}$ . In the background, we show traces recorded for 20 minutes each for a duration of 12 hours in sequential order from light grey to black. We find that after a short warm-up time when we start the experiment, the relative position of the MT with respect to SWT layers remains very stable.

instead, a lot of excitations are created as expected.

### 4.2.7 Deterministic Preparation in 2D

The preparation of ground states in the 2D-MT is conceptually the same as for the quasi-1D trap (see Figure 4.13 a). A gradient of  $B_z = 70 \text{ G/cm}$  is applied and the potential depth, proportional to  $P_{\text{MT}}$ , is lowered until only the desired number of bound states remains in the trap. We hold the trap at the spill level  $P_{\text{spill}}$  for 80 ms before ramping up the power again to ensure that all higher lying unbound atoms have left

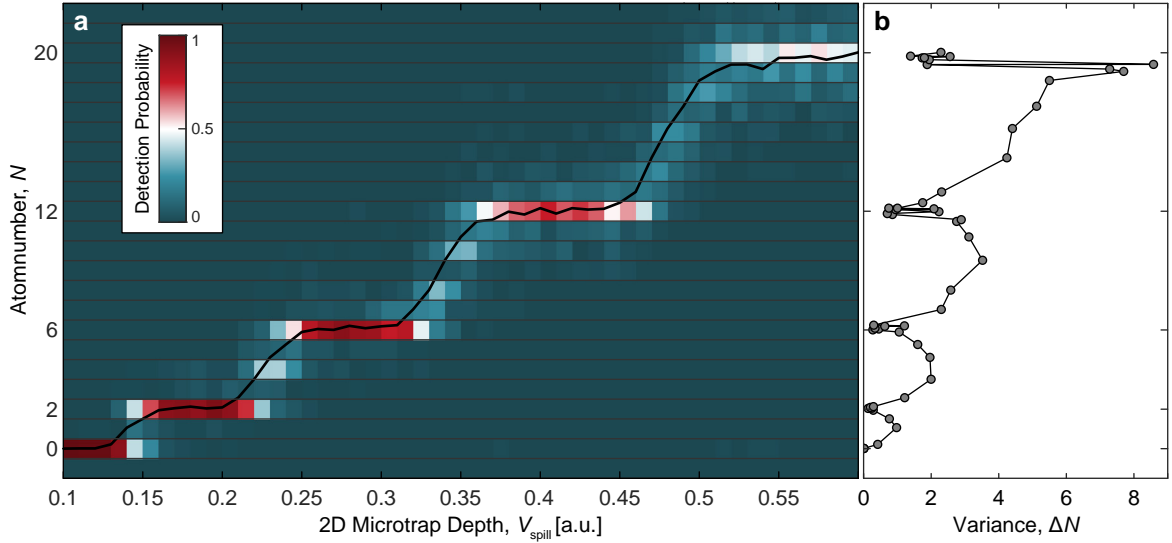


**Figure 4.14: Experimental preparation of ground states in a quasi-2D harmonic oscillator potential.** The mean atom number (black solid line) is shown as a function of the 2D-MT depth during the deterministic spilling process (a). The full counting statistics for each depth setting is shown as density plot in addition. We find stable plateaus at certain levels of 2, 6, 12 and 20 atoms. These numbers correspond to the closed shell configurations of a 2D harmonic oscillator (compare Figure 4.15), where the stability of the preparation increases significantly and the variance in prepared atom numbers becomes small (b).

the trapping region. A measurement of the final atom number as a function of the spill level is shown in Figure 4.14. The result can directly be compared to the deterministic spilling sequence in the quasi-1D MT (see Figure 4.10).

The measurements reveal stable plateaus at numbers of 2, 6, 12 and 20 atoms. These correspond exactly to the closed shell ground state configurations of a 2D harmonic oscillator potential (see section 2.1.2). Our deterministic spilling scheme allows us to reach these ground states deterministically and with high fidelities (see Figure 4.15). We are currently limited to  $n = 4$  filled shells or  $N = n(n + 1) = 20$  atoms for a deterministic preparation in the experiment. For larger atom numbers the anharmonicity of the potential leads to smaller spacing between the levels, making the adjustment of the spilling barrier more difficult. In addition the initial atom number of  $N = 50$  in the 2D-MT is too small to fill higher lying shells  $n > 4$  reliably after the dimensional crossover. Nevertheless, our method allows us to prepare very cold samples with en-

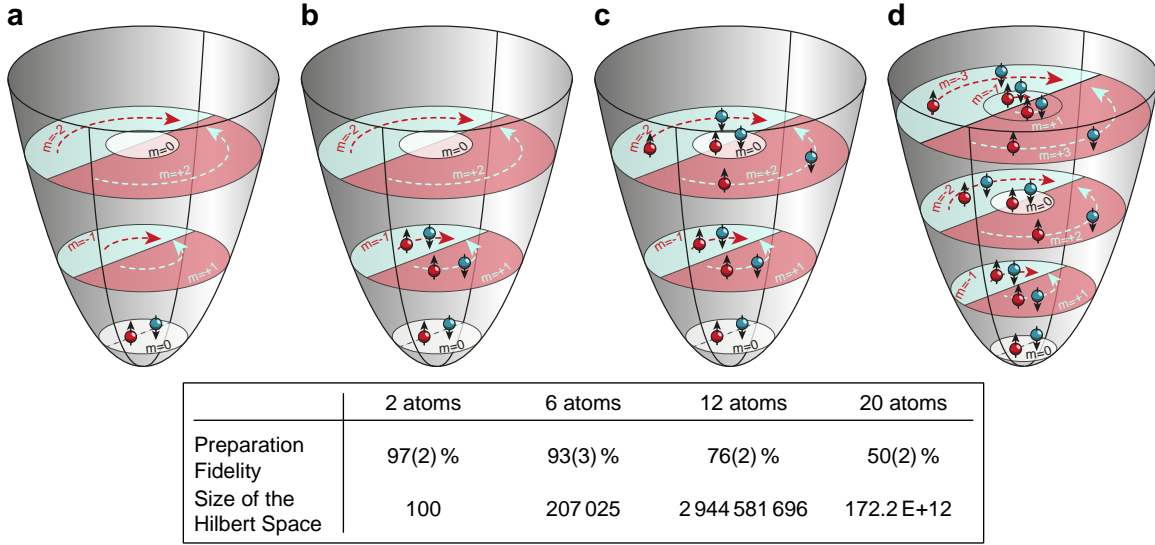


**Figure 4.15: Closed shell configurations of the 2D harmonic oscillator.** Our spilling scheme allows us to prepare the ground state configuration for two spin components and with up to 20 atoms with very high fidelity (a-d). While the preparation fidelity is significantly lower for larger atom numbers, it only indicates the probability to obtain the pure ground state. Even when some holes are present, for example for  $N = 20$  atoms, the system remains very cold. The entropy per particle is comparable to the quasi-1D spilling scheme with  $S/N = 0.1 k_B$ . The size of the total Hilbert spaces for each particle number and including two shells above the ground state are given as a comparison.

tries per particle on the order of  $S/N = 0.1 k_B$  and up to  $N = 50$  atoms in quasi-2D, even if they are not in the exact ground state.

For all our measurements, the experimental preparation stages after the MOT are typically carried out in the high-field regime  $B = 650 \dots 1000$  G and with strongly attractive interactions  $a \ll -2000 a_0$ . The only exception are measurements in completely non-interacting samples. These have to be prepared in the repulsive low-field regime  $B < 650$  G because a preparation at high-fields and consecutive ramp to low fields would produce tightly bound molecules instead (see Figure 3.5). The low-field preparation fidelities for 6 and 12 atoms are 57(1) % and 42(2) % respectively. They are reduced compared to a preparation in the high-field regime since we only have access to lower scattering rates here  $|a| < 900 a_0$ . The smaller attraction strength leads to a less efficient evaporation and reduced gaps of the avoided level crossings.

Recently, we have developed an experimental technique that allows us to switch from a  $|1\rangle|2\rangle$  mixture at low-fields to a  $|1\rangle|3\rangle$  mixture in the high-field regime while remaining in the motional ground state. So we can not only prepare non-interacting samples with higher fidelities than before but even the preparation of imbalanced ground states with strong interactions becomes possible. A further discussion of imbalanced samples, opening up a whole new field of physics to explore (FFLO, polarons), is found in chapter 9. General methods to manipulate the internal state of the atoms and switch between different hyperfine mixtures are discussed in the next section.

### 4.3 Internal State Manipulation

There are three important applications that require access to the internal degree of freedom of the atoms. First, by transferring only a fraction of the atoms from one hyperfine state to another, we can access the mixing ratio of our components. This is required in the first place to achieve a balanced mixture after the transfer of the atoms from the MOT but can also be used to create imbalanced samples at a later stage in the cycle. A small imbalance was one of the essential ingredients to the success of the measurement described in chapter 8. Even mixtures of three or more components are possible although their regime of collisional stability is strongly constrained [Ott08].

A full transfer of one of the hyperfine components modifies the collisional properties of the gas. Due to the distinct positions of the Feshbach resonances of different low-field seeking mixtures this allows us to quench the interactions between a strongly and weakly interacting regime (see Figure 3.7). Spin flips to high-field seeking states (see Figure 3.1), for example from  $|1\rangle|3\rangle$  to  $|1\rangle|4\rangle$  are even more valuable. They instantaneously project the sample onto a non-interacting state (see section 3.3.2). We typically prepare  $|1\rangle|3\rangle$  mixtures in the experiment since they require smaller magnetic fields and provide access to larger scattering lengths in the low-field regime.

Finally, by resolving the energy that is required for flipping from one hyperfine mixture to another it is possible to perform spectroscopic measurements on the initial or final state. This gives access to many central quantities of the many-body state like interaction energy shifts or pairing gaps and has become one of the central tools in cold atoms experiments [Che09].

#### 4.3.1 RF and MW Pulses

The most direct way to drive transitions between different hyperfine levels is to apply AC-magnetic fields. The required frequencies are in the RF regime (75...85 MHz) for transitions between the low-field seeking states  $|1\rangle - |3\rangle$  and in the MW regime

(1...2 GHz) to access the high field seeking states  $|4\rangle - |6\rangle$  (compare Figure 3.1). Since generating high power signals for both frequency ranges in a single circuit turned out to be difficult, we have implemented two separate antennas in our experiment. One is located in the vacuum chamber and connected to a high power MW amplifier with up to 15 W (see Figure 4.2). And one is located at the lower re-entrant window, connected to a 100 W RF amplifier (see Figure 4.6).

When applying an RF field with a constant power  $P_{\text{RF}} = 15 \text{ W}$  and at the resonance frequency for atoms at  $B = 750 \text{ G}$ , we observe Rabi oscillations with a frequency of:

$$\Omega_{|1\rangle \rightarrow |2\rangle} = 2\pi \times 960(90) \text{ Hz} \quad \text{and} \quad \Omega_{|2\rangle \rightarrow |3\rangle} = 2\pi \times 2074(300) \text{ Hz}. \quad (4.5)$$

This allows us to drive transitions between states in the low-field seeking manifold on timescales below 1 ms for  $\pi$  pulses. The MW transitions to the high field seeking manifold are much faster. They correspond to a flip of the electronic instead of the nuclear spin state and couple much stronger to the AC field. With the full amplifier power of  $P_{\text{MW}} = 15 \text{ W}$  and at  $B = 750 \text{ G}$ , we achieve:

$$\Omega_{|3\rangle \rightarrow |4\rangle} = 2\pi \times 109(5) \text{ kHz}. \quad (4.6)$$

### 4.3.2 Landau-Zener Sweeps

While  $\pi$ -pulses are the fastest method to transfer one hyperfine state into a different one, they are quite sensitive to noise and drifts in the power of the drive and the magnetic offset field. Landau-Zener sweeps, on the other hand, are intrinsically robust against such effects and enable us to achieve very high transfer probabilities of  $P_{\text{trans}} \gtrsim 99\%$  (see Figure 4.16). For this reason we utilize them almost exclusively when switching between spin components in the experiment. While keeping the rate on un-flipped atoms negligible, we achieve transfer times of  $t_{|1\rangle \rightarrow |2\rangle} = 4 \text{ ms}$  and  $t_{|2\rangle \rightarrow |3\rangle} = 2.5 \text{ ms}$  respectively.

The microwave allows us to use much faster sweep rates and we achieve up to  $t_{|3\rangle \rightarrow |4\rangle} = 25 \mu\text{s}$ . However, we are limited to a field of  $B = 750 \text{ G}$ . Our steel vacuum chamber acts as a cavity for the MW field and stops us from generating significant field amplitudes at other frequencies (see Figure 4.16 b). Therefore, we have implemented an alternative scheme to drive fast transitions between low- and high-field seeking states.

### 4.3.3 Raman Transitions

We have implemented two co-propagating laser beams in the experiment that are focused on the 2D-MT (see Figure 4.2 H) to drive Raman transitions between any of the hyperfine spin states (see Figure 4.16 c). The advantage of optical fields is that they

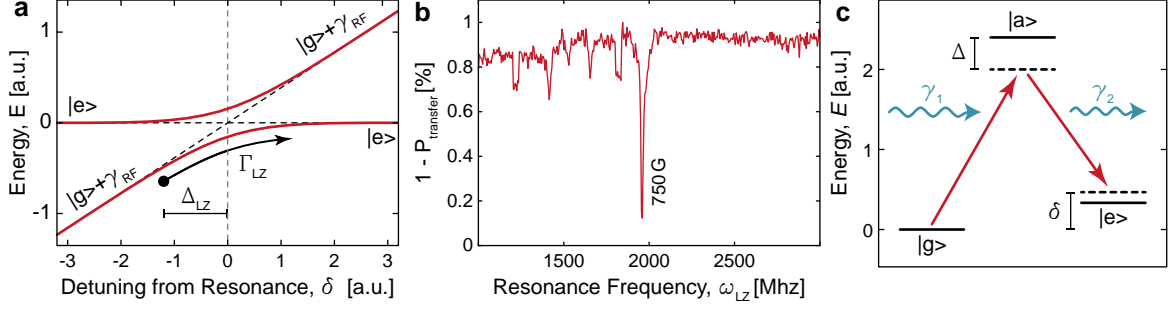


**Figure 4.16: Internal state manipulation.** Landau-Zener sweeps allow us to transfer between two hyperfine spin components, here indicated by  $|g\rangle$  and  $|e\rangle$  with a very high fidelity (a). To this end the AC field is swept across the resonance  $\omega_0$  from a detuning  $-\Delta_{LZ}$  to  $+\Delta_{LZ}$  and with the speed  $\Gamma_{LZ}$ . The transition probability  $P_{\text{trans}}$  for a MW sweep from  $|3\rangle$  to  $|4\rangle$  at fixed speed  $\Gamma_{LZ}$  depends strongly on the resonance frequency  $\omega_{LZ}$  of the transition (b). Only at 1951 MHz, corresponding to 750 G, the achievable transitions speeds meet our experimental requirements. With a Raman transfer, driven by two co-propagating laser beams, we can quasi-instantaneously switch between hyperfine levels at any magnetic field (c). Here, the detuning  $\Delta$  from the auxiliary state  $|a\rangle$  is chosen large enough that it can only be virtually populated.

are independent of any resonance of the vacuum chamber and work at any magnetic offset field  $B$ . In addition, much larger field strengths and thereby transitions rates can be achieved. By aligning the lasers such that they are co-propagating we ensure that the momentum transfer onto the atoms during the Raman transfer is negligible.

We control the frequency difference  $\delta$  between both Raman lasers using an optical phase-locked loop (PLL). With an optical power of  $P_{\text{Raman}} = 0.5 \text{ mW}$  per beam and a detuning  $\Delta = 5 \text{ GHz}$  below the  $D_2$ -line (i.e. exactly between  $D_1$  and  $D_2$  lines), we measure a Rabi rate at  $B = 750 \text{ G}$  of:

$$\Omega_{|3\rangle \rightarrow |4\rangle} = 2\pi \times 1.55(5) \text{ MHz}. \quad (4.7)$$

Thus we can project into a non-interacting  $|1\rangle|4\rangle$  mixture in  $t_\pi = 330 \text{ ns}$ . Since the projection is much faster than any other time scale of the system and with collision rates  $\nu \leq 50 \text{ kHz}$  it can be considered as instantaneous.

## 4.4 Imaging Schemes

Powerful detection techniques are equally important as the preparation of the initial state for successful quantum simulations. For ultracold quantum gases, there has been a persistent effort to develop more and more precise imaging schemes from the very beginning [Ott16; Gro21]. In this section, we present the most important methods applied in our experiment. While non-destructive imaging is possible (see for example [Pat14; Gaj16b; Kro20]), we generally only utilize methods that destroy the quantum state during the readout process. After each measurement the sample is discarded and the experimental cycle is repeated from the beginning [Sta12].

### 4.4.1 Absorption Imaging

*Absorption imaging* is performed by sending a resonant, collimated probe beam through the atom cloud and imaging the beam directly onto a camera. From the shadow of the cloud on the camera and by comparing it to a second reference image without any atoms, it is possible to calculate the integrated column density of the cloud  $\tilde{n}(x', y')$  [Rei07]. In our experiment, we drive the  $\sigma^-$  transition of the  $D_2$  line. We work in the high intensity regime  $I \gtrsim I_{\text{sat}}$  in order to reduce shot noise and atom diffusion during imaging. This requires a precise calibration of the imaging parameters to obtain the correct absolute values for the density  $\tilde{n}(x', y')$ . For our experiment, this calibration is explained in great detail in Ref. [Nei17].

We have implemented several beam paths to take absorption images in our experiment. Most important is an absorption beam in vertical- or z-direction from the top down (see Figure 4.6) for taking images in the plane of the quasi-2D confinement with a large region of interest of approximately 3 mm. Here, the integrated column density corresponds to the full 2D density of the quasi-2D system and only the trivial dependence along the z-axis is integrated out  $n_{2\text{D}}(x, y) \equiv \tilde{n}(x, y)$ . Further absorption beam paths in vertical and horizontal direction are used for alignment and diagnostic purposes only (see Figure 4.2 I, J and 4.6 D).

The Zeeman energy splitting in the high field regime of  $\Delta E \approx 80$  MHz between states  $|1\rangle$  to  $|3\rangle$  is much larger than the linewidth of the imaging transition  $\Gamma = 6$  MHz. So we can take spin selective images of the density  $n_\downarrow$  or  $n_\uparrow$  only. It is even possible to take both images in a single experimental cycle in quick succession in order to extract spin resolved density correlations [Nei17].

While absorption imaging is an adequate tool for studying large many-body samples in the SWT, its applications are limited. Due to photon shot noise it is difficult to achieve single atom detection with high fidelity [Mue13]. Detecting each particle with a large probability becomes particularly important when we study mesoscopic systems

of only  $N \leq 20$  particles. Here, each atom already represents a significant fraction of the whole system and high fidelity pair correlation measurements are only possible if no atoms are lost. To this end, we have developed two alternative detection schemes for studying mesoscopic systems.

#### 4.4.2 MOT Imaging

For spectroscopic measurements, some of which will be presented later in this thesis, it is enough to simply count the number of atoms remaining in the trap. Likewise, for the preparation of pure ground states, an accurate count of the particle number is already enough to reveal many of the intrinsic properties of the system (compare Figures 4.10 and 4.14). The centre of the MOT in our experiments overlaps with all other potentials used for measurements. In addition, the trap relies only on passive optical components without any moving parts (see Figure 4.2 and 4.6). As a result, we can quickly switch the MOT back on at the end of the experimental cycle to recapture all the leftover atoms. A lower bound for the recapture rate in our experiment is 99.1(1)%. We estimate that a complete recapture is even possible with optimized settings after imaging the cloud with resonant light, for example to take an absorption image.

The fluorescence signal the atoms produce in the MOT allows us to deduce their precise number after a sufficient integration time. We collect the signal on a camera (Grasshopper3 GS3-U3-15S5M) with a quantum efficiency of 60% and a NA of 0.15 that is placed off-axis with respect to all the MOT beams (see Figure 4.2 I). The parameters of the MOT are chosen such that the cloud becomes as small as possible without inducing losses from the trap. Currently, we use a gradient of  $dB/dz = 250 \text{ G/cm}$  and a detuning of  $\delta \approx 1.5\Gamma$ . We have identified an integration time of  $t_{\text{mot}} = 1 \text{ s}$  as optimal value for our experiment. We obtain a single fluorescence signal count  $\mathcal{I}_i$  for each experimental cycle  $i$  by subtracting a background image and summing over all camera pixels that contain a significant signal.

In Figure 4.17 a typical time series of the fluorescence count over 2000 experimental cycles and with an initial state of varying atom number is shown. Clear steps in the signal, corresponding to different atom numbers are visible. For each atom we estimate that we collect around 10 000 photons on the camera, corresponding to a total scattering rate of  $\gamma = 3.1 \times 10^6 \text{ photons/s}$ . To translate the fluorescence signal  $\mathcal{I}_i$  into exact atom numbers  $N_i$ , we compensate for long-term drifts of the signal by fitting the function  $\mathcal{I}_i = \Delta * N_i + \mathcal{I}_0$  to the data in a window of cycles  $[i - 100, i + 100]$  (see 4.17 a, dashed lines). Here, the offset  $\mathcal{I}_0$  and fluorescence signal per atom  $\Delta$  are fit parameters and measurements that lie outside of certain confidence intervals (grey bands) are discarded (blue points). The intervals are chosen such that the ratio of

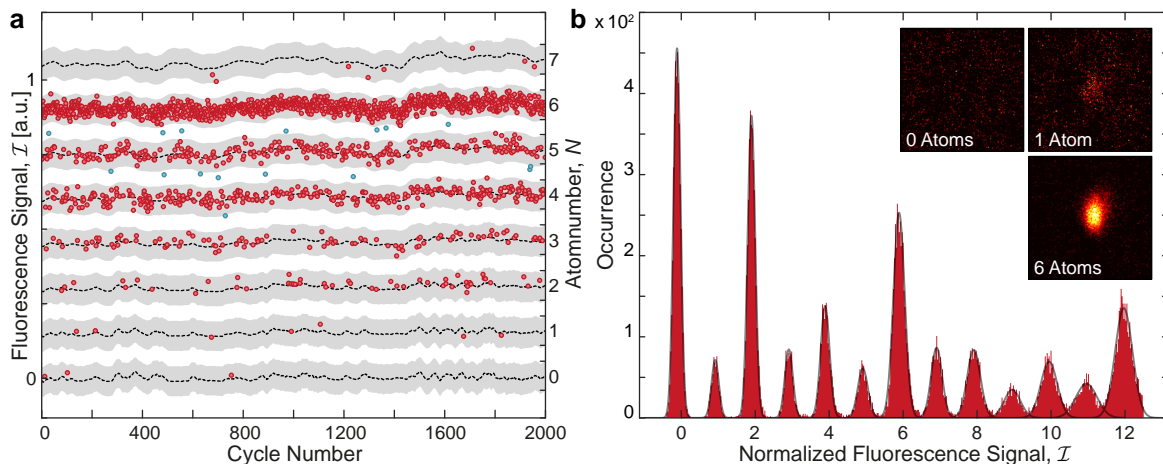


**Figure 4.17: Counting atoms in the MOT.** By recapturing the cloud in the MOT after the experimental sequence and integrating over the fluorescence signal, we can precisely determine the atom number  $N$ . We observe distinct steps, corresponding to the different atom numbers (a). Atoms that are outside certain confidence intervals (grey bands) are discarded (blue points). The different peaks corresponding to each atom number  $N$  are well separated (b). By approximating the signals by Gaussian functions, we estimate that our counting fidelity for  $N = 6$  is around  $P \gtrsim 99.9\%$  and for  $N = 12$  around  $P \gtrsim 98\%$ , after discarding only around 1% of the data. The insets show the actual fluorescence signal on the camera for different atom numbers.

discarded runs is negligible while retaining a very high counting fidelity (see Figure 4.17 b). The biggest limitations of the current setup are drifts in the frequency and power of the cooling laser and background light on the camera. By improving these in the future, single atom counting resolution with cloud sizes of up to several hundred atoms is possible [Hum13].

While counting in the MOT is very precise, all the information about the spin state, momentum and position of the atoms are lost. The MOT both traps and cycles between all different hyperfine states  $|1\rangle$  to  $|6\rangle$  of the ground state manifold. It is possible to extend the capabilities of the technique slightly by removing all the atoms in some spin or motional state prior to recapturing them. However, in this way it is not possible to obtain correlations between different atoms in a single experimental cycle. Furthermore, the method is limited to a very small number of degrees of freedom simply by the amount of required measurement time. For the studies of unknown quantum

many-body systems much more efficient imaging techniques, that extract much more information in a single experimental cycle, are required.

### 4.4.3 Fluorescence Imaging

Our fluorescence imaging technique enables us to detect single atoms in free space and without any cooling or trapping scheme required [Büc09]. It relies on detecting spontaneously emitted photons while exciting the atom cloud with resonant laser beams during a short pulse [Ber18]. Both the position of each atom in the imaging plane and their spin can be determined in this way. We achieve single atom detection fidelities of around 99%, comparable to those achieved in quantum gas microscope experiments [Gro21]. At the same time, the required exposure time is as small as  $T_{\text{img}} = 15 \mu\text{s}$  compared to the several seconds required for resolving single particles in an optical lattice. More details on the method can be found in Refs. [And17; Kli17] where the scheme has been first developed for a very similar experimental apparatus. Here, we focus on the details and modifications that are important for the measurements presented later in the thesis.

The imaging sequence is initiated by shining in two counter-propagating laser beams resonant to the  $\sigma^-$  transition of the  $D2$ -line and that are focused on the atom cloud (see Figure 4.2 F). Both lasers are switched on for a total exposure time of  $T_{\text{img}} = 15 \mu\text{s}$  and switched on and off alternately with a pulse duration of 200 ns each (see Figure 4.18 a). This ensures that no interference effects occur and that the atoms scatter equally many photons from both beams independent of their precise light power. We work at approximately  $I/I_{\text{sat}} = 8$  with scattering rates of 16 photons/s, close to the possible maximum. Due to the very short exposure time, no potentials or cooling are required for imaging and the amount of atom diffusion due to scattering of resonant light stays small enough. The remaining challenge is to clearly identify and localize particles with only around 240 fluorescence photons per atom.

### 4.4.4 Single Atom Detection

The first step to detect a single atom with very short exposure times is to collect as many photons as possible on a camera. To this end we use the same microscope objective that is also projecting the MT onto the atoms. The fluorescence beam path is divided from the trapping and cooling lasers through a dichroic mirror and PBS-cube respectively (see Figure 4.6). A mirror diverts it onto a second breadboard where everything is focused on an electron multiplying CCD camera (EM-CCD) (see Figure 4.19). Taking the NA, the dipole radiation pattern of the atoms and the losses at each

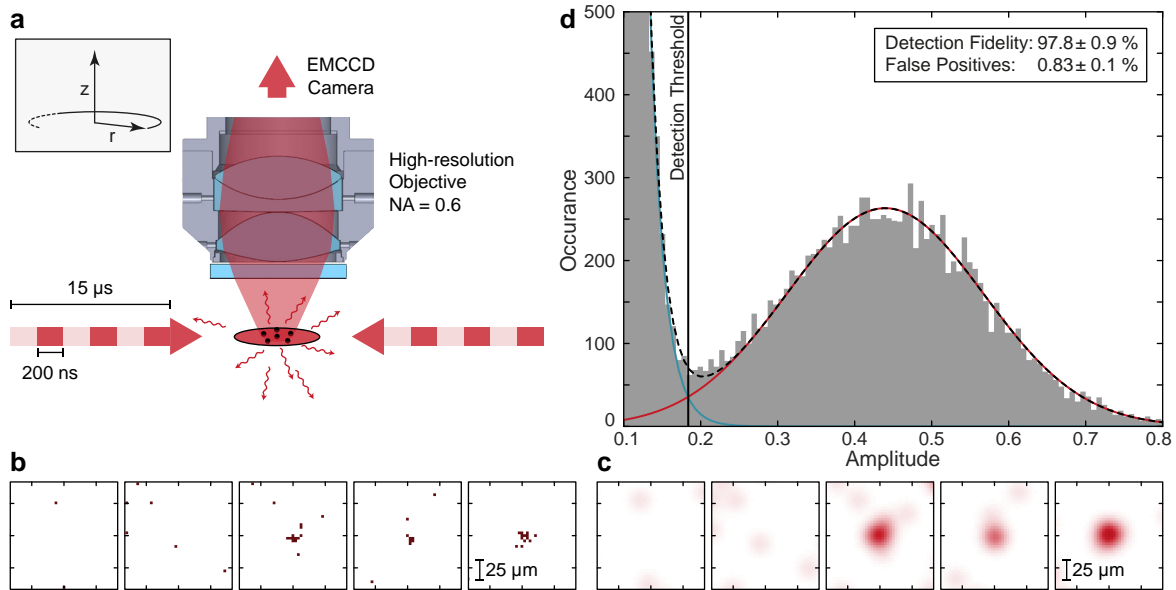


**Figure 4.18: Single atom resolved fluorescence imaging.** To image the atoms, two counter-propagating pulsed lasers resonant to the  $\sigma^-$  transition are focused on the atoms (a). Approximately 8% of the total number of scattered photons are collected through a microscope objective and focused onto an EM-CCD camera. The complete imaging time of  $T_{\text{img}} = 15 \mu\text{s}$  is short enough to limit the atom diffusion and no trapping or cooling is required. The raw camera images are analysed by first binarizing them (a). The first two images show typical background images with an open camera shutter. For the other images a single atom is located in the centre. To identify atoms, we use a low-pass filter together with a peak detection (c). In (d) a histogram of all the detected peak amplitudes in 2000 images with  $320 \times 320$  pixels and 6 atoms in each image is shown. The histogram allows us to clearly identify two separate peaks, corresponding to single atoms and background noise. The solid red and blue lines represent a Gaussian and exponential fit to the data respectively. Panel (a) recreated from [Ber18].

optical component into account, we collect an average of around 10% or 24 photons per atom on the camera chip.

The EM-CCD camera (Nüvü HNü 512) is especially designed for ultra low light environments and has the capability to detect single photons with a very high probability. Its quantum efficiency at  $\lambda = 671 \text{ nm}$  is specified at  $q = 95\%$ . To distinguish

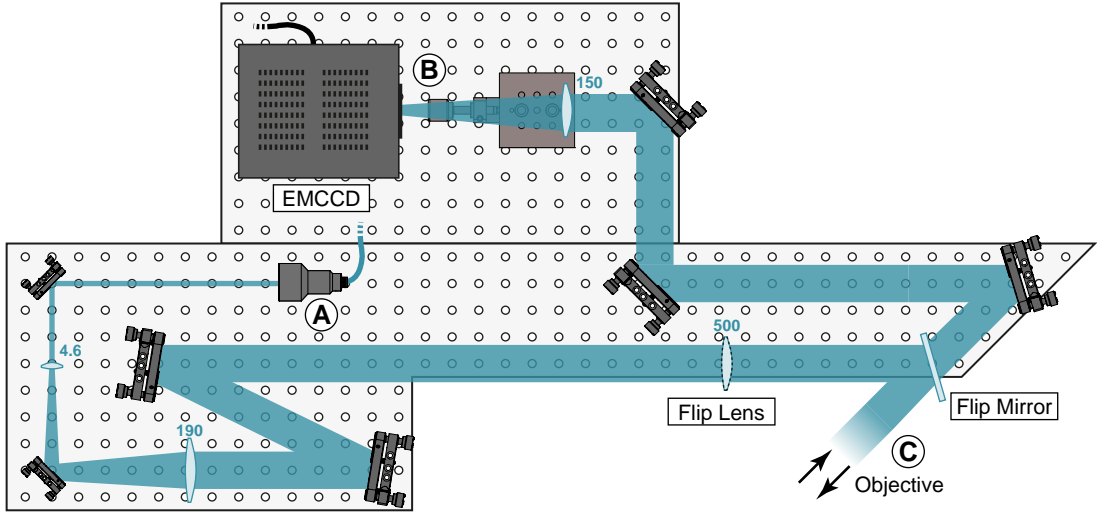


**Figure 4.19: Camera Breadboard.** The camera breadboard contains two different beam paths for imaging. In the primary mode of operation, fluorescent light collected by the objective is focused with a  $f = 150$  mm doublet onto the EM-CCD camera. This leads to an optical magnification of  $m = 7.4$  or  $m = 2.16 \mu\text{m}/\text{pixel}$  of the atom plane on the camera chip. Alternatively, a flip mirror can be used to shine in a resonant beam from the top down through the objective. This beam is used for absorption imaging with a large field of view on the secondary camera below the vacuum chamber (compare figure 4.6).

the single photoelectrons from the noise background of the readout electronics, an electron multiplication register is used (for more details see Ref. [Jan16]). Here, a high voltage is applied to generate a large amount of secondary electrons from each photoelectron on the CCD chip. Our camera reaches a maximum ratio of gain to readout noise of  $g/\sigma_{\text{read}} = 27$ . By choosing the detection threshold five standard deviations over the readout noise, this results in a single photoelectron detection fidelity of  $P = \exp(-5\sigma_{\text{read}}/g) \approx 82\%$  per pixel. Combined with the quantum efficiency  $q$  and optical setup we therefore expect to collect around 7.8% of the total amount of scattered photons as signal on the camera. This amounts to 1.25 photons/ $\mu\text{s}$  or a total of 19 photons per atom and agrees perfectly with the rate we find in the experiment of 1.24(8) photons/ $\mu\text{s}$ .

The main source of noise of EM-CCD cameras, when operated in the high gain mode, are so-called clock-induced charges (CICs). These form on the CCD chip during the shifting and readout process and cannot be distinguished from real photoelectrons (see

Figure 4.18 b). One essential ingredient for our high fidelity detection scheme is a low number of CICs. In our case, the probability for exciting a CIC on a single pixel during readout is 0.15 %. Unwanted background light leads to an additional amount of approximately 0.1 % bright pixel on the chip. The total amount of noise is therefore almost by a factor of ten lower than what can be achieved with EM-CCD cameras of competing manufacturers. This is why we can detect single atoms in a region of interest of  $320 \times 320$  pixels with fidelities of 97.8(9) % (see Figure 4.18 d). When compared to the detection fidelity of 99.4(3) % reported in [Ber18] with an area of  $21 \times 21$  pixels, we find that the sensitivity of the imaging technique has improved by more than two orders of magnitude.

The exponential amplification leads to a very non-linear electron signal that makes it difficult to distinguish between different numbers of photoelectrons on a single pixel. Therefore, the best detection efficiency is achieved when spreading the point spread function (PSF) of a single atom over the chip such that no pixel is hit by multiple photons on average. In the experiment, we have chosen a magnification of  $m = 7.4$  such that each pixel of the EM-CCD camera corresponds to  $2.16 \mu\text{m}$  in the atom plane. The raw images are analysed by binarizing them first (see Figure 4.18 b). Events with a count above the chosen threshold of  $5\sigma_{\text{read}}$  are counted as photons and set to one, all other pixels are set to zero. In the next step, a Gaussian low pass filter with an optimized width of the kernel of  $\sigma = 5$  pixels is applied to each image together with a simple peak detection algorithm (see Figure 4.18 c).

In Figure 4.18 d, a histogram of all the peak amplitudes in 2000 images of  $320 \times 320$  pixels is shown. We find a clear bimodal distribution with an exponential noise peak at low amplitudes and a Gaussian peak corresponding to single atoms. A fit allows us to determine the optimal setting for the threshold of atom identification. The detection fidelity indicates the probability to detect a single atom in the imaging plane. The rate of false positives depends on the number of real atoms in each image. The probability of falsely identifying background noise as an atom is around 5.0(5) % per image. In the example shown, there are six real atoms present in each image. This leads to a total rate of false to true detections of 0.83(10) %.

#### 4.4.5 Spin and Spatial Resolution

While being imaged, the atoms perform a random walk caused by the recoil of scattered photons. This leads to a broadened PSF compared to what could be achieved by the optical setup alone (see Figure 4.20). Nevertheless, the size of a single atom imaged in free space with  $\sigma_{\text{psf}} = 3.96(5) \mu\text{m}$  is much smaller than the available region of interest of our imaging setup. The effective resolution can be estimated using the full width at half maximum of the PSF as  $2\sqrt{2\ln 2}\sigma_{\text{psf}} = 9.3(1) \mu\text{m}$ . With our current setup, this enables

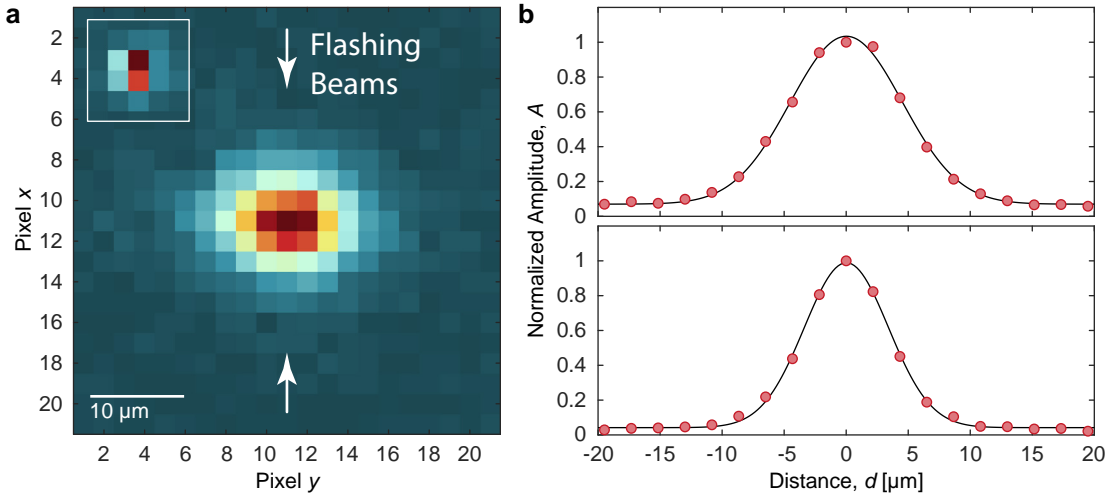


**Figure 4.20: Point spread function of a single atom.** We plot the average over 600 binary images, where an atom was located in the centre of the image (a). The data was taken for un-trapped atoms in free space. The inset shows the PSF of a single atom confined to a deep optical tweezer during imaging. The sum of the image along the x (y) axis is shown in b (c). The average width of the PSF of a single atom is given by  $\sigma_{\text{psf}} = 3.96(5) \mu\text{m}$ . We find a slight anisotropy, with a smaller distribution along the direction of the flashing beams. This can be explained by a reduced momentum transfer in this direction through stimulated emission events.

us to detect on the order of a few hundred particles in parallel on a single camera image provided that they are far enough apart. It is possible to take advantage of the complete optical resolution limit of the setup by pinning the atoms during the imaging pulse with a tight confinement. With a tweezer of depth  $V_0 = 40 \text{ MHz}$ , for example, the atom diffusion becomes negligible and much smaller than the optical resolution limit  $\sigma_{\text{diff}} \ll 1 \mu\text{m}$  (see Figure 4.20 inset). In our experiment, we have implemented a pinning lattice in a *bow-tie* configuration to reduce the atom diffusion during imaging (see Figure 4.2 G). With the power that is currently available for this lattice of around  $P_{\text{pin}} \approx 4 \text{ W}$  we reach a depth of  $V_0 \approx 4 \text{ MHz} = 138 E_{\text{recoil}}$ . This is not enough to reduce the width of the PSF by more than a few percent. In the future, we estimate that more focused lattice beams with higher beam power of  $P \approx 20 \text{ W}$  could significantly reduce the PSF of the atoms. For other species than  ${}^6\text{Li}$  with higher atomic masses or larger linewidths, the PSF is expected to be even smaller than what we report here.

To resolve the hyperfine spin of our atoms we take the same approach as for ab-

sorption imaging. Multiple images are taken in quick succession and for each image the laser is resonant to a single hyperfine component  $|1\rangle$ - $|3\rangle$  only. The minimal dead time between two images of a height of  $N_y$  pixels with the Nüvü camera is given by  $\Delta t = (0.5 \times N_y + 2) \mu\text{s}$ . This leads to a time of  $\Delta t = 162 \mu\text{s}$  for our typical image size, short enough that atoms on the second image have not moved significantly with respect to those on the first image.

#### 4.4.6 Momentum Space Imaging

As we have discussed in the previous section, we are able to prepare ground states of up to  $N = 20$  atoms in the 2D-MT with a waist of around  $w_0 = 5 \mu\text{m}$ . Clearly, this state is too small to resolve single atoms directly with our fluorescent imaging technique. Instead we use a ballistic time of flight (TOF) expansion to spread the atoms before imaging. In free space, this maps the in-situ momenta  $p_i$  of the atoms onto their position after the expansion  $p_i \rightarrow x'_i$  and becomes exact and independent of the initial positions  $x_i$  only for  $t_{\text{TOF}} \rightarrow \infty$ . We make use of a slightly more advanced technique also referred to as matter-wave focusing [Tun10; Mur14]. Here, the expansion takes place in a harmonic confinement of frequency  $\omega_{\text{TOF}}$  instead. In this case, the mapping to momentum space already becomes exact at an expansion time of a quarter trap period  $t_{\text{TOF}} = T/4$ . This is equivalent to an optical lens projecting the far field onto the focal plane at a finite distance.

We utilize different expansion schemes for mesoscopic systems in the 2D-MT and large clouds in the SWT. The ballistic expansion of mesoscopic samples is initiated by using the Raman lasers to instantaneously turn off all collisions (see section 4.3). At the same time, the MT is switched off such that the atoms expand radially in the remaining harmonic confinement of the SWT (see Figure 4.21 a,b). The axial confinement provided by the SWT is left unchanged such that the expansion occurs in the 2D plane and the atoms remain in the focus of the objective. After  $t_{\text{TOF}} \approx 11 \text{ ms}$  the momentum of the atoms has been mapped onto their position and the many-body wavefunction has increased its size by a magnification factor of approximately fifty. With typical inter-particle spacings of around  $d \gtrsim 50 \mu\text{m}$  we can now take successive images of all the atoms in each spin component (see Figure 4.21 c). Due to their fermionic nature, events where two atoms of the same spin component come closer than our combined imaging PSF are very rare (see chapter 5). This intrinsic spreading of particles in space makes our method especially suited for fermionic samples, where measurements with hundreds of atoms are well within reach in the near future.

Larger samples with several tens of thousands of atoms in the SWT can be imaged with either absorption or fluorescence imaging directly to obtain the locally averaged in situ density distribution. Nevertheless, it is useful to access the momentum distribution

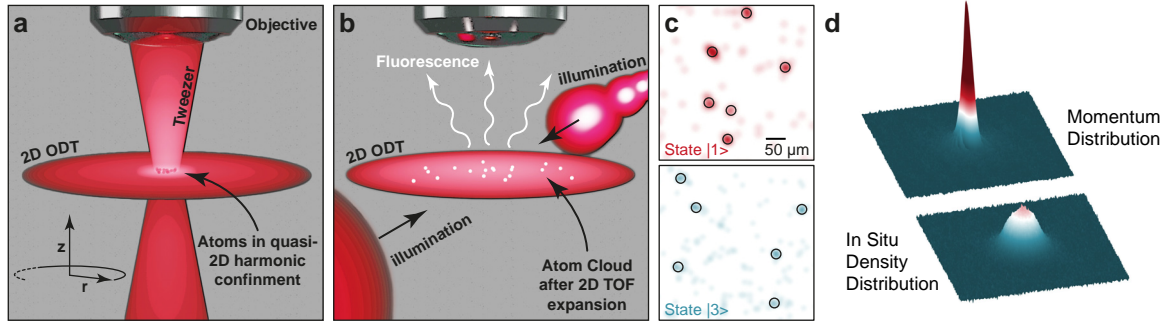


**Figure 4.21: Momentum space imaging.** By a TOF expansion the in situ momentum of the atoms can be projected onto their position and detected sequentially. For mesoscopic samples in the 2D-MT, we switch off the radial confinement and let the gas expand in the SWT layer (a,b). The Raman lasers are used at the beginning of the expansion to switch off all interactions. We extract the full spin and single particle resolved momentum distribution by taking one fluorescence image for each spin component in the gas (c). Large samples are mapped onto momentum space through a similar technique by switching off the SWT and projecting the gas onto molecules. The momentum distribution of molecules clearly reveals a condensate that is not visible in the in-situ density distribution (d). Panels (a,b) taken from [Hol21a].

as a second observable to gain better understanding of the many-body state under study. In this case, we start the expansion by switching of the SWT and ramping down the magnetic field in around  $150 \mu\text{s}$  [Mur14]. This leads to a quick expansion of the gas in axial direction, reducing its density significantly. At the same time, the field ramp leads to a projection of the particles onto deeply bound molecules with weak interactions. Both effects together ensure that collisions during the expansion are negligible. After  $t_{\text{TOF}} = 21 \text{ ms}$  of flight time in the remaining radial confinement provided by the magnetic field coils we can extract the momentum distribution of the molecules (see Figure 4.21 d).

#### 4.4.7 In Situ Imaging

With the bottom up approach it is essential to gain as much understanding as possible about the mesoscopic gases before scaling up the system size. Even for only a few particles access to in situ correlations in addition to momentum space can significantly enhance the amount of information that can be extracted [Ber19]. Therefore, it is

desirable to improve the effective resolution of our imaging scheme to study in-situ correlations on length scales of  $\sim 100$  nm far below the inter-particle distance in the 2D-MT. A large magnification of the in situ wavefunction is possible with the technique discussed in Ref. [Ast21]. The idea is to use a second  $T/4$  expansion after the first TOF to map the gas back from momentum space and to the in-situ density again. The final in-situ wavefunction is then magnified by the ratio of the trap frequencies during both expansions  $m = \omega_{\text{TOF},1}/\omega_{\text{TOF},2}$ .

In our experiment, we have implemented a second tweezer that is focused onto the atoms from the bottom (see Figure 4.6 E). It has a waist of  $w_0 \approx 30 \mu\text{m}$  and can be used for a first  $T/4$  expansion with a trap frequency of  $\omega_{\text{TOF},1} \simeq 1000$  Hz in the future. After a second expansion in the SWT with  $\omega_r = 22$  Hz this leads to a magnification of a factor of approximately 50 of the in situ wavefunction. We estimate that this scheme is going to allow us to extract single particle and spin resolved in situ correlations with an effective resolution on the order of 100 nm.

## 4.5 Characterizing the 2D gas

Having discussed the available preparation and detection schemes in detail, in this last section we summarize some of the important experimental sequences that are used to determine different parameters of the gas. In this thesis we exclusively study 2D two component Fermi gases in harmonic confinements. These bulk systems are characterized by a total of four energy scales that fully determine the behaviour of the gas and that have to be determined to map out the phase diagram (see section 2.1.5). These are the harmonic oscillator energy  $E_{\text{HO}}$ , the thermal energy  $E_{\text{T}}$ , the Fermi energy  $E_{\text{F}}$  and the binding energy  $E_{\text{B}}$  (for the special role of the binding energy in 2D see section 3.2.8). Generally, all other parameters (like temperature  $T$ , density  $n_{2\text{D}}$ , scattering length  $a$ , ...) can be derived from or related to one of these scales.

Depending on the initial state, some of the four energy scales might be negligible for the description of the gas. When we prepare pure quantum ground states with high fidelity, thermal excitations can be neglected, for example. Additionally, due to the small particle number, Fermi and harmonic oscillator energy are essentially on the same scale  $E_{\text{F}} \sim E_{\text{HO}}$ . For large samples prepared in the SWT, the harmonic level spacing  $E_{\text{HO}}$  is much smaller than the other three energy scales and can be neglected when mapping out the phase diagram (see Figure 2.6).

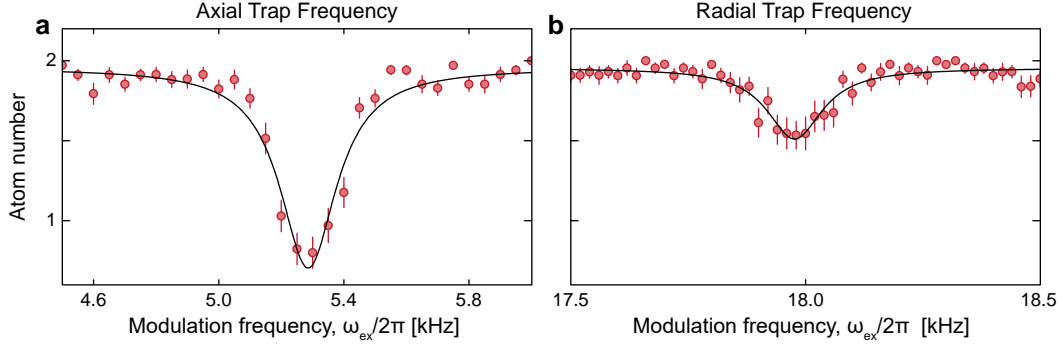


**Figure 4.22: Trap frequency determination in the MT.** In mesoscopic samples we prepare the atoms in a non-interacting ground state (here:  $N = 2$ ), modulate the system at some frequency  $\omega_{\text{ex}}$  and spill to the ground state again. The trap frequencies can be identified through particle loss resonances by counting the remaining atoms with the MOT imaging scheme (a,b). The solid lines are Lorentzian fits. Each data point is the average of around 50 repetitions of the experiment. Adapted from [Bay20b]

### 4.5.1 Fermi Energy

For mesoscopic systems, we directly set the Fermi energy  $E_F$  through the height of the spilling barrier or remaining total particle number  $N$ . In terms of the trap level spacing of the 2D harmonic oscillator it is given by  $E_F = 1/2(\sqrt{4N+1} - 1)\hbar\omega_r$ .

In the large system, the Fermi energy can be obtained directly from the in situ atom density  $n_{2D}(\mathbf{r})$  through calibrated absorption imaging [Nei17]. When the curvature imposed by the harmonic confinement is much smaller than the correlation length, it is convenient to treat the trapped gas as locally homogeneous system. This is also referred to as local density approximation (LDA). In this case, the local Fermi energy is related to the density as  $E_F = \hbar^2 k_F^2 / 2m$ , with Fermi momentum  $k_F(\mathbf{r}) = \sqrt{4\pi n_{2D}(\mathbf{r})}$ . The Fermi temperature is defined as  $T_F = E_F / k_B$ .

### 4.5.2 Trap Frequencies

The harmonic oscillator level spacing  $E_{\text{HO}} = \hbar\omega_r$  is determined through trap frequency measurements in radial direction. These are performed by preparing a non-interacting sample, for example at the zero crossing of the scattering length at  $B = 568$  G of the  $|1\rangle|3\rangle$  mixture. Mesoscopic samples, for example of two atoms in the ground state, are excited by modulating the power of the optical traps at some frequency  $\omega_{\text{ex}}$ . All

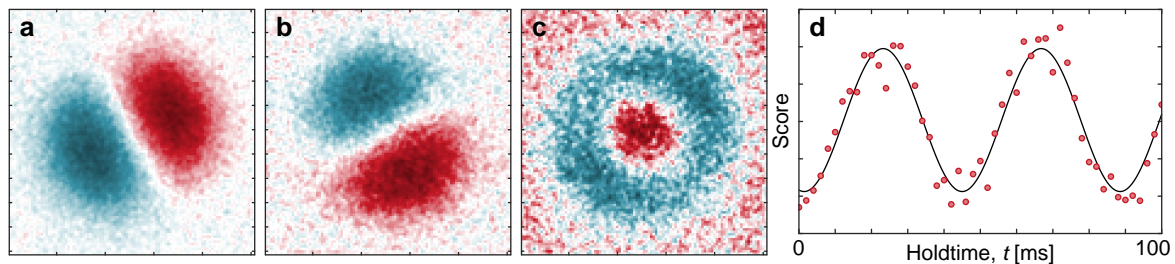


**Figure 4.23: Principal component analysis.** The principal component analysis (PCA) is applied to a time series of 200 images between  $t = 0$  and  $t = 400$  ms after exciting a gas of  $N = 20000$  particles in the SWT. The first three principal components, returned by the algorithm, correspond to two dipole modes along the principal trap axes (a,b) and the breathing or monopole mode (c). The oscillation frequency of each collective mode can be obtained by fitting a sine (solid line) to the *score* of the principal component as a function of time. In (d) the score of the first breathing mode (a) is shown as example.

excited atoms are removed by a second spilling step after the modulation is finished. The remaining atoms are counted in the MOT. Whenever the modulation frequency  $\omega_{\text{ex}}$  corresponds to an even multiple of the trap frequency, a resonance feature is observed. Only even numbered multiples of the frequency are observed since the symmetry of the modulation scheme forbids transitions from even ( $n = 1, 3, 5, \dots$ ) to odd ( $n = 2, 4, 6, \dots$ ) harmonic oscillator states and vice versa. In Figure 4.22 an example measurement of the axial and radial trap frequencies of the MT at a power of  $P_{\text{MT}} \approx 120 \mu\text{W}$  is shown.

An alternative method to extract trap frequencies is to study collective monopole (also referred to as breathing) or dipole modes of the cloud. Their frequencies in a non-interacting system are related to the trap frequency as  $\omega_{\text{D}} = \omega_r$  and  $\omega_{\text{B}} = 2\omega_r$  respectively. Both modes are excited by slowly lowering the intensity of the trapping beams such that the cloud expands and then suddenly quenching back to the final depth again. A time series of absorption images at different hold times  $t$  after the quench reveals the collective motion of the cloud. A very convenient way of extracting the different collective modes and their frequencies is to perform a PCA on the complete time series of pictures [Dub14]. The first three principal components returned by the PCA for a gas of around  $N = 20000$  particles in the SWT and excited as discussed above are shown in Figure 4.23. They correspond exactly to the single breathing and two dipole modes along the two principal axes of the trap.

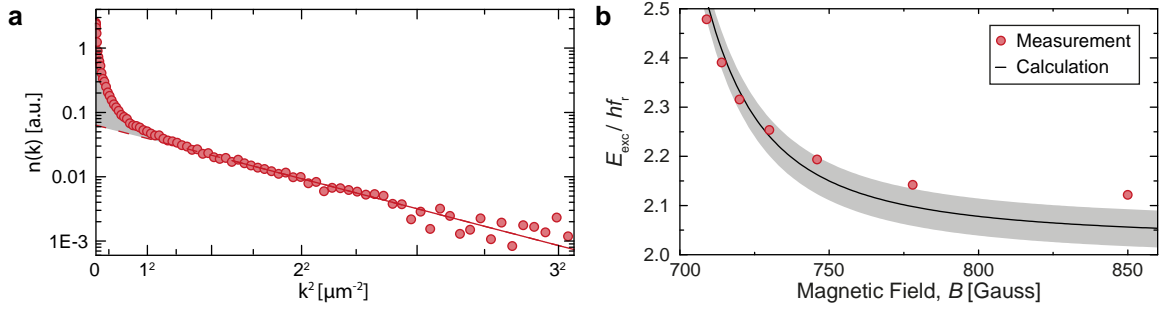


**Figure 4.24: Temperature and Interactions** The temperature or excitation energy can be obtained from the radial density distribution in momentum space  $n(k)$  (a). For many-body samples we simply fit a Boltzmann distribution to the thermal wing (solid line). Figure adapted from [Rie15a]. The binding energy  $E_B$  as a function of magnetic offset field  $B$  is calculated using the exact solutions for the two-body problem discussed in chapter 3. We have confirmed that the analytical solution of the spectrum agrees well with a measurement taken for  $N = 2$  particles in the trap (b). The remaining deviations can be explained with the anharmonicity and anisotropy of our harmonic trap. Figure adapted from [Bay20a].

### 4.5.3 Temperature

Due to the almost perfect isolation from the environment, it is not always correct to assume that a quantum gas of neutral atoms is in thermal equilibrium and can be well described by a thermal state. This is especially true when we prepare close to pure quantum states. Nevertheless, there is always some amount of excitation or thermal energy that can be used to characterize the deviation from the true ground state. There is a variety of methods that can be used for thermometry depending on the initial state and available observables, either in situ or in momentum space.

For small systems the entropy of the prepared state can be calculated directly from the full counting statistics as discussed in section 4.2.4. By post selecting on the correct atom number, the values of  $S/N = 0.1 k_B$  reported there can even be lowered further. In this case, the excess energy  $E_{\text{exec}}$  above the ground state  $E_g$ , at least for non-interacting states, can be read off directly from the single atom resolved images in momentum space. It is given by  $E_{\text{exec}} = 2 * \langle E_{\text{kin}} \rangle - E_g$ , where we have used the virial theorem for the harmonic oscillator initial state ( $\langle E_{\text{kin}} \rangle = \langle E_{\text{pot}} \rangle$ ) and  $\langle \dots \rangle$  denotes the average over many single images.

For many particle states we observe a bimodal distribution in the TOF images with a large condensate peak at low temperatures (see Figure 4.24 a). Here, the absolute

Temperature  $T$  of the cloud can be extracted by fitting a Boltzmann distribution to the outer, thermal wing of the cloud in momentum space. Even more accurate is the determination of the temperature directly from in-situ absorption images. We fit two reference equations of state  $n(\mu, T)$  to the measured density profile of the cloud  $n(\mathbf{r})$  [Boe16]. The procedure is described in detail in Ref. [Nei17] and allows us to determine both absolute temperature  $T$  and chemical potential  $\mu$  in each single shot and in the whole BCS-BEC crossover. The lowest temperatures we achieve in our many-body system are on the order of  $T = 50$  nK.

#### 4.5.4 Interaction Strength

The scattering length  $a_{2D}$  entering the interaction parameter  $\ln(k_F a_{2D})$  or equivalently (in 2D) the value of the binding energy  $E_B$  can be set from outside directly by Feshbach resonances. How these parameters depend on the magnetic offset field  $B$  for  ${}^6\text{Li}$  and how to calculate them for different potential environments has been discussed in detail in chapter 3. We have confirmed that the analytical solutions agree with a measurement taken for  $N = 2$  particles (see Figure 4.24 b).



# 5

## Observation of Pauli Crystals

Different phases of matter can be fully characterized and distinguished by their correlations [Alt04; Sch17; Hod17]. In the classical limit, we expect correlations to appear exclusively as the consequence of inter-particle interactions. In a non-interacting system, for example an ideal gas at room temperature, the detection of a single atom at a certain position has no influence on the expectation value for the positions of the others. This is different for a quantum mechanical ensemble of indistinguishable particles, as was demonstrated in 1956 by the groundbreaking experiments of Hanbury Brown and Twiss [Han56b]. They used two detectors, separated by a distance of a few meters, to detect photons falling to earth from a star several trillion kilometres far away [Han56a]. Due to their bosonic quantum statistics, photons tend to arrive at both detectors simultaneously and the measured intensity fluctuations as a function of time are correlated (*bunching*). When repeated with fermionic particles, the same experiment would show anti-correlated intensity fluctuations instead (*antibunching*).

The Pauli exclusion principle, as a consequence of the antisymmetric wavefunction of indistinguishable fermions, is one of the most fundamental laws underlying the structure of matter. No two identical fermions can occupy the same quantum state. This determines the electronic structure of the periodic table of elements for example. In the same way, it causes the shell structure we have observed directly when preparing closed-shell ground state configurations in a 2D harmonic oscillator (see section 4.2.7). While the same behaviour of non-interacting fermions avoiding each other is also expected in real space, a direct observation of the fermionic correlations is generally much more difficult in this case. In many cases, like electron beam experiments, strong repulsion between the particles obscures the signal. Almost pure quantum states of neutral particles are required together with high resolution imaging techniques.

Owing to the absence of strong Coulomb forces and with their precise control over the prepared quantum state, ultracold atom systems are the ideal platform for the observation of fermionic correlations. Pauli blocking has been detected indirectly through the suppression of contact interactions [DeM99; DeM01] and the emergence of an ef-

fective Fermi pressure [Tru01] at low temperatures in a degenerate Fermi gas. A direct observation of antibunching is possible in TOF measurements [Rom06; Jel07] or via a suppression of in-situ density fluctuations [Mül10; San10]. The first single particle resolved observation of the Pauli exclusion principle, enabled by the advances in quantum gas microscopy, has been achieved in the band insulating regime of a lattice potential [Omr15].

In this chapter, we report on the direct observation of antibunching in a continuous quantum system where the wavefunctions of all the particles overlap. The measurement is enabled by the experimental techniques that were presented in detail in the previous chapter. We prepare pure quantum ground states of up to  $N = 10$  indistinguishable fermions in the 2D harmonic oscillator potential. Our TOF imaging scheme allows us to sample the wavefunction with high resolution and single atom detection efficiency. We analyse the images by arranging them into so-called Pauli crystals. These unique structures are a result of higher-order density correlations and act as a striking visualization of the Pauli exclusion principle in real space. The measurements lay the foundation for all the studies using interacting samples that are presented in the following chapters. The non-interacting Fermi gas represents an excellent playground to test and fine-tune our different experimental capabilities. All the measurements presented in this chapter have been published in Ref. [Hol21b].

## 5.1 Sampling the Many-Body Wavefunction

To search for fermionic correlations in a continuous 2D Fermi gas, we start by loading mesoscopic samples in the 2D-MT (see Figure 5.1 a). Our spilling method, discussed in detail in chapter 4, allows us to prepare pure closed shell ground state configurations with high fidelities of 93(3)%, 76(2)% and 50(2)% for  $N = 3 + 3$ ,  $6 + 6$  and  $10 + 10$  atoms respectively. Collisions between both hyperfine levels  $|1\rangle$  and  $|3\rangle$  of the two component mixtures are required to improve the fidelity of the spilling sequence. To obtain a non-interacting mixture, once the ground state has been prepared, we perform an adiabatic magnetic field ramp to the zero crossing of the Feshbach resonance at  $B = 568$  G (see Figure 3.7). Here, interactions between the two components of the gas are completely absent, as required for the undisturbed observation of correlations due to the Pauli principle. The sample can be treated as two completely independent copies of  $N = 3$ ,  $6$  or  $10$  indistinguishable Fermions prepared in the closed-shell ground state configurations of a 2D harmonic oscillator (see Figure 5.1 b). Without any interactions, the theoretical description of the full many-body wavefunction becomes very simple.

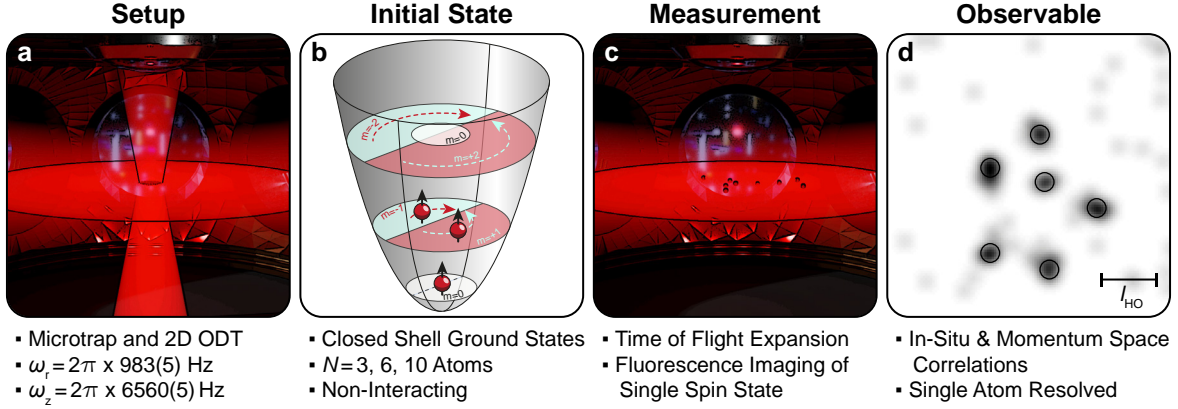


**Figure 5.1: Experimental sequence for the observation of Pauli crystals.** We prepare the system by loading a two component mixture in the 2D-MT, created by the superposition of an optical tweezer and a single 2D sheet of a lattice in vertical direction (a). Non-interacting closed shell ground state configurations for  $N = 3, 6$  or  $10$  atoms of a single spin component are initialized by our deterministic spilling scheme (b). Once the closed shell ground state is prepared, we switch off the radial confinement of the tweezer and let the wavefunction expand in the 2D plane (c). After the TOF, the atom positions are recorded with our single atom resolved fluorescence imaging scheme (d). This allows us to extract density correlations of the many-body wavefunction to any order and in position or momentum space.

### 5.1.1 Real Space Wavefunction

The single particle level spectrum of the 2D harmonic oscillator was already discussed in chapter 2. Each state can be labelled by the principal and the angular momentum quantum numbers  $n$  and  $m$  as  $|n, m\rangle$ . The energy of a particle in state  $|n, m\rangle$  is  $E_n = \hbar\omega_r (n + 1)$ . The wavefunctions  $\Psi_{n,m}$  in real space and polar coordinates  $(x, y) \rightarrow (r, \phi)$  are given by:

$$\Psi_{n,m}(r, \phi) = (-i)^n \sqrt{\frac{l!}{\pi \left(\frac{n+|m|}{2}\right)!}} (-1)^l r^{|m|} e^{-r^2/2} \mathcal{L}_l^{|m|}[r^2] e^{im\phi}, \quad (5.1)$$

where  $l = \frac{n-|m|}{2}$ ,  $\mathcal{L}_l^m[r]$  are the generalized Laguerre polynomials and the radius  $r$  is expressed in natural units of the harmonic oscillator  $r \rightarrow r/l_{\text{HO}}$ . The harmonic oscillator length is defined as  $l_{\text{HO}} = \sqrt{\hbar/m\omega_r}$  and the harmonic oscillator momentum

is  $p_{\text{HO}} = \hbar/l_{\text{HO}} = \sqrt{\hbar m \omega_r}$ . With the radial trap frequency of  $\omega_r = 2\pi \times 983(5)$  Hz in our experiment this leads to  $l_{\text{HO}} = 1.31(1)$   $\mu\text{m}$ . The axial trap frequency is given by  $\omega_z = 2\pi \times 6560(5)$  Hz.

Following the discussion in section 2.1.3, the full many-body wavefunction of the ground state  $\Psi_N(\mathbf{r}_1, \dots, \mathbf{r}_N)$  can be constructed via the Slater determinant as:

$$\Psi_N^{\text{asym.}}(\mathbf{r}_1, \dots, \mathbf{r}_N) = \frac{1}{\sqrt{N!}} \begin{vmatrix} \Psi_{E_1}(\mathbf{r}_1) & \Psi_{E_2}(\mathbf{r}_1) & \dots & \Psi_{E_N}(\mathbf{r}_1) \\ \Psi_{E_1}(\mathbf{r}_2) & \Psi_{E_2}(\mathbf{r}_2) & \dots & \Psi_{E_N}(\mathbf{r}_2) \\ \vdots & \vdots & \ddots & \vdots \\ \Psi_{E_1}(\mathbf{r}_N) & \Psi_{E_2}(\mathbf{r}_N) & \dots & \Psi_{E_N}(\mathbf{r}_N) \end{vmatrix}. \quad (5.2)$$

Taking the  $N = 3$  particle ground state, for example, the three levels  $|0, 0\rangle$ ,  $|1, 1\rangle$  and  $|1, -1\rangle$  are occupied. The full antisymmetric 3-body wavefunction  $\Psi_3$  in real space is then given by

$$\begin{aligned} \Psi_3^{\text{asym.}}(r_1, \phi_1, r_2, \phi_2, r_3, \phi_3) = \frac{1}{\sqrt{6}} & \left[ \Psi_{0,0}(r_1, \phi_1) \Psi_{1,1}(r_2, \phi_2) \Psi_{1,-1}(r_3, \phi_3) \right. \\ & + \Psi_{1,1}(r_1, \phi_1) \Psi_{1,-1}(r_2, \phi_2) \Psi_{0,0}(r_3, \phi_3) \\ & + \Psi_{1,-1}(r_1, \phi_1) \Psi_{0,0}(r_2, \phi_2) \Psi_{1,1}(r_3, \phi_3) \\ & - \Psi_{0,0}(r_1, \phi_1) \Psi_{1,-1}(r_2, \phi_2) \Psi_{1,1}(r_3, \phi_3) \\ & - \Psi_{1,-1}(r_1, \phi_1) \Psi_{1,1}(r_2, \phi_2) \Psi_{0,0}(r_3, \phi_3) \\ & \left. - \Psi_{1,1}(r_1, \phi_1) \Psi_{0,0}(r_2, \phi_2) \Psi_{1,-1}(r_3, \phi_3) \right]. \end{aligned} \quad (5.3)$$

Each term in the Slater determinant contains the same product over single particle states  $\Psi_i$  ( $i = 1, \dots, N$ ). This ensures that the wavefunction is fully antisymmetric when the positions of any two of the particles are exchanged  $r_i \leftrightarrow r_j$  ( $i \neq j$ ), as required for indistinguishable fermions. The total ground state energy  $E_N$  can be obtained by simply adding up the energy contributions of all occupied single particle levels. This leads to  $E_N = 1/6N(N+1)(2N+1)\hbar\omega_r$  or  $E_N = 5\hbar\omega_r$ ,  $14\hbar\omega_r$  and  $30\hbar\omega_r$  for 3, 6 and 10 atoms respectively.

The probability  $P$  of detecting the  $N$  particles in a given configuration in real space  $(\mathbf{r}_1, \dots, \mathbf{r}_N)$  is given by  $P(\mathbf{r}_1, \dots, \mathbf{r}_N) = |\Psi_N^{\text{asym.}}(\mathbf{r}_1, \dots, \mathbf{r}_N)|^2$ . The number of single particle wavefunctions contributing to the probability distribution  $P$  in real space scales with the particle number as  $N \cdot N!$ . For  $N = 3$  this leads to the 18 wavefunctions listed above, for 6 particles the distribution is made up of 4320 terms and for 10 the number already grows to 36 288 000. Sampling the probability distribution  $P$  numerically becomes very challenging and time consuming as the particle number is increased. This

is an impressive demonstration of how fast exponential scaling complicates numerical calculations, even for a non-interacting system. Our experiment, on the other hand, allows us to sample from the many-body wavefunction directly by repeated projections of the state onto some configuration  $(\mathbf{r}_1, \dots, \mathbf{r}_N)$  through measurements in real or momentum space.

### 5.1.2 Imaging Sequence

Once we have prepared the system of  $N$  single component fermions in the respective many-body wavefunction  $\Psi_N^{\text{asym.}}$  experimentally, the detection sequence is initialized. We make use of the TOF imaging scheme, discussed in detail in section 4.4.6 and Ref. [And17]. The optical tweezer providing the large radial confinement is switched off and the atoms expand in the 2D sheet created by the SWT (see Figure 5.1 c). The remaining harmonic confinement in radial direction during the TOF is given by  $\omega_{\text{TOF}} = 2\pi \times 20.7(5)$  Hz. After a quarter trap period this leads to an expansion of the many-body wavefunction by a factor of  $\omega_r/\omega_{\text{TOF}} = 47.5(10)$ . In addition, as a result of the expansion in the harmonic potential, the initial momenta  $\mathbf{p}_i$  of the atoms  $i = 1, \dots, N$  are mapped to their position after TOF  $\mathbf{p}_i \rightarrow \mathbf{r}'_i$ . Our fluorescence imaging technique allows us to record the final position of each atom  $\mathbf{r}'_i$  on our camera (see Figure 5.1 d). Each image corresponds to a single projection of the many body wavefunction  $\Psi_N^{\text{asym.}}$  in momentum space and we obtain a list of in-situ momenta  $\mathbf{p}_i$  for each atom  $i = 1, \dots, N$ . We generally express these momenta directly in natural units of the harmonic oscillator  $\mathbf{p}_i \rightarrow \mathbf{p}_i/p_{\text{HO}}$ .

The harmonic oscillator wavefunctions  $\Psi_{n,m}$  play an important role for our experiment. They are eigenfunctions of the continuous Fourier transform and therefore equivalent in real and momentum space ( $\Psi_{n,m}(x, y) \equiv \Psi_{n,m}(p_x, p_y)$ ). The many-body wavefunction is a superposition of many terms that each contain the same product over single particle wavefunctions (see equation (5.3)). As a result, the many-body wavefunction is an eigenfunction of the Fourier transform as well and the same statement holds ( $\Psi_N^{\text{asym.}}(\mathbf{x}, \mathbf{y}) \equiv \Psi_N^{\text{asym.}}(\mathbf{p}_x, \mathbf{p}_y)$ ). The measurements we take in momentum space after TOF are completely equivalent to measurements in real space and can be transformed into one another simply by replacing  $\mathbf{p}_i/p_{\text{HO}} \leftrightarrow \mathbf{r}_i/l_{\text{HO}}$ . Since both descriptions are completely equivalent, we treat momentum and position variables as equal in the following. The magnification of the many-body wavefunction by the TOF scheme by a factor of  $\approx 50$  allows us to study the in situ many-body wavefunction with an effective imaging resolution of approximately 250 nm. This is far below the typical inter-particle spacing of the state given by  $l_{\text{HO}} = 1.31(1) \mu\text{m}$  so we can reveal fermionic correlations directly.

### 5.1.3 Experimental Sampling of the Wavefunction

Each single image leads to a random projection onto a set of measured particle momenta  $p_{x,i}$  and  $p_{y,i}$  ( $i = 1, \dots, N$ ) according to the probability distribution  $P$ , defined above. To search for correlations between the momenta and sample the probability distribution  $P$  accurately, we repeat the projective measurements many times. For the  $N = 3, 6$  and 10 particle ground states we take 9994, 19291 and 25644 single images respectively. We further analyse only those images where the correct total number of atoms  $N$  has been detected. This leads to post selection fidelities of 25 %, 28 % and 36 % for each of the atom numbers. The increased detection rate for larger particle numbers  $N$  can be explained with experimental upgrades that have been implemented between each of the respective measurements. The  $N = 10$  atom data has been taken almost one year later than the  $N = 3$  and 6 atom pictures, after we had optimized the imaging and camera setting significantly. A post selection rate of 36 % of the images for  $N = 10$  particles combined with a preparation fidelity of 50 % corresponds to a single atom detection efficiency of around 97 %. This is in good agreement with the value of 97.8(9) % that was determined in section 4.4.4.

In Figure 5.2, a set of 38 samples from the  $N = 6$  particle ground state is shown. The raw images have been analysed, as described in chapter 4, by applying a low-pass filter and searching for peaks in the image. Any local maximum with an amplitude above a certain threshold is identified as an atom by our algorithm and indicated by black circles in the Figure. Other than for the correct total atom number, the images have not been selected further and represent a typical sample of the probability distribution defined by the many-body wavefunction.

By averaging the recorded atom positions over all images, we obtain the average single atom density defined as:

$$n(\mathbf{p}) = N \int \dots \int d\mathbf{p}_2 \dots d\mathbf{p}_N |\Psi_N^{\text{asym.}}(\mathbf{p}, \mathbf{p}_2, \dots, \mathbf{p}_N)|^2. \quad (5.4)$$

The density distribution  $n(\mathbf{p})$  expresses the probability of detecting a single atom at momentum  $\mathbf{p}$  (normalized by the number of atoms  $N$ ). From equation (5.2) follows that it is given by the sum of the absolute squares of all occupied single particle wavefunctions  $n(\mathbf{p}) = |\Psi_{0,0}(\mathbf{p})|^2 + \dots + |\Psi_{n,m}(\mathbf{p})|^2$ . The measured density distribution  $n(\mathbf{p})$  is continuous and spherically symmetric as expected for a gas in the ground state of the 2D harmonic oscillator potential (see Figure 5.2). No single orientation is preferred in the trap.

A second quantity that we can extract immediately from the images is the centre of mass momentum  $\bar{\mathbf{p}}$ , defined as

$$\bar{\mathbf{p}} = \frac{1}{N} \sum_{i=1}^N \mathbf{p}_i. \quad (5.5)$$

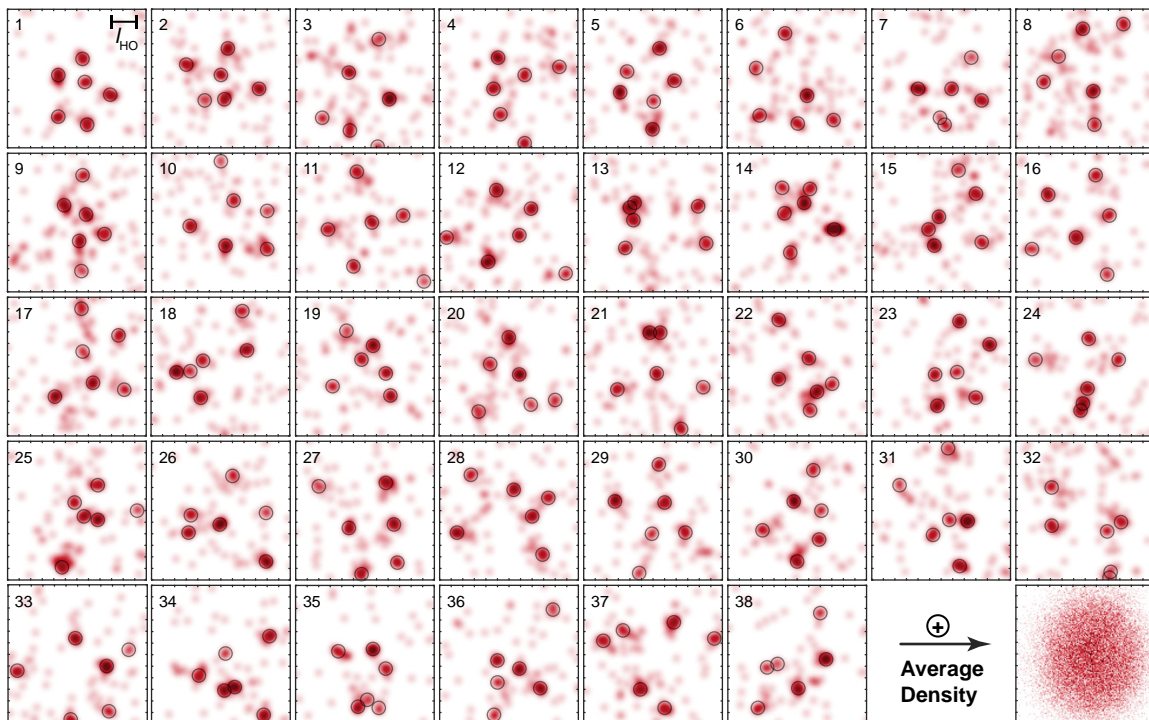


**Figure 5.2: Random selection of measured samples from the  $N = 6$  particle ground state.** The images have been postselected only for the correct number of measured atoms  $N$ . They represent typical samples from the probability distribution defined by the absolute square of the many-body wavefunction. Our imaging resolution is well below the average inter-particle spacing, given by the natural length scale of the harmonic oscillator  $l_{\text{HO}}$ . A histogram of the atom positions in all images leads to the average density  $n(p)$ .

In the harmonic oscillator, the centre of mass motion decouples from the relative movement of the particles. The solution for dynamics of the centre of mass system are equivalent to those of a single particle in the harmonic potential with total mass  $M = N \cdot m$ . The fluctuations of  $\bar{p}$  are therefore described by the Gaussian ground state wavefunction  $|\Psi_{0,0}|^2$  with a modified width  $\sigma = 1/(\sqrt{2N})p_{\text{HO}}$  (where  $p_{\text{HO}}$  is defined in terms of the single particle mass  $m$  as above).

The measured distributions of the centre of mass momentum  $\bar{p}_x$  in x-direction for both the  $N = 3$  and  $N = 6$  particle ground states are shown in Figure 5.3 a. We find Gaussian distributions with a width of  $\sigma_{N=3} = 0.44(1)p_{\text{HO}}$  and  $\sigma_{N=6} = 0.31(1)p_{\text{HO}}$  respectively. When the particle number is increased from  $N = 3$  to 6, the mass of the

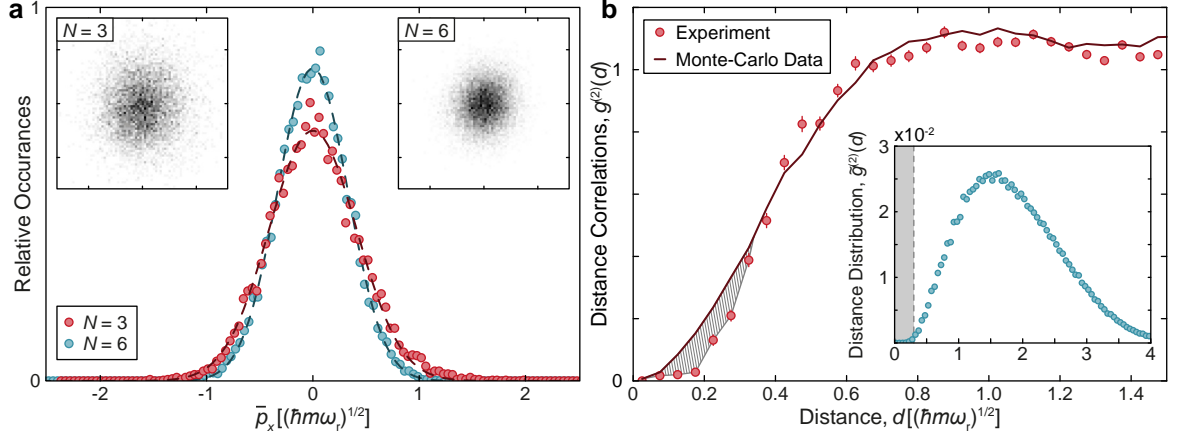


**Figure 5.3: Centre of mass and relative coordinates.** In (a), the distributions of the centre of mass momentum in x-direction over all images are shown for 3 (blue) and 6 particles (red). We observe Gaussian fluctuations with a width that agrees with the expectation from the harmonic oscillator ground state. The insets show the full 2D centre of mass distributions. The dashed lines are Gaussian fits to the data. Statistical errors are on the order of the symbol size. In (b), we show the correlation function  $g^{(2)}(d)$ . It corresponds to the normalized probability of finding two particles at a distance  $d = |\mathbf{p}_i - \mathbf{p}_j|$  in the same image, divided by the independent single particle detection probabilities at momenta  $\mathbf{p}_i$  and  $\mathbf{p}_j$ . The inset shows the same distribution  $\tilde{g}^{(2)}(d)$  without normalization. The solid line is calculated from samples of the ground state wavefunction that were obtained using a Monte Carlo algorithm. The distance correlations reveal a large suppression of detections at small distances as a result of the Pauli principle. The comparison to simulated data allows us to determine the resolution limit (grey shaded area). Panel (a) adapted from Ref. [Hol21b].

centre of mass system is doubled  $M \rightarrow 2M$ . This leads to reduction of the width of the fluctuations by a factor of  $\sigma_{N=3}/\sigma_{N=6} = 1.40(1) \approx \sqrt{2}$  as expected. The absolute magnitude of the fluctuations agrees well with the expected values for the ground state wavefunction of  $\sigma_{N=3} = 1/(\sqrt{6})p_{\text{HO}} = 0.41p_{\text{HO}}$  and  $\sigma_{N=6} = 0.29p_{\text{HO}}$ . This demonstrates that zero temperature quantum fluctuations dominate our measurements and classical noise sources like possible drifts in the TOF potential or thermal noise are negligible. We find the same behaviour for the centre of mass motion in y-direction  $\bar{p}_y$ .

### 5.1.4 Fermionic Antibunching

So far, we have extracted the average density and the centre of mass momentum distribution. Both these quantities are independent of the relative positions of the atoms in a single image and therefore insensitive to fermionic correlations. To search for antibunching, the direct approach is to study distance correlations in the single particle resolved momentum distribution. Due to the Pauli exclusion principle we expect that particles avoid each other and detections at small distances  $d = |\mathbf{p}_i - \mathbf{p}_j| \rightarrow 0$  are strongly suppressed. In Figure 5.3 b, we show the normalized distance correlation function  $g^{(2)}(d)$  for the  $N = 6$  particle ground state. It expresses the probability of finding two different atoms at two momenta  $\mathbf{p}_i$  and  $\mathbf{p}_j$  with distance  $d$  in a single image, divided by the product of the single particle detection probabilities at each momentum  $\mathbf{p}_i$  and  $\mathbf{p}_j$ . As a comparison we also plot  $\tilde{g}^{(2)}(\mathbf{d})$  the absolute probability of finding two particles at distance  $\mathbf{d}$  without normalization (inset).

For completely uncorrelated particles, we expect  $g^{(2)}(d) = 1$  by definition. Our measurements show that simultaneous detection of atoms at small momentum distances in a single image are strongly suppressed even though the particles are completely non-interacting. This is a direct observation of antibunching and the Pauli exclusion principle. The amplitude of the correlation signal is very large and we observe almost complete blocking at small distances  $g^{(2)}(d \rightarrow 0) \rightarrow 0$ . This is a feature of the single particle resolution in our experiment. Without high resolution imaging, only a small reduction in the amplitude of  $g^{(2)}(d \rightarrow 0)$  can be observed. In Ref. [Jel07], the correlations signal at small distances is reduced by only approximately 5% for example. The absolute distance scale at which Pauli blocking between the atoms becomes important is given by the harmonic oscillator momentum  $p_{\text{HO}}$ .

We compare our measurements to simulated data created with a Monte Carlo algorithm. The numerical method is discussed in detail in the next subsection and enables us to draw random samples according to the exact theoretical probability distribution  $P$  introduced in the beginning of the chapter. The Monte Carlo simulation shows very good agreement with our data. Only for very small distances  $d \lesssim 0.3 p_{\text{HO}}$ , we find significantly less particles than what is expected theoretically (grey dashed area). This can be explained by the finite resolution of our imaging scheme, which no longer allows us to distinguish between two particles if they are too close to each other. The absolute number of particles that are missed by our detection scheme due to the limited imaging resolution is very small, on the order of 0.1%. This is because the probability of two particles being closer together than  $d \lesssim 0.3 p_{\text{HO}}$  is very small in the first place. In addition to the suppression by Pauli blocking, small distances are less likely to occur due to the area element ( $r dr$ ) that enters the calculation of the distance distribution  $\tilde{g}^{(2)}$  in 2D (see Figure 5.3 b, inset).

The measurement of the  $g^{(2)}$  correlation function and its comparison to theoretical data allows us to determine the smallest distance at which our detection scheme can differentiate two atoms as  $d_{\min} \approx 0.2 p_{\text{HO}}$ . In real space, after the TOF sequence, this corresponds to an imaging resolution of  $12 \mu\text{m}$ . This agrees very well with the experimental limit of the resolution of  $9.3(1) \mu\text{m}$  that we determined from the PSF of single atoms in section 4.4.5. When the TOF sequence is viewed as a magnification of the wavefunction (for the special case of harmonic oscillator states), this corresponds to an effective imaging resolution for a measurement of the in-situ density of  $250 \mu\text{m}$ . In chapter 9 we will introduce a method to magnify arbitrary many-body wavefunctions, also beyond eigenfunction of the harmonic oscillator. This makes it possible to sample the in-situ density distribution of strongly interacting Fermi gases with a resolution below the typical inter-particle spacing.

### 5.1.5 Monte Carlo Sampling

Direct sampling from the probability distribution  $P = |\Psi_N^{\text{asym.}}(\mathbf{p}_1, \dots, \mathbf{p}_N)|^2$  is difficult. The distribution is both high-dimensional ( $d = 2N$ ) and highly oscillatory as a result of the fermionic exchange symmetry. To obtain a sequence of random samples  $(\mathbf{p}_1, \dots, \mathbf{p}_N)$ , we therefore use the Metropolis–Hastings algorithm as a Markov chain Monte Carlo (MCMC) method. It is straightforward to implement so we can sample the distribution  $P$  approximately without a large effort. The algorithm becomes exact in the limit of an infinite amount of samples drawn [Met53; Has70].

The method requires a second symmetric and more simple probability distribution  $Q$  that can be sampled directly. We choose the uniform distribution on a 2D disc in momentum space with radius  $p_0 = 3p_{\text{HO}}$ , defined as

$$Q(\mathbf{p}_i) = \begin{cases} \frac{1}{\mathcal{N}} & \text{for } |\mathbf{p}| \leq p_0, \\ 0 & \text{for } |\mathbf{p}| > p_0, \end{cases} \quad (5.6)$$

where the normalization factor is given by the area of the disc  $\mathcal{N} = \pi p_0^2$  and the momentum of each atom  $i = 1, \dots, N$  is sampled from  $Q$  independently. The Metropolis–Hastings sequence is initialized by drawing a first random sample of momenta  $s_1 = (\mathbf{p}_1, \dots, \mathbf{p}_N)$  from  $Q$  and calculating the probability density of  $s_1$  in the target distribution  $P_1 = P(s_1) = P(\mathbf{p}_1, \dots, \mathbf{p}_N)$ . The next sample  $s_{i+1}$  of the sequence is always determined in the following way: A candidate for the next set of momenta  $s_n = (\mathbf{p}_1, \dots, \mathbf{p}_N)$  is drawn from the distribution  $Q$  and its probability density according to  $P$  is calculated  $P_n = P(s_n)$ . If  $P_n \geq P_i$ , the candidate  $s_n$  is accepted ( $s_{i+1} = s_n$ ,  $P_{i+1} = P_n$ ) and the algorithm moves to the next iteration  $i \rightarrow i + 1$ . If  $P_n < P_i$ , the candidate is accepted with a probability  $P_n/P_i < 1$  and rejected otherwise. The

decision is made using a random number generator. In case the candidate is rejected, the next element of the sequence is set identical to the current one instead ( $s_{i+1} = s_i$ ,  $P_{i+1} = P_i$ ) and a new candidate is drawn  $i \rightarrow i + 1$ .

Using the MCMC method, we can sample from probability distributions of almost arbitrary complexity, given that enough computational resources are available. Following Ref. [Rak17], this enables us to study thermal or mixed states in addition to the pure ground state wavefunction. The probability distribution for finding  $N$  particles with momenta  $(\mathbf{p}_1, \dots, \mathbf{p}_N)$  of a non-interacting state of the 2D harmonic oscillator in a canonical ensemble can be defined as:

$$P(\mathbf{p}_1, \dots, \mathbf{p}_N) = \frac{\sum_i e^{E_i/k_B T} |\Psi_i(\mathbf{p}_1, \dots, \mathbf{p}_N)|^2}{\sum_i |\Psi_i(\mathbf{p}_1, \dots, \mathbf{p}_N)|^2}, \quad (5.7)$$

where the sum generally runs over all states  $i$  in the many-body spectrum of the 2D harmonic oscillator with energy  $E_i$  and  $T$  is the temperature. To reduce the computation time, we generally consider only states  $i$  with a maximum excitation energy of  $E_{\text{ex.}} = E_i - E_0 \leq E_{\text{cut-off}} = 6\hbar\omega_r$  over the ground state.

For the simulated data presented in this thesis, we draw  $2 \times 10^6$  samples  $s_i$  using the method described above. This ensures that the Metropolis–Hastings sequence samples the probability distribution  $P$  with high accuracy and the outcome is independent of the initial point  $s_1$ . The most time consuming part of the numerical calculation is the evaluation of the many-body wavefunction required for the calculation of  $P(s_i)$  at each iteration. The complete simulation takes about one week for 10 particles on a single high-end computer. We estimate that the same algorithm for the next larger  $N = 15$  ground state would run longer by a factor of approximately 500 000. This demonstrates again the challenges for numerical calculations imposed by exponential scaling. On the other hand, experimental sampling in an ultracold quantum gas is not limited by these problems. A quantum simulation is performed by directly preparing the complete many-body wavefunction required for the given probability distribution.

## 5.2 Pauli Crystals

Our measurements demonstrate that we can observe antibunching in a continuous system of non-interacting fermions. Compared to previous measurements, like in Ref. [Jel07] for example, we can observe the reduction of the correlation function  $g^{(2)}(d)$  by almost the full amplitude as the distance between the particles approaches zero due to the high resolution in our experiment. However, our data contain even more information. We measure the complete configuration of all  $N$  particles in each realization of the experiment. This allows us to extract correlation functions of any order that might

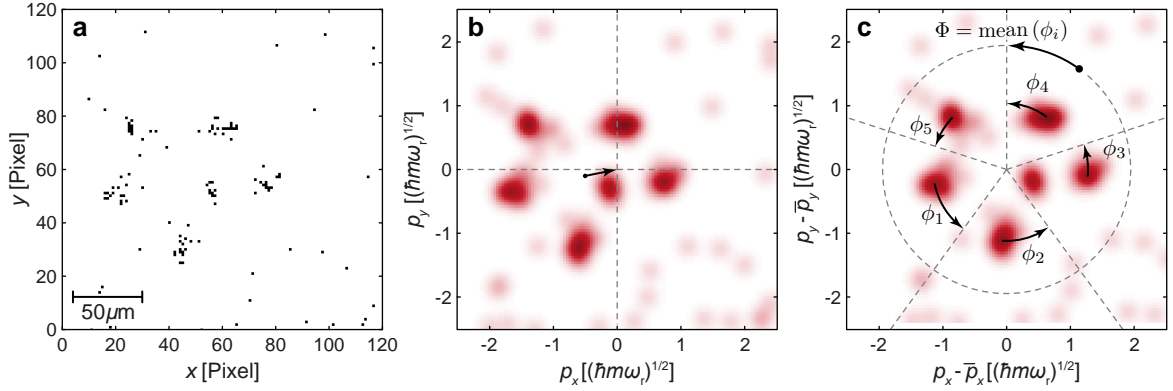


**Figure 5.4: Pauli crystal image analysis.** In (a) a raw binary image from the EM-CCD camera is shown. The bright pixels indicate where single photons have been detected. We can clearly identify the  $N = 6$  atoms in the ground state. In (b) the same image is shown after a low-pass filter has been applied. In the first step, we calculate the centre of mass momentum  $\bar{\mathbf{p}}$  and subtract it from the image (black arrow). To reveal the correlations, we define a target symmetry axis (c, dashed lines) and rotate the image by the angle that simultaneously minimizes the angular distance of the outer atoms to the reference positions. Panel (a) taken from [Hol21a].

appear as a result of the Pauli principle, also beyond the simple suppression of particles at small distances. A closer look at the samples from the  $N = 6$  atom ground state in Figure 5.2 reveals that an additional structure seems to be present. A configuration with one atom in the centre surrounded by an equally spaced ring of the five remaining atoms appears very frequently in the images (see numbers 1,2,5,6,10,11,...). The centre and angular orientation of the configuration are different in each image where it appears. In some cases, fluctuations of one or more atoms destroy the clear structure (see images 7,9,13,18,...).

### 5.2.1 Image Analysis

To analyse our images, we take an alternative approach to the conventional way of calculating density correlation functions of the form  $\mathcal{C}^{(n)} = \langle \hat{n}(\mathbf{p}_1) \dots \hat{n}(\mathbf{p}_n) \rangle$  and follow the procedure suggested in Ref. [Gaj16a]. Each image is analysed separately. Taking the  $N = 6$  ground state for example, we subtract the centre of mass momentum  $\mathbf{p}_i \rightarrow \mathbf{p}_i - \bar{\mathbf{p}}$  from each image in the first step (see Figure 5.4 b). Intuitively this aligns the configurations we have observed in the single images to the same centre, but they are

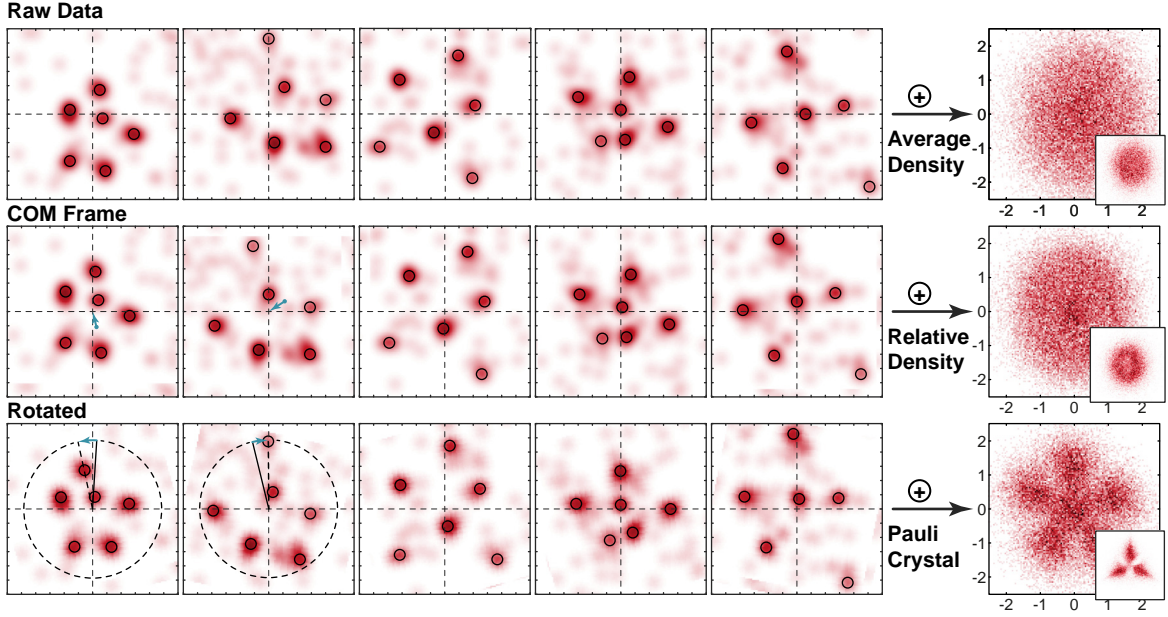


**Figure 5.5: Summary of the Pauli crystal image analysis.** A direct histogram of the atom momenta in the raw images leads to the average single particle momentum distribution  $n(\mathbf{p})$  (top row). When subtracting the centre of mass fluctuations in each image first, the same histogram leads to the single particle density in the centre of mass coordinate frame  $\bar{n}(\mathbf{p})$  (middle row). Fermionic correlations become visible only after aligning each image separately to the same global symmetry axis before creating the histogram (bottom row). The structures that are revealed in the so-called Pauli crystals are a direct consequence of the Pauli exclusion principle. The insets show the same three observables for the  $N = 3$  particle ground state. The axis labels are indicating the momentum in units of  $p_{\text{HO}}$ .

still rotated with respect to each other. Therefore, we define a set of target angles  $\varphi_{T,i} = 2\pi(i - 1)/5$  ( $i = 1\dots 5$ ) for the five momenta of the outer atoms of the configuration. The outer atoms are identified by finding largest absolute momenta after subtracting the centre of mass  $|\mathbf{p}_i - \bar{\mathbf{p}}|$ . In the second step, we rotate each image by an angle  $\Phi$  that minimizes the angular distance of the rotated to the target configuration (see Figure 5.4 b). We label the momenta in the rotated coordinate system as  $\tilde{\mathbf{p}}_i$ . The angle that minimizes the distance of the rotated configuration is then given by

$$\Phi = \text{mean}(\varphi_i - \varphi_{T,i}) = \text{mean}(\phi_i), \quad (5.8)$$

where  $\varphi_i$  ( $i = 1\dots 5$ ) are the angles of the five outer atoms before rotation in polar coordinates, sorted in ascending order (see Figure 5.4 c). As a result of the five-fold rotational symmetry of the  $N = 6$  particle configuration we can limit the rotation angle to  $\Phi \rightarrow \text{mod}(\Phi, 2\pi/5)$ .

When we calculate the histogram of the momenta  $\tilde{\mathbf{p}}_i$  in all the separately rotated images, strong correlations become apparent immediately (see Fig 5.5). The structures that become visible in this so-called configuration density are referred to as Pauli crystals [Gaj16a]. They are a direct consequence of the Pauli exclusion principle and a striking visualization of antibunching in real and momentum space. The atoms in our 2D harmonic oscillator potential avoid each other in relative coordinates and their most probable relative configuration is revealed by the configuration density. The average single particle density is insensitive to this structure. As a result of the radial symmetry of our system, the angular distribution of the atoms is completely homogeneous. The symmetry is only broken by the measurement itself, when the wavefunction is projected onto the final set of momenta  $\mathbf{p}_i$  and the particles align with respect to a random axis that is different each time. Almost pure quantum states together with single particle resolution and large detection efficiencies are a necessary requirement for the observation of Pauli crystals [Rak17].

### 5.2.2 Different Particle Numbers

The measurement of Pauli crystals can be extended to any pure quantum state of mesoscopic size. Since any of the open shell energy levels of the 2D harmonic oscillator are degenerate, the preparation of pure states, for example with  $N = 4$  particles, is more challenging. While spilling to some of the open shell configurations is still possible (see chapter 6), we limit ourselves to the closed-shell states here. In Figure 5.6, the results for the three lowest non-degenerate ground state configurations with  $N = 3, 6$  and 10 indistinguishable fermions are shown.

One of the essential steps in the analysis procedure leading to the  $N = 6$  Pauli crystal is the identification of the correct target configuration and target angles  $\varphi_{T,i}$  for the rotation of the images. For a general ground state, the target configuration can be identified by searching for the set of momenta  $(\mathbf{p}_1, \dots, \mathbf{p}_N)_{\text{max}}$  that maximizes the probability distribution  $|\Psi_N^{\text{asym.}}(\mathbf{p}_1, \dots, \mathbf{p}_N)|^2$  [Gaj16a]. This leads to a three-fold rotational symmetry for 3 atoms and a five-fold symmetry for 6 atoms, as discussed in detail in the previous section. The  $N = 10$  particle Pauli crystal shows no rotational symmetry. In the analysis, we first assign the particles to either the inner or outer ring by sorting them by their absolute momentum  $|\mathbf{p}_i|$  first and by their angle in polar coordinates  $\varphi_i$  second. The optimal rotation  $\Phi$  for each image is then determined analogously to the  $N = 6$  particle case by minimizing the distance from each atom to

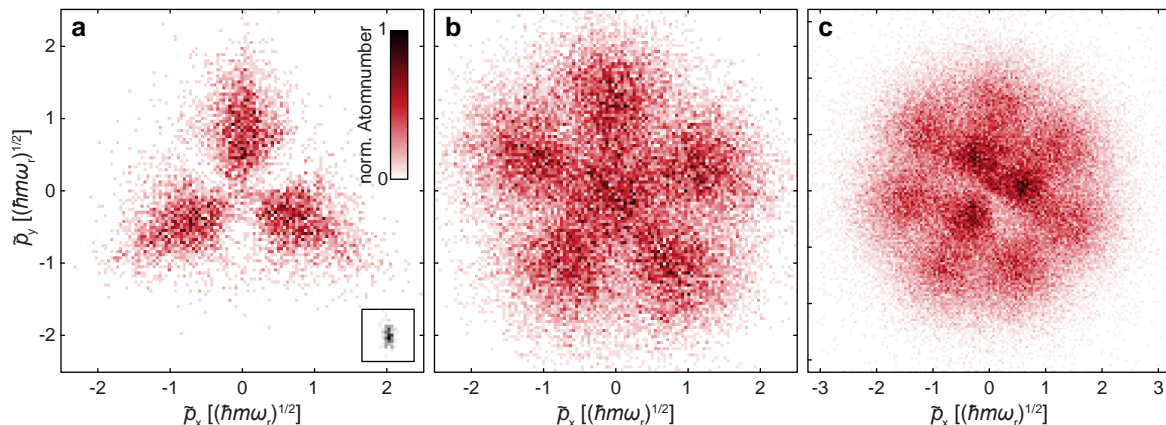


**Figure 5.6: Closed-Shell Pauli crystal configurations.** To reveal the higher order correlations between the relative momenta of the atoms, the configurations in each measurement have to be aligned to a common symmetry axis before creating a histogram over all images. The rotated momentum coordinate system is labelled by  $\tilde{\mathbf{p}}$ . The inset in (a) shows the PSF of a single atom. The Pauli crystals visualize in which configuration the  $N = 3$  (a), 6 (b) or 10 (c) atoms arrange themselves most frequently in the trap. The reduced contrast in the outer ring of seven atoms agrees with the theoretical expectations for the 10 particle ground state (c) [Gaj16a]. Panels (a) and (b) are adapted from [Hol21a].

its target angle  $\varphi_{T,i}$  simultaneously (see equation (5.8)). This method can be extended directly to Pauli crystals of arbitrary size. We are currently limited to  $N = 10$  particles in each hyperfine component by the fidelity of our ground state preparation scheme (see section 4.2.7).

## 5.3 Systematic Effects

The target configuration and rotational symmetry of the Pauli crystals are imposed by the algorithm that we apply to each image separately. Pattern matching algorithms can generally cause problems like a bias towards the target distribution, especially if non-linear distance measures are used [Fre20]. While our distance measure is linear (see equation (5.8)), it is nevertheless essential to rule out any artifacts that might be created by our analysis procedure.

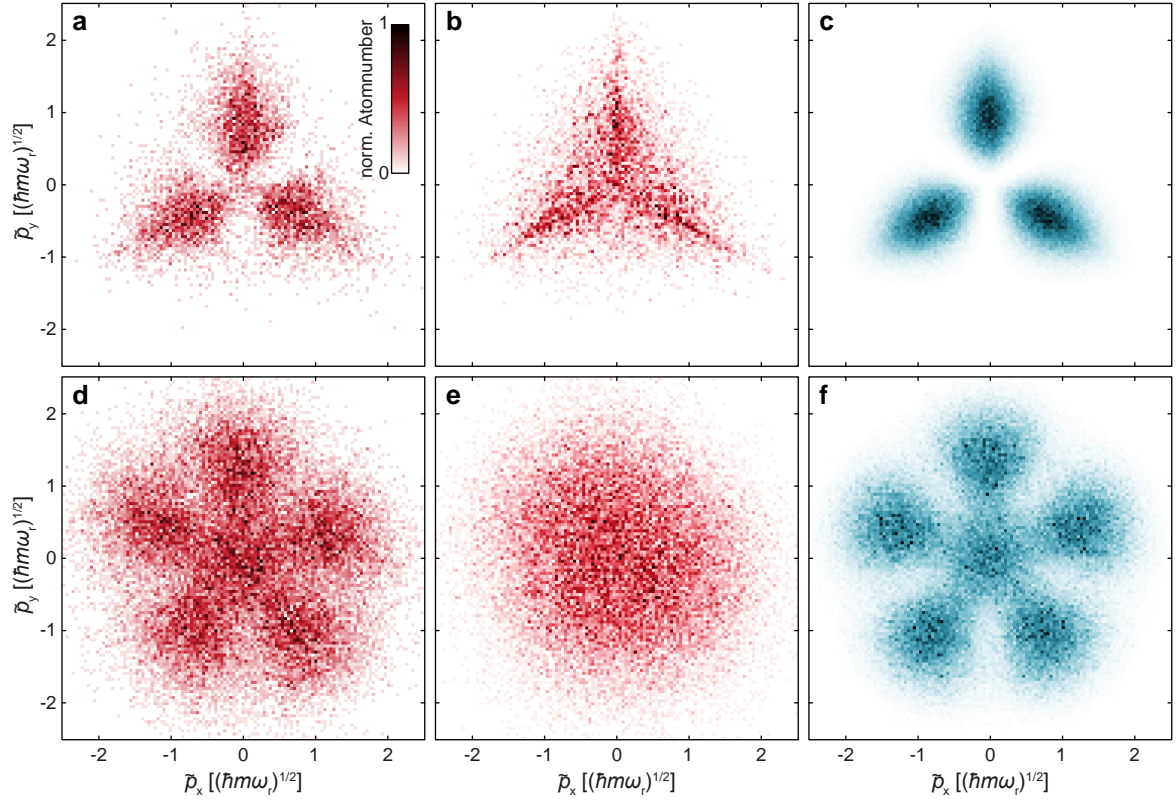


**Figure 5.7: Comparison to shuffled data and Monte Carlo simulations.** We compare our measured Pauli crystals (a,d) to the configuration densities we obtain by applying the same analysis algorithm to shuffled data (b,e). The shuffling is performed by drawing each atom momentum  $\mathbf{p}_i$  in a single sample ( $i = 1, \dots, N$ ) from  $N$  different images. We find no bias towards the target distribution for larger atom numbers  $N > 3$ . The artifact that is observed for the shuffled data of  $N = 3$  particles is a boundary effect that appears due to the small number of degrees of freedom of this system. In (c,f) we show the Pauli crystals that we obtain from sampling the zero temperature  $N$ -body wavefunction numerically. Figure adapted from [Hol21a].

### 5.3.1 Shuffled Data

A very direct method of confirming that our data does not create any bias towards the target distribution is to shuffle the data. To this end, we take a set of  $N$  atom momenta  $\mathbf{p}_i$  ( $i = 1, \dots, N$ ) not from a single image but from  $N$  different samples of the

wavefunction. We effectively shuffle the measured atom momenta  $\mathbf{p}_i$  between different experimental runs. This leaves the single particle densities in absolute and relative coordinates  $n(\mathbf{p})$  and  $\bar{n}(\mathbf{p})$  unchanged but removes all the fermionic correlations between the particles. Since two particles are now drawn from different images, we can label them by the image number and they are not indistinguishable any more.

The configuration densities that we obtain for shuffled data after performing the same pattern matching algorithm used for the Pauli crystals are shown in Figure 5.7. For larger atom numbers  $N > 3$  we observe no bias towards the target distribution. We have confirmed this also for open shell states, for example with  $N = 4$  particles, by sampling the wavefunction numerically. Instead of a Pauli crystal, the analysis produces a distribution that is radially symmetric and given by the single particle density  $\tilde{n}(\mathbf{p})$  in relative and rotated coordinates. No antibunching can be observed. For the  $N = 3$  particle case, we observe a residual structure even for shuffled data. This is a boundary effect appearing only for this lowest particle number due to the small number of degrees of freedom and not a general problem of the method.

As a comparison, we also show the Pauli crystals we obtain from sampling the  $N$  particle ground state wavefunction numerically in Figure 5.7. The predictions agree very well with our experimental data. We find that the measurements show a reduced contrast compared to the zero temperature calculation. This can be explained by the momentum resolution and by excitations above the ground state in our experiment.

### 5.3.2 Melting the Crystal

To study the effect of finite temperature and excitations above the ground state in more detail, we increase the energy of our initial state in the experiment. To this end, we modulate the confining potential in radial direction at twice the trap frequency  $2\omega_r$  for a duration of  $t = 50$  ms. The excitation amplitude is varied between 0 and 20% of the radial trap depth to control the amount of energy  $E_{\text{ex}}$  that is added to the system. This perturbation causes excitations of atoms in the closed shell configuration into higher harmonic oscillator levels. We take 3000 images of the momentum distribution at each modulation amplitude.

For the non-interacting system it is not expected that thermalization takes place. Instead, the regular harmonic oscillator level spacing could give rise to coherent phenomena, for example revival dynamics at the trap frequency. However, owing to the rather small size and Gaussian shape of the optical trap in the experiment, deviations from the harmonic level spacing are rather substantial, on the order of a few percent, and the wavefunction evolves at many different, incommensurate frequencies. The measurements are performed with a drive approximately fifty times longer than the inverse trap frequency, at which point we expect deviations from the harmonic potential to

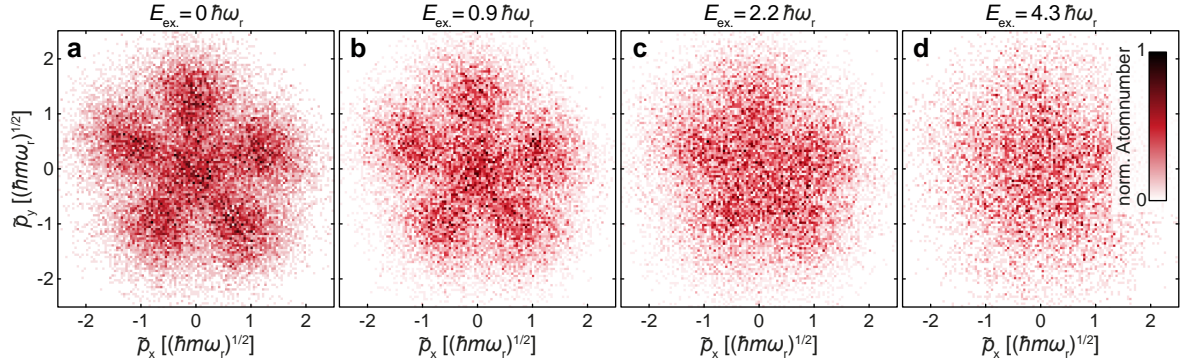


**Figure 5.8: Melting the  $N = 6$  particle Pauli crystal.** We increase the energy of the initial state by modulating the radial confinement at twice the trap frequency for some time. We find that the contrast in the configuration densities significantly reduces as soon as the excitation energy of the many body state above the ground state is on the order of the Fermi energy  $E_{\text{ex.}} \gtrsim E_{\text{F}}$ .

have dephased the many-body wavefunction substantially. Noise and small drifts in the potential together with the large Hilbert space of the system lead to a mixed state with correlations that are close to a thermal state. We do not observe any coherent oscillations for our modulation scheme and the measured correlations are robust to small changes in the drive amplitude and duration.

We extract the absolute mean energy of the initial state  $\langle E \rangle$  after the modulation, directly from the measured single particle resolved momentum space density. The total kinetic energy of all atoms in each image is given by  $E_{\text{kin}} = \sum p_i^2/2m$ . By averaging over all images and applying the equipartition theorem to the non-interacting harmonic oscillator states, we obtain  $\langle E \rangle = \langle E_{\text{pot}} \rangle + \langle E_{\text{kin}} \rangle = 2 \langle E_{\text{kin}} \rangle$ . Without modulation, i.e. for the lowest temperature state that we can prepare in our system, and for  $N = 6$  particles this leads to  $\langle E \rangle_0 = 13.10(15) \hbar\omega_r$ . This energy is 5% below the theoretical ground state energy of  $14 \hbar\omega_r$  that we expect for this particle number. This deviation of the absolute energy measurement can be explained by inaccuracies in the calibration of the particle momenta  $\mathbf{p}_i$  in the TOF images. The relative errors on the radial trap frequency measurement and the magnification of our optical setup are on the order of 2%. Both quantities enter quadratically into the absolute energy measurement. These uncertainties alone can account for the systematic shift towards lower energies that is observed for all data points. Relative energy shifts between initial states modulated with different amplitudes can still be detected with high accuracy.

When the excitation energy, defined as  $E_{\text{ex.}} = \langle E \rangle - \langle E \rangle_0$ , is increased, we observe

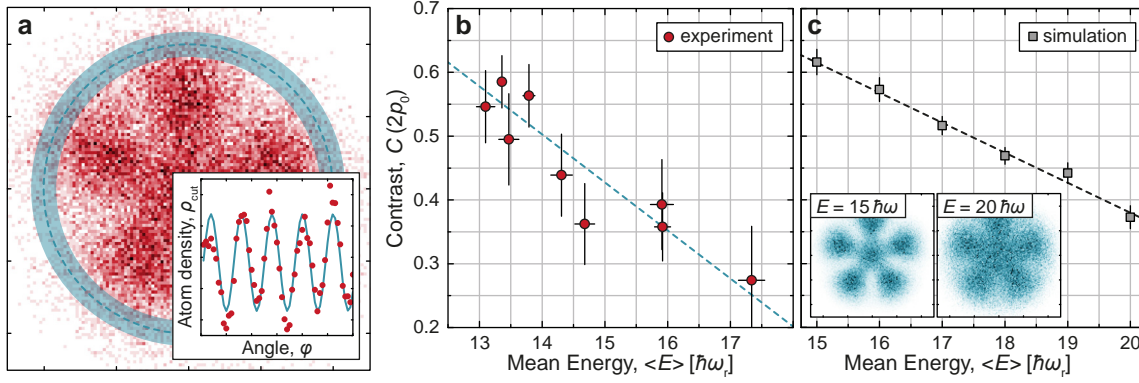


**Figure 5.9: Pauli crystal contrast  $C$  as a function of mean energy  $\langle E \rangle$ .** We extract the contrast  $C$  by fitting a sine function (a, inset) to the configuration density at a fixed momentum  $p = 2p_{\text{HO}}$  (a, shaded region). It reduces linearly with an increasing mean energy of the initial state  $\langle E \rangle$  (b). The Monte Carlo simulation qualitatively shows the same result for thermal states (c). The measured slope of the decay is faster in the experiment. Figure adapted from [Hol21a].

how the Pauli crystals “melt” and the contrast in the configuration density vanishes (see Figure 5.8). An energy increase by a small fraction of the ground state energy ( $E_{\text{ex.}}/14\hbar\omega_r \approx 15\%$ ) is enough to reduce the visibility almost to zero. This is expected since a large number of degenerate levels already becomes available when we add only a single quanta of energy  $\Delta E = \hbar\omega_r$  to the 2D harmonic oscillator ground state. In general, we expect that the Pauli crystals melt as soon as the excitation energy is on the order of the Fermi energy of the system  $E_{\text{ex.}} \gtrsim E_{\text{F}} = (n_{\text{F}} + 1)\hbar\omega_r$ .

To be able to describe the loss of the visibility of the Pauli crystals with increasing energy also more quantitatively, we define the contrast  $C$  as follows: We fit a sine function to the angular distribution of the configuration density at a fixed momentum  $p = 2p_{\text{HO}}$  (see Figure 5.9 a). The contrast  $C$  at this absolute momentum is then defined as  $C = 1 - \min/\max$  in terms of the minimum and maximum value of the sine function. We find that the contrast  $C$  decreases linearly with energy and with a slope of  $(dC/d\langle E \rangle)_{\text{exp.}} = -0.075(13)/\hbar\omega_r$  (b). Pauli crystals that were obtained from sampling thermal states using the Monte Carlo simulation show the same linear decrease of the contrast with energy (c). The slope of the decay is given by  $(dC/d\langle E \rangle)_{\text{theo.}} = -0.048(30)/\hbar\omega_r$  in this case.

The small but significant quantitative difference between experiment and simulation can be explained partially by the systematic uncertainty in our experimental measure-

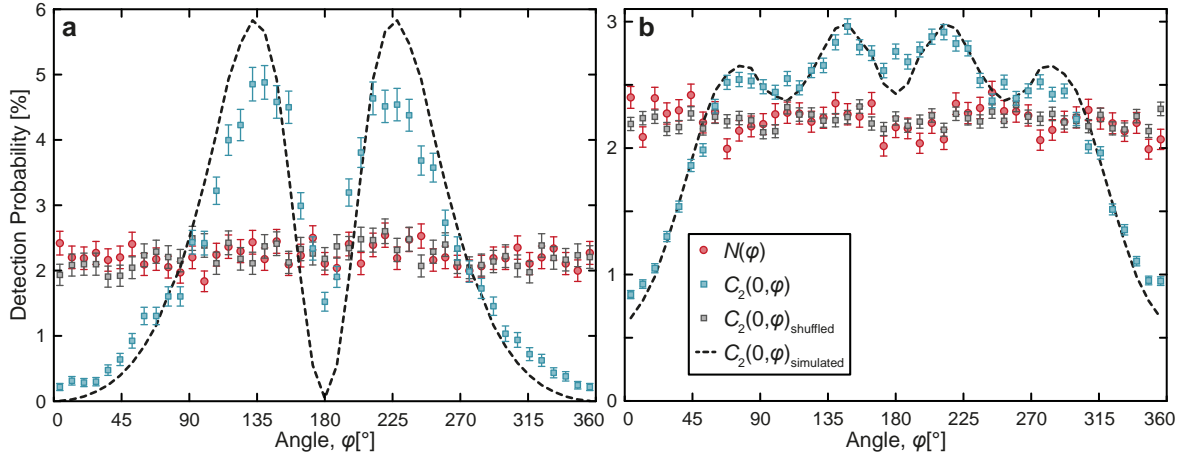


**Figure 5.10: Angle correlations  $C^{(2)}(0, \phi)$  in the closed-shell ground state.** The correlator  $C^{(2)}(0, \phi)$  is defined by the probability of a second particle at an angle  $\phi_2 = \phi$  given that a first particle is located at  $\phi_1 = 0$ . We observe the three and five-fold symmetries that are also revealed by the respective Pauli crystals. The total angular atom distribution in our trap  $N(\phi)$  is shown as a comparison. Figure adapted from [Hol21a].

ments of absolute energies. In addition, the thermal states in equation (5.7) that are used for the Monte Carlo simulation only describe the true initial state approximately. To model the mixed state that is created by our modulation more accurately, a more detailed knowledge of the exact geometry of all the trapping potentials would be required. The non-equilibrium and thermalization dynamics that appear in mesoscopic systems with and without interactions represent an interesting topic for future studies in our experiment.

In conclusion, we find the visibility of the Pauli crystals in the configuration density is very sensitive on the amount of non-coherent excitations in the initial state. We find that the observed contrast in our experiment is very close to the theoretical prediction at zero-temperature, especially after accounting for the finite momentum resolution in the measured images (see Figure 5.7). This demonstrates that our initial state is very close to the true absolute  $N$ -body ground state of the 2D harmonic oscillator. The ability to melt the crystals additionally shows that the observed correlations originate from the indistinguishability of our fermionic particles and are not a result of the pattern matching algorithm or other systematic effects. The energy of the initial state does not effect the detection or preparation fidelity in any way. The scale at which the visibility is lost almost completely is given by the Fermi energy  $E_{\text{ex.}} \gtrsim E_{\text{F}}$ .

### 5.3.3 Angular Correlations

Our single particle resolved data also allows us to calculate density correlations  $C^{(n)}$  in a more conventional manner. As a final validation of the presence of the Pauli crystal correlations in the ground state wavefunction, we extract the angular density-density correlation function  $C^{(2)}(0, \phi)$ . It is defined by the probability of detecting a second particle at an angle  $\phi_2 = \phi$  given that a first particle is located at  $\phi_1 = 0$ . The results for the  $N = 3$  and 6 particle ground states, together with their respective simulations, are shown in Figure 5.10. We find a good agreement between experiment and theory and observe the expected three and fivefold symmetries. The shuffled data, where the first and second particle in  $C^{(2)}(0, \phi)$  belong to different images, is radially symmetric without any structure.

## 5.4 Conclusion

In this chapter, we have studied samples of non-interacting and indistinguishable fermions, prepared in closed shell ground state configurations for a 2D harmonic oscillator. We have observed how the Pauli exclusion principle leads to higher order density correlations in the mesoscopic system. The correlations can be visualized with striking geometric configurations that have been termed Pauli crystals. They do not appear in the density distribution directly but only in relative position or momentum coordinates and reveal the most probable configuration of the particles in the trap.

Self-ordering and crystalline structures, akin to the observations here, are found in many interacting mesoscopic systems. Wigner crystals, formed by electrons due to their repulsive interactions [Wig34; Li21], or Coulomb crystals in ion traps [Win87; Die87] show a remarkable resemblance to Pauli crystals. Further examples are found in Dipolar gases [Kad16] or ensembles of Rydberg atoms [Sch15]. While this motivates the term *Pauli crystal*, it is important to emphasise that no translational symmetry breaking takes place in our case. The ground state is a coherent superposition of all possible configurations and no true long range order is present. The rotational symmetry is broken only by the measurement itself. The Pauli crystal configurations for larger atom numbers are truly unique, the  $N = 10$  electron Wigner crystal in 2D is made up of two particles in the centre, surrounded by the remaining eight, for example [Pee09].

Higher order density correlations and Pauli crystals are a general feature of mesoscopic fermion systems. Using our simulations, we find similar structures in a wide range of potentials, for example box geometries. Most interesting are samples with an approximately homogenous mean density and additional symmetries, like rotational

invariance, that are broken by the measurement. A large visibility of the correlations requires that the system size is not much larger than the typical inter-particle spacing. As the number of particles is increased and when entering further into the macroscopic world, we expect the contrast to reduce until the structures vanish for the homogeneous, infinite Fermi gas. This can already be observed for the  $N = 10$  particle measurement (see Figure 5.6).

The measurements in a non-interacting mesoscopic Fermi gas act as an important benchmark for our experiment. The system can be solved exactly and accurate numerical simulations are available. The Pauli crystal configurations match the theoretical predictions closely. With their high sensitivity on excitations above the ground state, this confirms that we can prepare up to  $N = 10 + 10$  particles in the closed-shell configuration and very close to zero temperature. Our measurements also demonstrate that it is now possible to access correlations in continuous systems at the single particle level. Taken together, these unique capabilities open up entirely new opportunities for the study of emergent phenomena in mesoscopic Fermi gases. As a first step in this direction, we will reintroduce interactions between both hyperfine particles in the next chapter. The study of single particle resolved density correlations in strongly interacting systems, enabled by extending our imaging scheme to the second spin component, is presented in chapter 7.

# 6

## Emergence of a Quantum Phase Transition

Emergent behaviour is characterized by phase transitions and universal low energy excitation spectra that are independent of the microscopic details of the system [And72; Alt06; Sac11]. We have demonstrated that we are able to prepare pure non-interacting ground states in mesoscopic samples of up to  $N = 10$  particles of a single spin component (see chapter 4). In this case, the many-body solution for arbitrary atom numbers is constructed directly via a simple superposition of single particle wavefunctions of the 2D harmonic oscillator potential. The macroscopic state is, after accounting for the Pauli exclusion principle (see chapter 5), no more than the sum of its parts. The most fundamental ingredient required for the emergence of collective behaviour is missing: significant inter-particle interactions.

In this chapter, we introduce strong interactions between both hyperfine components that are present in our mesoscopic samples. To this end, we make use of the broad Feshbach resonance of  ${}^6\text{Li}$  (see section 3.3.2) that allows us to explore the full range between weak ( $E_B \ll E_{\text{HO}}$ ) and completely dominating ( $E_B \gg E_{\text{HO}}$ ) attraction strengths. Previous studies of mesoscopic fermion systems in ultracold quantum gases with precisely prepared ground states and strong interactions have been limited to 1D geometries [Wen13a; Zür12b; Zür13; Mur15a]. The extension of these measurements to a 2D environment modifies the collective behaviour expected in the macroscopic limit significantly.

The degeneracies of the energy levels of the 2D harmonic oscillator lead to a shell structure and a gapped single particle spectrum for closed shell configurations. The interplay between Pauli blocking in closed shell configurations with the interactions lead to a quantum phase transition between a normal and a superfluid in the macroscopic limit (see chapter 2). Here, we study what remnants of this quantum phase transition can be found in mesoscopic samples of up to  $N = 10 + 10$  atoms. In similar systems like nuclei, superconducting grains or small helium droplets superfluid behaviour

has already been observed for particle numbers similar to what we can access in our experiment [Gre98; Del01; Lau17].

We analyse the many-body state using two different approaches. In a first set of studies, we vary the interaction strength between both hyperfine components during the preparation process to extract qualitative information about degeneracies in the many-body energy level spectrum and the nature of the ground state. More quantitative statements become possible with our second set of measurements where we use modulation spectroscopy to extract the low energy excitation spectrum. We find particular pair excitation modes with a non-trivial dependence on the interaction strength. A detailed comparison to theory [Bje16] allows us to identify them as precursors of the Higgs mode that is expected as universal low energy excitation for macroscopic superfluids. The pair excitations are a manifestation of emergent collective behaviour and appear for as few as  $N = 3 + 3$  particles. By taking measurements with different particle numbers we can study how the macroscopic limit is approached.

In the many-body limit, an approximate particle-hole symmetry is required for the observation of a stable Higgs mode as low energy excitation of a superfluid [Pek15]. In macroscopic samples the amplitude mode has been observed in different systems like superconductors [Soo80; Mat13; Kat18], ferromagnets [Rüe08] or ultracold quantum gases [Bis11; End12; Léo17; Beh18]. In the mesoscopic limit, the excitation is stabilized by the discrete and gapped single particle spectrum and long-lived even without the presence of an exact particle-hole symmetry (see chapter 2) [Bru14]. We pioneer the study of the emergence of quantum phase transitions and its associated Higgs modes starting from the mesoscopic limit and on the single particle level. A large part of the results presented in this chapter have been published in Ref. [Bay20a].

## 6.1 Ground State Preparation

Before studying the many-body excitation spectrum of closed shell configurations in the next section, it is instructive to revisit the spilling scheme that allows us to prepare ground states in the first place (see section 4.2.7). The starting point is a cloud of approximately  $N = 15 + 15$  atoms at almost zero temperature that is transferred into the 2D-MT (see Figure 6.1 a). The trap frequencies in the 2D-MT are given by  $\omega_r = 2\pi \times 1001(5)$  Hz and  $\omega_z = 2\pi \times 6803(5)$  Hz respectively. The small difference in trap frequencies compared to the values reported in the other chapters can be explained by drifts and adjustments of the optical setup between different measurements.

From the initial sample in the 2D-MT, we prepare the desired ground state by first applying a strong magnetic field gradient in axial direction that does not affect the radial symmetry or shell structure in the 2D plane. By reducing the optical power and

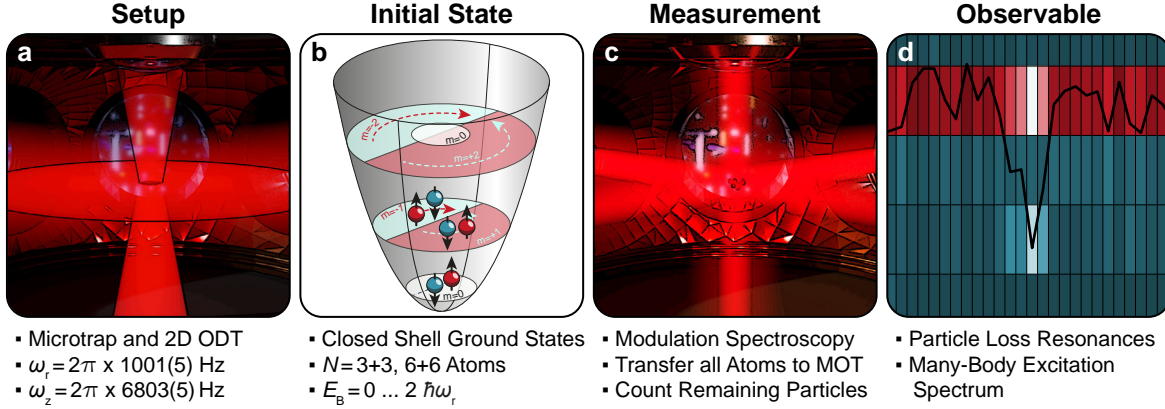


**Figure 6.1: Experimental sequence for observing the emergence of a phase transition.** The state is initialized by loading a two component mixture in the 2D-MT (a). We first spill to the closed-shell ground state configuration with the desired atom number  $N$  (b). The interaction strength  $E_B$  between both hyperfine components is set by an adiabatic ramp of the magnetic offset field  $B$  that is started once the ground state has been prepared. To study the nature of the ground state as a function of the interaction strength, we perform modulation spectroscopy on the system. We modulate the sample at some frequency  $\omega_{\text{ex}}$ , remove any atoms that were excited to higher energy levels and determine the remaining particle number in the trap using our accurate MOT counting scheme (c, see section 4.4.2). From the loss resonances that we observe in this way, we are able to reconstruct the complete low energy excitation spectrum of the mesoscopic Fermi gas (d).

thereby the potential depth to some value  $V_{\text{spill}}$  for a time of  $t_{\text{spill}} = 80$  ms, we remove all atoms initially trapped in higher energy levels. The final atom number as a function of the spill depth  $V_{\text{spill}}$  is obtained by transferring all the atoms back to the MOT once the spilling sequence is completed (see Figure 6.1 c). The integral of the total MOT fluorescence signal on a camera for a time of  $t_{\text{int}} = 1$  s leads to a particle count with almost perfect accuracy (see section 4.4.2). For non-interacting samples we observe plateaus that correspond to the shell structure of the 2D harmonic oscillator potential (see Figure 6.2 a). This allows us to set the desired atom number  $N$  of the final closed shell ground state, for example to  $3 + 3$  atoms (see Figure 6.1 b), by adjusting the spill depth  $V_{\text{spill}}$  appropriately.

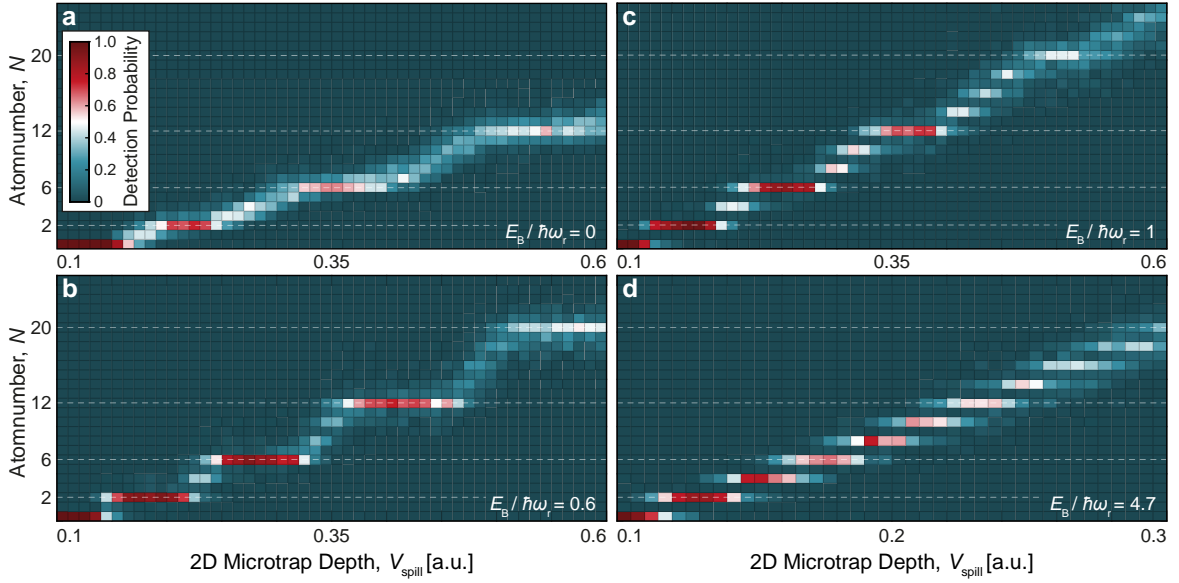


**Figure 6.2: Spilling at different attraction strengths.** The y-axis shows the probability of detecting  $N$  atoms remaining in the trap as a function of the final spill depth on the x-axis. The experiment is repeated 140 times for each setting of the final depth. In a weakly or non-interacting sample, we find stable plateaus for atom numbers that correspond to the closed-shell configurations of the harmonic oscillator, indicated by dashed white lines (a,b). When the attraction strength is increased until the binding energy dominates over the single particle gap  $E_B > E_{H0}$ , we find stable plateaus that are equally spaced at any even particle number. This is a strong indication for the emergence of pairing in the ground state as the interactions are increased.

### 6.1.1 Spilling with Interactions

Our preparation scheme allows us to gain some first qualitative insights into the nature of interacting ground states. To this end, we adiabatically ramp the magnetic field  $B$  to the desired final interaction strength setting  $E_B = 0, \dots, 5\hbar\omega_r$  even before the spilling process to the final atom number  $N$  is initiated. From the atom numbers for which we observe plateaus as a function of  $V_{\text{spill}}$  we can then infer the degeneracy of the energy levels of the interacting many-body state. In the non- or weakly-interacting regime ( $E_B < \hbar\omega_r$ ) pairing is suppressed by Pauli blocking and the degeneracy of energy levels in the many-body state is identical to that of the single particle 2D harmonic oscillator spectrum. Plateaus appear at numbers of  $N = 1 + 1, 3 + 3, 6 + 6$  or  $10 + 10$

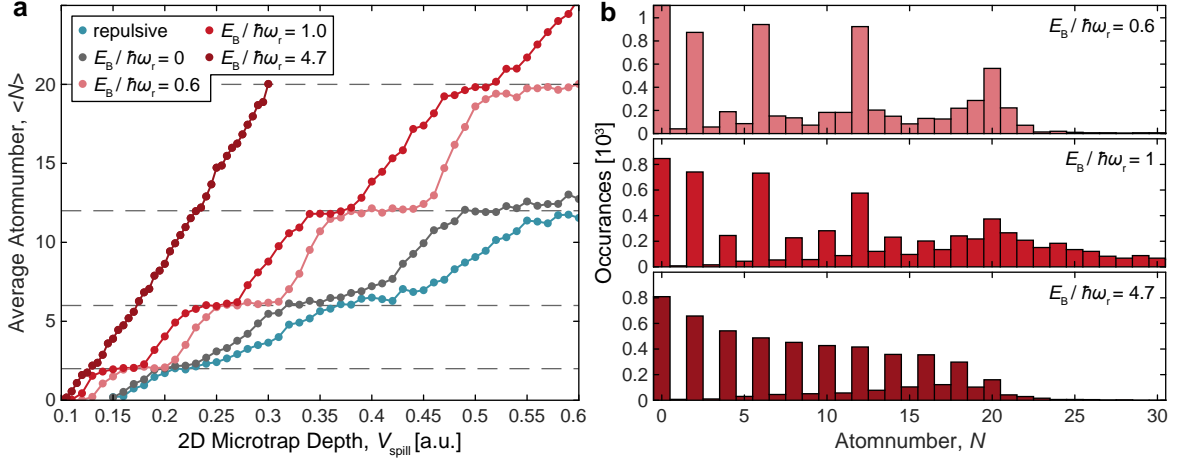


**Figure 6.3: Mean field interaction shift.** The average atom number  $\langle N \rangle$  as a function of the spill depth  $V_{\text{spill}}$  shows a strong dependence on the interaction strength (a). The number of atoms that remain trapped for the same optical potential depth increases significantly as the attraction is increased (black to dark red). For repulsive interactions we find the opposite shift, as expected (blue). A histogram of the detected atom numbers, integrated over all spill depths  $V_{\text{spill}}$ , clearly reveals the transition from the 2D harmonic oscillator shell structure (b, top) to a fully paired ground state (bottom).

atoms (see Figure 6.2 a). For weak attractive interactions, these plateaus remain stable and evidence for the presence of interactions can be observed only at the transitions between different plateaus when the spill level  $V_{\text{spill}}$  approaches the next bound energy level. Here, we find a strong correlation between particles tunnelling out of the trap, similar to what has been measured in 1D [Zür12b]. The probability of pair tunnelling is enhanced and odd particle numbers are strongly suppressed compared to the non-interacting state (see Figure 6.2 b).

When we increase the interacting strength that is present during the spilling process even further ( $E_B \gtrsim \hbar\omega_r$ ), the degeneracy of the energy levels of the ground state changes drastically (see Figure 6.2 c,d). The regions in which we observe the 2D harmonic oscillator shell atom numbers become smaller and smaller until they are replaced by a regularly spaced ladder of even atom numbers instead. This measurement indicates that pair formation is present in the system and that the ground state evolves to a gas of strongly bound molecules as the interactions are increased until they dominate over the single particle gap  $E_B \gg \hbar\omega_r$ .

The influence of strong attractive interactions is also revealed by comparing the absolute depths of the potential  $V_{\text{spill}}$  that are required for preparing the same atom number at different settings for  $E_B$  (see Figure 6.3 a). At the depth  $V_{\text{spill}} \approx 0.2$  where only a single harmonic oscillator level remains bound for a non interacting state and only two atoms stay in the trap after spilling (grey), we can prepare systems of almost ten atoms for our strongest interaction setting (dark red), for example. In a mean field picture, the attractive cloud acts as a second potential well for the atoms in addition to the optical confinement.

We have also taken measurements in the metastable repulsive branch (see Ref. [Zür12b]) that show an interaction shift in the opposite direction (see Figure 6.3 a, blue line). The measurement has been performed at an inverse scattering length of around  $l_z/a_{3D} \approx 4$ , where the effective repulsive coupling strength  $g \approx 0.3$  is rather small (see Figure 3.5). For larger repulsive interactions, we expect ferromagnetic correlations as a consequence of Hund's rule. In our system they would manifest themselves as additional plateaus that emerge for half filled shell configurations, for example with  $N = 4$  or  $N = 9$  atoms [Ron09]. When we keep increasing the repulsion in our experiment further, however, the system becomes unstable towards the decay into its lower ground state on the timescales that are required for our spilling process.

### 6.1.2 Interactions as a Feature

We use interactions during the spilling process not only to study the sample itself but also as a tool for improving the preparation cycle. Small attractive interactions preserve the shell structure and increase the preparation fidelity significantly (see Figure 6.2 b). Only by performing the spilling sequence at  $E_B/\hbar\omega_r = 0.6$ , we are able to achieve the fidelities of 93(3) %, 76(2) % and 50(2) % for the  $N = 3+3$ ,  $6+6$  and  $10+10$  closed shell configurations that have been reported previously. Stronger interactions, on the other hand, allow us to prepare any even atom number independently of the shell structure with fidelities between 80 % to 50 % for up to  $N = 7+7$  atoms (see Figure 6.2 d). This gives us access to open shell configurations in the experiment. Once the desired atom number  $N$  has been prepared and the optical depth is restored to its hold depth  $V_{\text{hold}}$ , we use an adiabatic magnetic field ramp to set  $E_B$  independent of the field  $B_{\text{spill}}$  and interactions during spilling.

In conclusion, we have found that interactions have a large influence on the many-body level spectrum in the trap. Qualitatively, we find strong indications for pair formation in the ground state as the interactions are increased far above the single particle gap  $E_{\text{HO}}$ . To gain a more quantitative understanding, especially about the nature of the ground state in the strongly correlated regime of intermediate interactions  $E_{\text{HO}} \sim E_B$  (see Figure 6.2 c), additional measurements are required. Following the

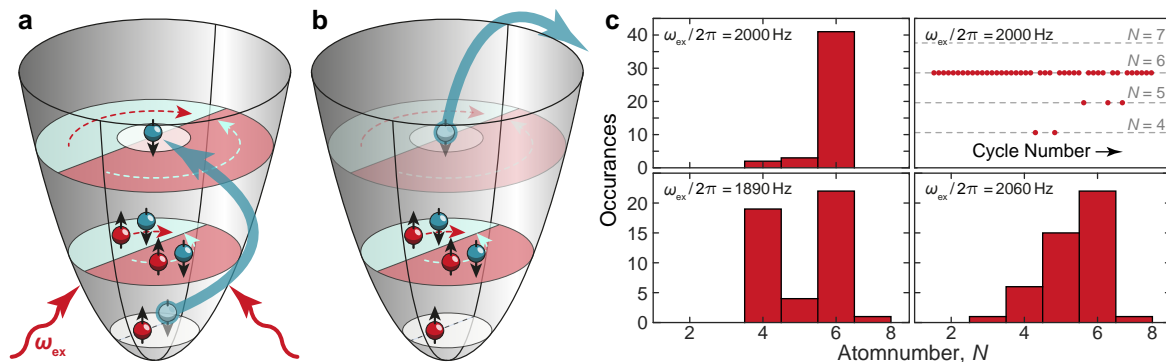


**Figure 6.4: Modulation spectroscopy.** We obtain the many-body energy level spectrum of the interacting mesoscopic Fermi gas in three steps: After the preparation of the ground state and an adiabatic ramp to the desired interaction strength  $E_B$ , the system is excited periodically at some frequency  $\omega_{\text{ex}}$  for a fixed time  $t_{\text{ex}}$ . (a). After the modulation, all the atoms that have been excited to higher harmonic oscillator shells are removed by a second spilling stage (b) and the remaining particles are counted (c). At each frequency setting, the experiment is repeated several times (c, top right). Three qualitatively different histograms of the set of particle numbers detected at various excitation frequencies are shown for example. Far away from excited energy levels in the spectrum, we primarily count  $N = 6$  remaining particles, indicating that the system remained in the ground state (top row). Excited state resonances appear as strong particle loss signals (lower row).

discussion in chapter 2, universal collective behaviour is generally expected in the low energy excitation spectrum of superfluids. As the next step to investigate the interacting closed-shell configurations, we therefore apply a modulation spectroscopy scheme to the Fermi gas.

## 6.2 Excitation Spectrum

We limit our spectroscopic measurements to closed-shell configurations. The interplay between gapped single particle spectrum and attractive interactions promises to give rise to particularly complex and interesting collective excitations in this case. We start by preparing the ground state of two filled shells and  $N = 3 + 3$  particles at small interaction strength of  $E_B = 0.6 \hbar\omega_r$ . This is followed by an adiabatic ramp of the magnetic offset field to the interaction strength  $E_B = 0, \dots, 2\hbar\omega_r$  we want to probe.

### 6.2.1 Experimental Sequence

To extract the many-body excitation spectrum, we introduce a small periodic perturbation at some fixed frequency  $\omega_{\text{ex}}$  or energy  $E_{\text{ex}} = \hbar\omega_{\text{ex}}$  to the sample. When the modulation is resonant to some higher energy state  $E'$  in the spectrum  $E_{\text{ex}} \approx E' - E_0$ , this leads to a finite transition probability into the excited state (see Figure 6.4 a). To detect the resonances, we apply our ground state preparation technique for a second time (see Figure 6.4 b). Atoms that have been excited to higher shells are removed and the remaining atoms are counted in the MOT (see Figure 6.4 c).

Different modulation schemes are available for our mesoscopic quantum gas. The choice of the type of periodic perturbation, described by a Hamiltonian  $\mathcal{H}'(t)$ , is important since it affects the coupling strength to excited levels  $|e\rangle$  via the transition matrix elements between ground and excited state  $\langle e | \mathcal{H}'(t) | g \rangle$ . Since we are interested in collective behaviour and interaction effects, we have chosen to modulate the interaction strength  $E_B$  of the system. The perturbation with a sinusoidal waveform has an amplitude of approximately  $\delta E_B / E_B = 2\%$  and is kept on for a duration of  $t_{\text{ex}} = 400$  ms. The modulation parameters have been determined by optimizing the signal of the particle loss resonances that we observe (see Figure 6.4 c). Since the perturbation is spatially isotropic, only monopole excitations between states with the same total angular momentum are driven. A comparison to other modulation schemes is found below in section 6.4.1.

Following the discussion in 3.2.8, the naive approach for the implementation of a periodic interaction strength perturbation is to make use of the Feshbach resonance and modulate the magnetic offset field  $B$ . However, we expect that the excitations in the many-body spectrum are at energies that are on the order of the single particle gap or larger  $\omega_{\text{ex}}/2\pi \gtrsim E_{\text{HO}}/h \approx 1000$  Hz. Magnetic field modulations with significant amplitudes are difficult to realize at these frequencies due to the large inductance of the coils in our experiment. In addition, due to the non-linear behaviour of the Feshbach resonance (see Figure 3.7), very different modulation amplitudes of the magnetic field  $\delta B/B$  would be required to keep the interaction modulation depth  $\delta E_B/E_B$  at each setting for  $E_B$  constant.

A preferable method is to modulate the axial confinement strength  $\omega_z$  instead. The axial confinement determines the size of the wavefunction in  $z$ -direction and therefore directly affects the binding energy  $E_B$  in the quasi-2D description we apply to our system (see equation (3.30)). Modulation frequencies of  $\omega_{\text{ex}} \ll \omega_z$  ensure that the wavefunction in  $z$ -direction follows adiabatically, no axial excitations are created and the quasi-2D description remains valid. A modulation of the depth of the SWT by 5% via the optical power is enough to achieve the desired perturbation of  $\delta E_B/E_B \approx 2\%$ . We have confirmed experimentally that the modulation of the magnetic field and the

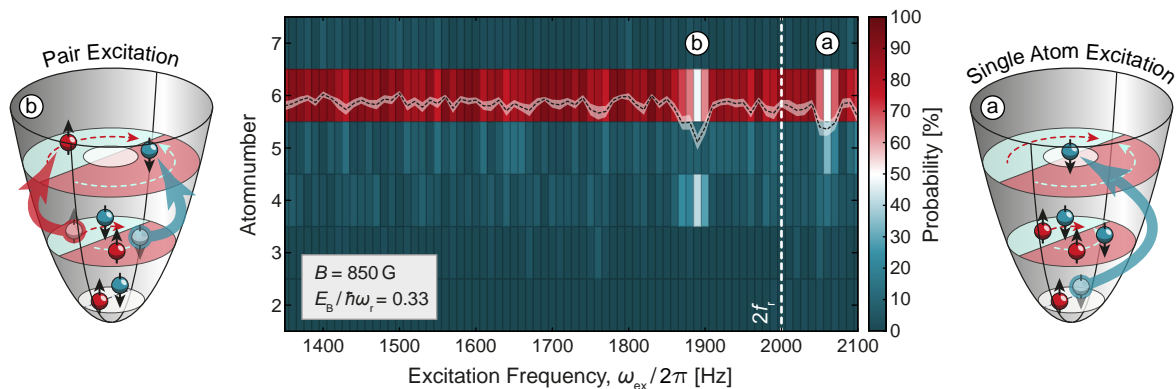


**Figure 6.5: Excitation spectrum of the interacting  $N = 3 + 3$  closed shell ground state.** We observe two clear resonances, above (a) and below (b) the lowest frequency monopole resonance in a non-interacting sample at  $\omega_{\text{ex}} = 2\omega_r$  (white dashed line). The first one corresponds to single particle excitations two shells up (a). It is shifted to larger energies by an attractive mean-field shift. The lower resonance corresponds to coherent pair excitations, indicated by the strong enhancement of the probability to detect four atoms  $P_4$  (b). Figure adapted from [Bay20a].

axial confinement lead to the same results.

### 6.2.2 Weakly Interacting Regime

The different atom number detection probabilities  $P_N$  as a function of the modulation frequency  $\omega_{\text{ex}}$  for a binding energy of  $E_B = 0.33\hbar\omega_r$  are shown in the spectrum in Figure 6.5. The probabilities are determined from a set of 45 repeated measurements at each frequency (see Figure 6.4 c, top right). Two clear atom loss resonances are visible in the spectrum. The white dashed line indicates the value of  $2\omega_r/2\pi = 2002$  Hz. This is the smallest frequency at which we expect monopole excitations starting from a non-interacting closed shell ground state. They correspond to the excitation of a single atom two shells up (see Figure 6.5 a). Excitations of a single atom by only one shell up, requiring an energy of only  $\Delta E = \hbar\omega_r$ , always change the angular momentum of the system and therefore do not couple to our modulation scheme (see Figure 2.2).

The higher resonance (a) is at  $\omega_{\text{ex}} = 2\pi \times 2060$  Hz, above the expected lowest non-interacting resonance position. This can be explained by the attractive mean-field shift we have also observed when spilling in the presence of attractive interactions (see Figure 6.3). The atom cloud acts as additional potential well, effectively increasing the

strength of the confinement for each atom. This leads to some additional interaction energy cost when exciting a single atom two shells up from the ground state into the more dilute excited state (see Figure 6.5 a). The probability of detecting four atoms corresponds to the square of the probability of detecting five atoms  $P_4 = 0.13\% \approx P_5^2$  with  $P_5 = 0.33\%$  (see Figure 6.4 c). This confirms that resonance (a) corresponds to the independent excitations of single atoms.

The lower resonance (b) is located at a frequency of  $\omega_{\text{ex}} = 2\pi \times 1890$  Hz, significantly below the lowest non-interaction monopole transition at  $\omega_{\text{ex}} = 2\omega_r$ . Even more striking is the atom number distribution we observe. At this frequency it is not possible to excite single atoms and  $P_5$  is not enhanced over the background. Instead, the modulation only produces single pairs of excited atoms, indicated by the strong increase of  $P_4$ . The lower resonance (b) corresponds to the coherent excitation of a pair of atoms one shell up (see Figure 6.5 b).

The simple mean-field model fails to explain the position of the lower resonance at  $\omega_{\text{ex}} < 2\omega_r$ . Even though the interactions are attractive, they reduce the cost of exciting a single pair compared to the non-interacting ground state. The effect can be explained by the interplay of shell structure and binding energy. In the weakly interacting regime  $E_B = 0.33\hbar\omega_r < E_{\text{HO}}$ , pairing is suppressed for closed shell configurations. No free states at the same energy are available for the atoms to increase their wavefunction overlap and form a pair. This is different for the excited state when a single pair is lifted from the second to the third shell (see Figure 6.5 b). The excited particles in the otherwise completely empty shell have several degenerate levels available to them that they can occupy without additional energy cost. Likewise, the remaining pairs in the second shell can increase their wavefunction overlap and gain binding energy by occupying the states that are now free. The pair excitation resonance is a genuine many-body effect that can only be understood by taking into account all the particles in the mesoscopic sample.

### 6.2.3 Interaction Dependence

The intuitive explanation for the frequency shift of the pair resonance holds only in the weakly interacting regime as long as the shell structure is important  $E_B < E_{\text{HO}}$ . To understand the evolution of the ground state as a function of the interactions in more detail, we make use of the Feshbach resonance to vary  $E_B$ . For each setting we obtain a spectrum like the one shown in Figure 6.5. We plot the atom loss coefficient, defined by the ratio between the probabilities of detecting four and six atoms  $P_4/P_6$ , in Figure 6.6. This quantity leads to a strong signal at the pair resonance frequency we want to track as a function of the interaction strength. At each setting for  $E_B$ , the data is normalized to the peak height of the pair correlation peak. The full dataset with the

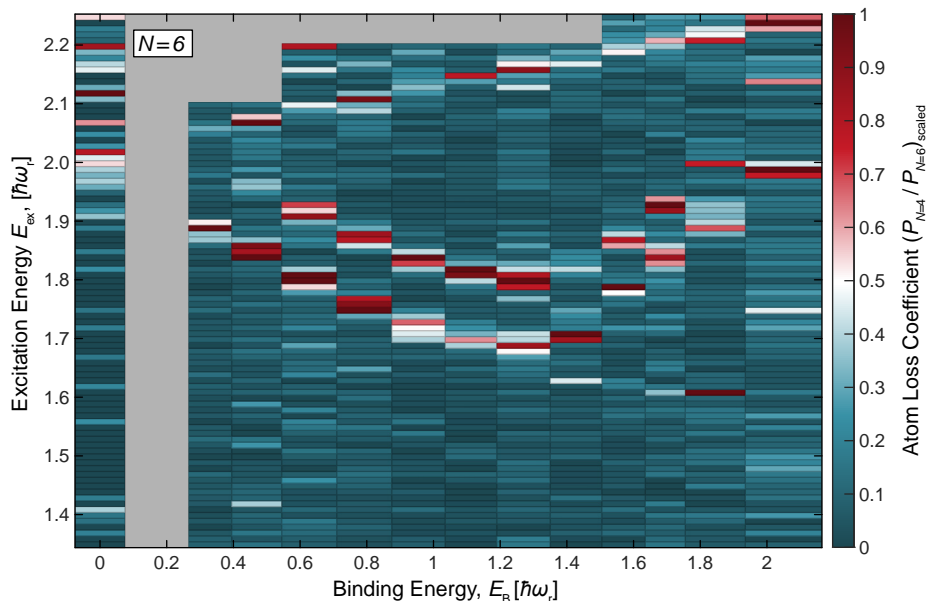


**Figure 6.6: Low energy spectrum of the  $N = 3 + 3$  closed shell ground state as a function of interaction strength.** The sample is excited by modulating the interaction strength for a fixed time, except for the data point at  $E_B = 0$  where the radial confinement is perturbed instead. We plot the normalized atom loss coefficient  $P_4/P_6$  to track the evolution of the different excitation branches. Since the data was taken outside the linear response regime, no direct conclusion about the coupling strength to the different excitation modes can be drawn. The higher single particle excitation branch increases monotonously with interactions as expected. The pair excitations  $\omega_{\text{ex}} < 2\omega_r$  behave non-monotonously and show a minimum when the binding energy approaches the single particle gap  $E_B \sim E_{\text{HO}}$ . Figure adapted from [Bay20a].

distribution of all atom numbers is shown in Figure 6.7 for completeness. The Feshbach resonance of  ${}^6\text{Li}$  does not allow us to access a small region between  $E_B \approx 0.1\hbar\omega_r$  and  $0.3\hbar\omega_r$  that is greyed out for this reason.

In Figure 6.6 we can follow the different excitation branches, starting from the weakly interacting limit. The single particle resonance at higher frequencies  $\omega_{\text{ex}} > 2\omega_r$  increases monotonously with the interaction strength. This behaviour agrees with the expectation of a larger mean-field shift for stronger attraction from our intuitive picture above. Surprisingly, the lower branches with  $\omega_{\text{ex}} < 2\omega_r$  show a completely different, non-monotonous behaviour instead. They correspond to coherent excitations of pairs

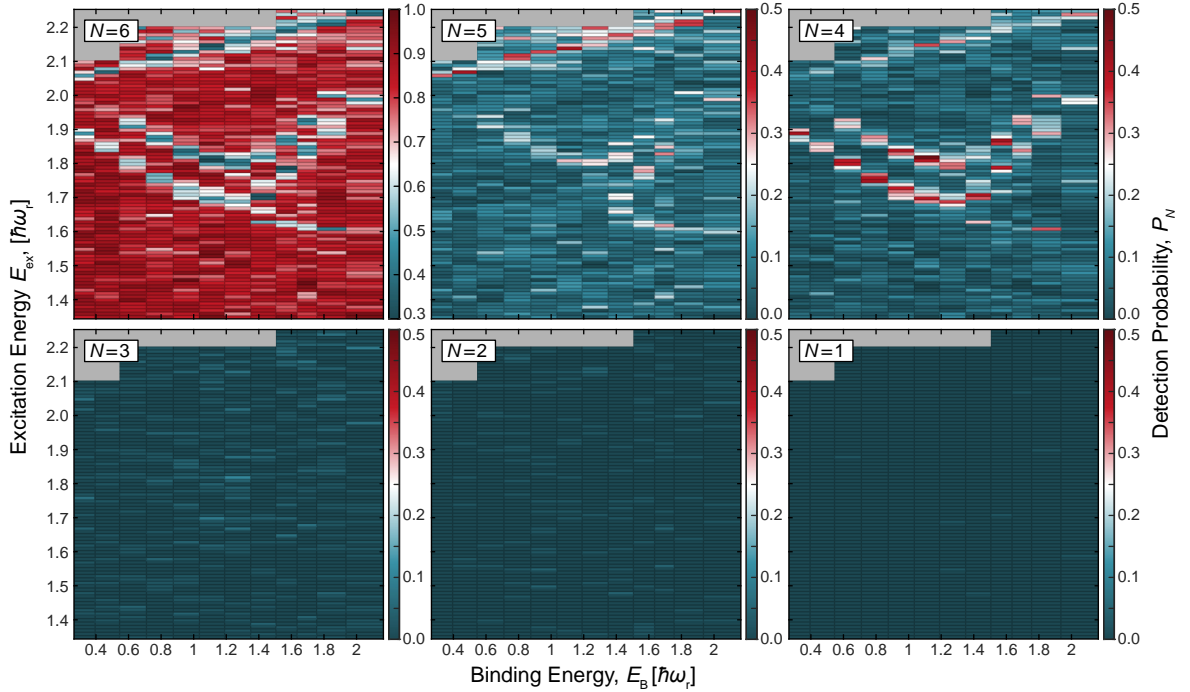


**Figure 6.7:** Atom number detection probabilities  $P_N$  in the two lowest shells after modulating the  $N = 3 + 3$  atom ground state. All the different excitation branches manifest themselves by a reduced probability of remaining in the ground state, corresponding to a reduction of  $P_6$ . The lower branches mainly consist of pair excitations that are visible as an enhancement of  $P_4$ . The higher single pair excitation lead to an independent loss of particles with most of the signal in  $P_5$  and  $P_4 \approx P_5^2$ . Figure adapted from [Bay20a].

with total angular momentum zero and  $\pm 2\hbar$  respectively. In Figure 6.5, we have only observed the lower of the two non-monotonous branches with zero angular momentum. The presence of the degenerate upper pair excitation branches with non-zero angular momentum will be discussed in more detail in section 6.3.

The remarkable behaviour of the pair excitation branches can be understood by starting from the weakly interacting limit. The particles gain binding energy by increasing their overlap using the degenerate empty states available in the excited state, as explained above. The energy gain increases with attraction strength, explaining the initial decrease of the pair excitation branch with increasing  $E_B$ . This picture breaks down when the binding energy approaches the single particle gap in the spectrum

$E_B \sim 1 \hbar\omega_r$ . Here, the pair excitation branches have a minimum and they start to increase with increasing attraction strength again. At large binding strengths it becomes energetically favourable even for the closed shell ground state to have an admixture of higher lying non-interacting oscillator levels to form pairs. Consequentially, the strength of pair correlation in the ground state increases significantly once the binding energy is on the order of or larger than the single particle spacing  $E_B > 1 \hbar\omega_r$ . The shell structure becomes less relevant and the ground state energy starts to decrease faster than that of the excited state when the attraction is increased. The non-monotonous behaviour of the pair excitation branch directly reveals how the nature of the ground state changes from a predominantly unpaired to a paired state in the different regimes  $E_B < E_{\text{HO}}$  and  $E_B > E_{\text{HO}}$ . We identify the position of the minimum with the critical binding energy  $E_B^{\text{C}} \approx 1.3\hbar\omega_r$ .

## 6.3 Many-Body Picture

To further support the qualitative explanations of our findings above, we have to connect the low energy excitation spectrum that we observe in our mesoscopic system to the many-body limit. In chapter 2, we have already discussed the infinite particle number limit of the closed shell configurations of the harmonic oscillator. Pairing is suppressed at weak binding energies and a quantum phase transition from a normal to a superfluid occurs at a finite critical binding strength  $E_B^{\text{C}}$  [Bru14]. In the normal phase the lowest energy modes in the spectrum correspond to coherent pair excitations. Their energy cost decreases until the excitation gap closes completely at the transition point  $E_B^{\text{C}}$  and the system spontaneously forms Cooper pairs. The superfluid phase has a universal excitation spectrum and the lowest mode corresponds to amplitude fluctuations of the order parameter with excitation energy  $\hbar\omega_{\text{ex}} = 2\Delta$ . This mode is generally also referred to as the Higgs mode (see Figure 2.7).

The Richardson solution, when applied to the  $N = 3 + 3$  particle system, provides some means to link our observations in the mesoscopic system to the macroscopic world. It predicts a spectrum that qualitatively matches what we observe in our experiment perfectly (see Figure 2.9) and converges towards the BCS solution when the particle number is increased. A more quantitative connection between experiment and theory requires a more exact calculation that relies on less rigorous approximations than the reduced BCS model.

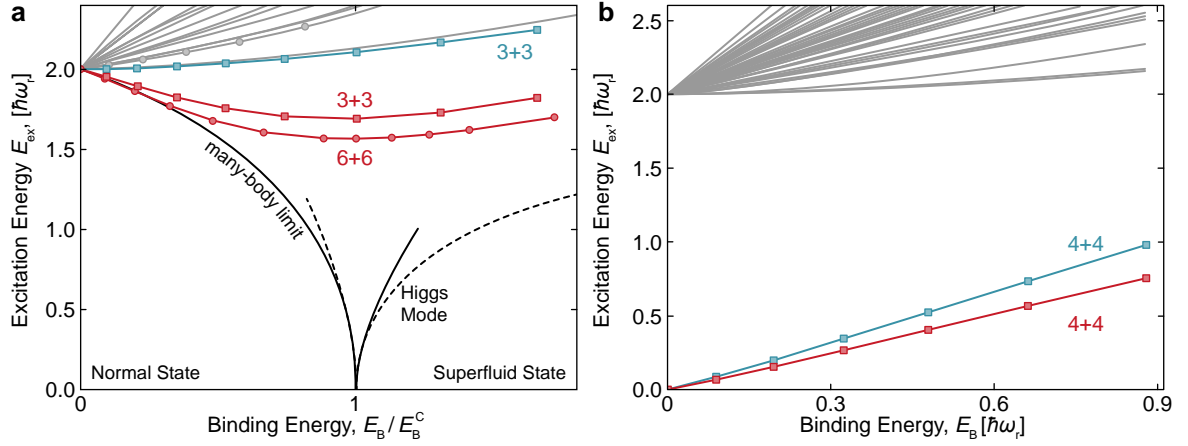


**Figure 6.8: Numerical solution for the excitation spectrum of the mesoscopic Fermi gas.** The lowest monopole excitations for closed shell configurations of  $N = 3 + 3$  (squares) and  $6 + 6$  (circles) particles are shown in (a). The black solid and dotted lines show numerical and analytical solutions of the many-body limit respectively [Bru14]. The blue and grey lines show additional single particle excitations at higher energies. The excitation modes in the mesoscopic system are the few-body precursors of the many-body spectrum and, in the superfluid regime, the Higgs mode. In (b) the gapless spectrum for the open shell configuration with  $N = 4 + 4$  atoms is shown as a comparison. Figure adapted from Ref. [Bje16] with permission.

### 6.3.1 Exact Diagonalization

In Ref. [Bje16] an exact numerical diagonalization of the microscopic Hamiltonian that describes our experiment (see equation (2.2)) is performed. This work also represents the first theoretical proposal of the measurements that we report in this chapter. The many-body excitation spectrum is calculated as a function of  $E_B$  and for  $N = 3 + 3$  and  $N = 6 + 6$  particles. Due to the exponential scaling of the Hilbert space, only a limited amount of harmonic oscillator shells is included and the many-body basis of non-interacting states is limited to some energy cut-off in addition. Already the next larger  $N = 10 + 10$  system is too large to achieve a complete numerical convergence as a function of the energy cut-off [Bje16].

The results of the numerical solutions for closed shell configurations are shown in Figure 6.8 together with the predictions for the many-body limit (black lines). The interaction strengths are normalized by the critical binding energies of  $E_B^C = 0.86 \hbar\omega_r$

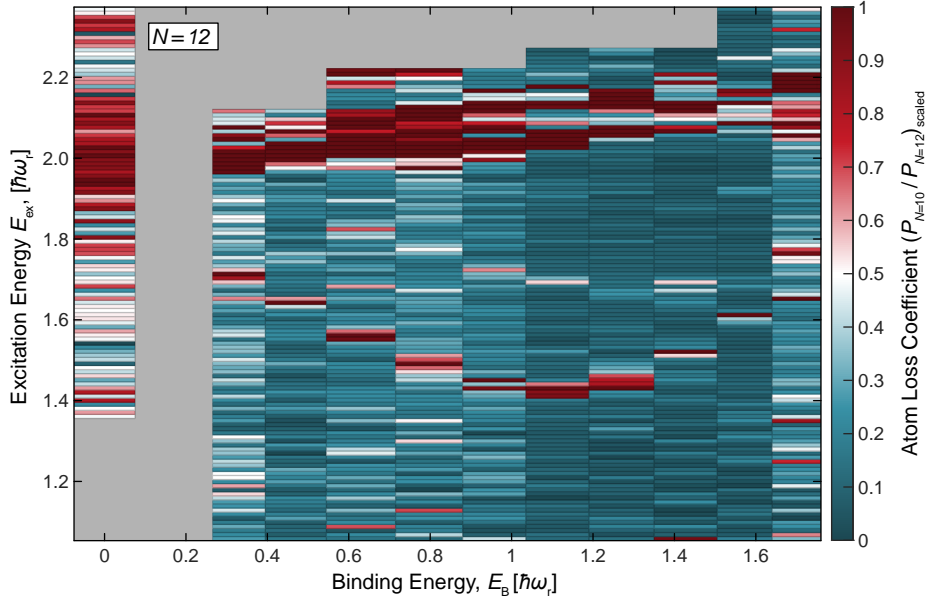


**Figure 6.9: Low energy spectrum of the  $N = 6 + 6$  closed shell configuration.** The sample is excited by modulating the interaction strength, except for the data point at  $E_B = 0$  where the radial confinement is perturbed instead. We plot the normalized atom loss coefficient, defined by the ratio of the probabilities of detecting ten and twelve atoms  $P_{10}/P_{12}$ , to track the evolution of the different excitation branches. The same qualitative behaviour as for  $3 + 3$  particles is observed with higher lying single particle- and non-monotonous pair excitation modes. Figure adapted from [Bay20a].

and  $E_B^C = 0.78 \hbar\omega_r$  for  $3 + 3$  and  $6 + 6$  particles respectively. The numerical predictions explain the behaviour of the non-monotonous branches in the spectrum: The observed pair excitations are the few-body precursors of the coherent low energy modes of the normal to superfluid phase transition. Compared to the mean-field solution in the many-body limit, the transition in the mesoscopic system is broadened and the gap in the spectrum does not close completely at  $E_B^C$ . As the particle number is increased, the numerical solution predicts a decrease of the minimal gap and a convergence towards the many-body solution. In addition, the critical binding energy moves towards smaller attraction strengths  $E_B^C \rightarrow 0$ .

All the qualitative features of the spectrum connected to the phase transition like the pair character and the non-monotonous interaction dependence of the lowest monopole mode can be observed in the mesoscopic system, starting already with only two filled

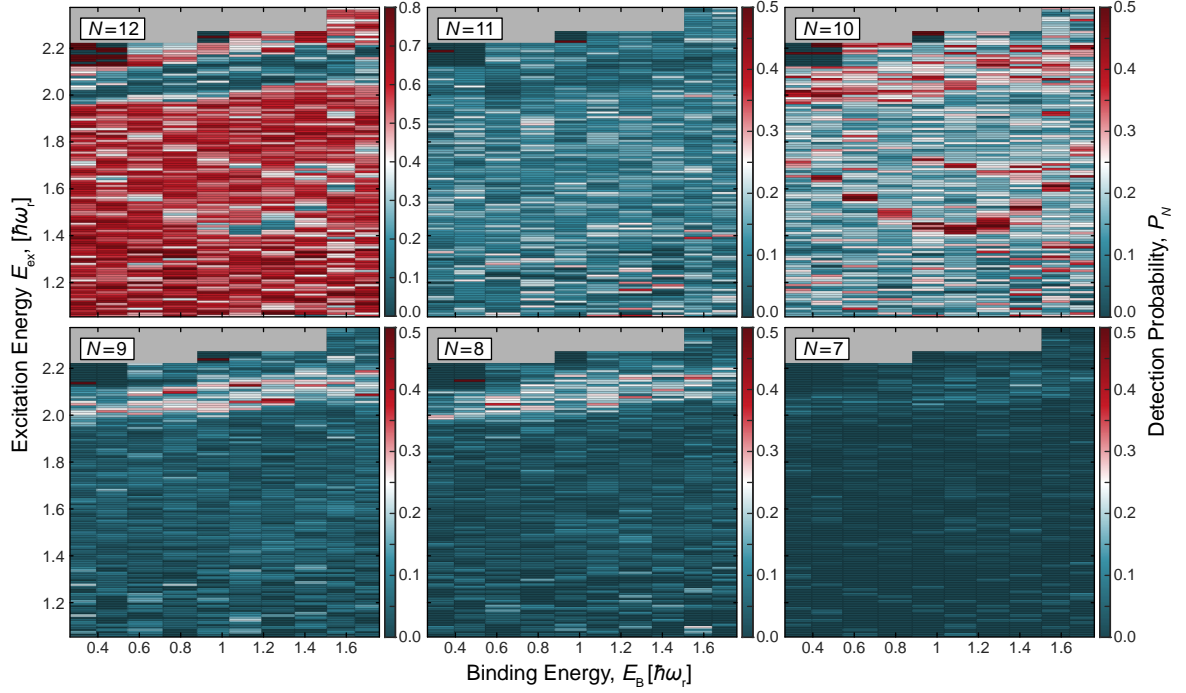


**Figure 6.10: Atom number detection probabilities  $P_N$  for the  $N = 6 + 6$  atom ground state.** All the different excitation branches manifest themselves by a reduced probability of remaining in the ground state, corresponding to a reduction of  $P_{12}$ . The lower branches mainly consist of pair excitations that are visible as an enhancement of  $P_{10}$ . The higher single pair excitations lead to independent loss of single atoms that is visible in  $P_{11}$  to  $P_7$ . Their average number depends on the modulation strength. Figure adapted from [Bay20a].

shell or  $N = 3 + 3$  particles. The predictions agree very well with our experiment for the same particle number (see Figure 6.6). In the strongly paired regime ( $E_B > E_B^C$ ) the lowest excitation we observe in our Fermi gas corresponds to the precursor of the amplitude or Higgs mode of the superfluid. In accordance with the theoretical predictions [Bru14], it is long lived and has a measured width of less than 10 Hz, consistent with Fourier broadening for our modulation time of  $t_{\text{ex}} = 400$  ms.

### 6.3.2 Filling the Next Shell

To confirm the picture that the lowest monopole modes act as the precursors of the many-body phase transition, we also perform measurements in the next larger closed

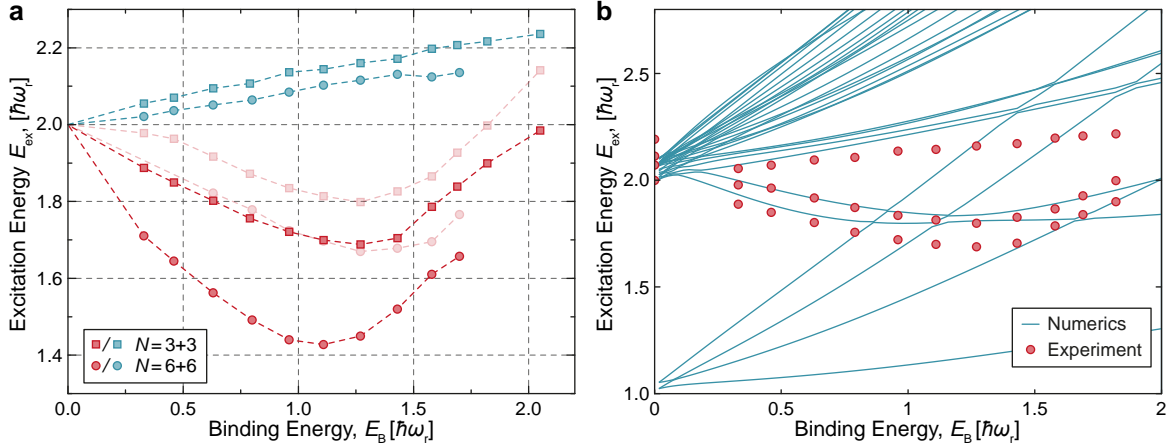


**Figure 6.11: Quantitative comparison of closed shell configurations with different particle numbers and to the theory.** We extract the centre position of the lowest single particle and pair excitations from Gaussian fits to the spectra (a). The minimal gap of the lowest pair excitation mode for the  $N = 6 + 6$  (red circles) system is significantly smaller than for  $3 + 3$  atoms (red squares) and the minimum is shifted to a smaller  $E_b^c$ . The excitation modes of pairs with angular momentum (light red) and of single particles (blue) are shown as a comparison. In (b) the experimental data for  $N = 3 + 3$  is compared to a numerical solution of the complete many-body spectrum that includes both anharmonicity and anisotropy of the trap. The presence of two non-monotonous excitation branches with zero and  $\pm 2\hbar$  angular momentum pairs respectively is correctly predicted by the numerical solution. Figure adapted from [Bay20a].

shell configuration, filled with  $N = 6 + 6$  particles. Apart from the atom number in the initial state, the experimental sequence is exactly the same. The resulting spectrum is shown in Figure 6.9 together with the full dataset including all relevant atom detection probabilities  $P_N$  in Figure 6.10.

Qualitatively, we find the same features as in the spectrum of the  $N = 3 + 3$  particle state. At higher frequencies  $\omega_{\text{ex}} > 2\omega_r$ , there is a dense cluster of single particle excitations. Their number is much larger than in the system with 2 filled shells as a result of the increased degeneracy of higher 2D harmonic oscillator levels. The lowest modes are non-monotonous and generated by pair excitations again (see  $P_{10}$  in Figure 6.10). For a quantitative comparison of the  $N = 6 + 6$  and  $N = 3 + 3$  spectra, we fit Gaussian peaks to each of the features in the spectrum. The centre frequencies

corresponding to the different excitation modes are extracted from the fit and shown in Figure 6.11 (a). We clearly observe the convergence towards the many-body limit, already for the first step from two to three filled shells. The minimal gap of the pair excitation modes decreases significantly and the location shifts to the left.

### 6.3.3 Numerical Modelling

The numerical solution in Figure 6.8 (a) from Ref. [Bje16] is based on the assumption of a perfectly harmonic and isotropic confinement. As a result of the exact radial symmetry, modes like the pair excitations with  $\pm 2\hbar$  that change the angular momentum are absent in the theoretical monopole spectrum. A more accurate model of our experiment can be obtained by taking the non-zero anharmonicity and anisotropy of the Gaussian optical potentials into account. From measurements of excitation spectra in the non-interacting system we estimate the anisotropy, defined as  $(\omega_x - \omega_y)/(\omega_x + \omega_y)$ , of our 2D-MT to be around 2%. The anharmonicity, defined by the energy difference between the transition between first to second and second to third shell respectively  $(E_{0 \rightarrow 1} - E_{1 \rightarrow 2})/E_{0 \rightarrow 1}$ , is on the order of 10% [Bay20a].

The full many-body level spectrum of the numerical solution for this more realistic potential for the  $N = 3 + 3$  system together with the experimental measurements are shown in Figure 6.11 (b). The presence of both the non-monotonous pair excitation branches is predicted correctly by the more advanced numerical solution. The model reveals that the upper branch is two-fold degenerate and confirms that the excitations correspond to pairs with an angular momentum of  $\pm 2\hbar$ . Several monotonous modes starting at  $E_{\text{ex}} = 1 \hbar\omega_r$  and crossing the spectrum from below are found in addition. They correspond to excitations of a single atom one shell up and change the angular momentum of the state by  $\pm\hbar$ .

Following the discussion in section 6.2.1, the many-body level spectrum alone is not enough to predict which modes appear in the experimental spectrum. We have to take into account the coupling of each of the excited states to the perturbation scheme. In Figure 6.12 we show the numerical spectrum weighted with the normalized transition matrix elements  $|\langle e | \mathcal{H}'(t) | g \rangle|^2$  for the periodic modulation of the interaction strength  $E_B$ . Both a completely isotropic (a) and an anisotropic (b) model potential are investigated. Their direct comparison fully explains the observations in our experiment. The broken radial symmetry leads to a coupling of the modulation scheme not only to monopole ( $\Delta L_z = 0$ ) but also to quadrupole excitations with  $\Delta L_z = \pm 2\hbar$ . The anisotropy is the reason we observe more than one non-monotonous pair branch in the experiment. The levels in the manifold starting at  $E_{\text{ex}} = 1$  with  $\Delta L_z = \pm 1\hbar$  are not excited on the other hand (to this end a modulation of the trap centre position  $x + \delta x(t)$  would be required).

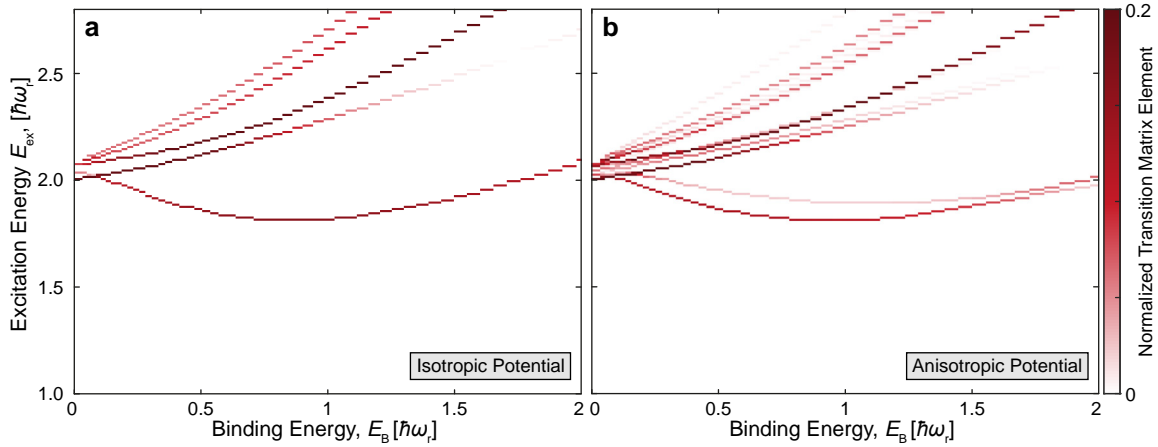


**Figure 6.12: Numerical calculation of the transition matrix elements for a modulation of the binding energy.** When we assume a completely isotropic model potential, the modulation leads to monopole excitations ( $\Delta L_z = 0$ ) alone and only the lowest of the pair excitation modes is observed (a). By introducing a small anisotropy of 2% the radial symmetry is broken. In this case the same modulation also couples to quadrupole excitations with  $\Delta L_z = \pm 2\hbar$  (b). This explains the observation of several non-monotonous modes in our experiment. Figure adapted from [Bay20a].

### 6.3.4 Limitations of the Model

The numerical model completely explains all of our measurements on a qualitative level. The quantitative agreement, however, is still not exact even after including the deviations from a harmonic potential to first order (see Figure 6.11 b). Several effects can explain the remaining discrepancies. First, compared to the initial solution in Ref. [Bje16], the slightly broken symmetry complicates the exact diagonalization procedure significantly [Bay20a]. Even after including up to ten million basis states for the  $N = 3 + 3$  system, full numerical convergence as a function of the shell number and cut-off energy can still not be observed (see Figure 6.13). The  $6 + 6$  particle system with broken radial symmetry is completely out of reach. The numerical model can be used to understand the essential features of the spectrum without providing exact quantitative predictions.

Regarding the experiment, there are several important approximations that have to be considered as well. The model potential used in the numerical calculation only considers the deviation from a harmonic potential to first order by matching the low

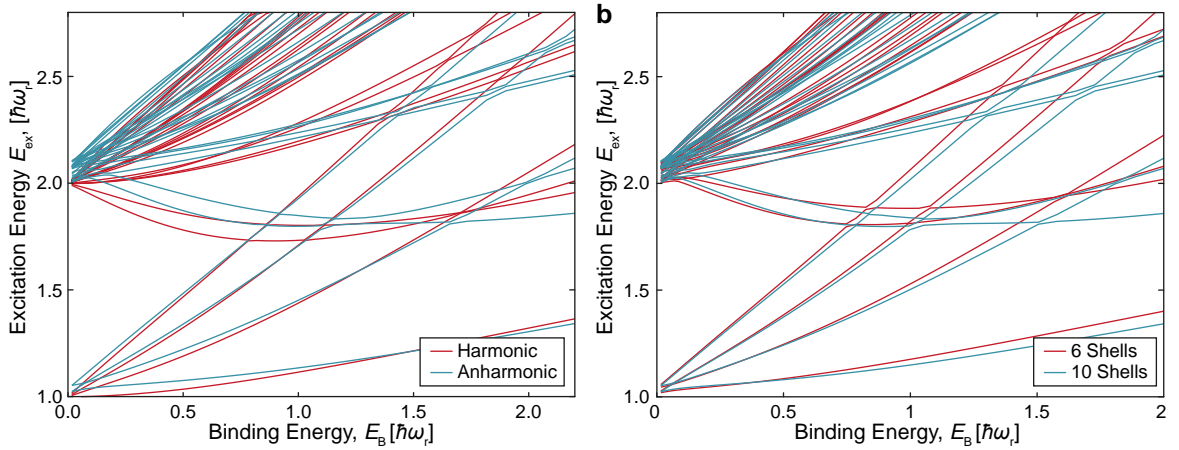


**Figure 6.13: Convergence of the numerical model as a function of shell number and energy cut-off.** The implementation of a small anharmonicity and anisotropy in the exact diagonalization lead to the coupling of many additional levels (a). This increases the computational complexity significantly. No full convergence of the quantitative values of the levels in the spectrum is observed as a function of the number of harmonic oscillator shells that are taken into account (b). As a result of the exponential scaling of the Hilbert space, it is not possible to increase the cut-off further by a significant amount. The data for the Figure has been provided by the authors from [Bje16].

energy non-interacting excitation spectrum to experimental data. Especially for higher oscillator levels ( $n \geq 4$ ), we expect that the differences between experimental and numerical potential are still significant. A much more detailed characterization of the trap in our experiment would be required to achieve a more precise agreement. Finally, the numerical model does not consider the presence of the third dimension in our experiment at all. With a moderate aspect ratio of  $\omega_z : \omega_r \approx 7 : 1$  residual excitations in axial direction become important as soon as the binding energy approaches the single particle gap in axial direction  $E_B \rightarrow \hbar\omega_z$ . Consistent with these considerations, we observe the largest difference between theory and experiment for largest attraction strengths.

In conclusion, we find that a quantitative numerical modelling of our experiment is very challenging. However, this does not affect the interpretation of our findings in any way. All the qualitative features that we find are robust to small variations in the microscopic parameters.

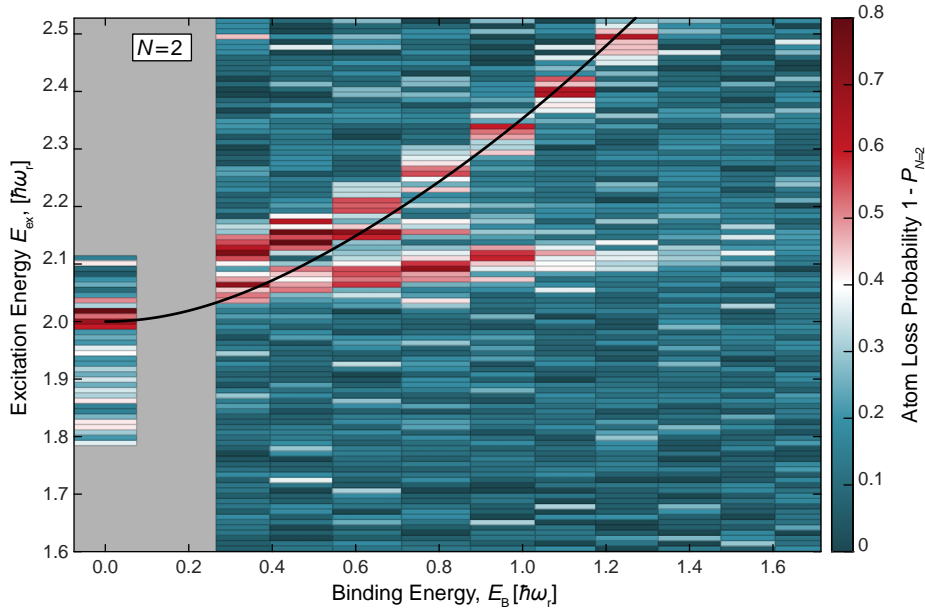


**Figure 6.14: Low energy spectrum of the  $N = 1 + 1$  closed shell configuration.** The sample is excited by modulating the interaction strength, except for the data point at  $E_B = 0$  where the radial confinement is perturbed instead. We plot the probability to excite the system above the ground state, given by  $1 - P_2$ . Two monotonous excitation branches, corresponding to the relative (upper mode) and centre of mass (lower mode) motion, can be observed. The black line indicates the exact analytical solution for two particles in a perfectly harmonic confinement (see equation (3.30)). Figure adapted from [Bay20a].

### 6.3.5 Two-Body Limit

We have studied the convergence towards the many-body limit by increasing the number of filled closed-shells in the ground state from two to three. It is instructive to also study the opposite direction and investigate the smallest possible system, consisting of a single filled shell or  $N = 1 + 1$  particles in the ground state. The measured spectrum for two atoms and modulation of the binding energy is shown in Figure 6.14. We observe two excitation modes, both rising monotonously with increasing binding energy. This demonstrates that the pair excitation we find for larger systems is a genuine many-body effect and that the presence of a (mesoscopic) Fermi surface is required for its emergence.

The two particle system can be divided into two single particle problems that describe

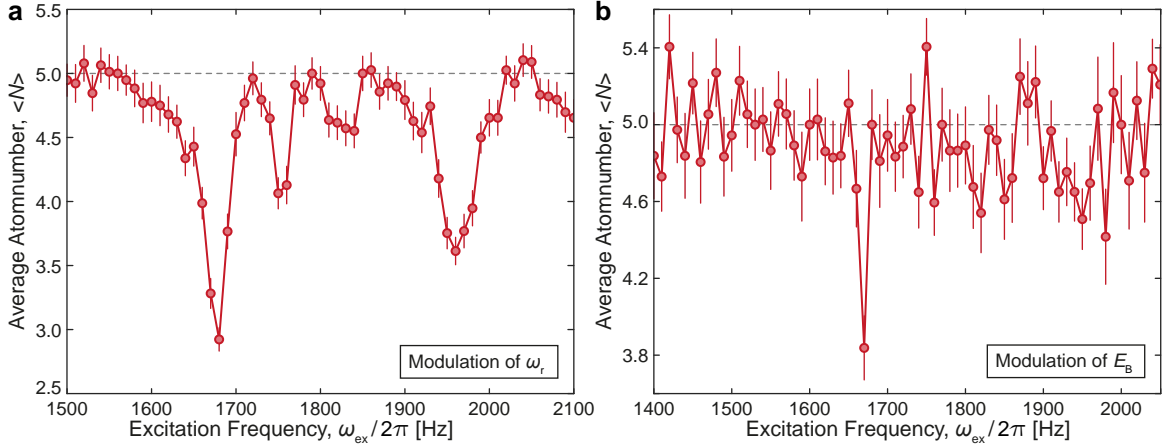


**Figure 6.15: Comparison between radial trap frequency  $\omega_r$  and Binding energy  $E_B$  modulation.** Both spectra were taken in the weakly interacting regime ( $E_B = 0.1 \hbar\omega_r$ ) with a radial trap frequency of  $\omega_r = 1660$  Hz. The modulation of the radial trap frequency (a) leads to a much stronger coupling to single particle excitations relative to the depth of the Higgs mode in the spectrum. This explains our choice of a binding energy modulation (b) for the study of emergent behaviour. Figure adapted from [Bay20a].

the relative and centre of mass motion respectively and that can be solved exactly (see section 3.2). The branch at higher excitation frequencies corresponds to an excitation of the relative motion. We compare it to the exact analytical solution for a harmonically confined system that depends on the measured radial and axial trap frequencies and the magnetic offset field (see equation (3.30)). We find good quantitative agreement between measurement and theory. The remaining discrepancies can be explained by the anharmonicity of our potential. Note that the excitation energy  $E_{\text{ex}}$  of the relative motion for the two-body ground state does not increase linearly with  $E_B$  since the excited state energy shifts with increasing attraction as well (see Figure 3.5 b). In contrast,  $E_B$  is defined with respect to the non-interacting energy level.

The second, lower lying branch corresponds to an excitation of the centre of mass motion. Its presence and interaction dependence can be explained with the anharmonicity of our potential. When the interaction strength is increased, the wavefunction becomes smaller. The atoms probe less of the deconfining  $r^4$ -term and the trap frequency  $\omega_r$  effectively increases. The same effect has been observed by performing a precise trap frequency calibration for a many-body system of  $N \approx 20\,000$  atoms trapped in the SWT (see chapter 8) [Hol18].

## 6.4 Different Modulation Schemes

All the spectroscopic measurements we have presented above make use of the exact same modulation scheme. The perturbation strength is far outside the linear response regime and does not allow us to draw conclusions about the coherence or coupling strength of different modes. In this last section we explore modulations of the modulation scheme in more detail.

### 6.4.1 Radial Trap Depth Modulation

The modulation of the axial confinement corresponds to a modulation of the binding energy  $E_B$ , one of the intrinsic energy scales of the mesoscopic Fermi gas. An alternative idea that occurs naturally as well is to instead perturb the second scale energy  $E_{H0} = \hbar\omega_r$  that determines the nature of the ground state. In Figure 6.15, we compare the measurements for both modulations schemes, taken in the weakly interacting regime ( $E_B = 0.1 \hbar\omega_r$ ) for the  $N = 3 + 3$  atom ground state.

The spectra clearly show that a modulation of  $E_B$  leads to a much stronger coupling to the pair excitation branches in relation to the higher single particle excitations. This agrees with the predictions obtained from the numerical model (see Figure 5 in Ref. [Bje16]) and can also be understood intuitively. A modulation of the radial confinement  $\omega_r$  corresponds to a perturbation with a single particle operator  $\mathcal{H}'(t) \propto r^2(t)$  that couples less to the coherent pair excitation involving many particles. This motivates our choice of modulating the attraction strength for all the spectroscopic measurements shown above.

### 6.4.2 Coherent Control

Up to this point, we have performed the modulation far outside the linear response regime with  $\delta E_B/E_B \approx 2\%$  and  $t_{\text{ex.}} = 400$  ms. A variation of the modulation strength allows us to gain further insight into the coherence and lifetime properties of the excited state. To this end, we drive the lowest pair excitation mode we observe at an attraction strength of  $E_B = 0.57\hbar\omega_r$  at its resonance frequency of  $\omega_{\text{ex}} = 1480$  Hz with different modulation times ( $t_{\text{ex.}}$ ). We observe a coherent oscillation between six and four atoms that dephases for long times (see Figure 6.16 a).

The measurement demonstrates that we are able to coherently create or remove pairs in the next higher shell. For future studies, this enables us to prepare the mesoscopic system not only in its ground- but also in highly correlated excited states. By fitting a damped sine function to the data (solid line), we obtain a Rabi rate of  $\Omega = 2\pi \times 8.0(1)$  Hz and a damping rate of  $\gamma = 4.5(5)$  Hz. The slow decay sets the lower limit for the

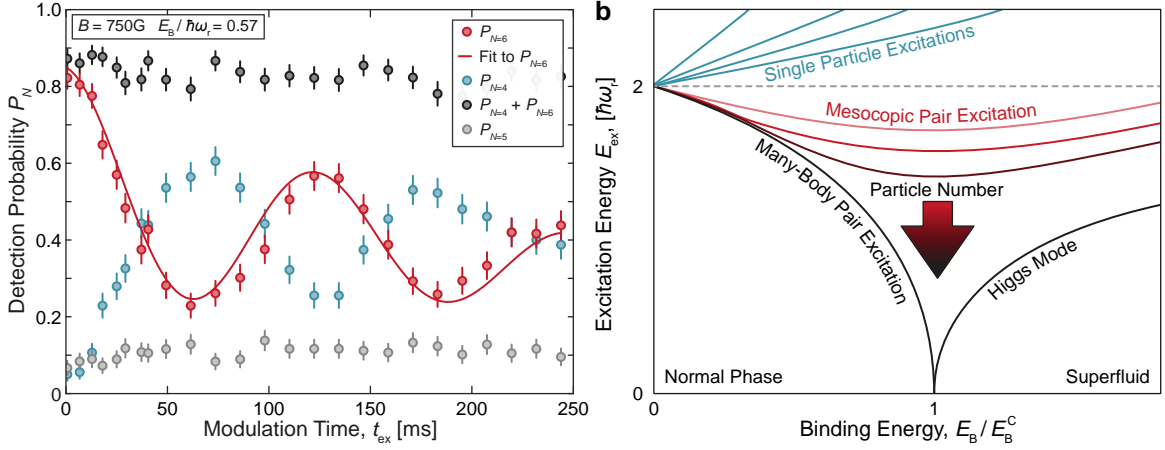


**Figure 6.16: Coherent excitation of the Higgs mode precursor.** We study the atom number detection probabilities  $P_N$  as a function of modulation time  $t_{\text{ex}}$  when exciting the  $N = 3 + 3$  system and the lowest pair mode frequency (a). For each time  $t_{\text{ex}}$ , the measurement is repeated 180 times. Consistent with a coherent pair oscillation, we observe a response to the perturbation only in  $P_4$  and  $P_6$ . The Rabi oscillations demonstrate that, to first order, the mesoscopic system can be treated as a two level system. The sketch in (b) summarizes the expected evolution of the low energy spectrum of the mesoscopic system towards the macroscopic limit. Figure adapted from [Bay20a].

lifetime of the Higgs mode precursor to  $\tau = 1/\gamma = 222(25)$  ms, more than a factor 300 longer than its transition period  $T = 2\pi/\omega_{\text{ex}} \approx 0.6$  ms. The long lifetime is a result of the isolated location of the pair excitation in energy and the discrete spectrum in general and does not require a particle hole symmetry (see chapter 2)[Bru14]. The remaining dephasing rate  $\gamma$  is consistent with small drifts of the trap frequency  $\omega_r$  we observe in our experiment. Finally, the results confirm that all our other measurements with  $t_{\text{ex}} = 400$  ms are far outside the linear response regime where the oscillations have completely dephased. This is consistent with the measured pair excitation probabilities of approximately  $P_{N-2} = P_N = 50\%$  for the various spectra (see Figure 6.7).

## 6.5 Conclusion

In conclusion, we have demonstrated that only a few interacting particles in a mesoscopic system are enough to observe emergent collective behaviour and the precursor

of a quantum phase transition from a normal to a superfluid state. When increasing the particle number, the sample evolves smoothly towards the many-body limit (see Figure 6.16 b) and no additional qualitative changes, for example for  $N = 10 + 10$  particles, are expected. In the strongly paired regime ( $E_B > E_B^C$ ), the pair excitation can be associated with a Higgs mode that is present as a universal feature of the low energy spectrum of macroscopic superfluids. Distinct Goldstone modes on the other hand can not be observed in our small Fermi gas. They are generated by phase fluctuations of the order parameter (see Figure 2.4) and become relevant only once the pair size or coherence length is smaller than the system size. This is equivalent to the limit where the many-body gap is much larger than the single particle gap in the spectrum  $\Delta \gg E_{\text{HO}}$  [Bru01].

The measurements in this chapter demonstrate the richness of emergent collective behaviour present in mesoscopic systems and starting already at the smallest sizes. They are obtained, however, by accurate atom number counts alone and their interpretation relies on a precise comparison to exact numerical solutions. To study fermionic superfluidity and Cooper pairing at a much more fundamental level, independent of theoretical calculations, we apply our fluorescence imaging scheme to interacting samples in the next step. As has been demonstrated in chapter 5, it allows us to access the full momentum distribution with a resolution far below the typical inter-particle spacing. This unique capability enables us to access the pairing correlations that emerge in the ground state as a function of the attraction strength directly, as we will see in the next chapter.



# 7

## Observation of Cooper Pairs

Correlation measurements are a fundamental tool to analyse quantum many-body systems [Alt04; Sch17]. In chapter 5, we have observed how the Pauli principle manifests itself through higher order density correlations in a gas of non-interacting fermions [Hol21b]. Phase transitions, for example between an insulating and a superfluid phase of neutral atoms in an optical lattice, can be identified directly through density-density correlation measurements in real or momentum space [Alt06]. However, the amount of the available information scales exponentially with the system size [Fla12]. It is therefore essential to identify and detect the correlations that most efficiently describe the state of matter to be studied [Zac20].

In the case of conventional superconductors, it took almost fifty years after their discovery [Van10] before the BCS theory was formulated as the first microscopic model explaining the effect [Bar57]. The key to the solution, found just one year before, is a mechanism by which bound states can form for two Fermions (a *Cooper pair*) on top of a Fermi sea starting already with infinitesimally small attraction strengths [Coo56]. It was soon understood that pairing correlations are, more generally, the fundamental ingredient to fermionic superfluidity and superconductivity [Yan62]. Experimental discoveries in conventional superconductors like the isotope effect [Max50; Rey51] indicated that the electron-phonon coupling is the origin for attractive interactions between the negatively charged electrons. For many other strongly correlated fermionic materials like high- $T_C$  superconductors, however, it is an ongoing challenge to find a microscopic explanation. It is believed that genuine fermionic correlations between itinerant electrons play an important role but the exact pairing mechanism remains unknown [Lee06; Zho21].

In the previous chapter, we have presented the detection of a precursor of a quantum phase transition from a normal to a superfluid in our mesoscopic Fermi gas [Bay20a]. The measurement demonstrates that the emergence of complex collective behaviour can be observed in interacting systems starting at the smallest scales. The observations were enabled by our deterministic preparation technique and an accurate counting of

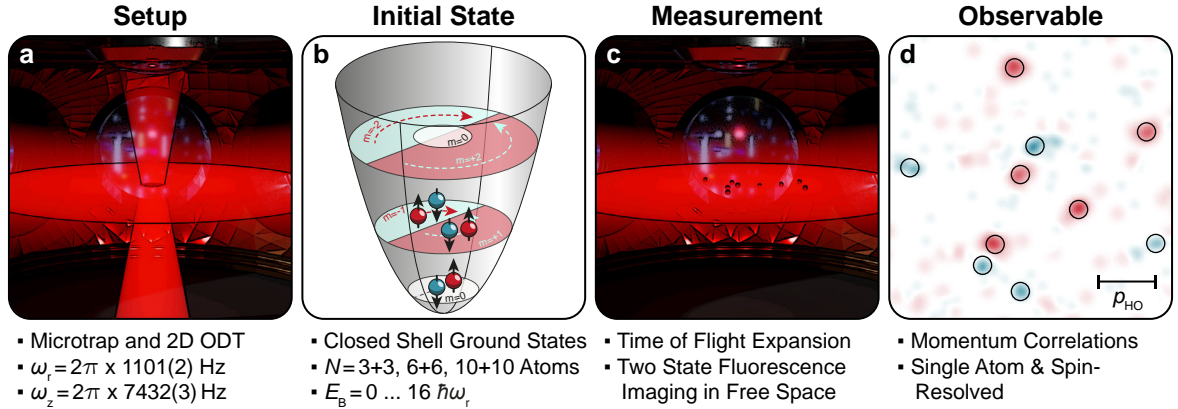


**Figure 7.1: Experimental sequence for the observation of Cooper pairs.** The state is initialized by preparing closed shell ground state configurations with up to  $N = 10+10$  atoms in the 2D-MT (a). The interaction strength  $E_B$  between both hyperfine components is set by an adiabatic ramp of the magnetic offset field  $B$  that is started once the ground state has been prepared (b). To study the nature of the ground state as a function of the interaction strength, we apply our TOF imaging scheme to the system (c). We instantaneously switch off both interactions and radial confinement and let the wavefunction expand in the 2D plane formed by the SWT. After the TOF, we detect the momentum of each atom on our camera by applying the single atom resolved fluorescence scheme to each spin state separately and in quick succession (d).

the atom number after exciting the sample and spilling to the ground state. The interpretation of the detected many-body spectra relied on a precise comparison to exact numerical calculations and in this way only indirectly gave us insight into the nature of the ground state. In this chapter, our goal is to go beyond counting the number of atoms and gain direct access to the fundamental pairing correlations that characterize the mesoscopic superfluid precursor. This allows us to extract information about our system much more efficiently and enables us to study the ground state independently of numerical predictions.

Dilute samples of ultracold neutral atoms are an ideal platform for studying higher order density correlations [Blo08; Blo12]. Even without single particle resolved imaging methods, spin resolved density correlations can be accessed in the atomic noise of an expanding gas [Alt04]. This method has been applied in a large variety of quantum gas experiments, revealing bosonic and fermionic correlations [Rom06; Jel07] as well as pairing [Gre05; Ten21] or phase transitions [Föl05; Spi07] through the correlation

measurements. With the development of quantum gas microscopy, access to single atom resolved in-situ density correlations has become a routine approach to study lattice systems and the Hubbard model [Bak09; She10; Par16; Koe20].

In this chapter, we present measurements that pioneer the study of single particle resolved density correlations in spatially continuous quantum gases. From a technical viewpoint the results represent the culmination of all the experimental capabilities we have developed through the measurements described in the previous chapters. We start with samples of up to  $N = 10 + 10$  Fermions prepared in the closed shell configurations of the 2D harmonic oscillator potential. Our fluorescence imaging technique allows us to extract the full single atom and spin resolved momentum distribution of the ground state at any desired interaction strength. In the weakly interacting regime, we directly observe Cooper pairs in our mesoscopic 2D Fermi gas. They are identified by positive correlations that emerge between particles with opposite momenta and spin at the Fermi surface. When the attractions are further increased, we observe how the pair character changes gradually and we find correlations also inside the Fermi sea. This indicates that there is a transition from Cooper pairs to more tightly bound molecules that form independently of the Fermi sea.

Our measurements demonstrate that pair correlations, as the fundamental ingredient to superfluidity, can be accessed directly in interacting systems of mesoscopic size. We extend the scope of quantum gas microscopy from lattices to continuous systems and momentum space. Together with the highly programmable environment, our work establishes a new pathway to study strongly interacting Fermi systems in general. We can now address many questions that have been raised in nuclear, atomic or condensed matter physics (see chapter 9). This chapter is based on the publication in Ref. [Hol21a].

## 7.1 Spin Resolved Imaging

For the initialization of the sample, we proceed analogously to the experiments discussed in detail in the previous chapters (see section 4.2.7). We start by spilling to the closed-shell ground state configurations with  $N = 3 + 3$ ,  $6 + 6$  or  $10 + 10$  atoms of hyperfine components  $|1\rangle$  and  $|3\rangle$  in the 2D-MT. Once the correct atom number is prepared, we ramp the magnetic offset field adiabatically to a final value  $B_0$  that sets the desired interaction strength  $E_B = 0, \dots, 16\hbar\omega_r$  (see Figure 7.1 a,b). Since we are interested in the correlations of the ground state itself, no further modulation is required and we can immediately start the imaging sequence once the sample has been prepared. The detection procedure can be separated into two parts. First, a free TOF expansion is used to increase the cloud size by a factor of approximately 50 and to map

the in-situ momentum of each particle on its final position (see section 4.4.6). Second, our fluorescence imaging scheme is used to record the position of each single atom with high detection fidelity and spin resolution on the EM-CCD camera (see section 4.4.3).

### 7.1.1 TOF Imaging Sequence

The TOF imaging scheme, described in detail in section 4.4.6, enables us to access the single particle and spin resolved momentum distribution of the ground state (see Figure 7.1 c,d). While the general concept remains the same as for the study of Pauli crystals (see section 5.1.2), important modifications are required in the case of interacting samples. We begin by switching off the MT that confines the gas radially. This leads to a quick radial expansion of the wavefunction in the remaining potential given by the superposition of the optical SWT with  $\omega_{\text{opt}} = 2\pi \times 19.1(10)$  Hz and the magnetic confinement with  $\omega_{\text{mag}} = 2\pi \times 12.6(10)$  Hz. A ballistic TOF expansion maps the in-situ momentum of each atom onto its final position after an expansion  $\mathbf{p}_i \rightarrow \mathbf{r}'_i$  of a quarter trap period in the harmonic confinement  $t_{\text{TOF}} = T/4$ . The true in-situ momentum distribution is obtained only when no scattering events occur during the expansion. However, for the interacting states studied here, the collision rates in the initial state are on the order of  $\nu \gtrsim 10$  kHz and much too large for the required TOF of  $t_{\text{TOF}} \approx 9$  ms. We therefore have to suppress the scattering events by reducing the interaction strength between both hyperfine components once the TOF expansion starts.

### 7.1.2 Interaction Switch-Off

The projection of the many-body wavefunction into a non-interacting state has to be instantaneous to enable us to measure the genuine momentum distribution of the in-situ state. For scattering rates of up to  $\nu \approx 50$  kHz in the initial sample, a switch-off time on the order of  $T_\pi \lesssim 1/\nu = 20$   $\mu\text{s}$  is required. The magnetic offset field coils fail to meet these requirements and therefore it is not feasible to make use of the Feshbach resonance for this purpose. Instead, we drive a spin flip to change from the initial state of atoms in hyperfine components  $|1\rangle |3\rangle$  to a  $|1\rangle |4\rangle$  mixture. A pair of Raman lasers allows us to drive this transition quasi-instantaneously in  $T_\pi = 330$  ns for all atoms initially in state  $|3\rangle$  simultaneously (see section 4.3). The spin flip is therefore almost two orders of magnitude faster than required.

There is no Feshbach resonance between the states  $|1\rangle$  and  $|4\rangle$  (see section 3.3.2) and all our observations are consistent with the scattering length  $a_{14}$  being close to zero. We have, for example, measured the spectrum of a  $N = 1 + 1$  system consisting of this hyperfine mixture in the 2D harmonic oscillator trap (see Figure 3.5). The first excited state shows no significant energy shift away from  $\omega_{\text{ex}} = 2\omega_r$ . As a result, we

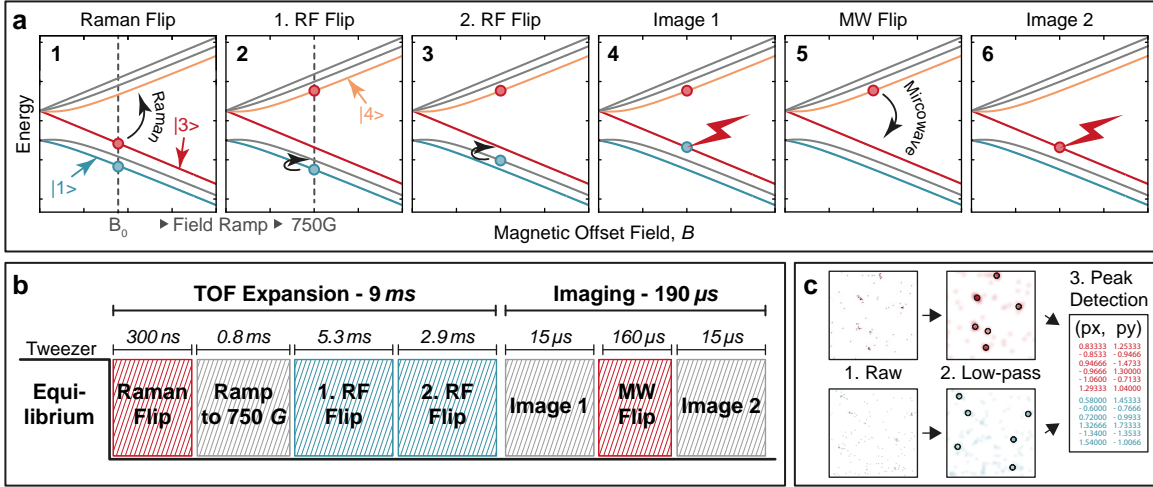


**Figure 7.2: Sketch of the imaging scheme for interacting samples.** The TOF sequence is initiated by removing the radial confinement provided by the optical MT. At the same time, a Raman transition into the  $|1\rangle$   $|4\rangle$  mixture is driven to quasi-instantaneously switch off all collisions (a, 1). A set of RF Landau-Zener sweeps is used in the following to prepare the system for imaging (a, 2-3). We make use of the closed imaging transition of hyperfine state  $|3\rangle$  for both initial states. The duration of the initial Raman transfer  $T_\pi = 330$  ns is chosen as fast as technically possible to prevent the atoms from scattering during the expansion (b). The Landau-Zener sweeps are optimized for the best possible fidelity in the total available expansion time  $T_{\text{TOF}} = 9$  ms. The duration of the MW flip between both images is set by the frame rate of the camera. In each experimental cycle we obtain two raw binary images, one for each of the two spin components (c). They are analysed by applying a low pass filter followed by a simple peak detection algorithm. Figure taken from [Hol21a].

can set an upper limit for the scattering length from the precision of our measurement as  $|a_{14}| < 500a_0$ , where  $a_0$  is the Bohr radius. The small absolute value for  $a_{14}$  together with the quasi-instantaneous spin flip ensures that collisions during the TOF expansion are negligible. We estimate that a maximum of one scattering event occurs in 50 experimental cycles for the  $N = 6 + 6$  closed-shell configuration.

The full sequence of spin flips used during the TOF expansion is shown in Figure 7.2. After the Raman transfer to the non-interacting state, we ramp the magnetic offset field from the value  $B_0$ , used to set the interaction strength  $E_B$  in the initial state, to

$B = 750$  G in  $t_B = 0.8$  ms (see Figure 7.2 a,b). The magnetic field ramp ensures that the remaining part of the imaging sequence is completely independent of the initial field  $B_0$  and improves the following spin transfer fidelities significantly. Since the atoms are already in states  $|1\rangle$  and  $|4\rangle$  at this point, the magnetic field ramp has no effect on the collision rate and the system remains non-interacting.

As the next step, we prepare the sample for our fluorescence imaging scheme (see section 4.4.3). Two counter-propagating illumination beams excite the  ${}^6\text{Li}$  atoms in one of the spin states and we collect the fluorescence light on our EM-CCD camera. The two spin components are resolved by taking two images in quick succession (see Figure 7.2 b,c). Without the implementation of a more complex repumping scheme, the highest atom detection fidelities are obtained for the closed imaging transition of state  $|3\rangle$  [Ber18]. Therefore, we use a set of RF and MW Landau-Zener sweeps to transfer each of the two hyperfine components to state  $|3\rangle$  prior to its detection. The first image allows us to determine the position  $\mathbf{r}'_{i,\uparrow}$  of all atoms initially in state  $|1\rangle$  after the TOF. Likewise, the second image shows the atoms initially in hyperfine level  $|3\rangle$ . The atoms of the second spin component rest in state  $|4\rangle$  while the first image is taken. Therefore, they are detuned by many-orders of magnitude ( $\sim 2$  GHz) compared to the natural linewidth of the imaging transition ( $\sim 6$  MHz) and do not scatter any photons from the illumination lasers that are switched on and resonant to level  $|3\rangle$  during that time.

### 7.1.3 Data Analysis

In each experimental run, we obtain two binary images, corresponding to the two hyperfine components  $|1\rangle$  and  $|3\rangle$  in the initial state. We analyse the images by applying a low pass filter and a peak detection algorithm (see Figure 7.2 c). Peaks with an amplitude above a given threshold are identified as atoms and their location is recorded (see section 4.4.3). This leads to a set of final atom locations  $\mathbf{r}'_{i,\uparrow}$  and  $\mathbf{r}'_{i,\downarrow}$  ( $i = 1, \dots, N$ ) for each experimental repetition.

In the first set of measurements, we only continue to analyse images where the correct total number of atoms  $N = N_\uparrow + N_\downarrow$  has been detected. This leads to postselection rates of only  $\approx 5\%$  for the  $N = 6 + 6$  atom ground state, significantly lower than what would be expected, for example from the Pauli crystal measurements (see section 5.1.3). The reason is the low fidelity of the simultaneous Raman transfer of six atoms in state  $|3\rangle$  to state  $|4\rangle$  of only  $\approx 10\%$  at the beginning of the detection sequence. The spin flip fidelity is currently limited by technical issues that have to be studied in more detail in the future. Since preparation and imaging scheme are completely independent in our experiment, the low postselection rate does not affect the interpretation of our data. The small fidelity simply increases the runtime required to obtain the same target

number of images where all atoms have been detected.

After the TOF expansion, the final positions of the atoms on the camera  $\mathbf{r}'_{i,\sigma}$  correspond to a projection of the many-body wavefunction in momentum space. For interacting initial states we cannot get additional access to the real space in-situ density distribution with our expansion scheme (in contrast to the Pauli crystal measurements where both bases are equivalent, see section 5.1.2). To study fermionic superfluidity momentum space imaging is advantageous, however, since it allows us to access the relevant correlations, like Cooper pairs, directly. In chapter 9 we introduce an enhanced expansion scheme to extract in-situ density correlations with single atom resolution in addition.

The mapping between final position  $\mathbf{r}'_i$  and in-situ momentum  $\mathbf{p}_i$  is slightly more complex in the interacting case compared to the Pauli crystal measurements. The atoms transferred to state  $|4\rangle$  at the beginning of the detection sequence expand in a low-field seeking state. The other component remains in the high-field seeking lower manifold. The combined trapping potentials during the expansion are therefore given by the sum and difference of the optical and magnetic confinements respectively  $\omega_{\text{TOF}}^2 \approx \omega_{\text{opt}}^2 \pm \omega_{\text{mag}}^2$ . In addition, due to the small delay between both images, the expansion times for each spin component are slightly different with  $t_{\text{tof},\uparrow} = 9$  ms and  $t_{\text{tof},\downarrow} = 9.2$  ms. To obtain the correct map  $\mathbf{r}'_{i,\sigma} \rightarrow \mathbf{p}_{i,\sigma}$  in both cases, we numerically solve the full equations of motion for the ballistic expansion. The solution also takes into account the Gaussian shape of the optical trap. It allows us to accurately convert the measured positions to the same in-situ momentum coordinate basis  $\mathbf{r}'_{i,\uparrow}, \mathbf{r}'_{i,\downarrow} \rightarrow \mathbf{p}_{i,\sigma}$  and to express them in natural units of the 2D harmonic oscillator potential  $p_{\text{HO}}$ .

### 7.1.4 Characteristic Scales

The harmonic confinement in radial direction  $\omega_r = 2\pi \times 1101(2)$  Hz defines a natural momentum scale  $p_{\text{HO}} = \sqrt{\hbar m \omega_r}$  for the system, where  $m$  is the mass of the  ${}^6\text{Li}$  atoms. The Fermi energy of the ground state is  $E_{\text{F}} = (n_{\text{F}} + 1) \hbar \omega_r$ , where  $n_{\text{F}} = \sqrt{2N + 1/4} - 3/2$  denotes the principal quantum number of the highest filled harmonic oscillator level and  $N = 1, 3, 6, \dots$  is the single-spin atom number. We define the Fermi momentum according to its continuum equation as  $p_{\text{F}} = \sqrt{2mE_{\text{F}}} = \sqrt{2(n_{\text{F}} + 1)} p_{\text{HO}}$ . For our mesoscopic system the momentum distribution of the harmonic oscillator states at the Fermi surface (i.e. with energy  $E_i = E_{\text{F}}$ ) is rather broad, with a width on the order of  $p_{\text{HO}}$ . Therefore, our definition of  $p_{\text{F}}$  is not unique and, in contrast to  $E_{\text{F}}$ , an unambiguous definition is not possible. Nevertheless, the microscopic sample can be characterized by two distinct momentum scales  $p_{\text{HO}}$  and  $p_{\text{F}}$  and the introduction of  $p_{\text{F}}$  is useful even for small particle numbers. Our choice ensures that the correct value is

approached in the infinite particle limit  $N \rightarrow \infty$  and when a LDA becomes applicable.

In conclusion, our imaging scheme allows us to obtain a projection of the full spin and single particle resolved momentum distribution of the interacting many-body wavefunction in each experimental cycle. The measurements correspond to a set of  $N = N_\uparrow + N_\downarrow$  momentum values  $\mathbf{p}_{i,\sigma}$  and therefore contain much more information than the atom counts collected in the previous chapter. Density correlations in momentum space of any order can be calculated from the images directly. The resolution of the setup for atoms in the same spin component was already studied in detail in section 5.1.4 and is, with  $d_{\min} \approx 0.2 p_{\text{HO}}$ , far below the typical inter-particle spacing. Atoms in different spin components are detected on separate images and can be resolved independently of their distance. The accuracy with which the momentum of a single atom can be determined is on the order of the PSF given by  $0.1 p_{\text{HO}}$  (see section 4.4.5).

## 7.2 Momentum Correlations

To study the nature of the ground state of our mesoscopic Fermi gas as a function of the interaction strength, we take 1000 samples of the momentum wavefunction at each setting for  $E_{\text{B}}$  (see Figure 7.3). The images are postselected only for the correct total number of atoms in each state.

### 7.2.1 Second Order Correlations

To search for pairing correlations, a natural choice is to start with the second order density correlation function  $\mathcal{C}^{(2)}$  for opposite spins, defined as:

$$\mathcal{C}^{(2)}(\mathbf{p}_\uparrow, \mathbf{p}_\downarrow) = \langle n(\mathbf{p}_\uparrow)n(\mathbf{p}_\downarrow) \rangle - \langle n(\mathbf{p}_\uparrow) \rangle \langle n(\mathbf{p}_\downarrow) \rangle. \quad (7.1)$$

Here,  $n$  is the density operator and  $\langle \dots \rangle$  denotes the average over all images. The correlation function  $\mathcal{C}^{(2)}$  expresses the conditional probability of detecting a spin up particle with momentum  $\mathbf{p}_\uparrow$  given that a reference spin down atom was detected at  $\mathbf{p}_\downarrow$ . We subtract the trivial contribution from single particle densities  $\langle n(\mathbf{p}_\uparrow) \rangle \langle n(\mathbf{p}_\downarrow) \rangle$  to the distribution in our definition. In 2D, second order density correlations depend on four coordinates. To visualize the data, they have to be processed further.

### 7.2.2 Relative and Centre of Mass Coordinates

A first possibility that appears naturally is to transform the data to relative and centre of mass coordinates  $\mathcal{C}^{(2)}(\mathbf{p}_\uparrow, \mathbf{p}_\downarrow) \rightarrow \mathcal{C}^{(2)}(\mathbf{p}_{\text{R}}, \mathbf{p}_{\text{C}})$ , where  $\mathbf{p}_{\text{R}} = \mathbf{p}_\uparrow - \mathbf{p}_\downarrow$  and  $\mathbf{p}_{\text{C}} = (\mathbf{p}_\uparrow + \mathbf{p}_\downarrow)/2$ . A 2D correlation function can be obtained, for example, by integrating over

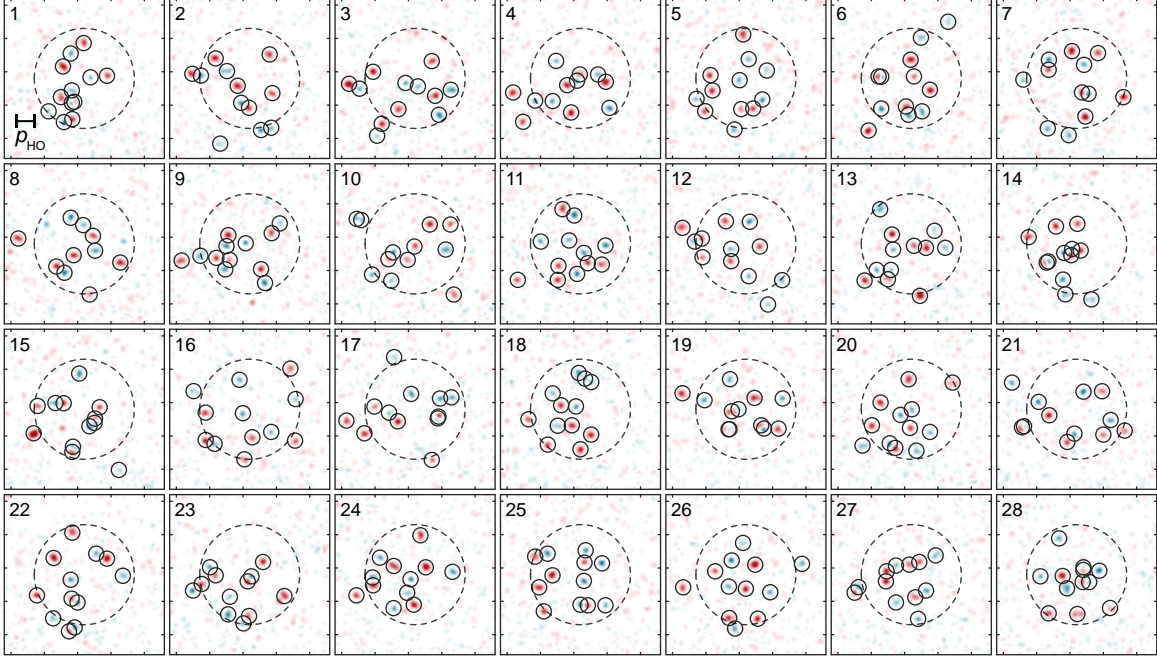


**Figure 7.3: Samples of the  $N = 6 + 6$  wavefunction at  $E_B = 1.97\hbar\omega_r$  in momentum space.** The images have been postselected for the correct number of atoms in each state. The dashed circle indicates the Fermi momentum  $p_F = \sqrt{6} p_{HO}$ . There are many images where particles with opposite spin and momenta are detected close to the Fermi surface (5,6,10,16,...). Figure taken from [Hol21a].

either of the variables. We define the pair correlation functions in relative and centre of mass momentum coordinates as

$$\begin{aligned} \mathcal{C}_R^{(2)}(\mathbf{p}_R) &= \int d\mathbf{p}_C \mathcal{C}^{(2)}(\mathbf{p}_R, \mathbf{p}_C), \\ \mathcal{C}_C^{(2)}(\mathbf{p}_C) &= \int d\mathbf{p}_R \mathcal{C}^{(2)}(\mathbf{p}_R, \mathbf{p}_C). \end{aligned} \quad (7.2)$$

They illustrate at which relative ( $\mathbf{p}_R$ ) and centre of mass ( $\mathbf{p}_C$ ) momenta pairs consisting of one spin up and one spin down atom are more frequently detected.

In Figure 7.4, the measured pair correlation functions for the  $N = 6 + 6$  closed-shell ground state configuration are shown as a function of the interaction strength  $E_B$ . In the non-interacting limit  $E_B = 0$ , no significant signal above the background from single particle densities is detected. Both spin components are completely uncorrelated as expected (a, f). This is different, when the attraction is increased. Significant

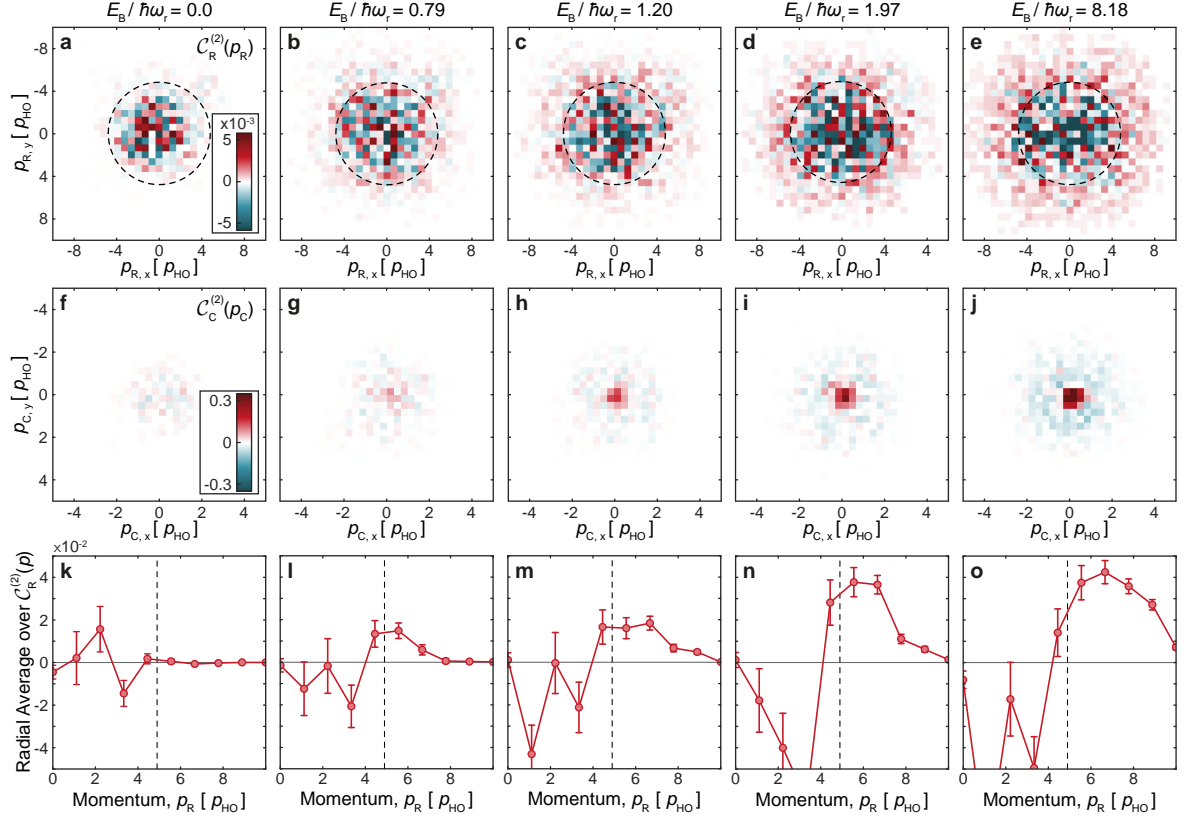


**Figure 7.4: Second order momentum correlations in relative and centre of mass coordinates for the  $N = 6 + 6$  particle ground state.** The 2D pair correlation functions  $\mathcal{C}_R(\mathbf{p}_R)$  and  $\mathcal{C}_C(\mathbf{p}_C)$  as a function of the interaction strength  $E_B$  are shown in (a-e) and (f-h) respectively. The dashed circles indicate the value of twice the Fermi momentum  $2p_F$ . In panels (k-o), we show the radial average of the relative pair correlation function (a-e) in addition. Figure taken from [Hol21a].

positive correlations are measured for pairs with a relative momentum around twice the Fermi surface  $p_R \gtrsim 2p_F$  (b-e) and with zero centre of mass momentum  $p_C \approx 0$  (g-j). The weight of the peak increases monotonously with increasing interaction strength  $E_B$ . For small relative momenta  $p_R < 2p_F$  and large centre of mass momenta  $p_C \gg 0$  we find small negative correlations, indicating a reduction of detected pairs with these properties compared to what would be expected from the cloud density alone.

The measurements demonstrate how pairing and collective behaviour emerge in the mesoscopic Fermi gas as the attraction strength is increased. In the previous chapter,

we have observed the precursor of a normal to superfluid phase transition indirectly by accessing the low energy excitation spectrum of the same system. The momentum space imaging allows us to directly access the pair correlations in the ground state as the fundamental ingredient of superfluidity and it reveals the emergent behaviour by a sharp peak at zero centre of mass momentum (see Figure 7.4 f-j).

The measured pair correlations are completely radially symmetric as expected for the geometry of our 2D trap. The width of the centre of mass momentum distribution of the pairs can be explained by the finite size of our system and is given by  $\approx 1/2 p_{\text{HO}}$ , in agreement with bosons of twice the atomic mass  $M_{\text{pair}} = 2m$  in the harmonic oscillator ground state (see section 5.1.3). In relative coordinates, the positive correlations start to appear at twice the Fermi momentum  $p_{\text{R}} \approx 2p_{\text{F}}$  (see Figure 7.4 k-m). This, together with the small centre of mass momentum, indicates that pairing is localized at the Fermi surface. For larger binding energies, positive correlations are present also at much larger relative momenta  $p_{\text{R}} \gg 2p_{\text{F}}$  (see Figure 7.4 m-o). This indicates that a transition to more tightly bound molecules occurs.

The fixed particle number, in contrast to a grand canonical ensemble, explains the negative signal at smaller relative momenta: positive correlations at one location always go hand in hand with negative correlations at a different location in momentum space. The total particle number has to be conserved. From the visualization of  $\mathcal{C}^{(2)}$  in Figure 7.4 alone, it is difficult to decide if particles inside the Fermi surface are paired as well. The relative angle between the spin up and down atoms is not taken into account. In addition, the positive correlations in relative coordinates  $\mathcal{C}_{\text{R}}^{(2)}$  are spread out over a large area in momentum space, reducing the signal to noise ratio. To reveal the character of pair correlations directly, a different representation of the four dimensional (4D) correlation function  $\mathcal{C}^{(2)}$  is required.

### 7.2.3 Cooper Pairs and Molecules

An alternative visualization of the correlation function  $\mathcal{C}^{(2)}$  can be obtained by fixing the position of the spin down particle to some reference momentum  $\mathbf{p}_{\downarrow} \rightarrow \bar{\mathbf{p}}_{\downarrow}$ . For each choice of the reference momentum  $\bar{\mathbf{p}}_{\downarrow}$  we obtain a different 2D slice of the 4D correlation function  $\mathcal{C}^{(2)}(\mathbf{p}_{\uparrow}, \mathbf{p}_{\downarrow}) \rightarrow \mathcal{C}_{\bar{\mathbf{p}}_{\downarrow}}^{(2)}(\mathbf{p}_{\uparrow})$ . In Figure 7.5, the data are shown as a function of the interaction strength  $E_{\text{B}}$  and for the  $N = 6 + 6$  closed shell ground state configuration. Here, we have taken advantage of the radial symmetry of our system to improve the signal to noise ratio as explained in the following.

It is useful to transform the data to polar coordinates, denoted as  $\mathbf{p} \rightarrow (p, \phi)$ , such that  $\mathcal{C}^{(2)}(\mathbf{p}_{\uparrow}, \mathbf{p}_{\downarrow}) \rightarrow \mathcal{C}^{(2)}(p_{\uparrow}, \phi_{\uparrow}, p_{\downarrow}, \phi_{\downarrow})$ . As a result of the radial symmetry of our mesoscopic system, the correlation function depends only on the relative angle between both

particles  $\Delta\phi = \phi_\uparrow - \phi_\downarrow$  but not on the absolute values of  $\phi_\uparrow$  and  $\phi_\downarrow$ . All the points with the same  $p_\uparrow$ ,  $p_\downarrow$  and  $\Delta\phi$ , are equivalent and the second order density correlations can be expressed as  $\mathcal{C}^{(2)}(p_\uparrow, \phi_\uparrow, p_\downarrow, \phi_\downarrow) \equiv \mathcal{C}^{(2)}(p_\uparrow, p_\downarrow, \Delta\phi)$ . Finally, we fix the position of the reference particle to some range in momentum space  $p_\downarrow \rightarrow \bar{p}_\downarrow \in [p_1, p_2]$ , as explained above, and obtain:

$$\mathcal{C}_{\bar{p}_\downarrow}^{(2)}(p_\uparrow, \Delta\phi) = \int_{p_1}^{p_2} \int_0^{2\pi} \int_0^{2\pi} \mathcal{C}^{(2)}(p_\uparrow, \phi'_\uparrow, p'_\downarrow, \phi'_\downarrow) \delta(\Delta\phi - (\phi'_\uparrow - \phi'_\downarrow)) p'_\downarrow dp'_\downarrow d\phi'_\downarrow d\phi'_\uparrow. \quad (7.3)$$

The 2D density plots of  $\mathcal{C}_{\bar{p}_\downarrow}^{(2)}$  in Figure 7.5 express at which momentum  $p_\uparrow$  and relative angle  $\Delta\phi$  a detection of a spin up particle is enhanced, given that a spin down atom is located in a momentum range  $\bar{p}_\downarrow$  and at angle  $\bar{\phi} = 0$ . The black cross in each image indicates the average momentum of the spin down particle, averaged over all images that contribute to the given momentum range (i.e. where an atom has been detected in the range  $[p_1, p_2]$  indicated by the black horizontal bars). We display two different momentum bins for the reference particle inside the Fermi sea  $\bar{p}_\downarrow \in [0.5 p_{\text{HO}}, 1.5 p_{\text{HO}}]$  (a-e) and at the Fermi surface  $\bar{p}_\downarrow \in [2 p_{\text{HO}}, 3 p_{\text{HO}}]$  (f-j). The dashed circles indicate the location of the Fermi surface for the  $N = 6 + 6$  particle ground state  $p_{\text{F}} = \sqrt{6} p_{\text{HO}}$ .

The measurements reveal how the character of pairing in the ground state is affected as a function of the interacting strength. For small binding energies  $E_{\text{B}} \lesssim E_{\text{F}}$  correlations are strongly suppressed inside the Fermi sea (see Figure 7.5 a-d). At the Fermi surface however, significant positive correlations appear as soon as the binding energy reaches the order of the single particle gap  $E_{\text{B}} \sim E_{\text{HO}}$  (f-i). A significant surplus of particles with opposite momentum to each other  $\mathbf{p}_\uparrow = -\mathbf{p}_\downarrow$  or  $\Delta\phi = \pi$  and located at the Fermi surface  $p_{\uparrow, \downarrow} \approx p_{\text{F}}$  is detected. These features allow us to identify Cooper pairs that we can observe directly in the ground state of our strongly correlated mesoscopic Fermi gas.

When increasing the attraction strength even further ( $E_{\text{B}} \gg E_{\text{F}}$ ), the weight in the correlation peaks increases significantly (see Figure 7.5 i-j). We observe how pair correlations emerge also inside the Fermi sea  $p_{\uparrow, \downarrow} < p_{\text{F}}$  (d,e). This indicates that a transition from Cooper pairing at the Fermi surface to more tightly bound molecules takes place. We observe the mesoscopic precursor of the 2D BCS-BEC crossover in the ground state (see section 2.2.4). To ensure that the pairs remain 2D and the condition  $E_{\text{B}} < \hbar\omega_z$  remains fulfilled, we have reduced the radial confinement to  $\omega_r = 2\pi \times 343(5)$  Hz for all measurements in the molecular regime.

### 7.2.4 Mesoscopic Cooper pairs

The density-density correlation function  $\mathcal{C}^{(2)}$  allows us to identify Cooper- and molecular pairing in the ground state of our mesoscopic Fermi gas through positive correlations

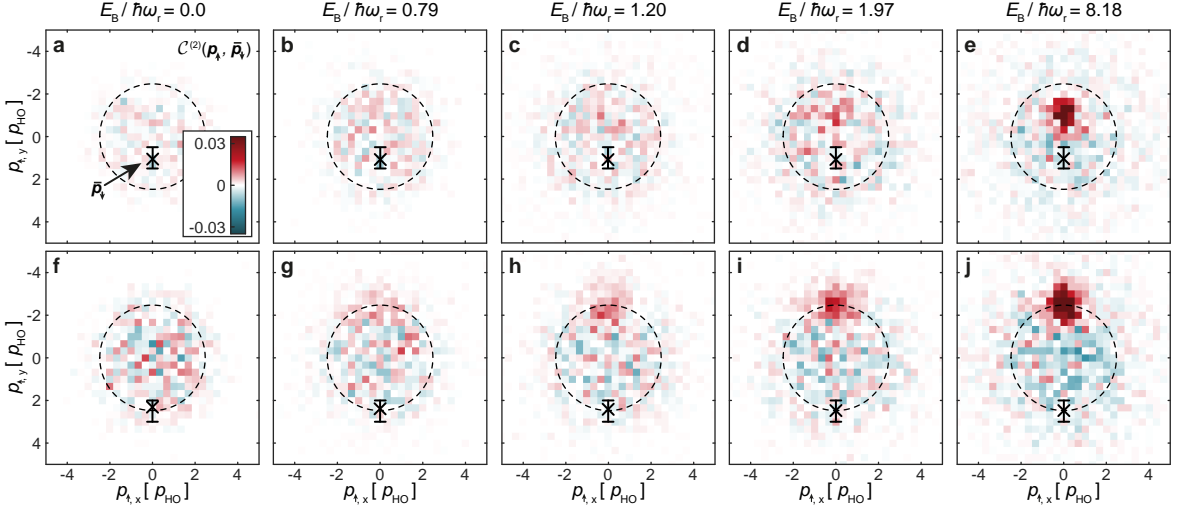


**Figure 7.5: Second order momentum correlations for the  $N = 6 + 6$  particle ground state.** The density plots (a-j) show  $C_{\bar{p}_\downarrow}^{(2)}$ , the normalized probabilities of detecting a spin up particle with momentum  $\mathbf{p}_\uparrow$  given that a spin down particle is located at  $\bar{\mathbf{p}}_\downarrow$  (black cross) in the same run. The dashed black circle marks the Fermi momentum  $p_F \approx 2.45 p_{\text{HO}}$ . In the weakly interacting regime ( $E_B < E_F$ ) pairing is suppressed inside the Fermi sea (a-d) and significant correlations appear only at the Fermi surface (f-i). For much stronger interactions, the Fermi surface is broken up and pair correlations are found at any momentum (e-j). This indicates a transition from Cooper pairing to molecules. Figure taken from [Hol21a].

for particles at opposite momenta. An even more intuitive and direct picture of Cooper pairing can be obtained by studying the single atom resolved samples of the momentum distribution. In Figure 7.6 we have highlighted all pairs of particles with opposite spin that are detected close to the Fermi surface with  $p_{\uparrow,\downarrow} > 2/3 p_F$  and opposite to each other with  $150^\circ < \Delta\phi < 210^\circ$ . Two sets of images are shown for a setting with larger attraction strengths  $E_B = 1.97 \hbar\omega_r$  (a) and in the non-interacting regime  $E_B = 0$  (b) respectively.

In the strongly interacting regime, it is significantly more likely to detect pairs at the Fermi surface than for the non-interacting sample. These additional pairs directly contribute to the positive correlation peak we have observed at the Fermi surface in Figures 7.4 and 7.5. Our detection scheme allows us to directly image Cooper pairs, the fundamental constituents of conventional superconductors. The pairs are not always located exactly at the Fermi surface or opposite to each other. This can be explained

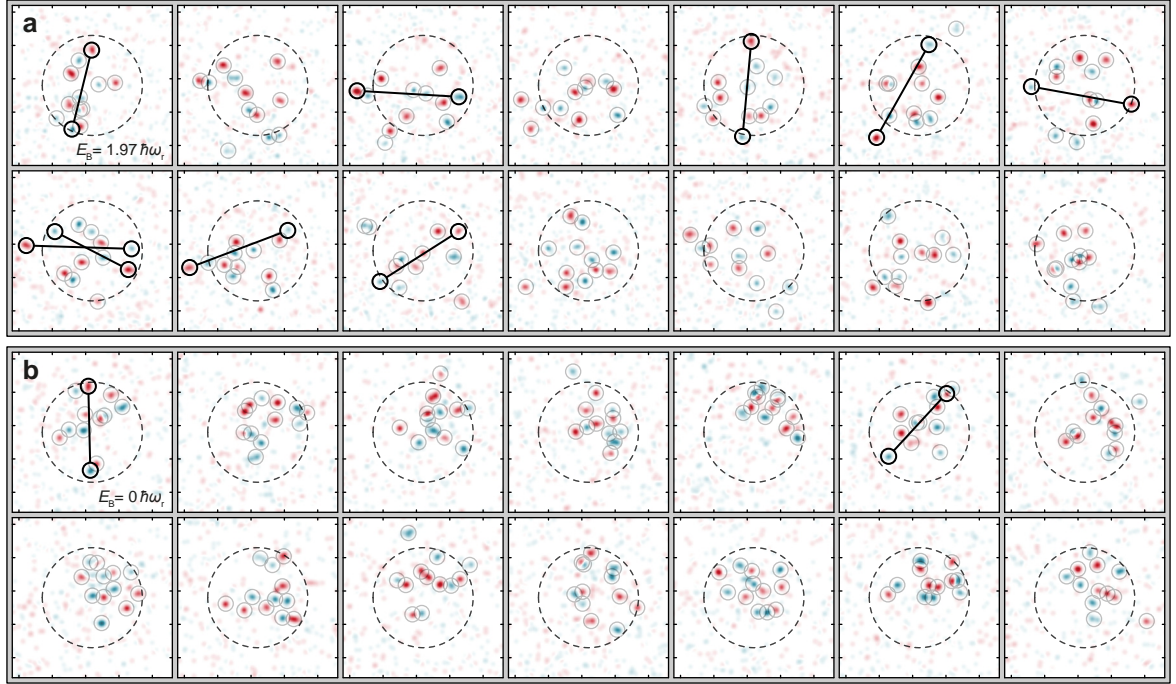


**Figure 7.6: Projections of the momentum space wavefunction for two different interaction strengths.** All detected pairs of atoms with opposite spins, opposite momenta and close to the Fermi surface are highlighted. The set of images has not been postselected other than for the correct total number of atoms. In the sample of the interacting ground state (a) we find significantly more pairs than in a non-interacting case (b). These pairs correspond to the peak at opposite momenta in the second order density correlation function. Figure adapted from [Hol21a].

by the finite size of our system. The Fermi surface  $p_F$  is not sharply defined in our mesoscopic sample but has a width on the order of the harmonic oscillator momentum. As a result, the centre of mass momentum of the pairs  $\mathbf{p}_C = (\mathbf{p}_\uparrow + \mathbf{p}_\downarrow)/2$  fluctuates around zero with a distribution of a width  $\Delta p_C \approx 0.5 p_{HO}$  close to the expectation from the ground state wavefunction of a pair with  $M_{\text{pair}} = 2m$  (see Figure 7.4 f-j).

### 7.3 Emergence of Pairing

At second order, we find significant correlations only between particles with opposite momenta  $\mathbf{p}_\uparrow = -\mathbf{p}_\downarrow$  (see Figures 7.4 and 7.5). This motivates a further reduction of

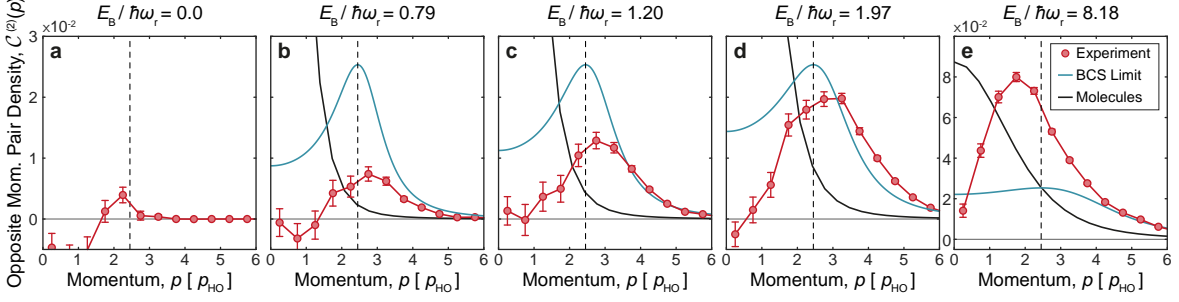


**Figure 7.7: Opposite Momentum Pair Density  $\mathcal{C}^{(2)}(p)$  for the  $N = 6 + 6$  atom ground state.** The correlation function visualizes at which momenta  $p$  pairs of atoms with opposite momenta  $p_{\uparrow} = p_{\downarrow}$  are detected more frequently. The vertical dashed line marks the Fermi momentum  $p_F$ . In the weakly interacting regime  $E_B \lesssim \hbar\omega_r$ , pairing starts to emerge at the Fermi surface (a-c). When the interactions are further increased, the weight in the correlation peak increases significantly and its maximum moves towards smaller momenta, below the Fermi surface (d-e). We compare the measurements to the predictions from the BCS theory (blue line) and a model system consisting of non-interaction molecules (solid black line). Figure taken from [Hol21a].

the four dimensional correlation function  $\mathcal{C}^{(2)}$  that enables us to study the emergence of pairing in our mesoscopic Fermi gas also from a more quantitative point of view. We define the opposite momentum pair density as  $\mathcal{C}^{(2)}(\mathbf{p}_{\uparrow} \rightarrow \mathbf{p}, \mathbf{p}_{\downarrow} \rightarrow -\mathbf{p})$  (see equation (7.1)). Due to the radial symmetry of our system,  $\mathcal{C}^{(2)}(\mathbf{p}, -\mathbf{p}) \equiv \mathcal{C}^{(2)}(p)$  must depend only on the magnitude of  $\mathbf{p}$  and can be expressed as 1D correlation function. The opposite momentum pair density  $\mathcal{C}^{(2)}(p)$  as a function of the binding energy is shown in Figure 7.7. We divide the following discussion into three different regimes of pairing we identify in our system. The weakly paired regime  $E_B \lesssim \hbar\omega_r$ , the regime of intermediate interaction strength  $E_B \sim E_F \gtrsim \hbar\omega_r$  and the limit of strongly bound molecules  $E_B \gg E_F$ .

In the weakly interacting regime, pairing correlations start to emerge at the Fermi surface of the system (see Figure 7.7 a-c). Consistent with our previous observations, they become much stronger with increasing interaction strength and their maximum starts to move towards lower momenta (d-e). We compare measurements to the BCS theory and a sample of non-interacting molecules as simple mean field models for our Fermi gas. We do not expect these models, valid only in the large particle number  $N \rightarrow \infty$  and weak and strongly interacting limits  $E_B \rightarrow 0, \infty$  respectively, to produce

accurate quantitative predictions for mesoscopic systems sizes or in the regime of intermediate interactions. Nevertheless, for our sample of only  $N = 6 + 6$  particles most of the qualitative features can already be found.

### 7.3.1 BCS Theory

The opposite momentum pair density  $\mathcal{C}^{(2)}(p)$  can be calculated directly in the BCS theory. Using our definition in equation (7.1), we obtain

$$\mathcal{C}^{(2)}(\mathbf{p}, -\mathbf{p}) = \langle c_{\mathbf{p}\uparrow}^\dagger c_{\mathbf{p}\uparrow} c_{-\mathbf{p}\downarrow}^\dagger c_{-\mathbf{p}\downarrow} \rangle - \langle c_{\mathbf{p}\uparrow}^\dagger c_{\mathbf{p}\uparrow} \rangle \langle c_{-\mathbf{p}\downarrow}^\dagger c_{-\mathbf{p}\downarrow} \rangle, \quad (7.4)$$

where  $c_{\mathbf{p}\sigma}^\dagger$  and  $c_{\mathbf{p}\sigma}$  are the fermionic particle creation and annihilation operators respectively. Both expectation values can be evaluated for the BCS ground state by applying the Bogoliubov transformation (see section 2.2.3). The particle creation and annihilation operators are replaced by fermionic quasi-particle operators ( $\gamma_{\mathbf{k}\sigma}, \gamma_{\mathbf{k}\sigma}^\dagger$ ) and we make use of the fact that the BCS ground state is the quasi-particle vacuum  $\gamma_{\mathbf{k}\sigma} |\text{BCS}\rangle = 0$  to arrive at:

$$\mathcal{C}^{(2)}(p) = \mathcal{N}^2 \frac{\Delta^2}{4(\xi_p^2 + \Delta^2)}. \quad (7.5)$$

Here,  $\Delta$  is the superfluid gap, and  $\xi_p = p^2/2m - E_F$  is the free particle dispersion with respect to the Fermi energy. The normalization factor  $\mathcal{N}$  is determined by fixing the total particle number in the non-interacting limit ( $\Delta = 0$ ):

$$N_\uparrow = \int \langle c_{\mathbf{p}\uparrow}^\dagger c_{\mathbf{p}\uparrow} \rangle d\mathbf{p} = 2\pi\mathcal{N} \int_0^\infty v_p^2 p dp. \quad (7.6)$$

In 2D, we can replace the superfluid gap by its mean-field value  $\Delta = \sqrt{2E_B E_F}$  in terms of the two-body bound state [Ran89] (see section 2.2.3).

### 7.3.2 2D Molecules

An even more simple model for our mesoscopic system, valid in the strong binding regime  $E_B \rightarrow \infty$ , is to assume that the particles form bosonic dimers that are non-interacting and all occupy the  $n = 0$  harmonic oscillator ground state. The binding energy of each dimer is directly given by  $E_B$  and for the relative wavefunction of the two-body state we take the ansatz [Zwi06]:

$$\Psi_{\text{rel}}(r) = \begin{cases} a_1 \times e^{-r/r_B} & \text{for } r > r_B, \\ -\log \frac{r}{r_B} + a_2 & \text{for } r_0 \leq r \leq r_B, \\ a_3 \times e^{-r^2/r_b^2} + a_4 & \text{for } r < r_0. \end{cases} \quad (7.7)$$

Here, the coefficients  $a_i$  are chosen such that the wavefunction is continuously differentiable and normalized to the correct total particle number. The molecular binding length is given by  $r_B = \hbar/\sqrt{2mE_B}$  and  $r = |\mathbf{r}_\uparrow - \mathbf{r}_\downarrow|$  is the distance between both particles. We have introduced a short distance cut-off  $r_0 = 0.1 r_B$  to remove the logarithmic divergence for  $r \rightarrow 0$ . We have confirmed that this renormalization does not effect the calculated density correlations at the relevant momenta.

The total wavefunction of the ground state is then given by  $N$  independent copies of the total wavefunction  $\Psi_{\text{tot}}(\mathbf{r}_\uparrow, \mathbf{r}_\downarrow) = \Psi_{\text{com}}(\mathbf{r}_\uparrow, \mathbf{r}_\downarrow)\Psi_{\text{rel}}(\mathbf{r}_\uparrow, \mathbf{r}_\downarrow)$ , where the centre of mass motion is described by the harmonic oscillator ground state  $\Psi_{\text{com}}(\mathbf{r}_\uparrow, \mathbf{r}_\downarrow) \rightarrow \Psi_{0,0}(\mathbf{R})$  (see equation (5.1)). We calculate the second order opposite momentum pair density  $\mathcal{C}^{(2)}(p)$  numerically by applying a 2D Fourier transform into momentum space and evaluating the expectation values directly. In the limit  $E_B \rightarrow \infty$  and  $\Delta \rightarrow \infty$ , the BCS ground state converges to the limit of non-interacting bosonic dimers. In this sense the two mean-field models describe the limits of weakest  $E_B \rightarrow 0$  and strongest interactions  $E_B \rightarrow \infty$  between the fermionic particles and in the macroscopic limit  $N \rightarrow \infty$ .

### 7.3.3 Emergence of Pairing

The BCS theory can qualitatively explain our measurements in the weakly interacting regime. A pair correlation peak with a maximum at  $p_F$ , we also find as the main feature in our measurements, is predicted (see Figure 7.7, blue line). The weight in the peak increases with increasing binding energy, while its maximum position stays the same. For 2D non-interacting molecules, on the other hand, we expect pair correlations with a maximum at zero momentum  $p = 0$  (black line). For stronger binding energies, we observe how the system evolves towards this limit (see Figure 7.7 e). Note that at the strongest binding energies of  $E_B \approx 16 \hbar\omega_R$  we can currently access in our experiment the interaction between molecules is still very large. The interaction parameter of our mesoscopic system is then  $\ln(k_F a_{2D}) \approx -0.5$ , corresponding to an effective molecular interaction parameter of  $\tilde{g} \approx 15$  [Rie15a] (see section 2.2.4). To reach the strongly bound limit of non-interacting bosons, we would have to increase the interaction strength even further.

From the opposite momentum pair density  $\mathcal{C}^{(2)}(p)$  we can extract the total number of pairs in the ground state. To this end we perform the 2D integral

$$N_{\text{pair}} = \int \mathcal{C}^{(2)}(\mathbf{p}, -\mathbf{p}) d\mathbf{p} = 2\pi \int \mathcal{C}^{(2)}(p) dp. \quad (7.8)$$

The result, as a function of the interaction strength, is shown in Figure 7.8 together with the prediction from the BCS limit. For the model of non-interacting molecules,

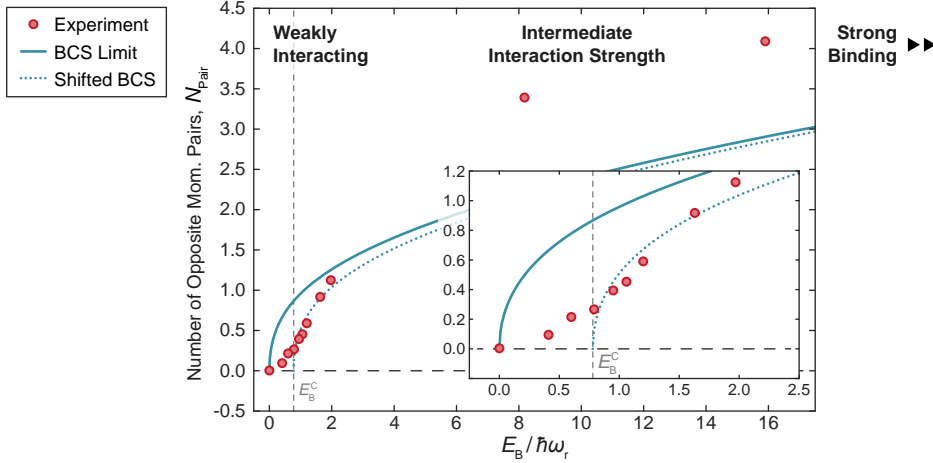


**Figure 7.8: Number of pairs in the  $N = 6 + 6$  closed-shell configuration as a function of interaction strength.** We obtain the pair number by integrating over the opposite momentum pair density in momentum space. The measurement reveals directly how the ground state evolves from an unpaired to a paired system. A precursor of a phase transition from a normal to a superfluid is expected at a critical binding energy of  $E_B^C = 0.78 \hbar\omega_r$  in our mesoscopic system (see chapter 6). We shift the BCS theory prediction (solid line) by the critical value  $E_B^C$  as first order approximation of the finite size effect (dotted line). Compared to a macroscopic sample, the small and fixed particle number leads to a much smoother transition. The inset shows the weakly paired region in more detail. Statistical errors are on the order of the symbol size. Figure taken from [Hol21a].

we always obtain the maximum possible pair number for the  $N = 6 + 6$  particle ground state  $N_{\text{pair}} = 6$  by definition. In the weakly interacting regime, only a small fraction of the system is paired. The number of pairs grows monotonously as  $E_B$  is increased to around  $1 \hbar\omega_r$  and then levels off for even larger values.

The behaviour of our mesoscopic Fermi gas can be understood by its connection to the macroscopic limit we have discussed in detail already in the previous chapter in section 6.3. The BCS theory predicts a superfluid ground state for our system at any value for the interaction strength. When the system size is decreased, however, until the coherence length is on the order of the system size quantum confinement effects become important. For the closed shell ground state configurations, the gap of  $1 \hbar\omega_r$  in the single particle spectrum leads to a breakdown of superfluidity at some critical value

$E_B^C$  as the attraction strength is reduced [Bru14]. A precursor of this phase transition between normal and superfluid can already be observed for mesoscopic particle numbers [Bje16; Bay20a]. For  $N = 6 + 6$  atoms, a value of  $E_B^C = 0.78 \hbar\omega_r$  is predicted by a numerical calculation based on the exact diagonalization of the Hamiltonian [Bje16] (see section 6.3.1).

We model the finite size effect to first order by offsetting the mean-field BCS prediction by the critical value  $E_B^C$  for the  $N = 6 + 6$  particle closed-shell configuration. In the weakly interacting regime ( $E_B \lesssim \hbar\omega_r$ ), the shifted model explains the measured transition into the paired ground state as a function of the interaction strength very well (see Figure 7.8 dotted line). As a result of the small and fixed particle number, the transition is much smoother than the sharp onset of pairing that would be expected in the macroscopic limit.

The large single particle gap  $\hbar\omega_r \approx h \times 1 \text{ kHz} \approx k_B \times 50 \text{ nK}$  can be seen as an important feature of our experiment. It allows us to access the weakly paired regime at much larger absolute energy and temperature scales than what would be required for larger systems. For measurements in macroscopic Fermi gases, the spacing in the single particle spectrum is typically much smaller, for example on the order of  $\hbar\omega_r \approx h \times 20 \text{ Hz} \approx k_B \times 1 \text{ nK}$  (see chapter 8). Here, the absolute critical temperature for the onset of pairing in the weakly paired regime ( $\Delta \lesssim \hbar\omega_r$ ) is far below what can currently be reached in ultracold quantum gas experiments  $T_C \approx \Delta/k_B \lesssim 1 \text{ nK}$ . This can be observed in the study where we have measured the phase diagram of BCS-BEC crossover for example [Rie15a] (see Figure 2.6). In contrast to the mesoscopic system, the superfluid at small temperatures  $T < T_C$  in the BCS limit cannot be reached experimentally in the macroscopic limit.

When further increasing the interaction strength, we enter the strongly correlated regime on intermediate interactions  $E_B \sim E_F$ . Here, the measured number of pairs  $N_{\text{pair}}$  is significantly larger than the mean-field prediction (see Figure 7.8). In this regime, fluctuations of the many-body gap around its mean-field value  $\Delta$  have to be considered in order to obtain a more accurate quantitative prediction [Ran89]. A promising analytical approach that includes such effects and can be solved exactly for mesoscopic systems is provided by the reduced BCS Hamiltonian [Del00]. It was originally introduced in the context of nuclear physics and has already been discussed in detail in section 2.3.2.

### 7.3.4 Richardson Model

The Richardson solution provides an exact analytical solution to the reduced BCS model, independent of mean-field approximations and for systems with a small and fixed particle number (see section 2.3.3). However, the reduced BCS Hamiltonian describes

the contact interactions in our mesoscopic Fermi gas only approximately. The same coupling strength  $g$  between all harmonic oscillator levels is assumed, independent of their wavefunction overlap (see section 2.3.2). It is not clear if this approximation of the interaction term in the Hamiltonian is justified in the mesoscopic limit as  $N \rightarrow 0$ .

From the analytical Richardson solution (see equation (2.41)), we obtain the ground state wavefunction in the basis of 2D non-interacting harmonic oscillator levels. This allows us to calculate the opposite momentum pair density  $\mathcal{C}^{(2)}(p)$  numerically. The results for the  $N = 3 + 3$  particle ground state configuration and a dimensionless coupling parameter of  $g = 0.06$  are shown in Figure 7.9 (red line). An interaction strength of  $E_B = 0.2 \hbar\omega_r$  in terms of the binding energy is determined by solving the  $N = 1+1$  system for the same coupling strength  $g = 0.06$ . In addition, we also show the angular pair density, defined as  $\mathcal{C}^{(2)}(\phi) = \mathcal{C}^{(2)}(p_\uparrow = 1.2 p_{\text{HO}}, p_\downarrow = 1.2 p_{\text{HO}}, \Delta\phi = \phi)$ . The angular correlation function  $\mathcal{C}^{(2)}(\phi)$  expresses at which relative angle  $\phi$  the probability to detect a pair of particles is enhanced when both atoms have the same absolute momentum  $p_\uparrow = p_\downarrow = 1.2 p_{\text{HO}}$ .

The Richardson model predicts the presence of significant pair correlations already at very small attraction strength  $E_B = 0.2 \hbar\omega_r$  in the  $N = 3+3$  particle ground state. The correlations appear between particles of opposite momenta  $\phi = \pi$  and their maximum is significantly below the Fermi surface  $p \approx 1.2 p_{\text{HO}} < p_{\text{F}}$ . Even in the weakly interacting regime, the model predicts strong pairing with molecular character. This indicates that the approximations of the contact interactions in the reduced BCS Hamiltonian are not justified in the mesoscopic limit and a more accurate description of our system has to be applied.

We compare the solution from the Richardson model to a trial many-body wavefunction for  $N = 3 + 3$  particles (see Figure 7.9 blue line). The trial wavefunction is obtained by assuming that the interacting ground state is a superposition of all possible combinations of time-reversed pair excitation above the ground state, weighted by their excitation energy  $\mathcal{N} \propto 0.02^{E_{\text{ex.}}/\hbar\omega_r}$  (see section 2.3.2). The trial wavefunction has the same occupation probability  $p_{\text{GS}} = 88\%$  of the non-interacting ground state as the Richardson solution for  $g = 0.06$ . The overlap between both many-body wavefunctions is  $|\langle \text{Trial} | \text{Rich.} \rangle|^2 = 97\%$ .

While the trial wavefunction overlaps almost perfectly with the Richardson solution, the predicted pair correlations are significantly different (see Figure 7.9). Even though the occupation probability of the non-interacting ground state for both wavefunctions is the same, the weight in the correlation peak for the trial wavefunction is much smaller. In addition, the maximum is shifted towards higher momenta  $p$ .

The trial wavefunction represents a simple guess of the many-body state and does not allow us to make further predictions. However, its comparison to the Richardson solution demonstrates the high sensitivity of our observables. Single particle resolved

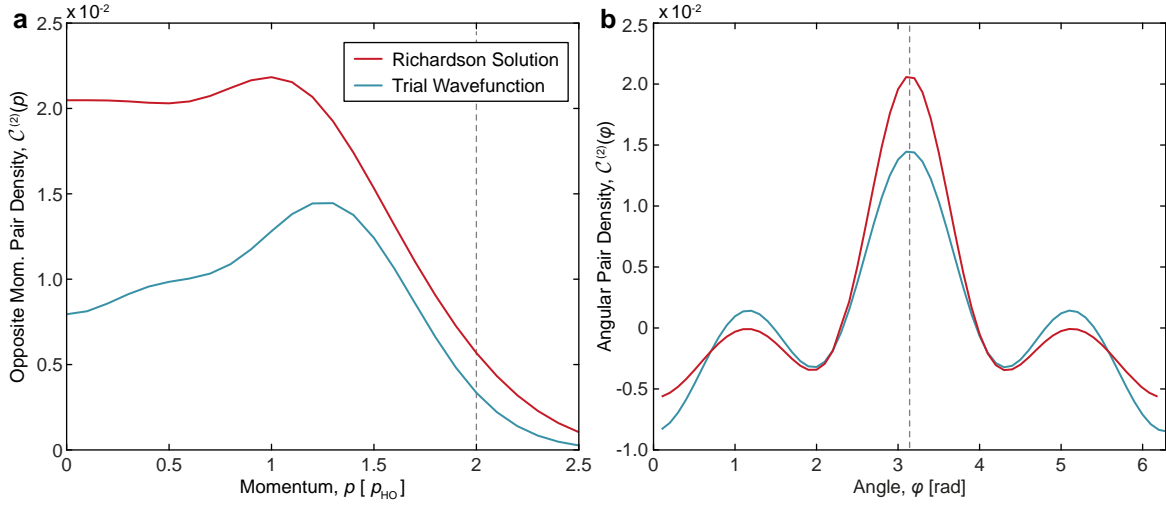


**Figure 7.9: Second order density correlations in the Richardson model for the  $N = 3 + 3$  ground state.** The opposite momentum pair density  $C^{(2)}(p)$  shows large positive correlations already for small binding energies  $E_B = 0.2 \hbar\omega_r$  (a, red line). Most of the pairs appear between particles of exactly opposite momenta  $\phi = \pi$  as demonstrated by the angular correlation function  $C^{(2)}(\phi)$  (b). The maximum of the momentum pair density is around  $p = 1.2 p_{\text{HO}}$ , significantly lower than the Fermi momentum of  $p_F = 2 p_{\text{HO}}$  for this system size. The blue line shows the same correlation functions for a trial wavefunction that is created by the excitation of time reversed pairs.

correlation measurements can reveal even the smallest changes in the many-body wavefunction. Our measurements can act as a benchmark to test different theoretical approaches with high accuracy. While the Richardson model, in its basic form, does not result in a quantitative agreement with our measurements, it nevertheless shows most of the qualitative features. A promising approach is to implement the contact interactions of our Fermi gas more accurately, for example using a variational method [Cla17], in the future.

### 7.3.5 Many-body limit

In Figure 7.10, a first dataset for different particle numbers is shown. We have measured the pair number  $N_{\text{pair}}$  in the ground state as a function of the number of filled shells at a fixed interaction strength of  $E_B = 1.2 \hbar\omega_r$ . We find a linear increase in the absolute pair number with the particle number that indicates a constant pair fraction  $N_{\text{pair}}/N$

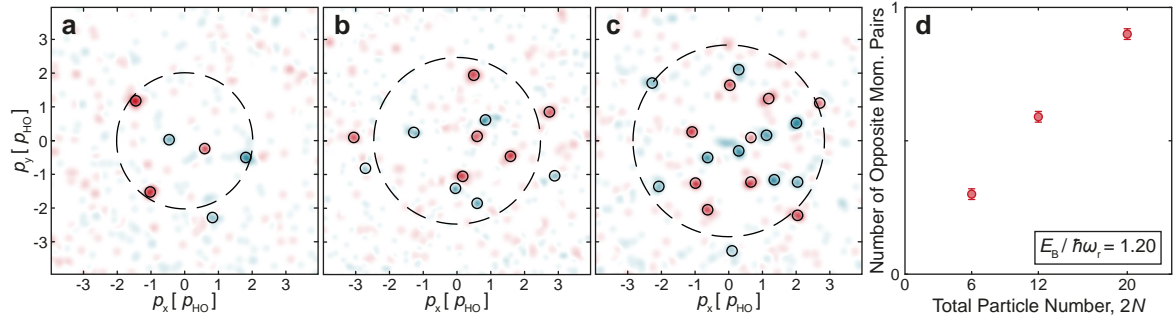


**Figure 7.10: Measurement with different particle numbers.** Our measurements of single particle and spin resolved momentum distributions can directly be extended to states with other particle numbers (a-c). The dashed lines indicate the Fermi momentum  $p_F = \sqrt{2(n_F + 1)}p_{HO}$  for each configuration. The measured total number of pairs  $N_{\text{pair}}$  in the ground state at a fixed interaction strength  $E_B$  increases linearly with  $N$  (d). Figure adapted from [Hol21a].

in the ground state. Since the Fermi energy scales only with the square root of the particle number  $E_F \propto \sqrt{N}$ , no large quantitative changes are expected as we change the number of filled shells by one from  $N = 6 + 6$  to  $10 + 10$  or  $3 + 3$  atoms respectively.

Pairing in the closed-shell ground state configurations is influenced in several ways as the particle number  $N$  and Fermi energy  $E_F \propto \sqrt{N}$  are increased. As the system size grows, the Fermi surface and Fermi momentum  $p_F$  become sharper and well-defined in a local density approximation (LDA). In the weakly interacting regime, the peak in the second order correlations will become narrower and more localized at the Fermi surface (see Figure 7.7). The fluctuations of the centre of mass momentum of the pairs decrease continuously until they vanish in the zero temperature and infinite size limit (see Figure 7.4 f-j). A condensate of pairs with zero momentum remains.

The critical interaction strength at which the precursor of a normal to superfluid phase transition occurs in the ground state scales as  $E_B^C \propto 1/\sqrt{E_F}$  [Bru14]. Consequently, the transition between the weakly paired and strongly correlated regime occurs at smaller absolute interaction strength  $E_B \sim E_B^C$  as more shells are filled. The transition also becomes sharper and quantitatively resembles a macroscopic quantum phase transition more closely (see Figure 7.8). At a fixed interaction strength  $E_B$ , the superfluid gap becomes larger  $\Delta \propto \sqrt{E_F}$  and the system is shifting towards the BEC regime of strong binding.

No qualitative changes are expected as the system evolves from the mesoscopic to the macroscopic world. All the essential features of Cooper pairing in 2D can already

be observed in a system of only  $N = 6 + 6$  particles. The pair wavefunction changes in a continuous fashion as the system size is increased. In the large particle number limit  $N \rightarrow \infty$ , we expect that the weakly interacting regime  $E_B \rightarrow 0$  is described accurately by the mean-field BCS theory. Likewise, the sample in the regime of infinite interactions  $E_B \rightarrow \infty$  converges towards a non-interacting molecular BEC. In the regime of intermediate interactions  $E_B \sim E_F$ , however, effects beyond a mean-field description have to be considered even in the macroscopic sample.

## 7.4 Systematic Effects

Both the preparation of interacting closed-shell ground state configuration and single atom resolved fluorescence imaging have already been studied in detail in chapters 5 and 6. The techniques are well established in our experiment and any possible systematic problems have been excluded. The only addition to the experimental sequence that is required for the measurements presented in this chapter is the quasi-instantaneous projection into a non-interacting system at the beginning of the TOF expansion.

### 7.4.1 Scattering during the TOF

Our pair of Raman lasers allows us to drive the transition from the initial  $|1\rangle|3\rangle$  to the final  $|1\rangle|4\rangle$  mixture in  $T_\pi = 330$  ns, many orders of magnitude faster than what would be required even for the highest scattering rates  $\nu \approx 50$  kHz we study in our experiment. Nevertheless, it is important to check that the projection to the non-interacting state is fast enough and does not alter the measured momentum correlations. To this end, we study the measured number of pairs  $N_{\text{pair}}$  and total kinetic energy  $E_{\text{kin}}$  as a function of the spin flip time  $T_\pi$  (see Figure 7.11 a). To vary  $T_\pi$ , we fix the magnetic offset field to  $B = 750$  G or  $E_B = 0.6 \hbar\omega_r$ , where we can use a MW pulse for the spin flip in place of the Raman lasers (see section 4.3). This improves the postselection fidelity significantly.

When the duration of the spin flip is increased, the strength of the measured momentum correlations reduces significantly until, at  $T_\pi \approx 2$  ms, no signal above the background is left and  $N_{\text{pair}} \approx 0$  (red circles). This effect can be explained by elastic collisions that happen between pairs of atoms while the gas is already expanding. Each elastic collision leads to a random redistribution of the momenta of both partaking atoms and the information about the momentum distribution in the initial ground state is lost. If one atom  $\mathbf{p}_\uparrow$  that corresponds to a Cooper pair scatters from a third particle just once during the expansion, for example, it receives a momentum kick  $\mathbf{p}_\uparrow \rightarrow \mathbf{p}'$  and does not appear at its original position  $\mathbf{p}_\uparrow = -\mathbf{p}_\downarrow$  anymore.

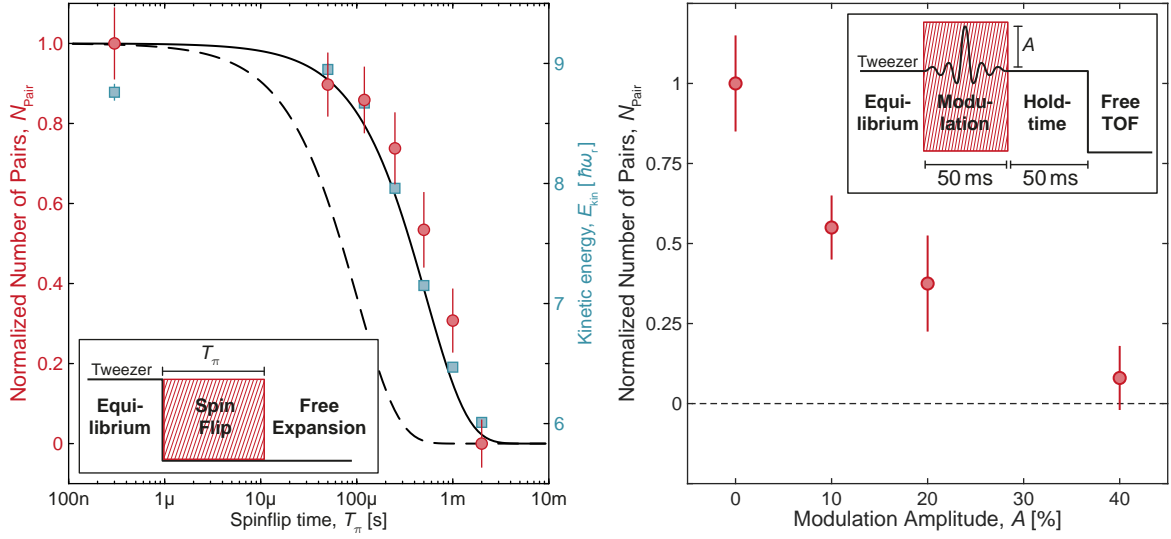


**Figure 7.11: Momentum correlations as a function of the projection time  $T_\pi$  and in heated samples.** We scan the number of detected pairs  $N_{\text{pair}}$  (red) and the measured kinetic energy  $E_{\text{kin}}$  (blue) as a function of the projection time  $T_\pi$  into a non-interacting wavefunction (a). The spin flip is started synchronously with the removal of the radial confinement of the atoms (inset). For durations  $T_\pi > 100 \mu\text{s}$  the number of detected pairs  $N_{\text{pair}}$  reduces significantly. The effect can be explained very well by a model that assumes that elastic scattering events during the TOF expansion destroy the correlations of all participating atoms (black line). We heat the sample by modulating the radial confinement after preparing the initial ground state (b, inset). This leads to a quick reduction of the pair correlations. Figure adapted from [Hol21a].

We model the effect by calculating the scattering rate  $\nu$  during the expansion in the initial state  $|1\rangle|3\rangle$  using the measured in-situ density and the magnetic offset field  $B = 750 \text{ G}$  as only input parameters (see Figure 7.11 black line). Here, we assume that each scattering event completely destroys all possible correlations for both the participating atoms. The predictions agree very well with our measurements. We extrapolate the same model also to the largest setting for the interaction strength used in the experiment at  $B = 674 \text{ G}$  with  $E_B \approx 15 \hbar\omega_r$  (dashed line). No significant loss of the correlation amplitude for our Raman spin flip time of  $T_\pi = 330 \text{ ns}$  is predicted. We conclude that our rough estimation based on the timescales alone at the beginning of the chapter was justified and that scattering events during the expansion can be

neglected completely.

The measured kinetic energy (blue squares) shows a very similar behaviour as the pair number  $N_{\text{pair}}$ . In section 5.3.2, we have already explained in detail how we can extract the kinetic energy from the single particle resolved density distribution in momentum space. The genuine value for the kinetic energy of the Fermi gas in its trapped state is only measured in the limit where  $T_{\pi} \rightarrow 0$ . When the particles still interact during the TOF, the expansion is slowed down significantly as a result of the attractive mean-field shift for  $E_B > 0$ . This leads to a reduction of the measured kinetic energy  $E_{\text{kin}}$  proportional to the number of scattering events during the expansion. This demonstrates again how important it is to switch off all the interactions during the TOF in order to extract the correct observables.

### 7.4.2 Heated Samples

We create excitations above the prepared  $N = 6+6$  particle ground state by modulating the radial confinement with a variable amplitude  $A$  for  $t_{\text{ex}} = 50$  ms. A sinc pulse with a centre of  $\omega_{\text{ex}} = 2\omega_r$  and a broad width in frequency space of  $\Delta\omega = 2\pi \times 700$  Hz is used to excite the system incoherently. After the modulation, we let the sample equilibrate for  $t = 50$  ms, much longer than the inverse scattering rate  $1/\nu \approx 0.1$  ms, before starting the detection sequence (see Figure 7.11 b, inset). The amplitude of the measured density correlations and the number of pairs  $N_{\text{pair}}$  in the ground state reduces quickly as the modulation amplitude is increased. Qualitatively the correlations disappear at much smaller modulation strengths as in the case of the Pauli crystals (see section 5.3.2). This is expected since this measurement is performed at  $E_B = 0.6\hbar\omega_r \ll E_F$ . Pauli crystals melt at temperatures on the order of  $T \approx T_F$  while the superfluid is broken already at  $T = T_C \ll T_F$ . For future studies of heated samples we have to develop an efficient thermometry procedure that works for interacting gases.

### 7.4.3 Momentum Space Densities

In Figure 7.12 the measured density distribution for the  $N = 6+6$  particle ground state is shown for a non-interacting sample (a) and  $E_B = 1.97\hbar\omega_r$  (b). In the non-interacting case, we find the distribution that is expected from the three filled harmonic oscillator shells. At a finite interaction strength, the distribution becomes significantly wider, indicating that the average kinetic energy of the fermionic particles in the ground state increases. By forming pairs and increasing their overlap, the particles lower their overall energy at the cost of occupying higher non-interacting harmonic oscillator levels. The measured kinetic energy increases linearly with binding energy (c). For the non-interacting state we measure a value of  $E_B = 7.65(5)\hbar\omega_r$ , very close to the expected

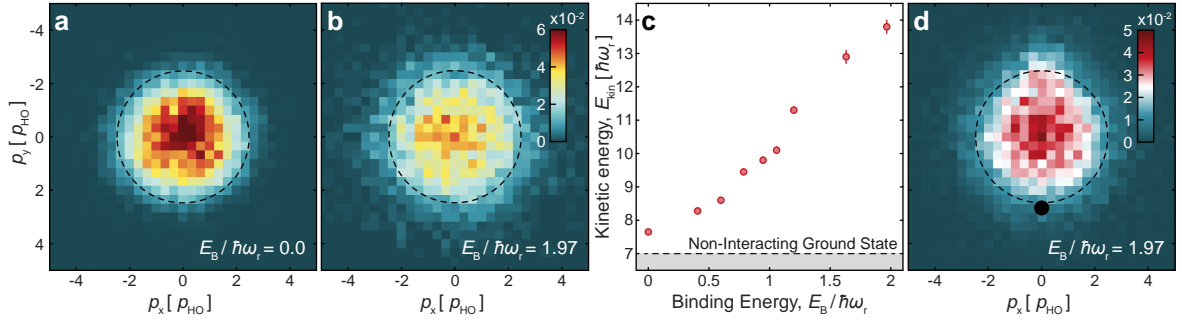


**Figure 7.12: Density distributions in momentum space.** The momentum space distributions  $\langle n(\mathbf{p}_\uparrow) \rangle$  for a single spin component and averaged over 1000 images are shown for a non-interacting sample (a) and  $E_B = 1.97\hbar\omega_r$  (b). The dashed circle indicates the Fermi momentum. With increasing interaction strength the particles form pairs to gain binding energy and larger non-interacting harmonic oscillator levels become occupied. This leads to an increase of the average kinetic energy (b,c). In panel (d) we show the non-normalized second order correlator  $\mathcal{C}'^{(2)}$ . It is equivalent to the definitions in equations (7.1) and (7.3) but without subtracting the term  $\langle n \rangle \langle n \rangle$ . It demonstrates that at large binding energies  $E_B \gg 1\hbar\omega_r$  the paired fraction in the ground state becomes large enough so that positive correlations become visible even without subtracting the contribution from single particle densities. Figure adapted from [Hol21a].

value for the  $N = 6 + 6$  ground state of  $E_0 = 7\hbar\omega_r$ .

## 7.5 Conclusion

We have demonstrated that the fundamental fermionic correlations can be accessed in continuous systems, even in the presence of strong interactions. Our single particle and spin resolved measurements in momentum space allow us to observe how Cooper pairs emerge at the Fermi surface of our sample. We are able to characterize the ground directly, independent of theoretical predictions, and we can identify different pairing mechanisms. In comparison to the spectroscopic measurements in chapter 6, our imaging technique enables us to extract much more information about the Fermi gas in each cycle of the experiment. Our measurements raise further questions like the presence of higher order pair-pair correlations and the onset of condensation we want to study in more detail in the future.

Our 2D Fermi gas is closely related to other mesoscopic materials like superconducting grains, quantum dots and systems from nuclear and atomic physics [Del01; Alh00; Lau17; Cas09]. Models like the BCS theory or the Richardson solution describe the main features we observe in our experiment qualitatively. Deviations from the theoretical descriptions can be explained with both finite size and beyond mean-field effects. The large quantitative discrepancies, in the strongly correlated regime for example, demonstrate that our experiment is very sensitive to beyond mean-field effects and that more elaborate theories are required.

We hope that our measurements trigger the development of new models for the description of strongly interacting Fermi gases. Numerical approaches are computationally very challenging, even for mesoscopic systems consisting of only  $N = 10 + 10$  particles for example. When truncating the basis to 6 harmonic oscillator shells in this case, the dimension of the Hilbert space is already  $\dim(\mathcal{H}) \approx 10^{11}$ . While an exact diagonalization for this system size might become possible in the future, anything larger is certainly out of reach. Correlation measurements, also beyond second order, can be used as a benchmark to test novel numerical and analytical approaches to the problem. Our experiment forms an important bridge between particle numbers  $N < 20$  for which exact numerical solutions are still within reach and everything above.

An upgrade of our apparatus allows us to access in-situ density correlations with single particle resolution in addition (see chapter 9). In this way, an even more thorough characterisation of the many-body wavefunction becomes possible. With the complete programmability of particle number, spin imbalance, interactions and external potentials (see chapter 4) our system opens up new pathways to study outstanding questions in mesoscopic systems and their connection to the macroscopic world. Very promising examples are imbalanced systems in 1D or 2D [Pec20; Che10], rotating samples [Pal20], or balanced mixtures with larger atom numbers (see Chapter 9). By increasing the number of particles further we gain access to a rich collection of intriguing phenomena in the macroscopic phase diagram of the BCS-BEC crossover that are not yet fully understood. The formation of many-body pairs in the normal phase of the gas [Mur18b] and a quantum anomaly that appears in 2D [Hol18] are two examples that we want to study in the near future. First studies of these effects are presented as an outlook of what to expect in the macroscopic world in the next chapter.



# 8

## The Macroscopic World

Our experiment enables us to take a completely new approach, from the bottom up, to strongly correlated systems in the macroscopic world. The balanced 2D Fermi gas with contact interactions, we have studied extensively at a mesoscopic size, is described in the framework of the BCS-BEC crossover in the many particle limit (see section 2.2.4). And while this model of fermionic superfluidity has been studied in detail both on the theoretical and experimental level [Zwe12; Par14], many questions remain unanswered [Str18]. This is especially true for the crossover region of intermediate interactions we have already identified in the previous chapter. Here, mean-field descriptions like the BCS theory fail and higher order corrections have to be taken into account. More generally, the BCS-BEC crossover provides a well controlled playground to develop new theories to address longstanding questions in the field of strongly interacting fermionic matter [Lau83; Lee06; Zho21].

In this chapter, we review two studies that have allowed us to shed some light on the nature of the Fermi gas in the crossover region between the BCS and the BEC limits. The measurements were taken with the previous version of our apparatus, without us having the degree of control over the quantum state and the single particle resolved observables that we have now (see chapter 4). The studies serve as an outlook into the fascinating manifestations of collective behaviour and pairing effects we expect once we increase the particle number again. Instead of an extensive discussion, we focus on the essential results at this point. Further details and systematic effects can be found in the original publications [Mur18b; Hol18; Mur19] or in Refs. [Nei17; Hol17; Mur18a; Kle21].

### 8.1 Pairing in the Normal Phase

All the measurements presented so far in this thesis were performed for samples prepared very close to the absolute ground state. In the macroscopic limit, when the single particle gaps in the spectrum become irrelevant ( $E_B \gg \hbar\omega_r$ ), the zero temperature state

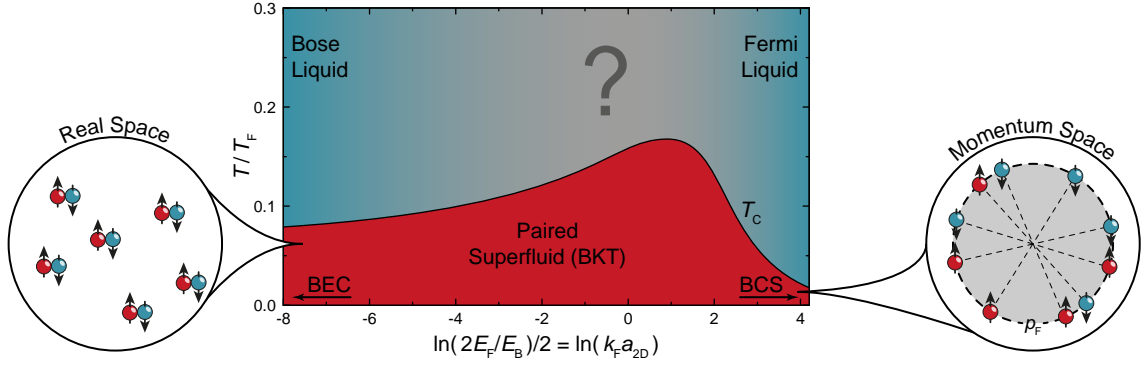


**Figure 8.1: Schematic phase diagram of the BCS-BEC crossover.** In the infinite particle number limit with  $E_B \gg \hbar\omega_r$ , the ground state of the 2D Fermi gas is always paired. A smooth crossover between tightly bound molecules (left) and Cooper pairs in momentum space (right) takes place as a function of the binding energy. The nature of the normal phase is less well understood. In the BCS limit the onsets of Cooper pairing and superfluidity occur at the same temperature  $T = T_C$ . In the BEC limit, when  $E_B \gg E_T$ , the normal phase can be described as Bose liquid of strongly bound dimers. Many questions about the exact nature of pairing remain for the strongly correlated crossover region between both limits, where mean-field models can not be applied.

of the 2D Fermi gas is a superfluid independent of the strength of the attractive interactions. The atoms are always bound and the pair character transitions smoothly from tightly bound molecules in the BEC regime to Cooper pairs in the BCS ground state (see Figure 8.1). This immediately raises important questions about the normal phase above the superfluid. Are pairing correlations present at temperatures  $T > T_C$  and if so, what is their nature?

In the limits of weak and infinite binding  $E_B \rightarrow 0, \infty$  simple mean-field models can be applied. Far in the BEC regime, the binding energy of the tightly bound dimers is much larger than the thermal energy  $E_T \ll E_B$ , even above the normal to superfluid transition  $T > T_C$ . Consequently, the particles remain bound and the gas can be described as a Bose liquid. The BCS theory, on the other hand, predicts that the onset of Cooper pairing and of superfluidity occur at the same transition temperature  $T_C$ . The Fermi liquid above has a gapless many-body spectrum [Frö12].

Most interesting is the strongly correlated region between both limiting cases. Similar to the phase diagram of cuprate high- $T_C$  superconductors, a so-called *pseudogap* regime exists in the normal phase [Mur18b] (see Figure 2.1). The density of states at the

Fermi surface is suppressed already above the critical temperature  $T > T_C$  and pair correlations are present in the gas. It is believed that obtaining a more complete understanding of this region in the phase diagram is an essential milestone towards unravelling the physics of high- $T_C$  superconductors [Che09; Lee14; Kas16; Mue17].

In cold atom experiments, the normal phase of strongly interacting Fermi gases has been studied to a great extent both in 3D [Sch07; Gae10; Nas11; Per11; Sag15] as well as in 2D [Fel11; Som12]. Nevertheless, open questions remain concerning, for example, the connection of the pseudogap phase to the superfluid below, the nature of pairing and the presence of higher order correlations [Bar14; Nga13; Mar15; Lev15; Tör16; Mue17]. In the future, single particle resolved correlation measurements in real and momentum space can help to increase the understanding of the normal phase significantly.

The measurements presented here rely on spatially resolved RF spectroscopy as a tool to identify different regimes of pairing in the gas. The spatial resolution is required since the RF response reveals a strong dependence on the local density of the atom cloud. We detect pair formation in the normal phase of the crossover region up to a very large temperature  $T \gg T_C$  and with an energy that is significantly larger than the two-body binding energy  $\Delta E \gg E_B$ . This indicates that genuine collective behaviour and many-body effects are required to describe the strongly interacting normal phase of the Fermi gas.

### 8.1.1 Experimental Sequence

To study the macroscopic limit of the interacting 2D Fermi gas, we load a sample of two hyperfine components with  $N \approx 30\,000$  atoms per spin state into a single layer of the SWT (see section 4.1). Compared to the measurement previously presented in this thesis, the MT that has been used to provide an additional radial confinement is not present here (see Figure 8.2 a). This leads to a final harmonic confinement with a very large aspect ratio of  $\omega_z : \omega_r \gtrsim 300 : 1$  and allows us to reach the kinematic 2D regime of the gas. Both the chemical potential ( $\mu$ ) and the temperature ( $T$ ) are small compared to the energy scale of the axial confinement ( $\hbar\omega_z$ ) and no axial excitations are present for the relevant degrees of freedom of the gas [Rie15a]. We tune the interaction strength  $E_B$  between both hyperfine components using the Feshbach resonance (see section 3.3.2) once the sample has been prepared. For macroscopic samples the general convention is to express the attraction strength in terms of the 2D interaction parameter  $\ln(k_F a_{2D}) = \ln(2E_F/E_B)/2$  instead of the binding energy  $E_B$ .

As a result of the harmonic confinement, the atomic cloud in the initial state is inhomogeneous with the highest density in the centre and a more dilute gas towards its wings (see Figure 8.2 b). This density dependence  $n(\mathbf{r})$  is one of the most essential features of our measurements as we discuss in the following. For our macroscopic 2D

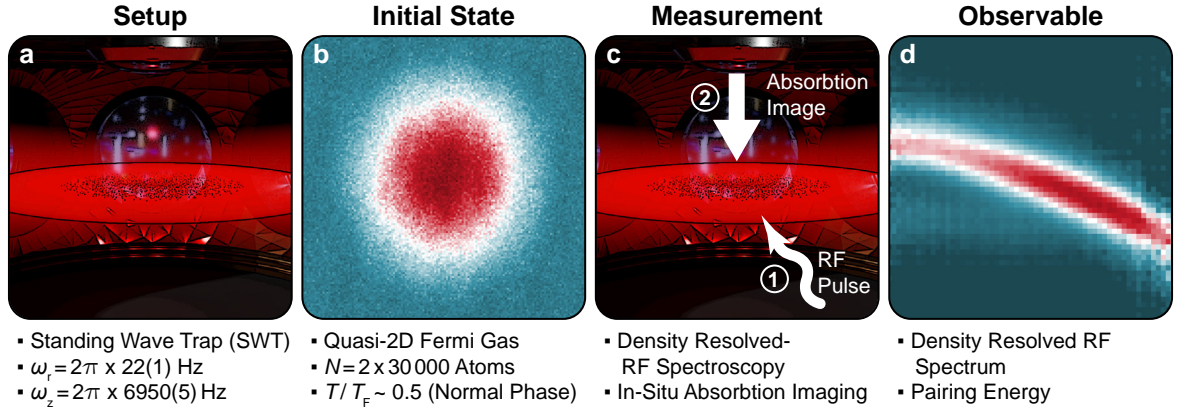


**Figure 8.2: Experimental sequence for the study of pairing in the normal phase.** The state is initialized by loading a large sample of atoms into a single layer of the SWT (a). This leads to a quasi-2D Fermi gas with an inhomogeneous density distribution  $n(\mathbf{r})$ . To search for pairing correlations in the normal phase, we apply spatially resolved RF spectroscopy. The response of the gas to the RF pulse is recorded using spin selective absorption imaging (c). The density dependent spectra we obtain in this way allow us to measure the pairing energy  $\Delta E$  as a function of interaction strength  $\ln(k_F a_{2D})$  and temperature  $T/T_F$ .

Fermi gas, the radial confinement varies only on length scales  $l_{HO}$  that are much larger than the inter-particle spacing  $1/k_F$  or, more importantly, the coherence length  $\xi$ . Locally, the radial confinement does not effect the properties of the system and, in a local density approximation (LDA), it can be treated as many independent instances of homogenous clouds with different densities. At each density  $n(\mathbf{r})$  or cloud radius  $r$  we probe a different point in the phase diagram of the BCS-BEC crossover. The local properties of the gas are given by  $\ln(k_F(\mathbf{r})a_{2D})$  and  $T/T_F(\mathbf{r})$ , indicating that as the radius increases and the density decreases  $n(r \rightarrow \infty) \rightarrow 0$  the effective temperature increases  $T/T_F \rightarrow \infty$  and we move towards the BEC regime  $\ln(k_F a_{2D}) \rightarrow -\infty$ .

To determine the in-situ density of either one of the spin components of the cloud  $n_\sigma(\mathbf{r})$  ( $\sigma = |1\rangle, |2\rangle, |3\rangle$ ), we make use of absorption imaging (see section 4.4). We illuminate the atoms using a laser beam from the top that is resonant to the desired hyperfine state and record the shadow of the cloud on a camera below the experiment (see Figure 8.2 c). From the density profiles  $n(r)$  of the atoms obtained in this way we can directly extract the absolute temperature  $T \approx 100$  nK of the gas (see section 4.5). This leads to local properties of the equilibrium state that range from a superfluid  $T/T_F \approx 0.1 < T_C$  in the centre, to the normal phase  $T/T_F \approx 0.1 \gg T_C$  at the edge of

the atom cloud. In this way, we can extract information about a large region of the phase diagram for a single setting of the absolute interaction strength  $E_B$  (or  $a_{2D}$ ) and of the absolute temperature  $T$ . At the same time, due to the inhomogeneous density distribution, it is essential to spatially resolve the response of the gas to the RF pulse, used to probe the system [Shi07]. Otherwise we average over signals from different regions of the BCS-BEC crossover.

### 8.1.2 Spatially Resolved RF Spectroscopy

Once the initial equilibrium state of the 2D Fermi gas is reached, we start an RF spectroscopy sequence to search for pairing in the system [Che09]. To this end, we apply a global RF pulse at a fixed frequency  $\omega_{\text{RF}}$  and for a time of  $t_{\text{RF}} = 4$  ms to the sample. When starting with a  $|1\rangle|2\rangle$  mixture, for example, the pulse is used to transfer atoms from state  $|2\rangle$  to  $|3\rangle$ . Interaction effects, like the formation of pairs, shift the frequency of the transition  $\omega_{|2\rangle\rightarrow|3\rangle}$  with respect to the expected value for free atoms  $\omega_0$  (see Figure 8.3 a). When the thermal state consists of a mixture of both pairs and free atoms, we expect that two energetically separate branches appear in the spectrum.

To extract the RF response as a function of the density  $n(r)$  and frequency  $\omega_{\text{RF}}$ , we take two separate absorption images of the cloud for the spin component  $|2\rangle$ . One image is taken in an experimental cycle with the RF pulse being applied ( $n'(r, \omega_{\text{RF}})$ ) and the other one in a cycle without ( $n_0(r)$ ) (see Figure 8.3 b). The spatially resolved spectral response function is then defined as the normalized difference between both density distributions

$$I(r, \omega_{\text{RF}}) = \frac{n_0(r) - n'(r, \omega_{\text{RF}})}{n_0(r)}. \quad (8.1)$$

The response function indicates at which frequency  $\omega_{\text{RF}}$  atoms in state  $|2\rangle$  are transferred to state  $|3\rangle$  as a function of the radius of the cloud  $r$ , or correspondingly, as a function of the interaction strength  $\ln(k_{\text{F}}a_{2D})$  and temperature  $T/T_{\text{F}}$ . We always display the RF frequencies  $\omega_{\text{RF}}$  relative to the bare transition frequency  $\omega_0$  from  $|2\rangle$  to  $|3\rangle$  for a single free atom.

In Figure 8.3 c, we show the measured spectral response function  $I(r, \omega_{\text{RF}})$  for an initial cloud with a very low absolute temperature  $T \approx 100$  nK and in the centre of the BCS-BEC crossover  $\ln(k_{\text{F}}a_{2D}) \approx 1.5$ . A single branch with a clear density dependence is observed. The density-dependence can be understood from the attractive mean-field shift of the atom cloud we have detected already in section 6.1. As the radius is reduced  $r \rightarrow 0$  and the density becomes larger, the atom cloud acts as an attractive potential well with increasing depth for the atoms. This increases the required energy for the hyperfine state transition into the less interacting mixture  $\omega_{|2\rangle\rightarrow|3\rangle} > \omega_0$ .

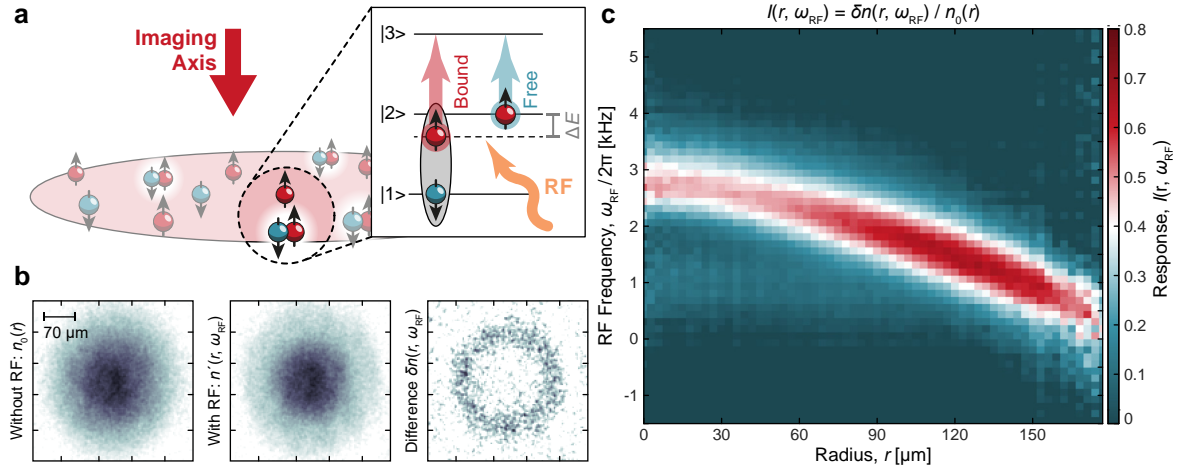


**Figure 8.3: Spatially resolved RF spectroscopy in a strongly interacting 2D Fermi gas.** If two particles in hyperfine states  $|1\rangle$  and  $|2\rangle$  form a pair, the transition frequency  $\omega_{|2\rangle \rightarrow |3\rangle}$  from  $|2\rangle$  to  $|3\rangle$  is shifted by the binding energy  $\Delta E$  with respect to the required frequency  $\omega_0$  for a free atom in  $|2\rangle$  (a). To extract the spatially resolved RF response, we take two absorption images of the density in component  $|2\rangle$  with and without RF pulse applied (b). Their difference  $\delta n(r, \omega_{\text{RF}})$  clearly reveals the density dependence of the resonance frequency. By repeating the measurement for many different RF frequencies  $\omega_{\text{RF}}$ , we obtain the full spectral response function  $I(r, \omega_{\text{RF}})$  (c). At low temperatures all the particles are bound and only a single, paired branch is visible. Adapted from Ref. [Mur18b].

At low temperatures, all the atoms in the balanced mixtures are paired and only one branch is observed. This makes it difficult to distinguish single particle interaction effects, like the mean-field shift that is present also for unpaired atoms, from shifts due to pairing and the binding energy. The key idea for the solution of this problem is to introduce a small imbalance of  $P = (N_{\uparrow} - N_{\downarrow}) / (N_{\uparrow} + N_{\downarrow}) \lesssim 0.15$  to the sample. Some atoms of the majority component  $N_{\uparrow}$  must always remain unpaired since they cannot find a partner. As a result, the free particle branch becomes visible in the spectrum in addition to the response of the paired atoms.

### 8.1.3 From Two-Body to Many-Body Pairing

In Figure 8.4 the measured spectral response functions  $I(r, \omega_{\text{RF}})$  for two different interaction strength settings, towards the BEC regime ( $\ln(k_{\text{F}} a_{2\text{D}}) \approx -0.5$ ) and in the centre

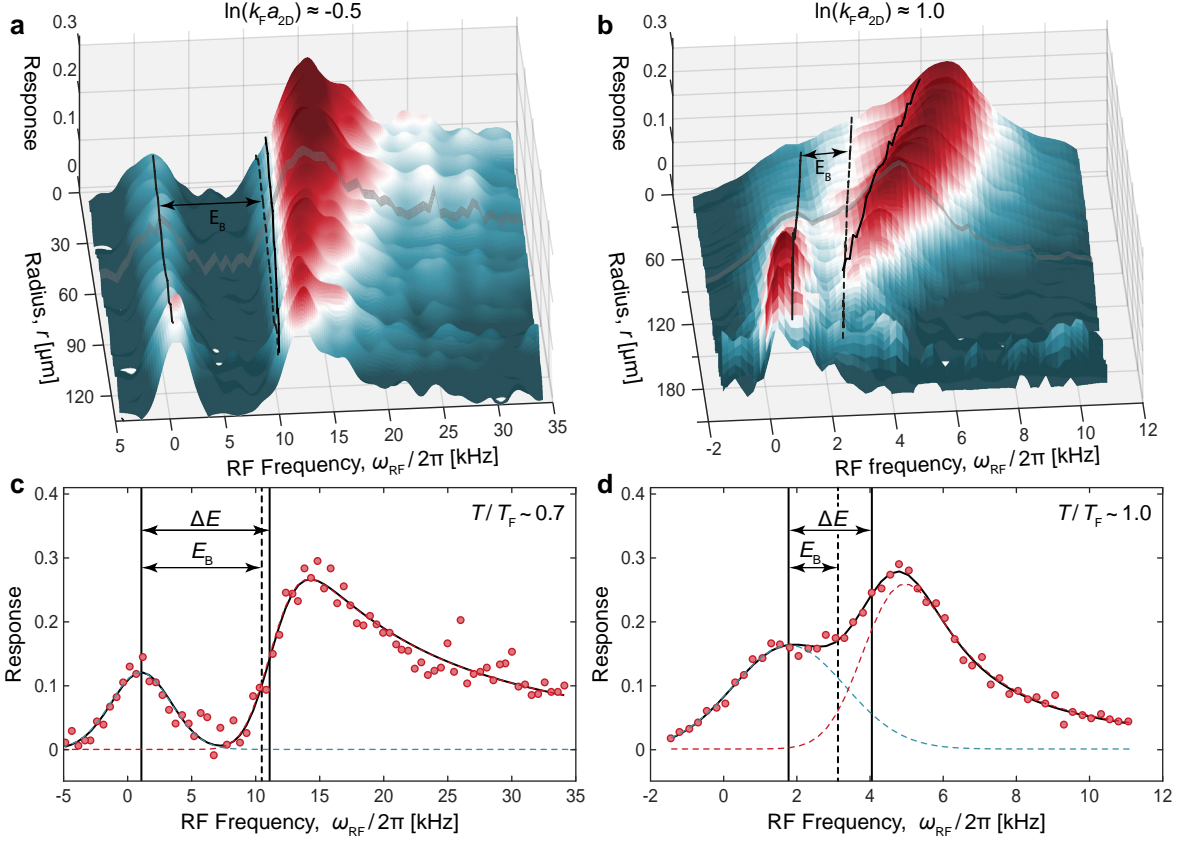


**Figure 8.4: Spectral response functions  $I(r, \omega_{\text{RF}})$  for a 2D Fermi gas with small spin imbalance.** Two different interaction settings, in the BEC regime (a) and in the centre of the crossover (b), are shown. At each setting for the RF frequency, we average over 30 samples of the density distributions  $n'(r)$  and  $n_0(r, \omega_{\text{RF}})$ . We fit a bimodal distribution to the measured spectra at each radius (c,d) allowing us to determine the centre of the free particle branch as well as the threshold of the pair energy (black solid lines). Their difference corresponds to the pairing energy  $\Delta E$ . The dashed line indicates at which frequency  $E_B/\hbar$  we would expect the onset of the paired branch according to the exact two-body solution. Adapted from Ref. [Mur18b].

of the crossover ( $\ln(k_F a_{2D}) \approx 1$ ), are shown for a sample with small imbalance. We clearly observe two excitation branches as a function of the RF frequency  $\omega_{\text{RF}}$ . The lower branch, starting around  $\omega_{\text{RF}} \approx 0$  in the low density limit  $r \rightarrow \infty$ , corresponds to free particle excitations (we report the RF frequencies relative to  $\omega_0$ ). The upper

branch, on the other hand, is the response from paired atoms we have observed already for the balanced gas (see Figure 8.3 c).

We extract the centre of the free particle response and the threshold for the onset of pairing respectively by a combined fit to both peaks at each radius [Mur18b]. Two examples for the local spectra corresponding to  $T/T_F \approx 0.7$  and  $T/T_F \approx 1.0$  respectively are shown in Figure 8.4 (c,d). The radii at which the cuts are taken are indicated by the grey shaded lines in (a) and (b). From the difference of both frequencies, we can directly extract the pairing energy  $\Delta E = \hbar \delta \omega_{\text{RF}}$  at each density. We compare the measurements to the expected value for the two-body binding energy  $E_B$  (dashed line) that is calculated using an exact analytical solution as discussed in detail in section 3.2.8.

The measurements reveal the qualitative nature of pairing in the normal phase 2D Fermi gas. Towards the BEC regime, we find a strongly occupied paired branch even at temperatures far above the superfluid transition  $T \gg T_C$  (see Figure 8.4 a). The pair energy is well explained by the two-body solution  $\Delta E \approx E_B$  and roughly constant as a function of density or radius. This indicates that the pairs are of molecular nature and no collective behaviour (beyond the two-body solution) is required for their description. In the crossover region this picture is modified drastically (see Figure 8.4 b). The amplitude of the paired branch is still very large and its threshold now shows a large density dependence. The pair binding energy exceeds the two-body model significantly  $\Delta E \gg E_B$ . This indicates that in the strongly correlated region ( $\ln(k_F a_{2D}) \sim 1$ ) a collective many-body gap already opens in the normal phase far above  $T_C/T_F \approx 0.1$ , in direct contradiction to the prediction from the BCS theory.

### 8.1.4 Normal Phase in the Crossover Regime

To characterize the normal phase of the BCS-BEC crossover in more detail, we take data points with further settings for the absolute interactions strength  $E_B$ . In addition, we assign the measured local densities  $n(r)$  to their respective points  $(\ln(k_F a_{2D}), T/T_F)$  in the phase diagram. To exclude systematic effects, for example given by final state interactions in the  $|2\rangle|3\rangle$  mixture, we also take data points for a  $|1\rangle|3\rangle$  hyperfine mixture in the initial state. Here, the RF transfer is driven from  $|3\rangle$  to  $|2\rangle$  instead of the other way around. We find that the measured values for the binding energy  $\Delta E$  are robust to the swap of the hyperfine mixture and thereby to a change of the final state interactions.

The measured pairing energies relative to the two-body bound state  $\Delta E/E_B$  as a function of temperature (a) and interaction strength (b) are shown in Figure 8.5. All the data lie at very large relative temperatures  $T/T_F \gtrsim 0.5$  in the normal phase, far above the highest measured point for the transition into the superfluid at  $T_C/T_F = 0.17$  (see Figure 2.6). In the BEC limit, for  $\ln(k_F a_{2D}) < 0.5$ , we find that pairing

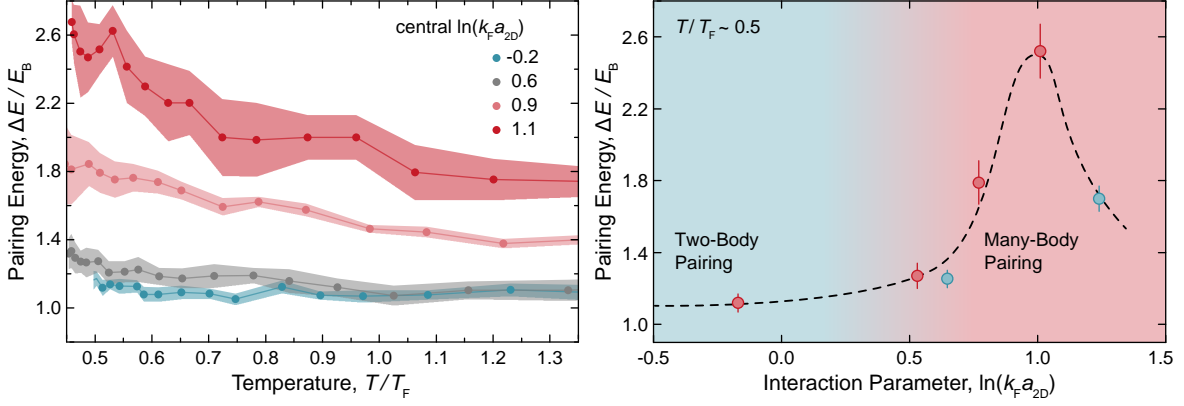


**Figure 8.5: Pairing in the normal phase of the BCS-BEC crossover.** The pairing energy  $\Delta E$  is determined from a bimodal fit to the RF response function at each density. We compare it to the binding energy  $E_B$  from the exact two-body solution. The pairing energy in the BEC limit is independent of density or temperature (a). As the crossover region is approached  $\ln(k_F a_{2D}) \gtrsim 0.5$ , a transition into a many-body paired regime occurs as indicated by the density dependence (a) and  $\Delta E/E_B \gg 1$  (b). All the data points are taken in the normal phase of the gas  $T/T_F \gtrsim 0.5 \gg T_C/T_F$ . Adapted from Ref. [Mur18b].

is consistent with the two-body solution  $\Delta/E_B \approx 1$  and no density or temperature dependence is observed. In contrast, the large density dependence of the pairing energy for  $\ln(k_F a_{2D}) \gtrsim 0.5$ , together with  $\Delta/E_B \gg 1$ , allows us to identify a region where many-body pairing occurs in the normal phase. The maximum in the relative pairing energy  $\Delta/E_B$  is found at  $\ln(k_F a_{2D}) \approx 1$ . Here, the value of the two-intrinsic energy or length scales of the system, given by the inter-particle spacing and the size of the bound state (see section 2.1.5), is precisely the same.

For even larger interactions  $\ln(k_F a_{2D}) > 1$ , we find a downwards trend of  $\Delta/E_B$ . This is consistent with the expectation that pairing is absent in the normal phase in the BCS limit [Frö12]. However, towards the BCS limit, the many-body gap  $\Delta$  becomes exponentially small as a function of the interaction strength (see Figure 8.1). As a result, resolving two different branches in the measured RF response function becomes infeasible in our experiment. A single branch with  $\omega_{\text{RF}} \approx 0$  is observed. For a definite confirmation that the normal phase in the BCS limit consists of a gapless Fermi liquid, further measurements are required.

### 8.1.5 Conclusion

Our measurements demonstrate that the emergence of collective behaviour is not limited to the ground state but also appears in the normal phase of the gas. We identify a region around  $\ln(k_F a_{2D}) \approx 1$  where many-body pairing occurs up to very high temperatures, far above the superfluid in the BCS-BEC crossover. This regime coincides with the strongly correlated region ( $E_B \sim E_F$ ) we have already identified when measuring pair correlations in the ground state of a mesoscopic system (see chapter 7). Here, mean-field descriptions fail and new numerical and analytical approaches including higher order terms have to be developed.

Our measurements reveal the presence of a many-body pairing in the 2D Fermi gas at high temperatures. A subsequent experiment, performed in a completely different apparatus and with solid-state superconductors, has confirmed our results [Nak21]. A pseudogap region, characterized by a reduction of the density of states at the Fermi surface, is observed at temperatures above the superfluid. Additional studies will be required to answer the question of how this pseudogap is related to the superfluid below and the increased critical temperature  $T_C$  in the same region [Tör16; Mue17]. The single particle resolved correlation measurements, as presented in the previous chapters, open up a completely new pathway to address these issues. When applied to the 2D Fermi gas in the normal phase, they allow us to extract the pair character directly and to compare their correlations to other bound states like Cooper pairs, for example. In addition, we can further extend the measurements presented here to the BCS regime and confirm that the normal phase is then gapless.

## 8.2 Observation of a Quantum Anomaly

Symmetries and their violations are a fundamental part of our understanding of emergent collective behaviour in many-body systems [And72]. In chapter 2, we have already introduced the concept of *spontaneous* symmetry breaking. It explains phase transitions, for example from a normal to a superfluid, and critical behaviour with dramatic effects for the physical properties of the given material. Two additional mechanisms by which some quantum state might violate the symmetries of its Hamiltonian exist: *explicit* and *anomalous* symmetry breaking [Hol14].

Quantum anomalies describe the violation of an exact symmetry of a classical action in the quantized version of the same theory [Wei96]. They are often found in quantum field and gauge theories and are an important ingredient to the standard model of particle physics [Geo72; Gro72] or string theories [Gre84; Alv84] for example. While the concepts of spontaneous and explicit symmetry breaking are frequently applied in

many different fields [Col15], quantum anomalies are generally associated with high-energy physics alone. A first exception was found in molecular physics for a  $1/r^2$  potential term [Cam01; Gir08]. This potential leads, exactly as the contact interaction term  $\mathcal{V}_{\text{int}} \propto \delta^2$  in our system, to a very special situation as we will discuss in the following.

### 8.2.1 Conformal Anomaly

The classical Hamiltonian we use to describe a free gas of ultracold atoms (see equation (2.2)) is scale invariant. This special symmetry, where the total Hamiltonian transforms as  $\mathcal{H} \rightarrow \mathcal{H}/\lambda^2$  when the system is rescaled as  $r \rightarrow \lambda r$  appears only as a result of the contact interactions in 2D ( $\delta^2 \rightarrow \delta^2/\lambda^2$ ). A direct quantization of the classical action is impossible, however. It gives rise to inconsistent results like the appearance of bound states with divergent energies. A well-defined quantum theory can only be obtained through a regularization and subsequent renormalization procedure [Mea91; Lev15]. A new length- ( $a_{2\text{D}}$ ) or energy scale ( $E_{\text{B}}$ ) has to be introduced to describe the interactions in 2D (see section 3.2). This additional length scale explicitly breaks the scale invariance of the classical Hamiltonian in its corresponding quantized version of the theory.

So-called *conformal anomalies*, where the scale invariance of the classical action is broken on the quantum mechanical level, are commonly found in field theories like quantum electrodynamics (QED) or quantum chromodynamics (QCD). Here, the renormalized coupling constants, like the electron charge  $e$  for example, depend on the energy scale. In ordinary quantum mechanics, on the other hand, the  $\delta^2$  and  $1/r^2$  potential represent two rare cases where a quantum anomaly appears [Hol93; Coo02]. Here, our goal is to find evidence for the presence of the conformal anomaly and to study what effect it has on the superfluid properties on the ground state of the 2D Fermi gas.

### 8.2.2 Trapped System

In our experiment, the atom cloud is confined to a harmonic potential in radial direction in addition ( $\mathcal{V}_{\text{ext}} \propto r^2$ ). This leads to a slightly modified picture. The scale invariance is replaced by a  $\text{SO}(2,1)$  symmetry of the classical action [Pit97; Wer06]. As a consequence of the  $\text{SO}(2,1)$  symmetry, the collective breathing mode of the atom cloud is predicted to be undamped and it has a constant frequency  $\omega_{\text{B}} = 2\omega_r$  independent of the interaction strength. As was first pointed out by Olshanii et al. [Ols10], this connection can be used as a tool to detect the quantum anomaly directly. When the renormalization of the  $\delta^2$  potential leads to a broken  $\text{SO}(2,1)$  symmetry on the quantum mechanical level, the breathing mode frequency  $\omega_{\text{B}}$  is shifted. The anomaly can be accessed directly through

accurate frequency measurements in quantum gas experiments with either fermionic or bosonic particles in 2D.

The anomalous breaking of the  $SO(2,1)$  symmetry has been studied extensively on a theoretical level both at zero [Tay12; Hof12; Gao12; Cha13; Hu19] and finite temperature [Mul18; Daz18]. In the ground state, frequency shifts above the scale invariant value of  $\omega_B = 2\omega_r$  of up to 10 % have been predicted [Hof12; Gao12]. At finite temperatures, perturbative solutions indicate that the frequency shift is much smaller, on the order of 1 %, or even negative such that  $\omega_B < 2\omega_r$ . In experiments, the effect has been elusive for both bosonic [Jac02; Che02; Hun11] as well as fermionic [Vog12; Bau13] studies in 2D. No significant frequency shift away from  $\omega_B = \omega_r$  has been observed in any of the measurements preceding our work. In the case of bosonic samples this has been attributed to insufficiently strong interaction strength, while the fermionic studies have been limited by statistical errors and high temperatures [Hof12]. Here, we perform a precision experiment with a macroscopic 2D Fermi gas and at very low temperatures  $T/T_F = 0.14(4)$ . This enables us to directly observe a significant frequency shift of the collective breathing mode oscillation  $\delta\omega_B$  as evidence for the presence of anomalous symmetry breaking.

### 8.2.3 Experimental Sequence

For the preparation of a 2D Fermi gas, we proceed exactly as in section 8.1.1. A two component mixture with  $N \approx 10\,000$  atoms per spin state is transferred to a single 2D layer of the SWT (see Figure 8.6 a,b). In contrast to the measurement described in the previous section, we work at the lowest accessible temperatures in our experiment and in the superfluid regime. The temperatures vary from  $T/T_F = 0.1$  in the BEC limit to 0.18 in the BCS regime. The interaction strength  $\ln(k_F a_{2D})$  is set using the magnetic offset field  $B$  once the initial state has been prepared.

To excite breathing mode oscillations, we start by adiabatically lowering the radial confinement  $\omega_r$  such that the gas expands in the trap. A sudden quench back to the initial value  $\omega_r = 22.5(1)$  Hz leads to both dipole and breathing oscillations with a small amplitude of  $\approx 8\%$  of the total cloud width. We do not find that higher order collective modes are excited using this procedure. To study the collective motion of the macroscopic cloud, we take a time series of 200 absorption images in steps of  $\Delta t = 2$  ms and starting at the potential quench (see Figure 8.6 c,d). The absorption images along the axial direction (see section 4.4) clearly reveal the breathing oscillation (see Figure 8.7 a-c). Using the other potentials in our apparatus, like the CBODT, we can also excite other collective oscillations, for example the quadrupole mode (see Figure 8.7 d-f). More details on the quadrupole mode, that can be used to access quantities like the shear viscosity  $\eta$  of the gas, can be found in Ref. [Hol17].

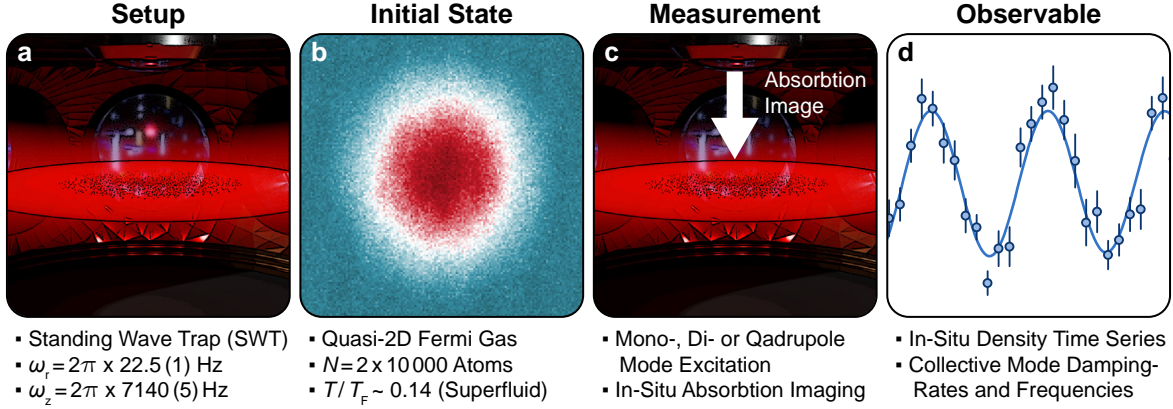


**Figure 8.6: Experimental sequence for the study of a quantum anomaly.** The state is initialized by loading a large sample of atoms into a single layer of the SWT (a). This leads to a quasi-2D Fermi gas within the superfluid regime of the BCS-BEC crossover (b). To reveal the quantum anomaly, we excite a breathing mode oscillation by quenching the strength of the radial confinement from a smaller to a larger value. The collective motion of the cloud is revealed by taking a time series of absorption images along the axial direction (c). Breathing ( $\omega_B$ ) and dipole mode ( $\omega_D$ ) frequencies are extracted by fitting a sine function to the cloud width and centre as a function of time respectively (d).

The 2D harmonic potential in radial direction has a slight anisotropy of  $(\omega_x - \omega_y)/(\omega_x + \omega_y) \approx 2\%$  in our experiment. We obtain the angle of the principal axis  $x$  and  $y$  in our trap using a principal component analysis (PCA) (see section 4.5.2). We extract the frequencies of the breathing ( $\omega_B$ ) and dipole ( $\omega_D$ ) modes along both principal trap axes independently. To this end, we fit a sine function to the width and centre position of the cloud as a function of time respectively. The result for a dataset in the  $x$ -direction is shown in Figure 8.7 g. In total we obtain four frequency measurements ( $\omega_{B,x}, \omega_{B,y}, \omega_{D,x}, \omega_{D,y}$ ) for each setting of the interaction strength  $\ln(k_F a_{2D})$  in this way.

For all interaction strengths we access in our experiment, we are in the hydrodynamic regime of the 2D Fermi gas [Hol17]. This leads to a *locking* of the breathing mode frequencies along both principal directions and  $\omega_B \equiv \omega_{B,x} = \omega_{B,y}$ . We average over the measurements in both directions. To reveal the presence of the quantum anomaly and to compare the measured breathing frequency to the scale invariant result  $\omega_B = 2\omega_r$ , a precise determination of the radial trap frequency is required.

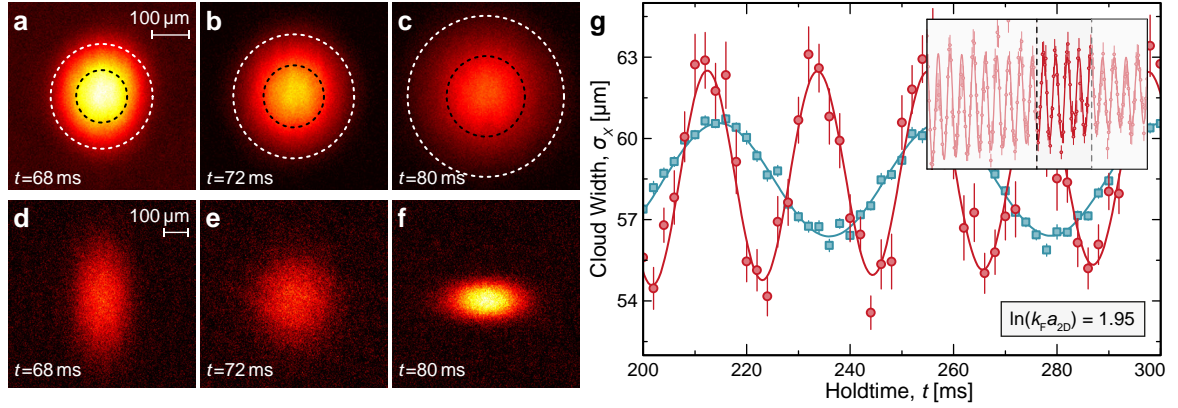


**Figure 8.7: Collective modes of a 2D Fermi gas in a harmonic confinement.**

Three absorption images of the in-situ density distribution, taken at different times after a quench of the radial confinement strength at  $t = 0$ , clearly reveal the breathing mode oscillation. The dashed black and white circles indicate the 1 and 2  $\sigma$  widths of a fit of a 2D Gaussian function to the data. The images were taken at a larger amplitude than the dataset used for the detection of the quantum anomaly to make the oscillation more apparent. Other optical potentials in our experiment allow us to excite higher order collective modes, like a quadrupole oscillation, in addition (d-f). The oscillation of the cloud width along one of the principal axes of the trap  $\sigma_x$  allows us to obtain the breathing mode frequency (g, red). The blue line shows the dipole mode oscillation of the cloud in the same direction as a comparison. The inset shows the full dataset from  $t = 0$  ms to 400 ms. Adapted from Ref. [Hol18].

### 8.2.4 Trap Frequency Characterization

The centre-of-mass oscillations of the cloud, or dipole modes, decouple as a result of the anisotropy ( $\omega_{D,x} \neq \omega_{D,y}$ ). Their oscillation frequency in each of the principal trap directions is given by the effective trap frequency  $\omega_{D,x/y} = \omega_{R,x/y}$  (see Figure 8.7 g, blue line). We take the average of both values as the reference trap frequency to compare the breathing mode to  $\omega_r = (\omega_{D,x} + \omega_{D,y})/2$ . This is justified in the hydrodynamic limit, where the breathing mode is insensitive to small anisotropies in the potential and, in a scale-invariant picture, oscillates at twice the average trap frequency up to very small corrections on the order of  $\approx 0.1\%$  [Hof12; Mer13; Hol17].

The effective radial trap frequency  $\omega_r$  depends on several systematic parameters in our system (see Figure 8.8). The confinement is given by the superposition of an

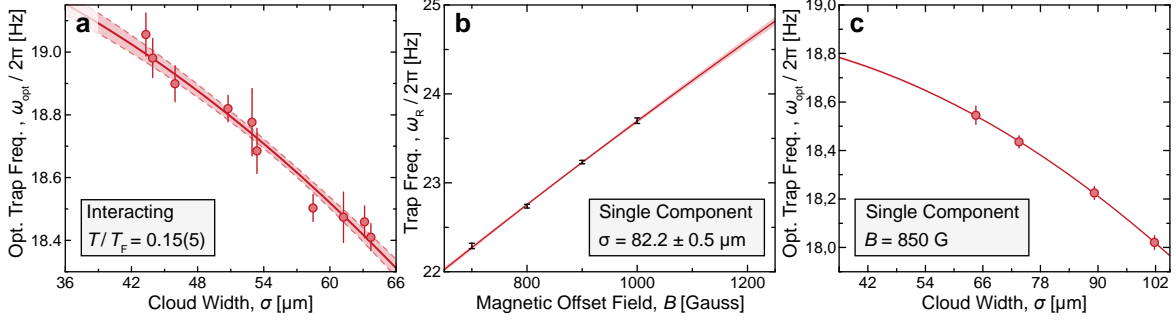


**Figure 8.8: Characterizing the radial trap frequency  $\omega_r$ .** The trap frequency can be determined by measuring the dipole mode oscillation frequency in an interacting sample (a). We compare the results to a model (solid line), where the effective trap frequency  $\omega_r(B, \sigma)$  depends on the magnetic offset field  $B$  and the width of the atomic cloud  $\sigma$ . The model depends on three parameters that are determined by fitting to the measured dipole mode frequencies in a non-interacting, single component gas (b,c). We find that the model explains our measurements with very high accuracy. Adapted from Ref. [Hol18].

optical and a magnetic potential (see section 4.1.4). The magnetic confinement  $\omega_r^{\text{mag}}$ , depends on the offset field  $B$  as  $\omega_r^{\text{mag}} = \sqrt{a \cdot B}$ , where  $a$  is some parameter that depends on the magnetic dipole moments of the atoms and the exact coil geometry. The effective optical confinement  $\omega_r^{\text{opt}}$  depends on the width of the cloud  $\sigma$ . This can be explained by the small anharmonicity of  $\approx 10\%$  of the Gaussian beam optical trap. In a Taylor expansion, larger systems are effected more by the deconfining  $r^4$ -term and their effective trap frequency  $\omega_r^{\text{opt}}$  is reduced.

To model all the systematic effects on the radial trap frequency, we use the following equation

$$\omega_r(B, \sigma) = \sqrt{(\omega_r^{\text{opt}})^2 + (\omega_r^{\text{mag}})^2} = \sqrt{\omega_0^2(1 - \delta\sigma^2)^2 + a \cdot B}, \quad (8.2)$$

where the parameters  $\omega_0$ ,  $\delta$  and  $a$  are determined from fits to several independent measurements performed in non-interacting, single component gases (see Figure 8.8 b,c). We find that the model explains all our dipole mode frequency measurements with very high accuracy, both for interacting as well as for non-interacting samples. This confirms that our experiment allows us to perform precise frequency measurements and that possible shifts, as the result of anomalous symmetry breaking, on the order of a few percent can be detected.

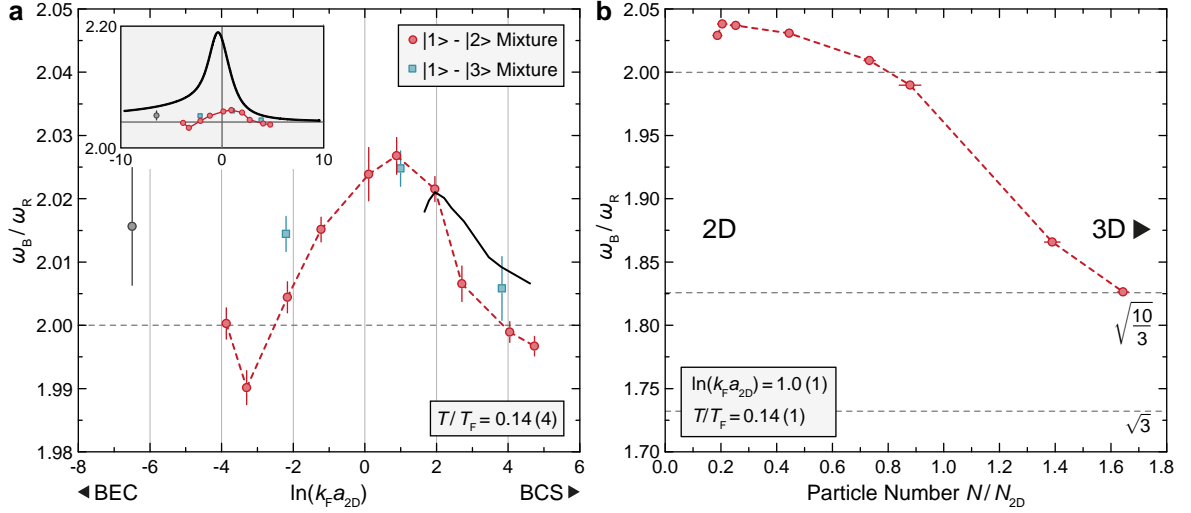


**Figure 8.9: Anomalous shift of the breathing mode frequency  $\omega_B$ .** At low temperatures, we find a significant frequency shift towards higher frequencies (a). Our data agree well with the mean-field approximation at  $T/T_F = 0.2$  from Ref. [Mul18] (solid black line). The inset compares our measurements to a calculation at zero temperature [Hof12]. To exclude systematic effects, we have taken measurements with two different spin mixtures (red and blue). Here, the same interaction parameter  $\ln(k_F a_{2D})$  is obtained for very different magnetic offset fields  $B$  and absolute radial trap frequencies  $\omega_r$ . As we increase the particle number, the frequency shift is reduced until it becomes negative towards the 3D regime of our gas (b). Adapted from Ref. [Hol18].

### 8.2.5 Anomalous Symmetry Breaking

The measured breathing mode frequencies in units of the radial trap frequency and as a function of the interaction strength are shown in Figure 8.9 a. We find a small but very significant shift of the breathing frequency with a maximum of 1.3% in the strongly interacting region  $\ln(k_F a_{2D}) \approx 1$ . In the BEC and the BCS limits, no shift is observed and the scale invariant result  $\omega_B = 2\omega_r$  is restored. The grey data point has been excluded from our analysis due to the large three body losses and small lifetimes we have observed for our sample this far in the BEC regime. The positive frequency shift is a direct manifestation of the quantum anomaly that is present in a 2D Fermi gas. All other effects that explicitly break the symmetry of the Hamiltonian are expected to cause a reduced breathing frequency instead [Hol18].

Compared to a calculation at zero temperature (inset), the shifts we observe in our

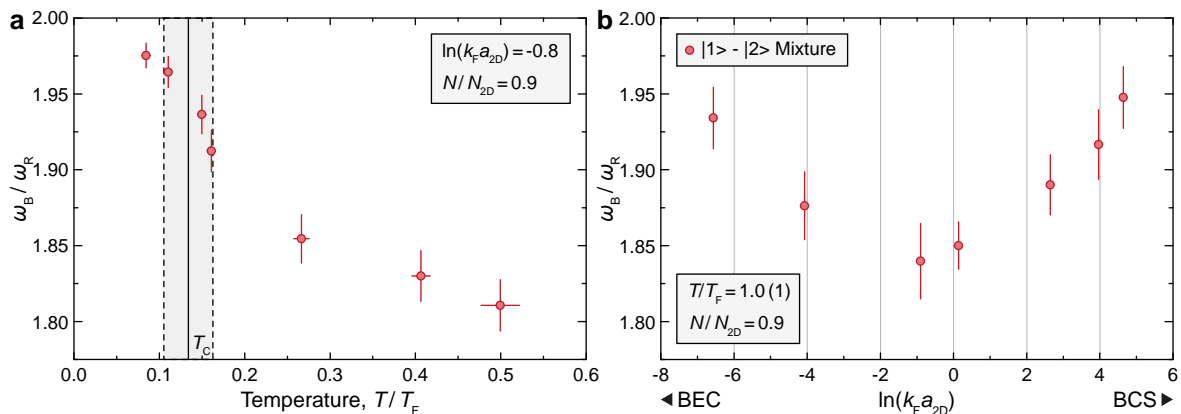


**Figure 8.10: Breathing mode frequency  $\omega_B$  at higher temperatures.** We heat the sample by modulating the radial confinement of the gas. As the temperature increases, the breathing mode frequency reduces significantly (a). This effect is strongest in the strongly interacting regime, while in both the BEC and BCS limits no large shifts away from the scale invariant frequency  $\omega_B = 2\omega_r$  are observed (b). Adapted from Ref. [Hol18].

experiment are much smaller in magnitude. This explains why anomalous symmetry breaking has not been observed in any of the previous experiments. There are several effects that can lead to a reduction of the frequency shift [Hu19; Tay12; Mul18; Yin20]. First is the presence of the third dimension in our experiment, leading to a quasi-2D description with only approximate validity. We study this effect by increasing the particle number  $N$  of our atom cloud (see Figure 8.9 b). In a non-interacting sample only a maximum of  $N_{2D} = 48\,000$  oscillator levels are available before higher states in axial direction become populated and the quasi-2D description breaks down.

As we approach the 3D limit,  $\omega_B$  reduces quickly (see Figure 8.9 b). The negative shift agrees with calculations of the breathing mode frequencies in the BEC and unitary limits of a 3D Fermi gas confined to a *pancake* shaped trap. In these two limits, respective values of  $\omega_B = \sqrt{10/3}\omega_r$  and  $\omega_B = \sqrt{3}\omega_r$  are expected [Ros15]. The explicit breaking of scale invariance by the presence of the third dimension has been studied in more detail for Bose gases in Refs. [Mer13; Ton18].

A second important effect we have to consider is the non-zero temperature of our gas. We have taken additional measurements of the breathing mode oscillation for heated samples (see Figure 8.10). We find that for larger temperatures, the frequency  $\omega_B$  reduces significantly, especially in the strongly correlated region. The negative shift is predicted by theoretical calculation at finite temperatures [Hof12; Mul18]. In the BEC and BCS limits, the scale invariant result is restored again, even at much higher

temperatures  $T/T_F = 1.0(1)$ . Taken together, both the effects of temperature and third dimension can explain an anomalous shift that is significantly reduced compared to a measurement at zero temperature and in the strict 2D limit. The small shift of the breathing frequency has been confirmed by an independent study that was performed simultaneously to our measurements [Pep18].

## 8.2.6 Microscopic Viewpoint

Starting from the microscopic Hamiltonian with the  $\delta^2$  contact interaction term, the presence of a quantum anomaly seems quite surprising. Even though the scaling symmetry is implemented exactly in the classical action, it is broken in any corresponding finite quantum theory of the same model we can write down. From a microscopic viewpoint, the quantum anomaly can be understood more intuitively. The  $\delta^2$  term describes the Van der Waals interactions between neutral atoms only approximately. For scattering processes at large energies or small radii  $r \rightarrow 0$ , a more accurate description has to be taken into account (see section 3.2). The full Hamiltonian, including the correct interaction potential  $\mathcal{V}_{\text{vdw}}$ , breaks the scaling symmetry explicitly and explains the frequency shift of the breathing mode in this way.

Quantum anomalies can generally be understood in this way. They appear in situations where the classical action fails to accurately describe the behaviour of the physical system at small lengths or high energy scales. In contrast to a gas of ultracold atoms, more accurate physical descriptions of the high energy behaviour are unknown in most other cases like the standard model for example. Quantum anomalies highlight both the value as well as the limits of renormalization theory in many-body physics. Universal descriptions of systems can be obtained in the low energy limit without taking into account, or sometimes even knowing, the correct model at small length scales.

## 8.2.7 Momentum Space

We have detected anomalous symmetry breaking by performing a precision study of the breathing frequency of the monopole mode of our cloud [Hol18]. This immediately raises the question whether the effect has any significance for the physical properties of the gas, for example in connection to its superfluid ground state. To find an answer, we have performed an additional study, where we extract the properties of the superfluid by taking absorption images in momentum space [Mur19]. The measurements of the pair momentum distribution  $n(k)$  (see section 4.4) allow us to extract important properties of the superfluid like the first-order coherence function  $g_1(r)$  [Mur14; Mur15b].

The presence of scale invariance simplifies the description of collective behaviour in our system significantly. The sample becomes fully integrable and the dynamics of the

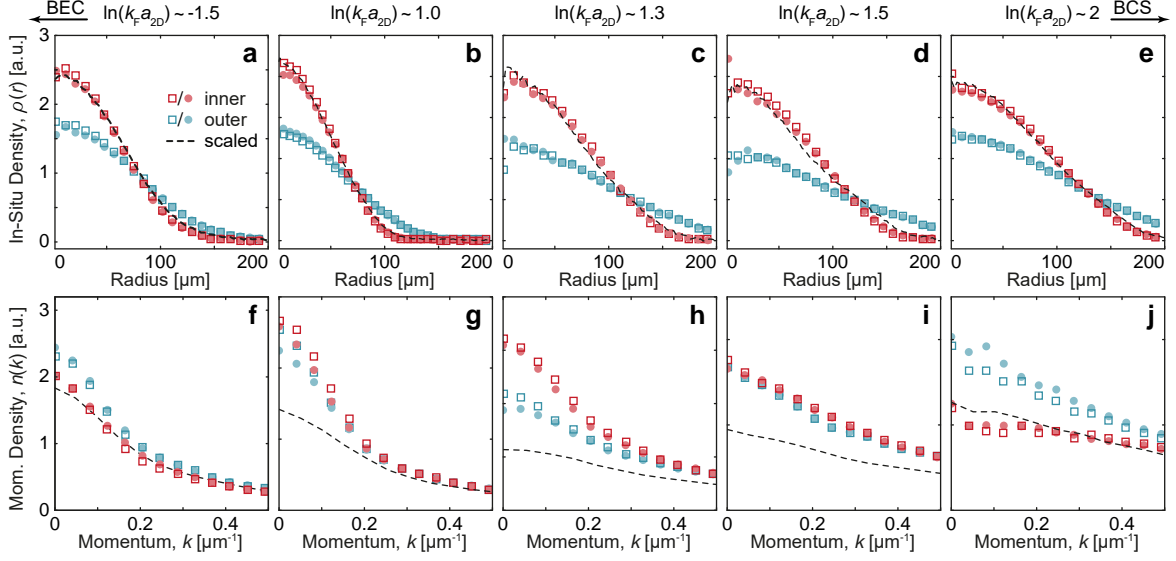


**Figure 8.11: Density scaling relations in real and momentum space.** The in-situ and momentum space density distributions are measured at two different times (circles and squares) for each of the two turning points (red=inner and blue=outer) of the breathing oscillation. The different in-situ density distribution can always be rescaled into one another with a single scaling factor  $\lambda$  and by applying equation (8.3) (dashed line). Scale invariance breaks down in momentum space, where we observe a significant deviation from the scaling relations in the strongly correlated crossover region (g-i). Adapted from Ref. [Mur19].

full time-dependent many-body wavefunction  $\Psi_N(\mathbf{r}_i, t)$  can be expressed directly in terms of the initial state  $\Psi_N(\mathbf{r}_i, t = 0)$  [Mur19]. In equilibrium, the in-situ  $\rho(r)$  and momentum  $n(k)$  distributions after a rescaling transformation  $r \rightarrow \lambda r$  can be obtained from the original distributions  $\rho_0$  and  $n_0$  directly as

$$\begin{aligned} \rho(r) &= 1/\lambda^2 \rho_0(r/\lambda), \\ n(k) &= \lambda^2 n_0(\lambda k). \end{aligned} \quad (8.3)$$

This implies that the superfluid properties, encoded in the pair momentum distribution  $n(k)$ , show universal behaviour and can simply be rescaled into one another independently of the absolute density  $\rho$ .

To check if the quantum anomaly effects the collective behaviour of our system, we excite the breathing mode oscillation again. At this point, we are not interested in its frequency, however. We rather use the collective motion as a tool to perform a scale

transformation  $r \rightarrow \lambda r$  directly in our experiment. The breathing oscillation has two turning points at times  $t = t_o$  and  $t = t_i$  where the gas is momentarily at rest and, since the breathing frequency is much smaller than the scattering rate  $\omega_B \approx 40 \text{ Hz} \ll 10 \text{ kHz}$ , in its equilibrium state. In the outer turning point the cloud is the largest and it has the lowest density while at the inner turning point a maximal density is reached before the expansion starts again (see Figure 8.7 a,c). This corresponds to a pure scale transformation  $r \rightarrow \lambda r$  between the clouds at these time points  $t = t_o, t_i$ , while all other physical properties like the interaction strength  $E_B$ , temperature  $T$  and particle number  $N$  remain the same.

In Figure 8.11, we show the measured density distributions in position  $\rho(r, t)$  and momentum space  $n(k, t)$  for the inner ( $t = t_i$ ) and outer turning point ( $t = t_o$ ) of the breathing oscillation. We try to rescale the density at the outer turning point to the distribution at the inner turning point by applying equations (8.3) and by fitting the scaling parameter  $\lambda$  to the in-situ distributions. The scaling relations hold both in the BEC (a, f) as well as in the BCS (e, j) limits. In the strongly correlated crossover region  $\ln(k_F a_{2D}) \approx 1$ , however, the simple picture breaks down (g-i). The momentum distribution  $n(k, t_i)$  at the inner more dense turning point can not be obtained by simply rescaling the distribution at the outer turning point  $n(k, t_o)$ . Instead, the measured momentum distribution  $n(k, t_i)$  shows a significant surplus of pairs with small momenta compared to the scaled solution. This is another manifestation of the quantum anomaly that reveals itself in momentum space distributions measured at different absolute cloud densities.

To understand the effect of the anomaly on the coherence properties of the gas, we extract the first-order correlations function  $g_1(r)$  in addition. It can be obtained from  $n(k)$  directly by performing a Fourier transform and expresses over which distance  $r$  particles are correlated in the superfluid [Mur15b]. In 2D the correlations decay algebraically  $n(k) \propto r^{-\eta}$  with some exponent  $\eta$ . In Figure 8.12 a, we show the measured coherence properties of the superfluid at the inner and outer turning points of the breathing oscillation respectively. In the BEC regime, the coherence properties of the two systems with different densities are the same and the decay coefficients agree  $\eta_i = \eta_o$  (top). In the crossover regime, on the other hand, the simple scaling relations are violated and the correlations at the inner turning point decay more slowly  $\eta_i < \eta_o$ . In Figure 8.12 b, we show the measured ratio  $\eta_i/\eta_o$  for different interactions across the BCS-BEC crossover. We find that the effect of the scale anomaly is strongest in the same region  $\ln(k_F a_{2D}) \approx 1$  we have already identified when studying the breathing mode frequency. Here, the pair size is of the order of the inter particle distance and the interplay between all intrinsic length scales of the system becomes important for its description.

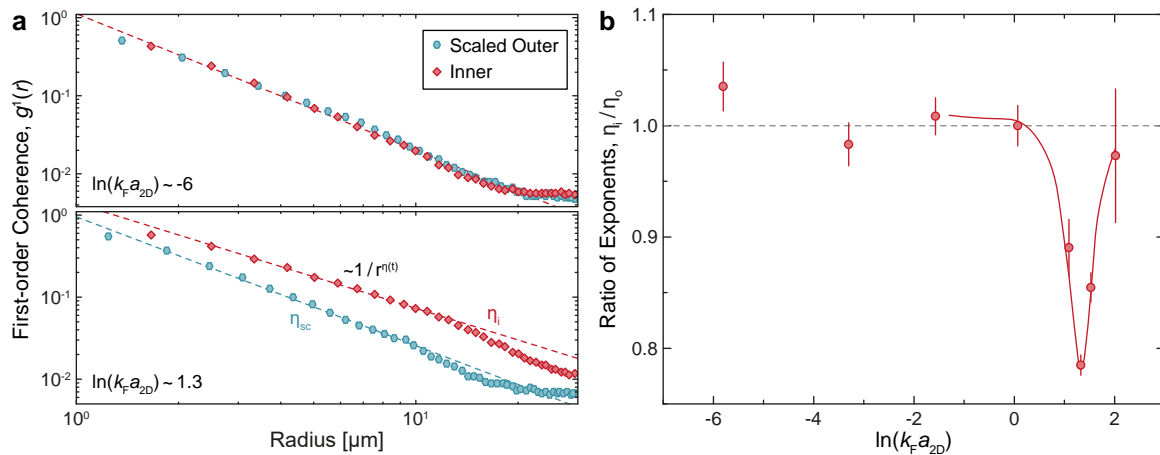


**Figure 8.12: Effect of the quantum anomaly on spatial coherence.** The first-order coherence function  $g_1(r)$  is obtained by Fourier transforming the measured momentum distributions  $n(k)$  at the inner and outer turning points. The correlations in the 2D superfluid decay algebraically with distance  $n(k) \propto r^{-\eta}$ . In the BEC regime the decay of the correlations at both turning points, after applying the scaling transformation, is described by the same coefficient  $\eta_i = \eta_o$  (a, top). This is different in the crossover region, where the scaling symmetry is broken anomalously (a, bottom). The inner, more dense, turning points show a slower decay of correlations than expected  $\eta_i < \eta_o$ . In (b), we plot the measured ratio of both decay coefficients as a function of the interaction parameter  $\ln(k_F a_{2D})$ . Adapted from Ref. [Mur19].

## 8.3 Conclusion

The violation of scale invariance can be understood by making the connection to the measurement of pairing in the normal phase we presented in the first section of this chapter. Here, in the same strongly interacting region, we find collective many-body pairs in the normal phase of the gas and with a strong dependence of their binding energy on the density. It is justified to assume that similar pairing correlations are also present in the superfluid region below. In both the BCS and BEC limits, pairing can be described with simple mean-field models  $E_B \rightarrow 0, \infty$  and in terms of two-body correlations alone. In the crossover regime, higher order correlations have to be considered and their strong density dependence, since two-body bound state size and inter particle distance are of the same order, leads to a violation of scale invariance. The smaller decay coefficient  $\eta$  at the denser inner turning point indicates that the

superfluid stiffness grows quicker with density than expected in this case and could also explain the increased transition temperature in the same region [Mur19].

The measurements in this chapter have demonstrated that even in the macroscopic system many exciting problems remain to be studied both in the ground state as well as for samples with higher temperatures. Here, we find another form of emergent collective behaviour not as a function of the particle number  $N \rightarrow \infty$ , as in chapter 6 for example, but as a function of the binding energy  $E_B$ . Complex behaviour with correlations between all the constituents of the system appears as soon as the different energy scales of the system become of the same order and compete against each other, for example when  $E_F \sim E_B$ .

Our new apparatus allows us to address many of the remaining questions that were raised in this chapter. For example, we can directly extract the single particle resolved pair correlations in momentum space in the normal phase of the gas. The preparation of quantum states at extremely low temperatures, close to the absolute ground state, and with very small particle numbers will enable us to finally resolve the question about the origin of the reduced anomalous shift of the breathing mode frequency. New measurements hopefully initiate the development of a more complete theoretical description beyond the mean-field level of the BCS-BEC crossover.

# 9

## Summary and Outlook

Emergent collective behaviour is at the heart of many of the biggest unresolved problems of the 21st century in physics. Even after many decades of extensive research, many-body systems are still full of surprises and a general understanding remains out of reach. In many fields, for example concerning highly non-linear phenomena like turbulence and chaos, mesoscopic systems like nuclei and large molecules or strongly correlated fermionic materials like high- $T_C$  superconductors or strange metals, new approaches are required to make further progress [Gin01].

In this thesis, we have presented a completely new approach — from the bottom-up — to emergent phenomena in strongly correlated Fermi systems. We have developed several techniques that give us an unrepresented degree of control over small ultracold samples of neutral  ${}^6\text{Li}$  atoms. We are able to prepare Fermi gases with deterministic particle numbers at extremely low temperatures and, for up to 20 particles, in the absolute ground state of our 2D harmonic confinement (see chapter 4). A fluorescence imaging technique allows us to obtain single particle and spin resolved samples of the full many-body wavefunction in momentum space, even for strongly interacting initial states. The method extends the scope of quantum gas microscopy from lattices to continuous systems.

When applied to small, non-interacting Fermi gases in the ground state, our imaging technique allows us to directly detect the influence of the Pauli principle (see chapter 5). We find strong higher-order correlations in the relative momentum coordinates of the particles that can be visualized as *Pauli crystals*. The measurements show that self organization can occur in many-body systems even in the complete absence of interactions and highlights the importance of the antisymmetrization for the description of the fermionic quantum state. A comparison of the obtained correlations to numerical calculations allows us to benchmark the performance of our imaging technique in detail.

When increasing the attractive interaction strength of the atoms in the mesoscopic 2D Fermi gas, we observe a precursor of a quantum phase transition from a normal to a superfluid (see chapter 6). The transition is revealed by a non-monotonous pair

excitation mode in the low energy spectrum of the system. The mode can be associated with a Higgs mode in the macroscopic limit that corresponds to amplitude vibrations of the order parameter. All the qualitative features of the phase transition can already be observed for very small particles numbers for example with as few as six atoms. The measurements demonstrate how universal collective behaviour emerges, starting at the mesoscopic scale. The observed effects originate from higher organising principles like spontaneous symmetry breaking and are very robust to changes in the microscopic model. Imperfections in the potential like an anharmonicity or anisotropy do not influence the transition significantly and even considerable approximations of the contact interaction term lead to the same qualitative result.

In chapter 7, we have directly accessed the fundamental correlations in the ground state. The measured second order density correlations reveal the transition from an unpaired ground state to a few-body precursor of a superfluid. In the weakly interacting regime, we directly observe Cooper pairs in the momentum space samples of our wavefunction. They manifest themselves as strong positive correlations between particles of opposite spin and momentum located at the Fermi surface. As the binding energy is gradually increased, the pairs transform to more tightly bound molecules and correlations appear also deep within the Fermi sea.

The results presented in this thesis demonstrate significant breakthroughs in the manipulation and detection of strongly interacting 2D Fermi gases. The access to single particle resolved samples of the many-body wavefunction enables measurements, like the direct observation of Cooper pairs, that have been out of reach for other systems like nuclei or solid state materials [Boh98; Del01]. Our highly programmable platform offers completely new possibilities to address many outstanding questions concerning mesoscopic Fermi systems and their connection to the macroscopic world (see chapter 8). In the following, we present a small excerpt of the most immediate applications.

## 9.1 Real Space Correlations

So far, our measurements of single particle and spin resolved density distributions have been limited to momentum space alone. An even more complete characterization of the many-body wavefunction and the density matrix requires additional measurements in other bases, for example in real space [Ber19]. In some occasions measurements of the in-situ density distribution also give a more straightforward access to the relevant correlations of the system under study. In the BEC regime of the BCS-BEC crossover, for example, molecules are expected to appear as a strong positive correlation peak at short distances  $\mathbf{r} \rightarrow 0$  in real space. The pairing signal is spread out much further in momentum space (see chapter 7).

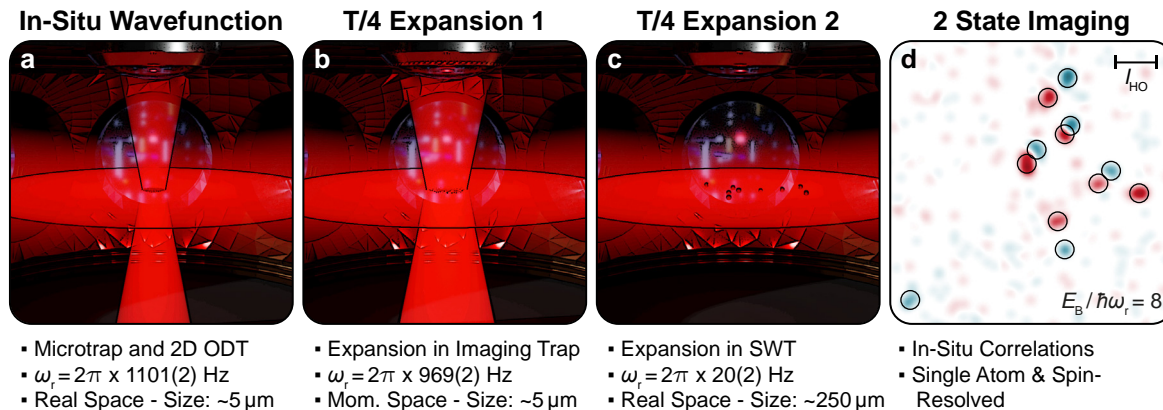


**Figure 9.1: Magnification of the in-situ many-body wavefunction.** A magnification technique is used to sample the in-situ wavefunction with single particle resolution, analogously to the images we obtain in momentum space. In the first step, the interactions of the in-situ sample (a) are switched off instantaneously and a ballistic expansion in a harmonic potential in radial direction is started (b). After a quarter trap period  $t_{\text{TOF}} = T/4$ , the in-situ density distribution has been mapped to the momentum distribution and vice versa. Subsequently, a second expansion is performed in the SWT (c). After a quarter trap period in this potential the wavefunction has expanded significantly. Momentum space is mapped back to real space again and by taking fluorescence images, we can excess the in-situ density distribution — magnified by a factor of almost 50 and with single particle resolution. For large interaction strength  $E_B = 8 \hbar\omega_r$ , we directly observe molecular short distance correlations in real space (d).

The finite resolution of our fluorescence imaging technique prevents us from directly taking single particle resolved snapshots of the in-situ density distribution of our 2D Fermi gas. The only notable exception are non-interacting harmonic oscillator ground states, where real and momentum space are completely equivalent and the TOF expansion can be seen as a pure magnification of the many-body wavefunction (see chapter 5). Through an extension of our TOF expansion scheme we are able to magnify the in-situ many-body wavefunction even for strongly interacting initial states (see Figure 9.1). The key idea is to perform a second ballistic expansion for a quarter trap period in some additional harmonic potential to map real to momentum space and vice versa before the final imaging TOF sequence begins [Ast21].

Our implementation allows us to magnify the in-situ wavefunction by a factor of  $\omega_{\text{TOF},1}/\omega_{\text{TOF},2} = 969 \text{ Hz}/20 \text{ Hz} \approx 50$ . First measurements in the strongly interacting

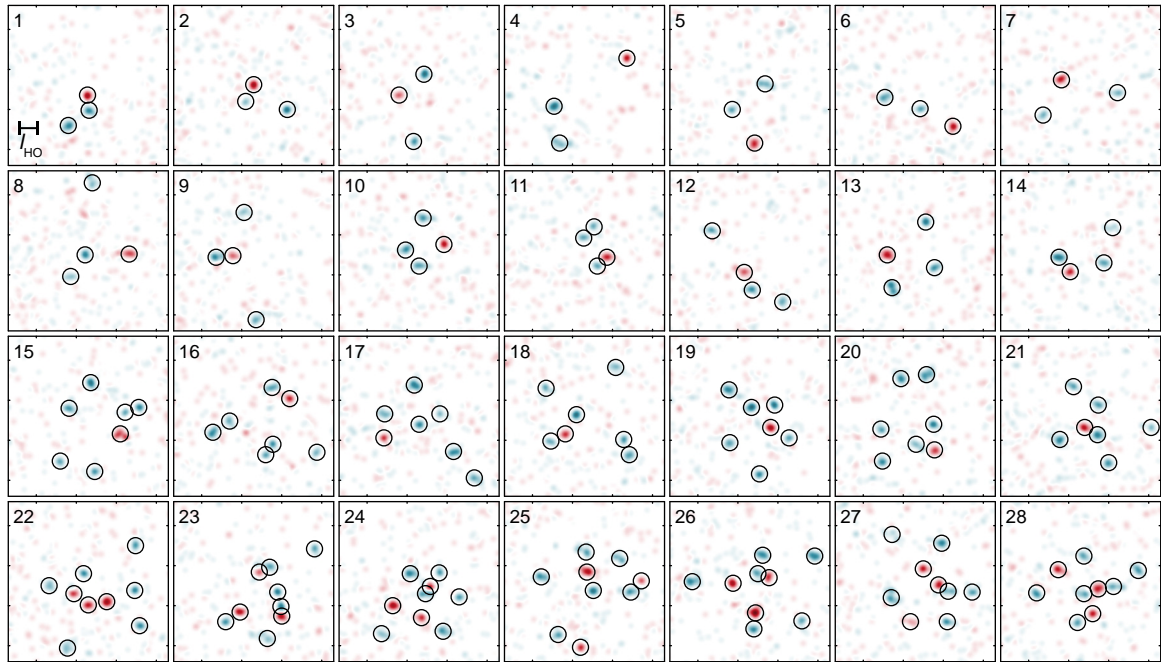


**Figure 9.2: Spin imbalanced ground state configurations.** Our deterministic spilling scheme in 2D can be extended for the preparation of spin imbalanced ground states in the 2D harmonic oscillator potential. Both open- (1-7) and closed-shell (8-28) configurations are possible. The images show single particle resolved images of the momentum distribution of the spin imbalanced ground state for different prepared initial state configurations in each row.

regime ( $E_B = 8 \hbar \omega_r$ ) reveal the presence of molecules in the gas (see Figure 9.1 d). The access to both in-situ and momentum correlations with full spin and single atom resolution opens up completely new pathways to address the complex physics of the strongly correlated central region of 2D BCS-BEC crossover in the future.

## 9.2 Spin Imbalanced Systems

BCS theory explains superconductivity through Cooper pairs that form between particles of opposite spin at the Fermi surface. The BCS ground state is therefore very sensitive to a mismatch in the number of both spin species [Che10]. Exotic states like the Fulde–Ferrell–Larkin–Ovchinnikov (FFLO) phase have been predicted to occur for

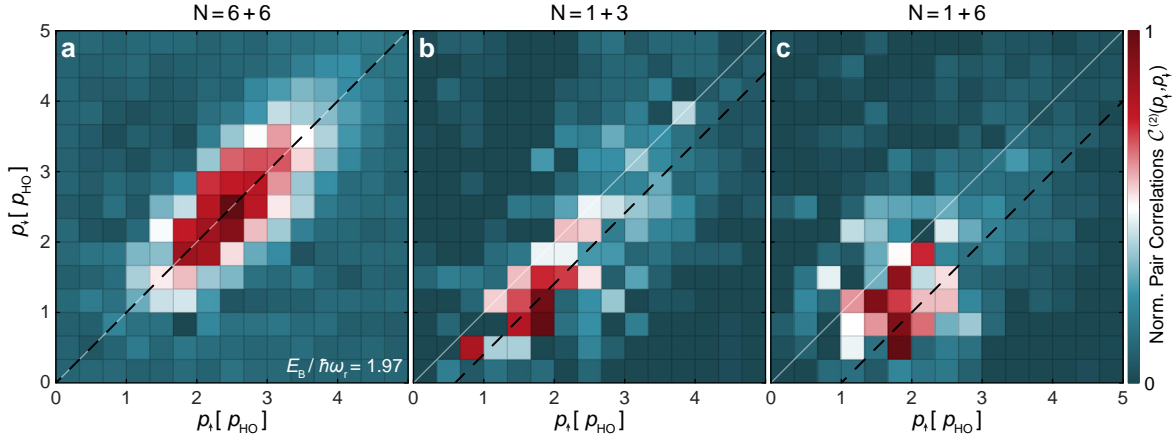


**Figure 9.3: Unconventional Cooper pairing.** We plot the second order density correlations in momentum space  $\mathcal{C}^{(2)}$  as defined by equation (7.3) as a function of  $p_{\uparrow}$  and  $p_{\downarrow}$  and with  $\Delta\phi = \pi$ . The correlation function expresses the probability of finding a spin up particle with momentum  $p_{\uparrow}$ , given that a spin down particle was detected moving in opposite direction and with momentum  $p_{\downarrow}$ . We subtract the contribution from single particle densities. For a spin balanced gas (a), we find that on average the pair correlations appear for exactly opposite momenta, as expected. When a spin imbalance is introduced (b,c), we find off-diagonal pair correlations with a finite centre of mass momentum ( $p_{\uparrow} \neq p_{\downarrow}$ ). The average momentum differences agree very well with the calculated mismatch between the Fermi surfaces of both spin states  $p_{F,\uparrow} - p_{F,\downarrow}$  (black dashed line). Here, the Fermi momentum  $p_{F,\sigma}$  is defined as in section 7.1.4 and calculated using the respective number of atoms in each spin component  $N_{\uparrow}$  and  $N_{\downarrow}$ .

spin imbalanced Fermi gases [Ful64; Lar64]. Here, unconventional Cooper pairs with a finite centre of mass momentum appear. Furthermore, imbalanced systems offer the possibility to study quasi particles like the Fermi polaron [Sch12; Nga12]. Ultracold quantum gases allow us to address many of the unresolved questions concerning imbalanced systems [Che10]. Important examples include the stability of the FFLO phase [Pec20; Att21] or the existence of a possible transition from a molecule to a polaron as a function of the interaction strength [Che10].

We use the deterministic spilling scheme, described in detail in chapter 4, to prepare the spin balanced closed shell ground state configurations of the 2D harmonic oscillator with  $N = 1 + 1$ ,  $3 + 3$ ,  $6 + 6$  or  $10 + 10$  particles. With only a few modifications the same method also enables us to prepare any desired ground state configuration with

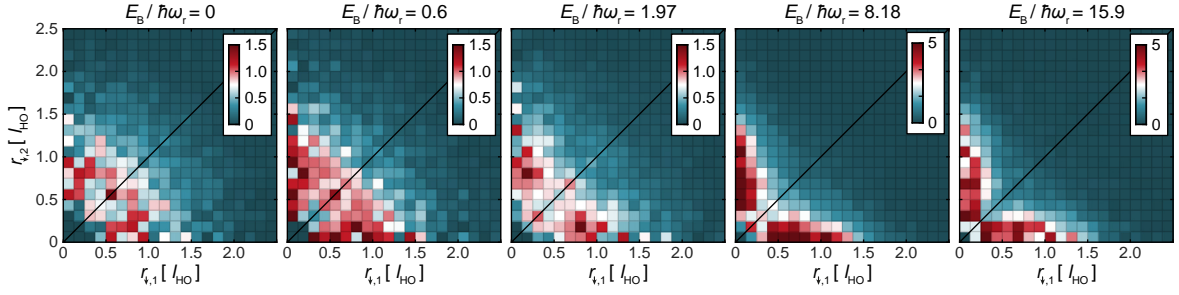


**Figure 9.4: In-situ correlations of a spin imbalanced 2D Fermi gas.** We show the measured in-situ correlations for the  $N = 1 + 3$  ground state as a function of the interaction strength. The data has been obtained by making use of the wavefunction magnification method described in the previous section. In each image we calculate the three distances ( $r_{\downarrow,1}$ ,  $r_{\downarrow,2}$ ,  $r_{\downarrow,3}$ ) from the majority atoms to the single spin up atom. The density plots show a histogram of the distribution of the two closest particles to the impurity ( $r_{\downarrow,1}$ ,  $r_{\downarrow,2} < r_{\downarrow,3}$ ). As the interaction strength is increased, we find clear indications of pairing in the system. When one of the particles is detected close to the minority in real space, all other particles are much further away. Whether the bound state is of molecular or polaronic nature and if there is a transition between both states as a function of interaction strength has to be studied in more detail in the future.

spin imbalance (see Figure 9.2). To this end, we apply the spilling technique in 2D starting from a  $|1\rangle|2\rangle$  mixture and at a magnetic offset field of  $B \approx 30$  G, where the magnetic momentum of state  $|2\rangle$  is exactly zero (see section 3.3). To obtain a strongly interacting state  $E_B > \hbar\omega_r$  in the high-field regime (see section 4.2.7), we perform a Landau-Zener sweep to the attractive branch of the  $|1\rangle|3\rangle$  mixture once the imbalanced ground state has been prepared.

We have performed first measurements with imbalanced ground states both in momentum and in real space. When the spin imbalance is increased, we find that the centre of mass momentum of the Cooper pairs in the ground states increases  $\langle p_{\text{pair}} \rangle > 0$  (see Figure 9.3). The increase in the average pair momentum agrees very well with the momentum mismatch of the Fermi surfaces of both spin components  $\langle p_{\text{pair}} \rangle = p_{F,\uparrow} - p_{F,\downarrow}$ . By forming pairs with finite centre of mass momentum, two atoms can increase their binding energy at the cost of additional kinetic energy. To understand finite size effects in our system in detail and to search for an FFLO state in the many-body phase diagram additional studies, also with larger samples sizes, are required.

In real space, we find strong indications for the presence of non-trivial bound states

and quasi-particles in the system. In Figure 9.4, we show the measured 2D histograms of the distances of the two atoms that are closest to the impurity for the  $N = 1 + 3$  atom ground state and as a function of the interaction strength. In a non-interacting gas the atoms are uncorrelated, apart from the Pauli blocked region for small distances  $r \rightarrow 0$ . In the strongly interacting region, however, the different spin down atoms are strongly correlated also for larger distances. One of both particles sits very close to the impurity ( $r_{\downarrow,i} \approx 0$ ) while the other atom is much further away ( $r_{\downarrow,j} > r_{\downarrow,i}$ ,  $i \neq j$ ). Note that for simplicity we have fixed the single spin up atom at  $r_{\uparrow} = 0$ , here. Further studies will allow us to determine the exact nature of the bound state and search for a possible transition between a molecule and a polaron. The first measurements shown here demonstrate that we can prepare imbalanced mesoscopic Fermi gases close to zero temperature and that we have access to the fundamental correlations of the system.

### 9.3 Increasing the Complexity

Our methods can directly be extended to a wide range of systems, also of even higher complexity. One simple step, that has already been discussed in the previous chapter, is to increase the particle number to study imbalance or the quantum anomaly in the macroscopic limit of the BCS-BEC crossover [Hol18; Mur19]. By increasing the temperature, we can conclusively answer the question about the nature of pairing in the normal phase and in the strongly correlated region [Mur18b]. By setting the gas in rotation, we can study the formation of vortices and quantum hall physics [Pal20]. Systems far from equilibrium, quantum turbulence and the thermalization dynamics in mesoscopic systems are further exciting topic to study [Eis15; Tsa16; Now16].

The Hamiltonian of the ultracold 2D Fermi gas in our experiment is highly programmable. It is possible to prepare mixtures of three hyperfine components  $|1\rangle$ ,  $|2\rangle$  and  $|3\rangle$  and to study three-component mixtures [Ott08]. A  $p$ -wave Feshbach resonance allows us to study more complex interaction terms beyond  $s$ -wave scattering [Ger19]. Optical dipole potentials, in combination with our SLM, allow us to freely shape the potential landscape of the atoms, for example to create two separate copies of the gas or a mesoscopic Josephson junction [Lui20]. The list of strongly correlated Fermi systems with different Hamiltonians we plan to explore with our apparatus could be extended further almost indefinitely. Here, we have restrained ourselves to some of the most obvious ideas.

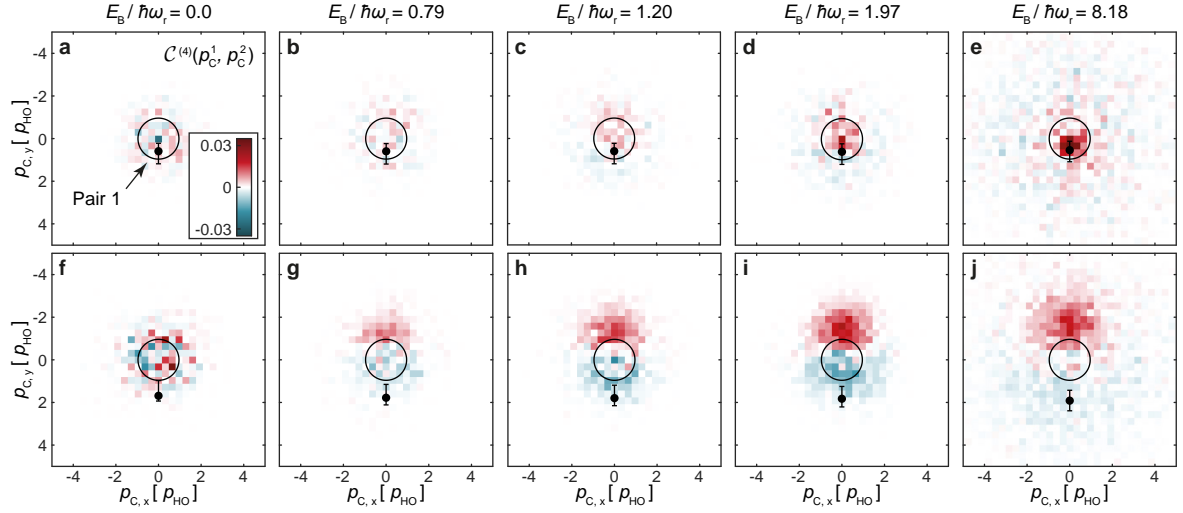


**Figure 9.5: Beyond second order density correlations.** Our images allow us to extract correlation functions of arbitrary order. Here, a first analysis of fourth order, or pair-pair, correlations for images of the  $N = 6 + 6$  particle ground state is shown. The correlation function  $\mathcal{C}^{(4)}$  is defined analogously to  $\mathcal{C}^{(2)}$  (see chapter 7) by replacing density operators by pair operators  $n_\sigma(\mathbf{p}) \rightarrow n_\uparrow(\mathbf{p}_\uparrow)n_\downarrow(\mathbf{p}_\downarrow)$ . We find significant correlations between different pairs. A more detailed analysis is required to check to what extent these fourth order correlations can be expressed as a function of lower order correlations (i.e. the disconnected part) and to study what effects come from the finite size of our system.

## 9.4 Heidelberg Quantum Architecture

The correlations presented in this thesis have been limited to second order. With the help of our single atom resolved images we are in principle able to extract density correlation functions of any desired order. This allows us to observe effects beyond standard Cooper pairing, for example when studying pair-pair correlations in the sample. In Figure 9.5, some preliminary analysis of fourth order correlations for the  $N = 6 + 6$  particle ground state is shown. The amount of statistics required for the analysis of higher order correlations scales exponentially with the number of operators in the correlation function. In 2D the pair-pair correlations are already eight dimensional functions in terms of the momentum or position coordinates of single atoms, for example.

For future studies of higher order correlation functions, one essential step is to reduce the experimental cycle time significantly. To this end, our group is working on the

next generation of quantum gas experiment — the Heidelberg Quantum Architecture (HQA). The ideas for the apparatus are based on the preparation schemes we have presented in chapter 4. We have demonstrated that it is possible to prepare deeply degenerate systems of up to 100 atoms with very low entropies of  $0.1 k_B$  per atom in very short times  $t_{\text{spill}} \approx 20$  ms. By extending these methods and optimizing the different laser cooling stages, we estimate that with the HQA we will achieve cycle rates significantly exceeding 1 Hz. Together with the imaging techniques presented in this thesis, the new apparatus hold the potential to open up a new chapter in the simulation of many-body physics with ultracold quantum gases.



# Bibliography

- [Aad12] G. Aad et al. *Observation of a new particle in the search for the Standard Model Higgs boson with the ATLAS detector at the LHC*. *Physics Letters B* 716.1 (2012), pp. 1–29.
- [Alh00] Y. Alhassid. *The statistical theory of quantum dots*. *Reviews of Modern Physics* 72.4 (2000), pp. 895–968.
- [Alt06] A. Altland and B. Simons. *Condensed Matter Field Theory*. Cambridge: Cambridge University Press, 2006. ISBN: 9780511804236.
- [Alt04] E. Altman, E. Demler, and M. D. Lukin. *Probing many-body states of ultracold atoms via noise correlations*. *Physical Review A* 70.1 (2004), p. 013603.
- [Alv84] L. Alvarez-Gaumé and E. Witten. *Gravitational anomalies*. *Nuclear Physics B* 234.2 (1984), pp. 269–330.
- [And72] P. W. Andersen. *More is different*. *Science* 177.4047 (1972), pp. 393–396.
- [And95] M. H. Anderson, J. R. Ensher, M. R. Matthews, C. E. Wieman, and E. A. Cornell. *Observation of Bose-Einstein condensation in a dilute atomic vapor*. *Science* 269.5221 (1995), pp. 198–201.
- [And59] P. Anderson. *Theory of dirty superconductors*. *Journal of Physics and Chemistry of Solids* 11.1-2 (1959), pp. 26–30.
- [And17] Andrea Bergschneider. *Strong correlations in few-fermion systems*. PhD thesis. University of Heidelberg, 2017.
- [Ast21] L. Asteria, H. P. Zahn, M. N. Kosch, K. Sengstock, and C. Weitenberg. *Quantum gas magnifier for sub-lattice-resolved imaging of 3D quantum systems*. *Nature* 599.7886 (2021), pp. 571–575.
- [Att21] F. Attanasio, L. Rammelmüller, J. E. Drut, and J. Braun. *Pairing patterns in polarized unitary Fermi gases above the superfluid transition*. *arXiv preprint* 2112.07309 (2021).
- [Bak09] W. S. Bakr, J. I. Gillen, A. Peng, S. Fölling, and M. Greiner. *A quantum gas microscope for detecting single atoms in a Hubbard-regime optical lattice*. *Nature* 462.7269 (2009), pp. 74–77.

- [Bar12] M. A. Baranov, M. Dalmonte, G. Pupillo, and P. Zoller. *Condensed Matter Theory of Dipolar Quantum Gases*. *Chemical Reviews* 112.9 (2012), pp. 5012–5061.
- [Bar57] J. Bardeen, L. N. Cooper, and J. R. Schrieffer. *Theory of superconductivity*. *Physical Review* 108.5 (1957), pp. 1175–1204.
- [Bar18] D. Barredo, V. Lienhard, S. de Léséleuc, T. Lahaye, and A. Browaeys. *Synthetic three-dimensional atomic structures assembled atom by atom*. *Nature* 561.7721 (2018), pp. 79–82.
- [Bar14] M. Barth and J. Hofmann. *Pairing effects in the nondegenerate limit of the two-dimensional Fermi gas*. *Physical Review A* 89.1 (2014), p. 013614.
- [Bau13] S. K. Baur, E. Vogt, M. Köhl, and G. M. Bruun. *Collective modes of a two-dimensional spin-1/2 Fermi gas in a harmonic trap*. *Physical Review A - Atomic, Molecular, and Optical Physics* 87.4 (2013), p. 043612.
- [Bay20a] L. Bayha, M. Holten, R. Klemt, K. Subramanian, J. Bjerlin, S. M. Reimann, G. M. Bruun, P. M. Preiss, and S. Jochim. *Observing the emergence of a quantum phase transition shell by shell*. *Nature* 587.7835 (2020), pp. 583–587.
- [Bay20b] L. X. Bayha. *Emergence of Many-Body Physics in Two-Dimensional Few-Fermion Systems*. PhD thesis. University of Heidelberg, 2020.
- [Bed86] J. G. Bednorz and K. A. Müller. *Possible high- $T_c$  superconductivity in the Ba-La-Cu-O system*. *Zeitschrift für Physik B Condensed Matter* 64.2 (1986), pp. 189–193.
- [Beh18] A. Behrle, T. Harrison, J. Kombe, K. Gao, M. Link, J.-S. Bernier, C. Kollath, and M. Köhl. *Higgs mode in a strongly interacting fermionic superfluid*. 2018.
- [Ber72] V. Berezinsky. *Destruction of Long-range Order in One-dimensional and Two-dimensional Systems Possessing a Continuous Symmetry Group. II. Quantum Systems*. *Journal of Experimental and Theoretical Physics* 34.3 (1972), p. 610.
- [Ber04] S. Bergamini, B. Darquié, M. Jones, L. Jacubowicz, A. Browaeys, and P. Grangier. *Holographic generation of microtrap arrays for single atoms by use of a programmable phase modulator*. *Journal of the Optical Society of America B* 21.11 (2004), p. 1889.

- 
- [Ber19] A. Bergschneider, V. M. Klinkhamer, J. H. Becher, R. Klemt, L. Palm, G. Zürn, S. Jochim, and P. M. Preiss. *Experimental characterization of two-particle entanglement through position and momentum correlations*. *Nature Physics* 15.7 (2019), pp. 640–644.
- [Ber18] A. Bergschneider, V. M. Klinkhamer, J. H. Becher, R. Klemt, G. Zürn, P. M. Preiss, and S. Jochim. *Spin-resolved single-atom imaging of  ${}^6\text{Li}$  in free space*. *Physical Review A* 97.6 (2018), p. 063613.
- [Bij13] R. M. W. Bijnen van. *Quantum engineering with ultracold atoms*. PhD thesis. Eindhoven University of Technology, 2013.
- [Bis11] U. Bissbort, S. Götze, Y. Li, J. Heinze, J. S. Krauser, M. Weinberg, C. Becker, K. Sengstock, and W. Hofstetter. *Detecting the Amplitude Mode of Strongly Interacting Lattice Bosons by Bragg Scattering*. *Physical Review Letters* 106.20 (2011), p. 205303.
- [Bje16] J. Bjerlin, S. M. Reimann, and G. M. Bruun. *Few-Body Precursor of the Higgs Mode in a Fermi Gas*. *Physical Review Letters* 116.15 (2016), p. 155302.
- [Bla96] C. T. Black, D. C. Ralph, and M. Tinkham. *Spectroscopy of the Superconducting Gap in Individual Nanometer-Scale Aluminum Particles*. *Physical Review Letters* 76.4 (1996), pp. 688–691.
- [Blo12] I. Bloch, J. Dalibard, and S. Nascimbène. *Quantum simulations with ultracold quantum gases*. *Nature Physics* 8.4 (2012), pp. 267–276.
- [Blo08] I. Bloch, J. Dalibard, and W. Zwerger. *Many-body physics with ultracold gases*. *Reviews of Modern Physics* 80.3 (2008), pp. 885–964.
- [Boe16] I. Boettcher, L. Bayha, D. Kedar, P. A. Murthy, M. Neidig, M. G. Ries, A. N. Wenz, G. Zürn, S. Jochim, and T. Enss. *Equation of State of Ultracold Fermions in the 2D BEC-BCS Crossover Region*. *Physical Review Letters* 116.4 (2016), p. 045303.
- [Bog58] N. N. Bogoljubov. *On a new method in the theory of superconductivity. II*. *Nuovo Cimento* 7.6 (1958), pp. 794–805.
- [Boh98] A. Bohr and B. R. Mottelson. *Nuclear Structure*. New York: World Scientific Publishing Company, 1998. ISBN: 9789810231972.
- [Bol16] M. Boll, T. A. Hilker, G. Salomon, A. Omran, J. Nespolo, L. Pollet, I. Bloch, and C. Gross. *Spin- and density-resolved microscopy of antiferromagnetic correlations in Fermi-Hubbard chains*. *Science* 353.6305 (2016), pp. 1257–1260.

- [Bri05] D. M. Brink and R. A. Broglia. *Nuclear Superfluidity*. Cambridge: Cambridge University Press, 2005. ISBN: 9780521395403.
- [Bru02a] G. M. Bruun. *Low-Energy Monopole Modes of a Trapped Atomic Fermi Gas*. *Physical Review Letters* 89.26 (2002), p. 263002.
- [Bru14] G. M. Bruun. *Long-lived Higgs mode in a two-dimensional confined Fermi system*. *Physical Review A* 90.2 (2014), p. 023621.
- [Bru02b] G. M. Bruun and H. Heiselberg. *Cooper pairing and single-particle properties of trapped Fermi gases*. *Physical Review A* 65.5 (2002), p. 053407.
- [Bru01] G. M. Bruun and B. R. Mottelson. *Low Energy Collective Modes of a Superfluid Trapped Atomic Fermi Gas*. *Physical Review Letters* 87.27 (2001), p. 270403.
- [Büc09] R. Bücker, A. Perrin, S. Manz, T. Betz, C. Koller, T. Plisson, J. Rottmann, T. Schumm, and J. Schmiedmayer. *Single-particle-sensitive imaging of freely propagating ultracold atoms*. *New Journal of Physics* 11.10 (2009), p. 103039.
- [Bus98] T. Busch, B. G. Englert, K. Rzazewski, and M. Wilkens. *Two Cold Atoms in a Harmonic Trap*. *Foundations of Physics* 28.4 (1998), pp. 549–559.
- [Cam01] H. E. Camblong, L. N. Epele, H. Fanchiotti, and C. A. García Canal. *Quantum Anomaly in Molecular Physics*. *Physical Review Letters* 87.22 (2001), p. 220402.
- [Cas09] A. W. Castleman and S. N. Khanna. *Clusters, Superatoms, and Building Blocks of New Materials*. *The Journal of Physical Chemistry C* 113.7 (2009), pp. 2664–2675.
- [Cha13] C. Chafin and T. Schäfer. *Scale breaking and fluid dynamics in a dilute two-dimensional Fermi gas*. *Physical Review A* 88.4 (2013), p. 043636.
- [Che09] Q. Chen, Y. He, C.-C. Chien, and K. Levin. *Theory of radio frequency spectroscopy experiments in ultracold Fermi gases and their relation to photoemission in the cuprates*. *Reports on Progress in Physics* 72.12 (2009), p. 122501.
- [Che20] Y. Chen, D.-W. W. Xiao, R. Zhang, and P. Zhang. *Analytical solution for the spectrum of two ultracold atoms in a completely anisotropic confinement*. *Physical Review A* 101.5 (2020), p. 053624.
- [Che02] F. Chevy, V. Bretin, P. Rosenbusch, K. W. Madison, and J. Dalibard. *Transverse Breathing Mode of an Elongated Bose-Einstein Condensate*. *Physical Review Letters* 88.25 (2002), p. 250402.

- 
- [Che10] F. Chevy and C. Mora. *Ultra-cold polarized Fermi gases*. *Reports on Progress in Physics* 73.11 (2010), p. 112401.
- [Chi10] C. Chin, R. Grimm, P. Julienne, and E. Tiesinga. *Feshbach resonances in ultracold gases*. *Reviews of Modern Physics* 82.2 (2010), pp. 1225–1286.
- [Chi18] C. S. Chiu, G. Ji, A. Mazurenko, D. Greif, and M. Greiner. *Quantum State Engineering of a Hubbard System with Ultracold Fermions*. *Physical Review Letters* 120.24 (2018).
- [Cla17] P. W. Claeys, J.-S. Caux, D. Van Neck, and S. De Baerdemacker. *Variational method for integrability-breaking Richardson-Gaudin models*. *Physical Review B* 96.15 (2017), p. 155149.
- [Col03] P. Coleman. *Many Body Physics: Unfinished Revolution*. *Annales Henri Poincaré* 4.S2 (2003), pp. 559–580.
- [Col15] P. Coleman. *Introduction to Many-Body Physics*. Cambridge: Cambridge University Press, 2015. ISBN: 9780521864886.
- [Coo02] S. A. Coon and B. R. Holstein. *Anomalies in quantum mechanics: The  $1/r^2$  potential*. *American Journal of Physics* 70.5 (2002), pp. 513–519.
- [Coo56] L. N. Cooper. *Bound Electron Pairs in a Degenerate Fermi Gas*. *Physical Review* 104.4 (1956), pp. 1189–1190.
- [Dal99] J. Dalibard. *Collisional dynamics of ultra-cold atomic gases*. In: *Proceedings of the International School of Physics - Enrico Fermi*. 1999, pp. 321–349.
- [Dav95] K. B. Davis, M. O. Mewes, M. R. Andrews, N. J. Van Druten, D. S. Durfee, D. M. Kurn, and W. Ketterle. *Bose-Einstein condensation in a gas of sodium atoms*. *Physical Review Letters* 75.22 (1995), pp. 3969–3973.
- [Daz18] W. Daza, J. E. Drut, C. Lin, and C. Ordóñez. *Virial expansion for the Tan contact and Beth-Uhlenbeck formula from two-dimensional  $SO(2,1)$  anomalies*. *Physical Review A* 97.3 (2018), p. 033630.
- [Del00] J. von Delft and F. Braun. *Superconductivity in Ultrasmall Grains: Introduction to Richardson’s Exact Solution*. In: *Quantum Mesoscopic Phenomena and Mesoscopic Devices in Microelectronics*. 2000, pp. 361–370.
- [Del01] J. von Delft. *Superconductivity in ultrasmall metallic grains*. *Annalen der Physik (Leipzig)* 10.3 (2001), pp. 219–276.
- [DeM99] B. DeMarco and D. S. Jin. *Onset of Fermi Degeneracy in a Trapped Atomic Gas*. *Science* 285.5434 (1999), pp. 1703–1706.

- [DeM01] B. DeMarco, S. B. Papp, and D. S. Jin. *Pauli Blocking of Collisions in a Quantum Degenerate Atomic Fermi Gas*. *Physical Review Letters* 86.24 (2001), pp. 5409–5412.
- [Dem06] W. Demtröder. *Atoms, molecules and photons: An introduction to atomic-, molecular- and quantum-physics*. 2006. ISBN: 3540206310.
- [Die87] F. Diedrich, E. Peik, J. M. Chen, W. Quint, and H. Walther. *Observation of a Phase Transition of Stored Laser-Cooled Ions*. *Physical Review Letters* 59.26 (1987), pp. 2931–2934.
- [Dub14] R. Dubessy, C. De Rossi, T. Badr, L. Longchambon, and H. Perrin. *Imaging the collective excitations of an ultracold gas using statistical correlations*. *New Journal of Physics* 16.12 (2014), p. 122001.
- [Eis15] J. Eisert, M. Friesdorf, and C. Gogolin. *Quantum many-body systems out of equilibrium*. *Nature Physics* 11.2 (2015), pp. 124–130.
- [End12] M. Endres, T. Fukuhara, D. Pekker, M. Cheneau, P. Schauß, C. Gross, E. Demler, S. Kuhr, and I. Bloch. *The ‘Higgs’ amplitude mode at the two-dimensional superfluid/Mott insulator transition*. *Nature* 487.7408 (2012), pp. 454–458.
- [Eng15] J. L. England. *Dissipative adaptation in driven self-assembly*. *Nature Nanotechnology* 10.11 (2015), pp. 919–923.
- [Fel11] M. Feld, B. Fröhlich, E. Vogt, M. Koschorreck, and M. Köhl. *Observation of a pairing pseudogap in a two-dimensional Fermi gas*. *Nature* 480.7375 (2011), pp. 75–78.
- [Fla12] S. T. Flammia, D. Gross, Y.-K. Liu, and J. Eisert. *Quantum tomography via compressed sensing: error bounds, sample complexity and efficient estimators*. *New Journal of Physics* 14.9 (2012), p. 095022.
- [Föll05] S. Fölling, F. Gerbier, A. Widera, O. Mandel, T. Gericke, and I. Bloch. *Spatial quantum noise interferometry in expanding ultracold atom clouds*. *Nature* 434.7032 (2005), pp. 481–484.
- [Foo05] C. J. Foot. *Atomic Physics*. Oxford University Press, 2005. ISBN: 978-0-19-850695-9.
- [Fre20] M. Fremling and J. K. Slingerland. *An investigation of pre-crystalline order, ruling out Pauli crystals and introducing Pauli anti-crystals*. *Scientific Reports* 10.1 (2020), p. 3710.
- [Fri13] H. Friedrich. *Scattering Theory*. Berlin, Heidelberg: Springer Berlin Heidelberg, 2013. ISBN: 978-3-642-38281-9.

- 
- [Frö12] B. Fröhlich, M. Feld, E. Vogt, M. Koschorreck, M. Köhl, C. Berthod, and T. Giamarchi. *Two-Dimensional Fermi Liquid with Attractive Interactions*. *Physical Review Letters* 109.13 (2012), p. 130403.
- [Ful64] P. Fulde and R. A. Ferrell. *Superconductivity in a Strong Spin-Exchange Field*. *Physical Review* 135.3A (1964), A550–A563.
- [Gae10] J. P. Gaebler, J. T. Stewart, T. E. Drake, D. S. Jin, A. Perali, P. Pieri, and G. C. Strinati. *Observation of pseudogap behaviour in a strongly interacting Fermi gas*. *Nature Physics* 6.8 (2010), pp. 569–573.
- [Gaj16a] M. Gajda, J. Mostowski, T. Sowiński, and M. Załuska-Kotur. *Single-shot imaging of trapped Fermi gas*. *EPL (Europhysics Letters)* 115.2 (2016), p. 20012.
- [Gaj16b] M. Gajdacz, A. J. Hilliard, M. A. Kristensen, P. L. Pedersen, C. Klempt, J. J. Arlt, and J. F. Sherson. *Preparation of Ultracold Atom Clouds at the Shot Noise Level*. *Physical Review Letters* 117.7 (2016), p. 073604.
- [Gao12] C. Gao and Z. Yu. *Breathing mode of two-dimensional atomic Fermi gases in harmonic traps*. *Physical Review A* 86.4 (2012), p. 043609.
- [Gau16] G. Gauthier, I. Lenton, N. McKay Parry, M. Baker, M. J. Davis, H. Rubinsztein-Dunlop, and T. W. Neely. *Direct imaging of a digital-micromirror device for configurable microscopic optical potentials*. *Optica* 3.10 (2016), p. 1136.
- [Geh03] M. E. Gehm. *Properties of  $^6\text{Li}$* . *Jetlab* (2003), pp. 1–33.
- [Geo72] H. Georgi and S. L. Glashow. *Gauge Theories Without Anomalies*. *Physical Review D* 6.2 (1972), pp. 429–431.
- [Ger19] M. Gerken, B. Tran, S. Häfner, E. Tiemann, B. Zhu, and M. Weidemüller. *Observation of dipolar splittings in high-resolution atom-loss spectroscopy of  $^6\text{Li}$  p-wave Feshbach resonances*. *Physical Review A* 100.5 (2019), p. 050701.
- [Gin50] V. L. Ginzburg and L. D. Landau. *To the Theory of Superconductivity*. *Zh. Eksp. Teor. Fiz.* 20 (1950), p. 1064.
- [Gin01] V. Ginzburg. *The Physics of a Lifetime: Reflections the Problems and Personalities Century Physics*. Berlin, Heidelberg: Springer Berlin Heidelberg, 2001. ISBN: 978-3-540-67534-1.
- [Gio08] S. Giorgini, L. P. Pitaevskii, and S. Stringari. *Theory of ultracold atomic Fermi gases*. *Reviews of Modern Physics* 80.4 (2008), pp. 1215–1274.

- [Gir08] P. R. Giri, K. S. Gupta, S. Meljanac, and A. Samsarov. *Electron capture and scaling anomaly in polar molecules*. *Physics Letters A* 372.17 (2008), pp. 2967–2970.
- [Gol48] M. Goldhaber and E. Teller. *On nuclear dipole vibrations*. *Physical Review* 74.9 (1948), pp. 1046–1049.
- [Gol62] J. Goldstone, A. Salam, and S. Weinberg. *Broken Symmetries*. *Physical Review* 127.3 (1962), pp. 965–970.
- [Gor59] L. P. Gor’kov. *Microscopic Derivation of the Ginzburg-Landau Equations in the Theory of Sup. Sov. Phys. JETP* 36.1364 (1959), pp. 1918–1923.
- [Gre98] S. Grebenev, J. P. Toennies, and A. F. Vilesov. *Superfluidity Within a Small Helium-4 Cluster: The Microscopic Andronikashvili Experiment*. *Science* 279.5359 (1998), pp. 2083–2086.
- [Gre84] M. B. Green and J. H. Schwarz. *Anomaly cancellations in supersymmetric  $D = 10$  gauge theory and superstring theory*. *Physics Letters B* 149.1-3 (1984), pp. 117–122.
- [Gre05] M. Greiner, C. A. Regal, J. T. Stewart, and D. S. Jin. *Probing Pair-Correlated Fermionic Atoms through Correlations in Atom Shot Noise*. *Physical Review Letters* 94.11 (2005), p. 110401.
- [Gre02] M. Greiner, O. Mandel, T. Esslinger, T. W. Hänsch, and I. Bloch. *Quantum phase transition from a superfluid to a Mott insulator in a gas of ultracold atoms*. *Nature* 415.6867 (2002), pp. 39–44.
- [Gre03] M. Greiner, C. A. Regal, and D. S. Jin. *Emergence of a molecular Bose-Einstein condensate from a Fermi gas*. *Nature* 426.6966 (2003), pp. 537–540.
- [Gri00] R. Grimm, M. Weidemüller, and Y. B. Ovchinnikov. *Optical Dipole Traps for Neutral Atoms*. In: *Advances in Atomic, Molecular and Optical Physics*. Vol. 42. C. 2000, pp. 95–170.
- [Gro21] C. Gross and W. S. Bakr. *Quantum gas microscopy for single atom and spin detection*. *Nature Physics* 17.12 (2021), pp. 1316–1323.
- [Gro72] D. J. Gross and R. Jackiw. *Effect of Anomalies on Quasi-Renormalizable Theories*. *Physical Review D* 6.2 (1972), pp. 477–493.
- [Had11] Z. Hadzibabic and J. Dalibard. *Two-dimensional Bose fluids: An atomic physics perspective*. *Rivista del Nuovo Cimento* 34.6 (2011), pp. 389–434.
- [Han56a] R. Hanbury Brown and R. Q. Twiss. *A test of a new type of stellar interferometer on Sirius*. *Nature* 178.4541 (1956), pp. 1046–1048.

- 
- [Han56b] R. Hanbury Brown and R. Q. Twiss. *Correlation between photons in two coherent beams of light*. *Nature* 177.4497 (1956), pp. 27–29.
- [Har14] T. Harte, G. D. Bruce, J. Keeling, and D. Cassettari. *Conjugate gradient minimisation approach to generating holographic traps for ultracold atoms*. *Optics Express* 22.22 (2014), p. 26548.
- [Has70] W. K. Hastings. *Monte Carlo sampling methods using Markov chains and their applications*. *Biometrika* 57.1 (1970), pp. 97–109.
- [Hei20] C. Heintze. *Projection of repulsive potentials in ultracold quantum gases with a Digital Micromirror Device*. Master Thesis. University of Heidelberg, 2020.
- [Hei02] H. Heiselberg and B. Mottelson. *Shell Structure and Pairing for Interacting Fermions in a Trap*. *Physical Review Letters* 88.19 (2002), p. 190401.
- [Her87] H. Hertz. *Ueber einen Einfluss des ultravioletten Lichtes auf die elektrische Entladung*. *Annalen der Physik* 267.8 (1887), pp. 983–1000.
- [Hig64] P. Higgs. *Broken symmetries, massless particles and gauge fields*. *Physics Letters* 12.2 (1964), pp. 132–133.
- [Hod17] S. S. Hodgman, R. I. Khakimov, R. J. Lewis-Swan, A. G. Truscott, and K. V. Kheruntsyan. *Solving the Quantum Many-Body Problem via Correlations Measured with a Momentum Microscope*. *Physical Review Letters* 118.24 (2017), p. 240402.
- [Hof12] J. Hofmann. *Quantum Anomaly, Universal Relations, and Breathing Mode of a Two-Dimensional Fermi Gas*. *Physical Review Letters* 108.18 (2012), p. 185303.
- [Hoh67] P. C. Hohenberg. *Existence of Long-Range Order in One and Two Dimensions*. *Physical Review* 158.2 (1967), pp. 383–386.
- [Hol93] B. R. Holstein. *Anomalies for pedestrians*. *American Journal of Physics* 61.2 (1993), pp. 142–147.
- [Hol14] B. R. Holstein. *Understanding an anomaly*. *American Journal of Physics* 82.6 (2014), pp. 591–596.
- [Hol18] M. Holten, L. Bayha, A. C. Klein, P. A. Murthy, P. M. Preiss, and S. Jochim. *Anomalous Breaking of Scale Invariance in a Two-Dimensional Fermi Gas*. *Physical Review Letters* 121.12 (2018), p. 120401.
- [Hol17] M. Holten. *Collective Modes and Turbulence in Two-Dimensional Fermi Gases*. Master Thesis. University of Heidelberg, 2017.

- [Hol21a] M. Holten, L. Bayha, K. Subramanian, S. Brandstetter, C. Heintze, P. Lunt, P. M. Preiss, and S. Jochim. *Observation of Cooper Pairs in a Mesoscopic 2D Fermi Gas*. *ArXiv Preprint* 2109.11511 (2021).
- [Hol21b] M. Holten, L. Bayha, K. Subramanian, C. Heintze, P. M. Preiss, and S. Jochim. *Observation of Pauli Crystals*. *Physical Review Letters* 126.2 (2021), p. 020401.
- [Hu19] H. Hu, B. C. Mulkerin, U. Toniolo, L. He, and X.-J. Liu. *Reduced Quantum Anomaly in a Quasi-Two-Dimensional Fermi Superfluid: Significance of the Confinement-Induced Effective Range of Interactions*. *Physical Review Letters* 122.7 (2019), p. 070401.
- [Hum13] D. B. Hume, I. Stroescu, M. Joos, W. Muessel, H. Strobel, and M. K. Oberthaler. *Accurate Atom Counting in Mesoscopic Ensembles*. *Physical Review Letters* 111.25 (2013), p. 253001.
- [Hun11] C.-L. Hung, X. Zhang, N. Gemelke, and C. Chin. *Observation of scale invariance and universality in two-dimensional Bose gases*. *Nature* 470.7333 (2011), pp. 236–239.
- [Idz06] Z. Idziaszek and T. Calarco. *Analytical solutions for the dynamics of two trapped interacting ultracold atoms*. *Physical Review A* 74.2 (2006), p. 022712.
- [Jac02] B. Jackson and E. Zaremba. *Accidental Suppression of Landau Damping of the Transverse Breathing Mode in Elongated Bose-Einstein Condensates*. *Physical Review Letters* 89.15 (2002), p. 150402.
- [Jan16] Jan Hendrik Willibald Becher. *Towards Spin and Site-Resolved, Single-Atom Imaging of  $^6\text{Li}$  Atoms in a Multiwell Potential*. Master Thesis. University of Heidelberg, 2016.
- [Jel07] T. Jelte et al. *Comparison of the Hanbury Brown–Twiss effect for bosons and fermions*. *Nature* 445.7126 (2007), pp. 402–405.
- [Joc03] S. Jochim, M. Bartenstein, A. Altmeyer, G. Hendl, S. Riedl, C. Chin, J. Hecker Denschlag, and R. Grimm. *Bose-Einstein Condensation of Molecules*. *Science* 302.5653 (2003), pp. 2101–2103.
- [Kad16] H. Kadau, M. Schmitt, M. Wenzel, C. Wink, T. Maier, I. Ferrier-Barbut, and T. Pfau. *Observing the Rosensweig instability of a quantum ferrofluid*. *Nature* 530.7589 (2016), pp. 194–197.
- [Kas16] S. Kasahara et al. *Giant superconducting fluctuations in the compensated semimetal FeSe at the BCS–BEC crossover*. *Nature Communications* 7.1 (2016), p. 12843.

- 
- [Kat18] K. Katsumi, N. Tsuji, Y. I. Hamada, R. Matsunaga, J. Schneeloch, R. D. Zhong, G. D. Gu, H. Aoki, Y. Gallais, and R. Shimano. *Higgs Mode in the  $d$ -Wave Superconductor  $\text{Bi}_2\text{Sr}_2\text{CaCu}_2\text{O}_{8+x}$  Driven by an Intense Terahertz Pulse*. *Physical Review Letters* 120.11 (2018), p. 117001.
- [Ket08] W. Ketterle and M. W. Zwierlein. *Making, probing and understanding ultracold Fermi gases*. *Rivista del Nuovo Cimento* 31.5-6 (2008), pp. 247–422.
- [Kha03] S. N. Khanna and A. W. Castleman. *Quantum Phenomena in Clusters and Nanostructures*. Springer Series in Cluster Physics. Berlin: Springer Berlin Heidelberg, 2003. ISBN: 978-3-642-05503-4.
- [Kle18] A. C. Klein. *Versatile Platform for Cold Atom Physics with  $^6\text{Li}$  based on Holographic Potentials*. Master Thesis. University of Heidelberg, 2018.
- [Kle21] R. Klemt. *Correlations from Microscopic to Macroscopic Quantum Systems: Interactions vs Indistinguishability*. PhD thesis. University of Heidelberg, 2021.
- [Kli17] V. M. Klinkhamer. *Few-Fermion Systems under a Matterwave Microscope*. PhD thesis. University of Heidelberg, 2017.
- [Koe20] J. Koepsell, S. Hirthe, D. Bourgund, P. Sompet, J. Vijayan, G. Salomon, C. Gross, and I. Bloch. *Robust Bilayer Charge Pumping for Spin- and Density-Resolved Quantum Gas Microscopy*. *Physical Review Letters* 125.1 (2020), p. 010403.
- [Koh90] M. Kohmoto and Y. Takada. *Superconductivity from an Insulator*. *Journal of the Physical Society of Japan* 59.5 (1990), pp. 1541–1544.
- [Kos73] J. M. Kosterlitz and D. J. Thouless. *Ordering, metastability and phase transitions in two-dimensional systems*. *Journal of Physics C: Solid State Physics* 6.7 (1973), pp. 1181–1203.
- [Kro20] K. Kroeger, N. Dogra, R. Rosa-Medina, M. Paluch, F. Ferri, T. Donner, and T. Esslinger. *Continuous feedback on a quantum gas coupled to an optical cavity*. *New Journal of Physics* 22.3 (2020), p. 033020.
- [Lan36] L. Landau. *The theory of phase transitions*. *Nature* 138.3498 (1936), pp. 840–841.
- [Lan37] L. Landau. *On the Theory of Phase Transitions*. *Zh. Eksp. Teor. Fiz.* 7 (1937), pp. 19–32.
- [Lan66] L. D. Landau. *Collected papers of L. D. Landau*. Elsevier, 1966. ISBN: 97800-80105864.

- [Lar64] A. I. Larkin and Y. N. Ovchinnikov. *Nonuniform state of superconductors*. *Zh. Eksp. Teor. Fiz.* 47 (1964), pp. 1136–1146.
- [Lau83] R. B. Laughlin. *Anomalous quantum Hall effect: An incompressible quantum fluid with fractionally charged excitations*. *Physical Review Letters* 50.18 (1983), pp. 1395–1398.
- [Lau00a] R. B. Laughlin and D. Pines. *The theory of everything*. *Proceedings of the National Academy of Sciences of the United States of America* 97.1 (2000), pp. 28–31.
- [Lau00b] R. B. Laughlin, D. Pines, J. Schmalian, B. P. Stojković, and P. Wolyneš. *The middle way*. *Proceedings of the National Academy of Sciences of the United States of America* 97.1 (2000), pp. 32–37.
- [Lau05] R. B. Laughlin. *A different universe: reinventing physics from the bottom down*. New York: Basic Books, 2005. ISBN: 9780465038282.
- [Lau17] K. D. Launey. *Emergent Phenomena in Atomic Nuclei from Large-Scale Modeling*. Singapore: World Scientific Publishing Company, 2017. ISBN: 978-981-314-604-4.
- [Lee14] J. J. Lee et al. *Interfacial mode coupling as the origin of the enhancement of  $T_c$  in FeSe films on SrTiO<sub>3</sub>*. *Nature* 515.7526 (2014), pp. 245–248.
- [Lee06] P. A. Lee, N. Nagaosa, and X.-G. Wen. *Doping a Mott insulator: Physics of high-temperature superconductivity*. *Reviews of Modern Physics* 78.1 (2006), pp. 17–85.
- [Léo17] J. Léonard, A. Morales, P. Zupancic, T. Donner, and T. Esslinger. *Monitoring and manipulating Higgs and Goldstone modes in a supersolid quantum gas*. *Science* 358.6369 (2017), pp. 1415–1418.
- [Lev15] J. Levinsen and M. M. Parish. *Strongly interacting two-dimensional Fermi gases*. In: *Annual Review of Cold Atoms and Molecules*. 2015. Chap. 1, pp. 1–75.
- [Li21] H. Li et al. *Imaging two-dimensional generalized Wigner crystals*. *Nature* 597.7878 (2021), pp. 650–654.
- [Lui20] N. Luick, L. Sobirey, M. Bohlen, V. P. Singh, L. Mathey, T. Lompe, and H. Moritz. *An ideal Josephson junction in an ultracold two-dimensional Fermi gas*. *Science* 369.6499 (2020), pp. 89–91.
- [Mar15] F. Marsiglio, P. Pieri, A. Perali, F. Palestini, and G. C. Strinati. *Pairing effects in the normal phase of a two-dimensional Fermi gas*. *Physical Review B* 91.5 (2015), p. 054509.

- 
- [Mat13] R. Matsunaga, Y. I. Hamada, K. Makise, Y. Uzawa, H. Terai, Z. Wang, and R. Shimano. *Higgs amplitude mode in the BCS superconductors  $Nb_{1-x}Ti_xN$  induced by terahertz pulse excitation*. *Physical Review Letters* 111.5 (2013), p. 057002.
- [Max50] E. Maxwell. *Isotope Effect in the Superconductivity of Mercury*. *Physical Review* 78.4 (1950), pp. 477–477.
- [Mea91] L. R. Mead and J. Godines. *An analytical example of renormalization in two-dimensional quantum mechanics*. *American Journal of Physics* 59.10 (1991), pp. 935–937.
- [M ea14] M. A. M easson, Y. Gallais, M. Cazayous, B. Clair, P. Rodi ere, L. Cario, and A. Sacuto. *Amplitude Higgs mode in the 2H - NbSe<sub>2</sub> superconductor*. *Physical Review B - Condensed Matter and Materials Physics* 89.6 (2014), p. 060503.
- [Mer13] K. Merloti, R. Dubessy, L. Longchambon, M. Olshanii, and H. Perrin. *Breakdown of scale invariance in a quasi-two-dimensional Bose gas due to the presence of the third dimension*. *Physical Review A* 88.6 (2013), p. 061603.
- [Mer66] N. D. Mermin and H. Wagner. *Absence of Ferromagnetism or Antiferromagnetism in One- or Two-Dimensional Isotropic Heisenberg Models*. *Physical Review Letters* 17.22 (1966), pp. 1133–1136.
- [Met53] N. Metropolis, A. W. Rosenbluth, M. N. Rosenbluth, A. H. Teller, and E. Teller. *Equation of State Calculations by Fast Computing Machines*. *The Journal of Chemical Physics* 21.6 (1953), pp. 1087–1092.
- [Mic87] A. A. Michelson and E. W. Morley. *On the relative motion of the Earth and the luminiferous ether*. *American Journal of Science* s3-34.203 (1887), pp. 333–345.
- [Mig59] A. B. Migdal. *Superfluidity and the moments of inertia of nuclei*. *Nuclear Physics* 13.5 (1959), pp. 655–674.
- [Mue17] E. J. Mueller. *Review of pseudogaps in strongly interacting Fermi gases*. *Reports on Progress in Physics* 80.10 (2017), p. 104401.
- [Mue13] W. Muessel, H. Strobel, M. Joos, E. Nicklas, I. Stroescu, J. Tomkovi c, D. B. Hume, and M. K. Oberthaler. *Optimized absorption imaging of mesoscopic atomic clouds*. *Applied Physics B: Lasers and Optics* 113.1 (2013), pp. 69–73.

- [Mul18] B. C. Mulkerin, X.-J. Liu, and H. Hu. *Collective modes of a two-dimensional Fermi gas at finite temperature*. *Physical Review A* 97.5 (2018), p. 053612.
- [Mül10] T. Müller, B. Zimmermann, J. Meineke, J.-P. Brantut, T. Esslinger, and H. Moritz. *Local Observation of Antibunching in a Trapped Fermi Gas*. *Physical Review Letters* 105.4 (2010), p. 040401.
- [Mur15a] S. Murmann, F. Deuretzbacher, G. Zürn, J. Bjerlin, S. M. Reimann, L. Santos, T. Lompe, and S. Jochim. *Antiferromagnetic Heisenberg Spin Chain of a Few Cold Atoms in a One-Dimensional Trap*. *Physical Review Letters* 115.21 (2015), p. 215301.
- [Mur15b] P. A. Murthy, I. Boettcher, L. Bayha, M. Holzmann, D. Kedar, M. Neidig, M. G. Ries, A. N. Wenz, G. Zürn, and S. Jochim. *Observation of the Berezinskii-Kosterlitz-Thouless Phase Transition in an Ultracold Fermi Gas*. *Physical Review Letters* 115.1 (2015), p. 010401.
- [Mur14] P. A. Murthy, D. Kedar, T. Lompe, M. Neidig, M. G. Ries, A. N. Wenz, G. Zürn, and S. Jochim. *Matter-wave Fourier optics with a strongly interacting two-dimensional Fermi gas*. *Physical Review A* 90.4 (2014), p. 043611.
- [Mur18a] P. A. Murthy. *Emergent phenomena in two-dimensional Fermi systems*. PhD thesis. University of Heidelberg, 2018.
- [Mur19] P. A. Murthy, N. Defenu, L. Bayha, M. Holten, P. M. Preiss, T. Enss, and S. Jochim. *Quantum scale anomaly and spatial coherence in a 2D Fermi superfluid*. *Science* 365.6450 (2019), pp. 268–272.
- [Mur18b] P. A. Murthy, M. Neidig, R. Klemt, L. Bayha, I. Boettcher, T. Enss, M. Holten, G. Zürn, P. M. Preiss, and S. Jochim. *High-temperature pairing in a strongly interacting two-dimensional Fermi gas*. *Science* 359.6374 (2018), pp. 452–455.
- [Nak21] Y. Nakagawa, Y. Kasahara, T. Nomoto, R. Arita, T. Nojima, and Y. Iwasa. *Gate-controlled BCS-BEC crossover in a two-dimensional superconductor*. *Science* 372.6538 (2021), pp. 190–195.
- [Nas11] S. Nascimbène, N. Navon, S. Pilati, F. Chevy, S. Giorgini, A. Georges, and C. Salomon. *Fermi-Liquid Behavior of the Normal Phase of a Strongly Interacting Gas of Cold Atoms*. *Physical Review Letters* 106.21 (2011), p. 215303.
- [Neg18] J. W. Negele and H. Orland. *Quantum many-particle systems*. Boca Raton: CRC Press, 2018, pp. 1–459. ISBN: 9780429966477.

- 
- [Nei17] M. Neidig. *Many-Body Pairing in a Two-Dimensional Fermi Gas*. PhD thesis. University of Heidelberg, 2017.
- [Nga12] V. Ngampruetikorn, J. Levinsen, and M. M. Parish. *Repulsive polarons in two-dimensional Fermi gases*. *EPL (Europhysics Letters)* 98.3 (2012), p. 30005.
- [Nga13] V. Ngampruetikorn, J. Levinsen, and M. M. Parish. *Pair Correlations in the Two-Dimensional Fermi Gas*. *Physical Review Letters* 111.26 (2013), p. 265301.
- [Now16] B. Nowak, S. Erne, M. Karl, J. Schole, D. Sexty, and T. Gasenzer. *Non-thermal fixed points: universality, topology, and turbulence in Bose gases*. Oxford: Oxford University Press, 2016, pp. 443–482.
- [Noz99] P. Nozières and F. Pistolesi. *From semiconductors to superconductors: a simple model for pseudogaps*. *The European Physical Journal B* 10.4 (1999), pp. 649–662.
- [Ols10] M. Olshanii, H. Perrin, and V. Lorent. *Example of a Quantum Anomaly in the Physics of Ultracold Gases*. *Physical Review Letters* 105.9 (2010), p. 095302.
- [Omr15] A. Omran, M. Boll, T. A. Hilker, K. Kleinlein, G. Salomon, I. Bloch, and C. Gross. *Microscopic Observation of Pauli Blocking in Degenerate Fermionic Lattice Gases*. *Physical Review Letters* 115.26 (2015), p. 263001.
- [Ott16] H. Ott. *Single atom detection in ultracold quantum gases: a review of current progress*. *Reports on Progress in Physics* 79.5 (2016), p. 054401.
- [Ott08] T. B. Ottenstein, T. Lompe, M. Kohnen, A. N. Wenz, and S. Jochim. *Collisional Stability of a Three-Component Degenerate Fermi Gas*. *Physical Review Letters* 101.20 (2008), p. 203202.
- [Pal20] L. Palm, F. Grusdt, and P. M. Preiss. *Skyrmion ground states of rapidly rotating few-fermion systems*. *New Journal of Physics* 22.8 (2020), p. 083037.
- [Par14] M. M. Parish. *The BCS–BEC Crossover*. In: *Quantum Gas Experiments*. Imperial College Press, 2014. Chap. 9, pp. 179–197.
- [Par16] M. F. Parsons, A. Mazurenko, C. S. Chiu, G. Ji, D. Greif, and M. Greiner. *Site-resolved measurement of the spin-correlation function in the Fermi-Hubbard model*. *Science* 353.6305 (2016), pp. 1253–1256.
- [Pas08] M. Pasienski and B. DeMarco. *A high-accuracy algorithm for designing arbitrary holographic atom traps*. *Optics Express* 16.3 (2008), p. 2176.

- [Pat14] Y. S. Patil, S. Chakram, L. M. Aycock, and M. Vengalattore. *Nondestructive imaging of an ultracold lattice gas*. *Physical Review A* 90.3 (2014), p. 033422.
- [Pec20] D. Pecak and T. Sowiński. *Signatures of unconventional pairing in spin-imbanced one-dimensional few-fermion systems*. *Physical Review Research* 2.1 (2020), p. 012077.
- [Pee09] F. Peeters. *Electron crystallites floating on superfluid helium*. *Physics* 2 (2009), p. 4.
- [Pek15] D. Pekker and C. Varma. *Amplitude/Higgs Modes in Condensed Matter Physics*. *Annual Review of Condensed Matter Physics* 6.1 (2015), pp. 269–297.
- [Pen56] O. Penrose and L. Onsager. *Bose-Einstein Condensation and Liquid Helium*. *Physical Review* 104.3 (1956), pp. 576–584.
- [Pep18] T. Pepler, P. Dyke, M. Zamorano, I. Herrera, S. Hoinka, and C. J. Vale. *Quantum Anomaly and 2D-3D Crossover in Strongly Interacting Fermi Gases*. *Physical Review Letters* 121.12 (2018), p. 120402.
- [Per11] A. Perali, F. Palestini, P. Pieri, G. C. Strinati, J. T. Stewart, J. P. Gaebler, T. E. Drake, and D. S. Jin. *Evolution of the Normal State of a Strongly Interacting Fermi Gas from a Pseudogap Phase to a Molecular Bose Gas*. *Physical Review Letters* 106.6 (2011), p. 060402.
- [Pet08] C. J. Pethick and H. Smith. *Bose–Einstein condensation in dilute gases*. Cambridge: Cambridge University Press, 2008. ISBN: 9780511802850.
- [Pet01] D. S. Petrov and G. V. Shlyapnikov. *Interatomic collisions in a tightly confined Bose gas*. *Physical Review A* 64.1 (2001), p. 012706.
- [Pit97] L. P. Pitaevskii and A. Rosch. *Breathing modes and hidden symmetry of trapped atoms in two dimensions*. *Physical Review A* 55.2 (1997), pp. 853–856.
- [Poo03] C. P. Poole and F. J. Owens. *Introduction To Nanotechnology*. New Jersey: John Wiley & Sons, 2003. ISBN: 9780471079354.
- [Pop99] J. A. Pople. *Nobel lecture: Quantum chemical models*. *Reviews of Modern Physics* 71.5 (1999), pp. 1267–1274.
- [Rak17] D. Rakshit, J. Mostowski, T. Sowiński, M. Załuska-Kotur, and M. Gajda. *On the observability of Pauli crystals in experiments with ultracold trapped Fermi gases*. *Scientific Reports* 7.1 (2017), p. 15004.

- 
- [Ran90] M. Randeria, J. M. Duan, and L. Y. Shieh. *Superconductivity in a two-dimensional Fermi gas: Evolution from Cooper pairing to Bose condensation*. *Physical Review B* 41.1 (1990), pp. 327–343.
- [Ran89] M. Randeria, J.-M. M. Duan, and L.-Y. Y. Shieh. *Bound states, Cooper pairing, and Bose condensation in two dimensions*. *Physical Review Letters* 62.9 (1989), pp. 981–984.
- [Rei07] G. Reinaudi, T. Lahaye, Z. Wang, and D. Guéry-Odelin. *Strong saturation absorption imaging of dense clouds of ultracold atoms*. *Optics Letters* 32.21 (2007), p. 3143.
- [Rey51] C. A. Reynolds, B. Serin, and L. B. Nesbitt. *The Isotope Effect in Superconductivity. I. Mercury*. *Physical Review* 84.4 (1951), pp. 691–694.
- [Ric63] R. W. Richardson. *A restricted class of exact eigenstates of the pairing-force Hamiltonian*. *Physics Letters* 3.6 (1963), pp. 277–279.
- [Ric64] R. W. Richardson and N. Sherman. *Exact eigenstates of the pairing-force Hamiltonian*. *Nuclear Physics* 52.C (1964), pp. 221–238.
- [Rie15a] M. G. Ries, A. N. Wenz, G. Zürn, L. Bayha, I. Boettcher, D. Kedar, P. A. Murthy, M. Neidig, T. Lompe, and S. Jochim. *Observation of pair condensation in the Quasi-2D BEC-BCS Crossover*. *Physical Review Letters* 114.23 (2015), p. 230401.
- [Rie10] M. G. Ries. *A magneto-optical trap for the preparation of a three-component Fermi gas in an optical lattice*. PhD thesis. University of Heidelberg, 2010.
- [Rie15b] M. G. Ries. *A Two-Dimensional Fermi Gas in the BEC-BCS Crossover*. PhD thesis. University of Heidelberg, 2015.
- [Rom06] T. Rom, T. Best, D. van Oosten, U. Schneider, S. Fölling, B. Paredes, and I. Bloch. *Free fermion antibunching in a degenerate atomic Fermi gas released from an optical lattice*. *Nature* 444.7120 (2006), pp. 733–736.
- [Ron09] M. Rontani, J. R. Armstrong, Y. Yu, S. Åberg, and S. M. Reimann. *Cold fermionic atoms in two-dimensional traps: Pairing versus Hund’s rule*. *Physical Review Letters* 102.6 (2009), p. 060401.
- [Ros15] G. D. Rosi and S. Stringari. *Collective oscillations of a trapped quantum gas in low dimensions*. *Physical Review A* 92.5 (2015), p. 053617.
- [Rüe08] C. Rüegg, B. Normand, M. Matsumoto, A. Furrer, D. F. McMorrow, K. W. Krämer, H. U. Güdel, S. N. Gvasaliya, H. Mutka, and M. Boehm. *Quantum magnets under pressure: Controlling elementary excitations in  $TlCuCl_3$* . *Physical Review Letters* 100.20 (2008), p. 205701.

- [Sac11] S. Sachdev. *Quantum Phase Transitions*. 2nd ed. Cambridge: Cambridge University Press, 2011, pp. 1–501. ISBN: 9780511973765.
- [Sag15] Y. Sagi, T. E. Drake, R. Paudel, R. Chapurin, and D. S. Jin. *Breakdown of the Fermi Liquid Description for Strongly Interacting Fermions*. *Physical Review Letters* 114.7 (2015), p. 075301.
- [Sak17] J. J. Sakurai and J. Napolitano. *Modern Quantum Mechanics*. Cambridge: Cambridge University Press, 2017. ISBN: 9781108499996.
- [San10] C. Sanner, E. J. Su, A. Keshet, R. Gommers, Y.-i. Shin, W. Huang, and W. Ketterle. *Suppression of Density Fluctuations in a Quantum Degenerate Fermi Gas*. *Physical Review Letters* 105.4 (2010), p. 040402.
- [Sch15] P. Schauß, J. Zeiher, T. Fukuhara, S. Hild, M. Cheneau, T. Macrì, T. Pohl, I. Bloch, and C. Gross. *Crystallization in Ising quantum magnets*. *Science* 347.6229 (2015), pp. 1455–1458.
- [Sch12] R. Schmidt, T. Enss, V. Pietilä, and E. Demler. *Fermi polarons in two dimensions*. *Physical Review A* 85.2 (2012), p. 021602.
- [Sch07] C. H. Schunck, Y. Shin, A. Schirotzek, M. W. Zwierlein, and W. Ketterle. *Pairing Without Superfluidity: The Ground State of an Imbalanced Fermi Mixture*. *Science* 316.5826 (2007), pp. 867–870.
- [Sch06] F. Schwabl. *Statistische Mechanik*. Springer-Lehrbuch. Berlin, Heidelberg: Springer-Verlag, 2006. ISBN: 3540310959.
- [Sch17] T. Schweigler, V. Kasper, S. Erne, I. Mazets, B. Rauer, F. Cataldini, T. Langen, T. Gasenzer, J. Berges, and J. Schmiedmayer. *Experimental characterization of a quantum many-body system via higher-order correlations*. *Nature* 545.7654 (2017), pp. 323–326.
- [Ser11a] F. Serwane, G. Zürn, T. Lompe, T. B. Ottenstein, A. N. Wenz, and S. Jochim. *Deterministic preparation of a tunable few-fermion system*. *Science* 332.6027 (2011), pp. 336–338.
- [Ser11b] F. Serwane. *Deterministic preparation of a tunable few-fermion system*. PhD thesis. University of Heidelberg, 2011.
- [She10] J. F. Sherson, C. Weitenberg, M. Endres, M. Cheneau, I. Bloch, and S. Kuhr. *Single-atom-resolved fluorescence imaging of an atomic Mott insulator*. *Nature* 467.7311 (2010), pp. 68–72.
- [Shi07] Y. Shin, C. H. Schunck, A. Schirotzek, and W. Ketterle. *Tomographic rf Spectroscopy of a Trapped Fermi Gas at Unitarity*. *Physical Review Letters* 99.9 (2007), p. 090403.

- 
- [Sim10] P. Simon. *Apparatus for the preparation of ultracold Fermi gases*. PhD thesis. University of Heidelberg, 2010.
- [Sob21] L. Sobirey, H. Biss, N. Luick, M. Bohlen, H. Moritz, and T. Lompe. *Comparing fermionic superfluids in two and three dimensions*. *arXiv preprint* 2106.11893 (2021).
- [Som12] A. T. Sommer, L. W. Cheuk, M. J. H. Ku, W. S. Bakr, and M. W. Zwierlein. *Evolution of Fermion Pairing from Three to Two Dimensions*. *Physical Review Letters* 108.4 (2012), p. 045302.
- [Soo80] R. Sooryakumar and M. V. Klein. *Raman scattering by superconducting-gap excitations and their coupling to charge-density waves*. *Physical Review Letters* 45.8 (1980), pp. 660–662.
- [Spi07] I. Spielman, W. Phillips, and J. Porto. *Mott-Insulator Transition in a Two-Dimensional Atomic Bose Gas*. *Physical Review Letters* 98.8 (2007), p. 080404.
- [Sta98] D. M. Stamper-Kurn, H.-J. Miesner, A. P. Chikkatur, S. Inouye, J. Stenger, and W. Ketterle. *Reversible Formation of a Bose-Einstein Condensate*. *Physical Review Letters* 81.11 (1998), pp. 2194–2197.
- [Sta12] D. M. Stamper-Kurn and J. H. Thywissen. *Experimental methods of ultracold atomic physics*. In: *Contemporary Concepts of Condensed Matter Science*. Vol. 5. Elsevier, 2012. Chap. 1, pp. 1–26. ISBN: 9780444538574.
- [Str18] G. C. Strinati, P. Pieri, G. Röpke, P. Schuck, and M. Urban. *The BCS–BEC crossover: From ultra-cold Fermi gases to nuclear systems*. *Physics Reports* 738 (2018), pp. 1–76.
- [Tay12] E. Taylor and M. Randeria. *Apparent Low-Energy Scale Invariance in Two-Dimensional Fermi Gases*. *Physical Review Letters* 109.13 (2012), p. 135301.
- [Ten21] A. Tenart, G. Hercé, J.-P. Bureik, A. Dureau, and D. Clément. *Observation of pairs of atoms at opposite momenta in an equilibrium interacting Bose gas*. *Nature Physics* 17.12 (2021), pp. 1364–1368.
- [Tin04] M. Tinkham. *Introduction to Superconductivity*. 2nd ed. Dover: Dover Publications, 2004. ISBN: 9780486435039.
- [Ton18] U. Toniolo, B. C. Mulkerin, X.-J. Liu, and H. Hu. *Breathing-mode frequency of a strongly interacting Fermi gas across the two- to three-dimensional crossover*. *Physical Review A* 97.6 (2018), p. 063622.
- [Tör16] P. Törmä. *Physics of ultracold Fermi gases revealed by spectroscopies*. *Physica Scripta* 91.4 (2016), p. 043006.

- [Tru01] A. G. Truscott, K. E. Strecker, W. I. McAlexander, G. B. Partridge, and R. G. Hulet. *Observation of fermi pressure in a gas of trapped atoms*. *Science* (2001).
- [Tsa16] M. C. Tsatsos, P. E. Tavares, A. Cidrim, A. R. Fritsch, M. A. Caracanhas, F. E. A. dos Santos, C. F. Barenghi, and V. S. Bagnato. *Quantum turbulence in trapped atomic Bose–Einstein condensates*. *Physics Reports* 622 (2016), pp. 1–52.
- [Tsu82] D. C. Tsui, H. L. Stormer, and A. C. Gossard. *Two-dimensional magnetotransport in the extreme quantum limit*. *Physical Review Letters* 48.22 (1982), pp. 1559–1562.
- [Tun10] S. Tung, G. Lamporesi, D. Lobser, L. Xia, and E. A. Cornell. *Observation of the Presuperfluid Regime in a Two-Dimensional Bose Gas*. *Physical Review Letters* 105.23 (2010), p. 230408.
- [Van10] D. Van Delft and P. Kes. *The discovery of superconductivity*. *Physics Today* 63.9 (2010), pp. 38–43.
- [Vog12] E. Vogt, M. Feld, B. Fröhlich, D. Pertot, M. Koschorreck, and M. Köhl. *Scale Invariance and Viscosity of a Two-Dimensional Fermi Gas*. *Physical Review Letters* 108.7 (2012), p. 070404.
- [Wal19] J. T. M. Walraven. *Lecture Notes: Quantum Gases*. University of Amsterdam, 2019.
- [Wei07] S. Weinberg and S. Kauffman. *Beyond Reductionism: Reinventing the Sacred*. *Zygon* 42.4 (2007), pp. 903–914.
- [Wei96] S. Weinberg. *The Quantum Theory of Fields*. New York: Cambridge University Press, 1996. ISBN: 9780521550024.
- [Wei81] V. F. Weisskopf. *The formation of cooper pairs and the nature of superconducting currents*. *Contemporary Physics* 22.4 (1981), pp. 375–395.
- [Wen07] X.-G. Wen. *Quantum Field Theory of Many-Body Systems*. New York: Oxford University Press, 2007. ISBN: 9780199227259.
- [Wen13a] A. N. Wenz, G. Zürn, S. Murmann, I. Brouzos, T. Lompe, and S. Jochim. *From few to many: Observing the formation of a Fermi sea one atom at a time*. *Science* 342.6157 (2013), pp. 457–460.
- [Wen13b] A. N. Wenz. *From Few to Many: Ultracold Atoms in Reduced Dimensions*. PhD thesis. University of Heidelberg, 2013.
- [Wer06] F. Werner and Y. Castin. *Unitary gas in an isotropic harmonic trap: Symmetry properties and applications*. *Physical Review A* 74.5 (2006), p. 053604.

- 
- [Wig34] E. Wigner. *On the Interaction of Electrons in Metals*. *Physical Review* 46.11 (1934), pp. 1002–1011.
- [Win87] D. J. Wineland, J. C. Bergquist, W. M. Itano, J. J. Bollinger, and C. H. Manney. *Atomic-Ion Coulomb Clusters in an Ion Trap*. *Physical Review Letters* 59.26 (1987), pp. 2935–2938.
- [Yan62] C. N. Yang. *Concept of off-diagonal long-range order and the quantum phases of liquid He and of superconductors*. *Reviews of Modern Physics* 34.4 (1962), pp. 694–704.
- [Yin20] X. Y. Yin, H. Hu, and X.-J. Liu. *Few-Body Perspective of a Quantum Anomaly in Two-Dimensional Fermi Gases*. *Physical Review Letters* 124.1 (2020), p. 013401.
- [Yu19] Y. Yu, L. Ma, P. Cai, R. Zhong, C. Ye, J. Shen, G. D. Gu, X. H. Chen, and Y. Zhang. *High-temperature superconductivity in monolayer  $Bi_2Sr_2CaCu_2O_{8+\delta}$* . *Nature* 575.7781 (2019), pp. 156–163.
- [Zac20] T. V. Zache, T. Schweigler, S. Erne, J. Schmiedmayer, and J. Berges. *Extracting the Field Theory Description of a Quantum Many-Body System from Experimental Data*. *Physical Review X* 10.1 (2020), p. 011020.
- [Zha04] J. Zhang, E. G. M. Van Kempen, T. Bourdel, L. Khaykovich, J. Cubizolles, F. Chevy, M. Teichmann, L. Tarruell, S. J. J. M. F. Kokkelmans, and C. Salomon. *P-wave Feshbach resonances of ultra-cold  $^6Li$* . *Physical Review A* 70.3 (2004), p. 030702.
- [Zho21] X. Zhou, W.-S. S. Lee, M. Imada, N. Trivedi, P. Phillips, H.-Y. Y. Kee, P. Törmä, and M. Eremets. *High-temperature superconductivity*. *Nature Reviews Physics* 3.7 (2021), pp. 462–465.
- [Zup16] P. Zupancic, P. M. Preiss, R. Ma, A. Lukin, M. Eric Tai, M. Rispoli, R. Islam, and M. Greiner. *Ultra-precise holographic beam shaping for microscopic quantum control*. *Optics Express* 24.13 (2016), p. 13881.
- [Zür12a] G. Zürn, T. Lompe, A. N. Wenz, S. Jochim, P. S. Julienne, and J. M. Hutson. *Precise characterization of  $^6Li$  Feshbach resonances using trap-sideband resolved RF spectroscopy of weakly bound molecules*. *Physical Review Letters* 110.13 (2012), p. 135301.
- [Zür12b] G. Zürn, F. Serwane, T. Lompe, A. N. Wenz, M. G. Ries, J. E. Bohn, and S. Jochim. *Fermionization of Two Distinguishable Fermions*. *Physical Review Letters* 108.7 (2012), p. 075303.

- [Zür13] G. Zürn, A. N. Wenz, S. Murmann, A. Bergschneider, T. Lompe, and S. Jochim. *Pairing in Few-Fermion Systems with Attractive Interactions*. *Physical Review Letters* 111.17 (2013), p. 175302.
- [Zwe12] W. Zwerger. *The BCS-BEC Crossover and the Unitary Fermi Gas*. Lecture Notes in Physics. Berlin: Springer, 2012. ISBN: 978-3-642-21977-1.
- [Zwe16] W. Zwerger. *Strongly Interacting Fermi Gases*. *Proceedings of the International School of Physics "Enrico Fermi"* 191 (2016), pp. 63–141.
- [Zwi03] M. W. Zwierlein, C. A. Stan, C. H. Schunck, S. M. F. Raupach, S. Gupta, Z. Hadzibabic, and W. Ketterle. *Observation of Bose-Einstein Condensation of Molecules*. *Physical Review Letters* 91.25 (2003), p. 250401.
- [Zwi06] M. W. Zwierlein. *High-Temperature Superfluidity in an Ultracold Fermi Gas*. PhD thesis. Massachusetts Institute of Technology, 2006.

# Acknowledgements

I would like to thank everyone who has contributed either directly or indirectly to this thesis and the work presented here. My time as PhD student has been wonderful and the accomplishments we have achieved with our experiment would not have been possible without the help of a large amount of people.

First, I would like to thank Selim Jochim for his guidance and amazing support as a mentor and group leader. Joining your group was certainly one of the best decisions I could have made! Your enthusiasm for the field and the endless amount of ideas are irreplaceable for our group.

I would also like to thank everyone in our group I had the chance to interact with during my time in Heidelberg. Starting with the first generation that has introduced me to the fascinating field of ultracold quantum gases — Andre Wenz, Martin Ries, Simon Murmann, Mathias Neidig, Vincent Klinkhammer, Andrea Bergschneider and Puneet Murthy. You have made me feel comfortable in the group from the very beginning. Your advice and the countless exciting discussions helped me in many occasions.

From my generation, I am grateful for the great team that I have spent many hours in the laboratory with — Keerthan Subramanian, Jan-Hendrik Becher, Ralf Klemt and especially Luca Bayha. In your company, I have always enjoyed working on the experiment and implementing new upgrades. You have made even the sometimes seemingly endless search for broken components much more endurable.

I also thank the next generation that is starting to take over the experiments now — Sandra Brandstetter, Carl Heintze, Philipp Lunt, Paul Hill, Tobias Hammel and Maximilian Kaiser. I am looking forward to the discoveries you are going to make and I am certain that all three experiments are in good hands.

I thank our two postdocs Philipp Preiss and Gerhard Zuern. Your support and supervision has helped tremendously, especially when facing very complex problems or for the preparation of manuscripts.

Even the best experimental data is not very useful without a profound understanding of the theoretical background. To this end, I would like to thank all the theorists that me and our group in general had the chance to collaborate with during the years — Tilman Enss and Nicolás Defenu as experts for macroscopic Fermi gases and Johannes Bjerlin, Stephanie Reimann, Georg Bruun and Alexandre Faribault for any questions in the mesoscopic limit.

I would also like to thank Claudia Kraemer for taking care of the administrative tasks.

Considering my thesis, I want to thank everyone who has helped me with proof reading — Keerthan, Luca, Sandra, Carl, Philipp L., Tobias, Maximilian and especially Alexandra. I am grateful that Markus Oberthaler agreed to read my thesis as the second referee. I would also like to thank the other members of my committee — José R. Crespo López-Urrutia and Joerg Jaeckel.

Last but not least, I would like to thank my friends and family for their continuous support over the years. Without you achieving my goals would not have been possible. I thank my parents Alexandra and Thomas, my relatives Annette, Uschi, Werner and Maria and my friends who have accompanied me since I have started my studies — Nick, Max, Andre and Michele.

Most importantly, I thank Johanna for always being there for me and supporting me in all possible ways.